Polaron Physics and Phase Transitions in Light-Matter Systems

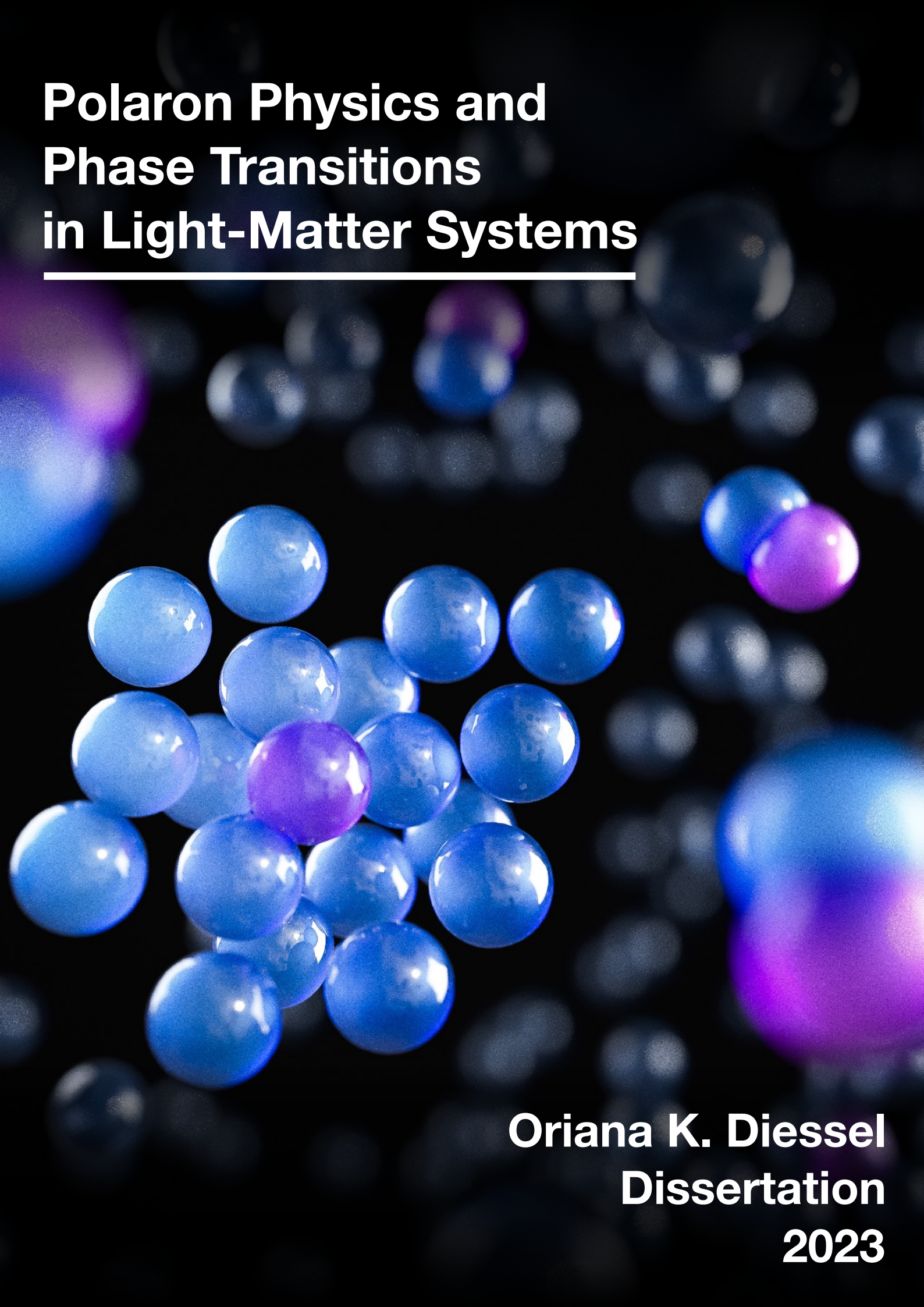

Oriana K. Diessel

Dissertation

2023

Cover illustration by Christoph Hohmann/MQCST

TECHNISCHE UNIVERSITÄT MÜNCHEN

TUM School of Natural Sciences

Polaron Physics and Phase Transitions in Light-Matter Systems

Oriana K. Dießel

Vollständiger Abdruck der von der TUM School of Natural Sciences zur Erlangung des akademischen Grades einer

Doktorin der Naturwissenschaften (Dr. rer. nat.)

gehnehmigten Dissertation.

Vorsitz:	Prof. Jonathan J. Finley, Ph.D.
*Prüfer*innen der Dissertation:*	1. Hon.-Prof. Dr. J. Ignacio Cirac
	2. Prof. Dr. Jan von Delft

Die Dissertation wurde am 24.07.2023 bei der Technischen Universität München eingereicht und durch die TUM School of Natural Sciences am 05.09.2023 angenommen.

Abstract

This doctoral thesis deals with the physics of quantum many-body systems and is divided into two parts: The physics of polarons and the physics of phase transitions in light-matter systems. The first part is devoted to the study of Fermi and Bose polarons in ultracold atoms and in TMD materials. Using the Chevy Ansatz for Fermi polarons and molarons, we theoretically calculate Raman spectra for both injection and ejection protocols in ultracold atom setups. Furthermore, we provide a theoretical description of the experimental realization of Bose polarons in a monolayer of $MoSe_2$ embedded in an optical cavity, where polaritons with different polarizations can act as impurities or baths. We show here that by exploiting a biexciton Feshbach resonance, the interaction between polarons can be tuned between repulsive and attractive. The second part of the thesis deals with phase transitions in light-matter systems. We first show that driven-dissipative Bose gases featuring a quadratic drive can exhibit a phase diagram radically different from the one exhibited by its equilibrium counterpart. The non-equilibrium nature of the fluctuations can suppress the condensate and the BKT phases present at equilibrium and replace them with a disordered phase where the correlation exhibits a KPZ-like scaling. This physics can be reproduced in experiments with exciton-polaritons. Finally, we consider the case of systems with tunable long-range interactions (realizable with cavity photons coupled to matter degrees of freedom) and show that, upon increasing the range of the interaction, symmetry-broken phases usually hosting Goldstone modes can be substantially modified. In particular, the dispersion of the Goldstone modes can acquire unusual dependencies at small momenta, and even become gapped if the interactions are long-range enough. We show this for different spin systems and for a Bose gas, and demonstrate that these effects should be visible in current experimental setups with ultracold atoms in an optical cavity.

Kurzzusammenfassung

Diese Doktorarbeit befasst sich mit der Physik von Quantenvielteilchensystemen und ist in zwei Teile gegliedert: Die Physik von Polaronen und die Physik von Phasenübergängen in Licht-Materie-Systemen. Der erste Teil ist der Untersuchung von Fermi- und Bose-Polaronen in ultrakalten Atomen und in TMD-Materialien gewidmet. Die ersten Ergebnisse drehen sich um Experimente mit ultrakalten Fermi-Gasen. Unter Verwendung des Chevy-Ansatzes für Fermi-Polaronen und Molaronen berechnen wir theoretisch Raman-Spektren sowohl für Injection- als auch für Ejection-Protokolle. Darüber hinaus liefern wir eine theoretische Beschreibung der experimentellen Realisierung von Bose-Polaronen in einer Monolage aus $MoSe_2$, die in eine optische Cavity eingebettet ist. Hier können Polaritonen mit unterschiedlicher Polarisation entweder als Störstellen oder als Bad fungieren. Wir zeigen, dass durch Ausnutzung einer Biexzitonen-Feshbach-Resonanz die Wechselwirkung zwischen Polaronen variiert, und sogar von repulsiv zu attraktiv durchgestimmt werden kann. Der zweite Teil der Arbeit beschäftigt sich mit Phasenübergängen in Licht-Materie-Systemen. Wir zeigen zunächst, dass getrieben-dissipative Bose-Gase mit einem quadratischen Antrieb ein im Vergleich zum Gleichgewicht stark modifiziertes Phasendiagramm aufweisen können. Der Nicht-Gleichgewichtscharakter der Fluktuationen kann die Kondensat- und die BKT-Phase im Gleichgewicht unterdrücken und sie durch eine ungeordnete Phase ersetzen, in der Korrelationen eine KPZ-ähnliche Skalierung aufweisen. Diese Physik kann in Experimenten mit Exziton-Polaritonen sichtbar gemacht werden. Schließlich betrachten wir den Fall von Systemen mit abstimmbaren langreichweitigen Wechselwirkungen (realisierbar beispielsweise Licht-Materie-Systemen) und zeigen, dass bei Erhöhung der Reichweite der Wechselwirkung die Goldstone-Moden, assoziiert mit den symmetriegebrochene Phasen, erheblich modifiziert werden können. Die Dispersion der Goldstone-Moden kann bei kleinen Impulsen ungewöhnliche Abhängigkeiten annehmen und, wenn die Wechselwirkungen langreichweitig genug sind, sogar ein Gap entwickeln. Wir zeigen dies für verschiedene Spinsysteme und für Bose-Gase mit langreichweitigen Wechselwirkungen, und demonstrieren, dass diese Effekte in aktuellen Experimenten mit ultrakalten Atomen in Cavities sichtbar sein sollten.

Publications

This work is based on the following articles, ordered by appearance in this thesis. The last publication is not the subject of this dissertation.

[P1] *Observation of a Smooth Polaron-Molecule Transition in a Degenerate Fermi Gas*
Gal Ness, Constantine Shkedrov, Yanay Florshaim, **Oriana K. Diessel**, Jonas von Milczewski, Richard Schmidt, and Yoav Sagi,
Phys. Rev. X **10**, 041019 (2020).

[P2] *Probing molecular spectral functions and unconventional pairing using Raman spectroscopy*
Oriana K. Diessel, Jonas von Milczewski, Arthur Christianen, and Richard Schmidt,
arXiv:2209.11758 (2022).

[P3] *Bose Polaron Interactions in a Cavity-Coupled Monolayer Semiconductor*
Li Bing Tan*, **Oriana K. Diessel***, Alexander Popert, Richard Schmidt, Ataç İmamoğlu, and Martin Kroner, **equal contribution*,
Phys. Rev. X **13**, 031036 (2023).

[P4] *Emergent Kardar-Parisi-Zhang Phase in Quadratically Driven Condensates*
Oriana K. Diessel, Sebastian Diehl, and Alessio Chiocchetta,
Phys. Rev. Lett. **128**, 070401 (2022).

[P5] *Generalized Higgs mechanism in long-range-interacting quantum systems*
Oriana K. Diessel, Sebastian Diehl, Nicolò Defenu, Achim Rosch and Alessio Chiocchetta,
Phys. Rev. Res. **5**, 033038 (2023).

[P6] *Floquet-Engineered Nonlinearities and Controllable Pair-Hopping Processes: From Optical Kerr Cavities to Correlated Quantum Matter*
Nathan Goldman, **Oriana K. Diessel**, Luca Barbiero, Maximilian Prüfer, Marco Di Liberto, and Lucila Peralta Gavensky,
PRX Quantum **4**, 040327 (2023).

Contents

Preface

Our daily lives rely on a wide range of physical phenomena that often go unnoticed. Simply switching on our phone in the morning to check our emails makes heavy use of the semiconducting character of silicon chips, as well as of the properties of several magnetic materials (e.g. NdFeB), which are needed for the haptics in the phone's alarm clock or for wireless charging. While these macroscopic material properties may seem trivial, they are in fact rooted in the collective behavior of objects nearly ten orders of magnitude smaller than those of our every-day experience. A single gram of the silicon used in the chips in our smartphones contains approximately 10^{23} electrons. It is the interaction between these electrons that gives rise to much of the world we observe around us. If we seek to comprehend it, we must first develop a deeper understanding of the underlying physics.

This task falls to the area of physics known as quantum-many-body physics, which studies systems consisting of a large number of interacting particles obeying the laws of quantum mechanics and exhibiting quantum properties at a macroscopic scale under certain conditions (e.g., at low temperature). The distinctive feature of many-body systems such as silicon is that their properties emerge from the collective behavior of the components of the system and cannot be understood by looking at individual particles in isolation.

One of the keys to the success of quantum-many-body physics lies in its ability to explain and predict the *emergent phenomena* and *collective behavior* exhibited by those materials, such as magnetism and phase transitions. But, its predictive power is not limited to the every-day experiences mentioned above. Indeed, quantum-many-body physics also reveals to us stranger and more peculiar phenomena, such as superconductivity and superfluidity.

However, the study of quantum many-body systems is an immense challenge both analytically and numerically, as they involve a large number of degrees of freedom, interactions between particles, and statistical and quantum fluctuations. One therefore has to frequently resort to approximations: on the analytical side, for example, a common approach consists in identifying the quasiparticles in the system and using them as main ingredients to predict the system properties. On the numerical side, one typically considers small system sizes and tries to extrapolate the results towards the thermodynamical limit. In this regard, *quantum impurity problems* hold a special place, because in these settings interactions only occur with a single (mobile) impurity, and the bath particles either do not or only weakly interact with each other. This makes quantum impurity problems simpler to describe and provides a natural starting point for successively including more impurities (and thereby interactions), thus moving towards the full interacting quantum many-body system in a controlled way.

Complementary to the theoretical approach, the extraordinary advances in experimental techniques over the past two decades have made it possible to simulate quantum many-body systems in the lab, exploring previously inaccessible regimes including the limit of only very few quantum impurities. Ultracold quantum gases, for example, feature extremely precise and versatile experimental control as well as a great degree of tunability in regard to the system's geometry, dimensionality and interactions between the single components. They therefore provide a very clean testbed for simulating quantum systems and comparing the results to predictions of quantum many-body theory. Another type of experimental platform that has flourished in the past two decades are light-matter systems. These refer to physical systems composed of both photons and matter degrees of freedom (such as electrons, atoms or excitons) which are made to interact with each other. This field is undergoing rapid evolution, combining various methods that enable the manipulation and control of quantum matter by utilizing electromagnetic fields. Light-matter systems provide an ideal platform to engineer and study extreme physical conditions as, for example, driven-dissipative systems or systems with long-range interactions.

This thesis addresses two different topics within the field of theoretical quantum many-body physics: In the

first part of the thesis, we delve into the physics of mobile quantum impurities, called polarons, and investigate the implications of moving beyond the single impurity limit to finite impurity density. In the second part of the thesis, our focus lies on phase transitions and emergent phenomena in light-matter systems.

Part 1: Impurity and composite excitations in quantum many-body systems

This part is devoted to the study of polarons and molarons, which are single and composite quasiparticles that arise from the interaction between a moving impurity and the surrounding medium. These quasiparticles are fascinating objects themselves, as they can have the same or different statistics than the underlying impurity and modified properties, such as effective mass, lifetime and dispersion. Here, we are specifically interested in the implications of moving beyond the single impurity limit to finite impurity density. Our work is inspired by experimental studies of polarons and molarons in ulracold atom setups and atomically thin semiconductors.

In Chap. 1, we start with an introduction to ultracold quantum gases and the Fermi polaron problem. We specifically focus on the theoretical description of Raman spectroscopy in ultracold Fermi gases with impurities. Firstly, we show how Raman spectroscopy can be used to study the fate of the polaron-to-molecule transition in the finite temperature and impurity density regime, where the statistics of quantum impurities and thermal effects become relevant. In a theory-experiment collaboration with the Sagi group at the Technion, we found that several quantities, including the quasiparticle spectral weight and the contact parameter, show a smooth transition with no sudden changes around the predicted polaron-to-molaron transition [7, 8], both in experiment and theory [P1]. This strongly suggests a coexistence phase of polarons and molarons around the interaction strength where the first-order transition in the single-impurity limit takes place. Remarkably, up to now it has not been possible to experimentally characterize the molaron state due to a lack of spectroscopic methods. In the second part of Chap. 1, we propose a new spectroscopic protocol based on Raman transitions that tackles this challenge and allows to probe the momentum-resolved spectral function of the molaron [P2]. Furthermore, we show a remarkable link between the finite momentum properties of molarons and the emergence of the elusive Fulde–Ferrell–Larkin–Ovchinnikov (FFLO) phase (governed by unconventional pairing of electrons into finite momentum Cooper pairs [9, 10]) which is predicted to occur in imbalanced Fermi-Fermi mixtures. This connection implies a simple picture of the FFLO phase as emerging from a condensate of molarons. A precursor of this phase can now be readily probed using our proposed molecular injection spectroscopy technique.

In Chap. 2, we turn to the description of Bose polarons, i.e. a single impurity immersed in a Bose-Einstein condensate. Specifically, we focus on the case of their experimental realization in atomically thin semiconductors coupled to an optical cavity. In a theory-experiment collaboration with the İmamoğlu group at ETH Zurich, we investigated interactions between impurities mediated by the medium by monitoring the changes in the polaron spectrum as a function of the impurity density. We show both experimentally and theoretically how the interaction between impurity particles depends on the density of the impurities, and how they can be manipulated and changed in sign and magnitude, e.g., from repulsive to attractive interactions [P3]. Our findings thus suggest that the observation of pairing between polarons may be in reach in two-dimensional materials.

Part 2: Phase transitions in light-matter systems

The second part of the thesis deals with collective behavior in light-matter interacting systems. The increasing level of control over the interactions between light and atomic or solid-state systems makes them ideal platforms to engineer and study unconventional physics, for example, driven-dissipative systems or systems with long-range interactions. In fact, the inherently finite lifetime of photons in cavities requires the continuous injection of new photons, giving light-matter systems a driven dissipative nature: this, in turn, has a typical nonequilibrium character, and cannot be described using the textbook tools of quantum statistical physics. Additionally, in open quantum systems, the competition between dissipative and coherent processes can produces a wealth of collective phenomena, absent in their equilibrium counterpart. Conventional states, such as ordered magnetic states, can be replaced by novel collective behaviors such as, for instance, time crystals [11] and chiral dynamics in driven-dissipative quantum magnets [12]. Photons in cavities can moreover

generate effective long-range interactions between the matter degrees of freedom: these kinds of interactions can generate states of matter which are qualitatively different from their short-range counterparts and which can escape some paradigms of condensed matter physics, such as the Mermin-Wagner and the Goldstone theorem, even at thermal equilibrium.

After providing introductions to light-matter systems and phase transitions in Chaps. 3 and 4, we turn to the theoretical study of quadratically driven-dissipative bosons in Chap. 5. Here we particularly focus again on the case of exciton-polaritons. We discuss a novel incarnation of the Kardar-Parisi-Zhang (KPZ) phase in these systems, which represents one of the most paradigmatic examples of nonequilibrium universality. While KPZ signatures are abundant in one-dimensional physical systems, they have remained experimentally elusive and even numerically difficult to tackle quantitatively in the two-dimensional case. Using nonequilibrium field theory and renormalization group methods, we show that in two dimensions, a phase described by KPZ scaling emerges on experimentally accessible length scales, and this KPZ phase replaces the Ising phase expected for equilibrium gases, providing a novel example of how nonequilibrium fluctuations might dramatically modify equilibrium behavior [P4].

In Chap. 6, we investigate the connection between the expanding research field of quantum long-range interacting systems and the celebrated Higgs mechanism. Specifically, we study the low-energy excitations of several long-range interacting quantum systems, including spin models and interacting Bose gases, in the ordered phase associated with the spontaneous breaking of U(1) and SU(2) symmetries. Instead of the expected gapless Goldstone modes, we find three qualitatively different regimes, depending on the range of the interaction [P5]. In the first regime, the Goldstone modes are gapped, realizing a generalized Higgs mechanism. In the remaining two regimes the Goldstone modes are still gapless but with an anomalous algebraic dispersion or with the usual one for short-range interacting systems. We furthermore demonstrated the visibility of this mechanism in current experiments of atomic gases in optical cavities. Finally, we conclude the thesis with summarizing remarks and an outlook on future avenues and interesting directions.

Part I

Impurity and composite excitations in quantum many-body systems

Chapter 1

Impurity spectroscopy in ultracold quantum gases

This chapter is based on the following publications
G. Ness, C. Shkedrov, Y. Florshaim, O. K. Diessel, J. von Milczewski, R. Schmidt, and Y. Sagi, *Observation of a Smooth Polaron-Molecule Transition in a Degenerate Fermi Gas*,

Phys. Rev. X **10**, 041019 (2020)

O. K. Diessel, J. von Milczewski, A. Christianen, and R. Schmidt, *Probing molecular spectral functions and unconventional pairing using Raman spectroscopy*,

arXiv:2209.11758v1 (2022)

1.1 Introduction

This chapter will discuss spectroscopic protocols used to study impurity physics in ultracold fermionic quantum gases. The situation where a single (usually mobile) impurity is embedded and interacting with a degenerate gas of fermions is called the Fermi polaron problem. The Fermi polaron problem appears in a multitude of different physical systems ranging from ultracold quantum gases and semiconductors [13] to neutron stars [14].

Depending on the impurity's quantum statistics, the Fermi polaron problem also represents the extreme limit of an imbalanced Fermi-Fermi or Bose-Fermi mixture. Both of these systems are of particular interest, as they are expected to feature rich many-body physics: On the one hand, strongly interacting Fermi systems exhibit many complex phases, including the elusive Fulde-Ferrell-Larkin-Ovchinnikov (FFLO) phase [9, 10] and itinerant ferromagnetism [15, 16]. On the other hand, phases in strongly interacting Bose-Fermi systems include boson-induced unconventional superconductivity [17, 18] and supersolid charge density wave states [19]. However, strongly interacting mixtures are theoretically extremely hard to describe and their phase diagrams remain largely unexplored, making them the subject of current research [20–22]. In this respect, the Fermi polaron problem represents a controlled starting point for the investigation of two-component mixtures.

One platform to investigate the Fermi polaron problem in a clean and controlled environment are ultracold atomic gases. Here, Feshbach resonances allow for tunable interactions between the bath and the impurity particle, and spectroscopic methods enable the creation and study of impurities. Furthermore, the density ratio between impurity and bath particles can be tuned, which allows one to enter the regime of a finite impurity number and thereby the subsequent study of strongly interacting two-component mixtures.

After a short overview of ultracold quantum gases and Feshbach resonances, we introduce the Fermi polaron problem and show how this can be modelled theoretically. Next, we turn to a brief discussion of spectroscopic

methods in ultracold quantum gases. In Sec. 1.2, we show how the polaron-to-molaron transition, defined in the single impurity limit, is modified by a finite density of impurities and finite temperature. We furthermore demonstrate how this can be probed using Raman ejection spectroscopy. In Sec. 1.3, we introduce a new spectroscopic protocol based on Raman transitions that allows us to access a class of quasiparticles known as molarons; composite states which appear in the Fermi polaron problem. Moreover, we show a remarkable link between the finite momentum properties of molarons and the elusive FFLO phase which emerges for finite population imbalance. A precursor of this FFLO phase can now be probed using our proposed protocol.

1.1.1 Ultracold quantum gases

The first experimental realization of Bose-Einstein condensates in 1995 [23, 24], followed by the creation of degenerate Fermi gases four years later [25], initiated a flurry of experimental activity with ultracold quantum gases. Ultracold atoms are a well-established platform used to study and simulate a broad variety of physical phenomena, including the exploration of polaron physics. This is due to the fact that firstly, ultracold gases allow for high experimental controllability, secondly, the atoms behave like point-like particles with short-range interactions at the prevailing energies, making them easy for theoretical modelling, and thirdly, they allow for tunable interaction strengths in the form of Feshbach resonances.

The physics of ultracold quantum gases is determined by the interplay of several scales. Given a d-dimensional homogeneous gas of atoms with density n, one can define the inter-particle spacing as

$$l = n^{-\frac{1}{d}}.$$

In experiments the ultracold atoms are confined in (usually harmonic) optical traps. Therefore, the density of the atoms is not homogeneous but instead depends on space. The length scale associated with a harmonic trap is called oscillator length, and is given by

$$l_{\text{osc}} = \left(\frac{\hbar}{m\omega_0}\right)^{1/2} \tag{1.1}$$

with ω_0 the trapping frequency. It is typically the largest length scale in the system and the physics under consideration occurs on much smaller scales. Therefore, in many cases, it is justified to assume a locally homogeneous system which is known as the local density approximation. We will discuss how this is done in Sec. 1.2, when we compare theoretical calculations to measurements performed on harmonically trapped atoms.

According to wave-particle duality, the de Broglie wavelength is the wavelength associated with all quantum mechanical objects, and determines the probability density of finding the object at a given point in space. It is given by

$$\lambda_{\text{dB}} = \frac{2\pi\hbar}{p} = \left(\frac{2\pi\hbar^2}{mk_{\text{B}}T}\right)^{1/2}, \tag{1.2}$$

where p and m are momentum and mass of the object, k_{B} is the Bolzmann constant and T is the temperature. The second equivalence comes from connecting the particle's kinetic energy to the temperature via $p^2/2m = \pi k_B T$. Thus the de Broglie wavelength determines the length scale above which the quantum coherence is suppressed by thermal fluctuations. Comparing the inter-particle distance to the de Broglie wavelength of the particles provides information about how quantum a system behaves: If $l \gg \lambda_{\text{dB}}$, the wave packets of individual particles do not overlap, and the gas can be described classically. However, for $l \lesssim \lambda_{\text{dB}}$, the wavepackets strongly overlap. In this case, one speaks of an *ultracold*, or *degenerate* gas.

Let us additionally consider interactions between particles. The alkali (single valence electron) atoms used in ultracold gas experiments are neutral and interact via van der Waals forces. At a small separation r between

atomic radius r_A/a_0	van der Waals length l_{vdW}/a_0	interparticle spacing l/a_0	de Broglie wavelength $\lambda_{\mathrm{dB}}/a_0$	trap size l_{osc}/a_0
$2-4$	$30-100$	$(0.8-10)\times 10^3$	$(3-40)\times 10^3$	$(3-300)\times 10^3$

Table 1.1: Typical length scales of ultracold alkali atoms in units of the Bohr radius $a_0 = 0.53 \times 10^{-10}$m [26].

two atoms, the interaction potential $V(r)$ is strongly repulsive, stemming from the Pauli principle which forbids the overlap of their respective electronic clouds.

For a separation between two atoms much larger than their size ($\sim r_A$), the atoms experience an attraction that originates from the polarizability of the electron clouds. Each atom then behaves as an induced dipole, resulting in an attraction between two atoms according to $V(r) = -C_6/r^6$ for $r \to \infty$. At the low energies prevailing in an ultracold gas, next order interaction terms such as dipole-quadrupole or quadrupole-quadrupole are subleading.

A characteristic length scale for the interaction can be obtained from equating the kinetic and the potential energy of the two interacting particles, which renders the van der Waals length

$$l_{\mathrm{vdW}} = \left(\frac{2\mu C_6}{\hbar^2}\right)^{1/4},$$

where μ is the reduced mass of the particles. For alkali atoms, the van der Waals length is between one and two orders of magnitude larger than the atomic radii r_A, but crucially, is much smaller than the interparticle spacing and the de Broglie wavelength (typical values for alkali atoms can be found in Tab. 1.1). The van der Waals length represents a natural scale for the interaction between two particles.

In ultracold quantum gases, the scattering between two particles can be well approximated by s-wave (angular momentum $L = 0$) scattering[1]; This is due to the presence of a centrifugal barrier term in the Schrödinger equation of relative motion for finite angular momentum. At the typical energy scales of ultracold gases, this term is dominant and prohibits higher order scattering processes. The low momentum scattering is mainly described by the *s-wave scattering length* a. This length scale characterizes two-body collisions in potentials of sufficiently short range, such as the van der Waals potential. It can be extracted from the zero energy limit of the scattering amplitude. The next-order expansion coefficient of the scattering amplitude after the exact zero energy limit, is the *effective range* r_e[2]. The effective range parameter needs to be included for the description of scattering processes for example in the vicinity of a closed channel-dominated Feshbach resonances, as described below.

Due to the separation of scales present in ultracold atom systems, the de Broglie wavelength of atoms prevents them from resolving the precise shape of the scattering potential. Therefore, the true interaction potential can be replaced by a pseudo potential which correctly reproduces low-energy observables like the scattering length a and the effective range r_e.

In order to obtain an intuitive understanding of the scattering length a, let us consider two attractively interacting particles in three dimensions in the center-of-mass frame. Following our argument above, the microscopic interaction potential can be replaced by a pseudo potential. Here we assume a square well potential located at radial distance $r = 0$ with variable depth V_0 corresponding to tunable interactions between the particles (Fig. 1.1). In the vicinity of the potential, the wavefunction of the mobile particle is drawn towards it, and for large distances takes the form $\psi(r) \sim \sin(kr + \delta)$. The asymptotic behaviour of the wavefunction is characterized by only one constant, the phaseshift δ which, for a finite range potential, has a power series

[1] Due to Pauli blocking, two identical fermions cannot scatter in the s-wave channel. In fermionic ultracold gases, identical fermions are therefore nearly non-interacting.

[2] It can be obtained by expanding the scattering amplitude in the relative momentum between the two scattering atoms.

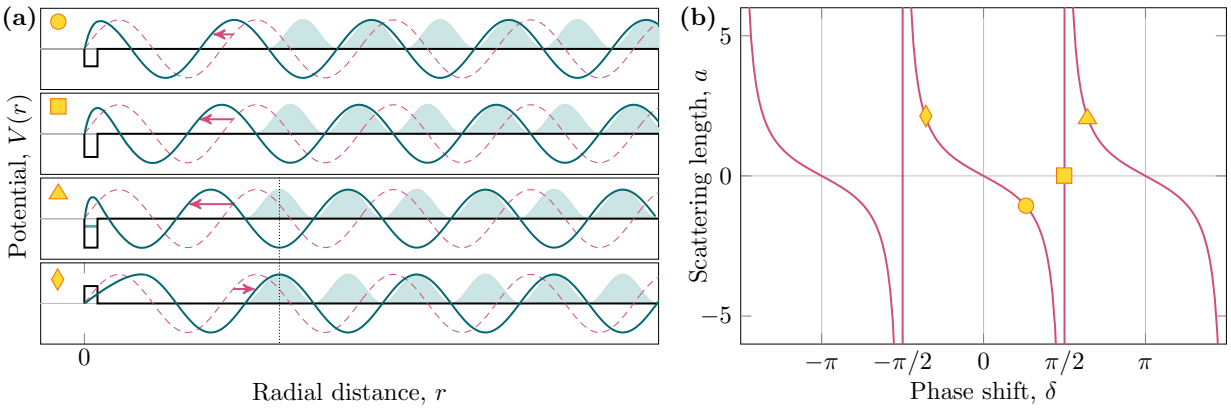

Figure 1.1: (a) Radial wavefunction of a particle (blue) scattering off a square well potential (black), compared to the wavefunction of a particle which does not see any potential (pink, dashed). The pink arrows indicate the phase shift δ. The corresponding scattering lengths a can be inferred from subfigure **(b)**. The blue shaded region shows the absolute value squared of the wavefunction in presence of a potential. *Circle:* For a shallow potential, the wavefunction of the scattered particle is only slightly drawn towards the potential, corresponing to a negative scattering length a and a phaseshift $0 < \delta < \pi/2$. *Square:* At resonance, $\delta = \pi/2$, the scattering length diverges. *Triangle:* For a potential of sufficient depth, a bound state emerges. The scattering lengths becomes positive and the phaseshift $\delta > \pi/2$. *Diamond:* Remarkably, a repulsive potential can lead to the same squared wave function profile as an attractive potential featuring a bound state, resulting in the same scattering length a. However in this case the scattering length can not exceed the range of the potential, unlike in the case of an attractive potential.

expansion around $k = 0$:

$$k \cot(\delta) = -\frac{1}{a} + \frac{1}{2} r_e k^2 + \mathcal{O}(k^4). \tag{1.3}$$

In the zero energy limit[3], the phase shift is related to the scattering length a via

$$a = -\lim_{k \to 0} \frac{\tan(\delta)}{k}.$$

From this expression it becomes apparent that the scattering length can take both positive and negative values, despite the purely attractive interactions present on a microscopic level. As depicted in Fig. 1.1, one can discriminate between three different regimes:

1. For small attractions, the phase shift is $0 < \delta < \pi/2$ and the scattering length is negative. The intercept of the asymptotic wave function is negative, and it appears as though the particles are attracted to each other (see circle in Fig. 1.1 (a)).

2. If the phase shift becomes $\delta = \pi/2$, the scattering length diverges (see square in Fig. 1.1 (b)), thus becoming the largest length scales in the system. In this situation, the physics becomes independent of a. This is called the unitary regime.

3. For strong interactions, the phase shift is $\delta > \pi/2$ and the potential is deep enough to feature a bound state. The scattering length is positive. The intercept of the asymptotic wave function is positive and the particles appear to repeal each other (see triangle in Fig. 1.1 (b)).

When the potential is sufficiently deep, a scattering resonance with an associated bound state occurs. In contrast to the model potential, interaction potentials between real atoms in general do not have a variable depth. However, there exists a tool to tune the scattering length of ultracold atoms to arbitrary values $-\infty \leq a \leq \infty$ in a controlled way. Underlying this principle are Feshbach resonances, which are discussed in the following subsection.

[3] Disregarding the effective range correction.

1.1.2 Feshbach resonances

The main properties of Feshbach resonances can be explained using a simple picture. As discussed above, the scattering potential between two atoms at distance r can be modelled by the Lennard-Jones potential

$$V_o(r) \sim \frac{C_{12}}{r^{12}} - \frac{C_6}{r^6}, \tag{1.4}$$

which asymptotically connects to two eigenstates of the free atoms. Here we have included a subscript o, as in the context of Feshbach resonances, this potential is commonly referred to as the open channel.

We now consider a second potential V_c, which asymptotically connects to two eigenstates of the free atoms with different magnetic moment (see Fig. 1.2 (a)). These excited eigenstates are higher in energy and therefore asymptotically not accessible to ultracold atoms. The corresponding potential is commonly referred to as the closed channel. The essential requirement for a Feshbach resonance to exist is the presence of a bound state in the closed channel.

A Feshbach resonance occurs when the bound state in the closed channel resonantly couples to the atoms scattering in the open channel. In experiments, the energy difference between both channels can be controlled via a magnetic field. The scattering length close to a Feshbach resonance as a function of the magnetic field B can be described by

$$a(B) = a_{\text{bg}} - \frac{2}{r^* \delta\mu (B - B_0)}. \tag{1.5}$$

The background scattering length a_{bg} is associated with the open channel potential. The parameter B_0 denotes the position of the resonance at which the scattering length diverges, r^* characterizes the resonance width as a function of the magnetic field[4], and $\delta\mu$ is the difference in magnetic moments of the open and closed channels. At the scattering resonance ($a \to \infty$), a molecular bound state emerges which becomes more tightly bound for decreasing positive scattering lengths. Its energy is shown in Fig. 1.2 (b). Near resonance, the coupling between the open and closed-channel mixes their contributions. The energy of the molecular state in this (universal) regime is given by

$$E_b = \frac{\hbar^2}{2\mu a^2}, \tag{1.6}$$

with μ the reduced mass of the two atoms. Far from the resonance, the bound state energy depends linearly on the magnetic field with a slope given by $\delta\mu$.

Feshbach resonances can be divided into open- and closed-channel dominated Feshbach resonances. To this end, one can define the dimensionless resonance strength parameter [27]

$$s_{\text{res}} = \frac{\bar{a}}{r^*} \tag{1.7}$$

which depends on r^* and the mean scattering length $\bar{a} = 4\pi l_{\text{vdW}}/\Gamma(1/4)^2$ with $\Gamma(x)$ the Gamma function.

When $s_{\text{res}} \ll 1$, the resonance is called a closed-channel dominated resonance. In this case, the bound state has the character of the open channel only over a small fraction of the resonance width near the resonance position (see Fig. 1.2 (b)). Systems close to a closed-channel dominated resonance need to be modelled by a coupled channels description, taking into account the scattering length a and the effective range parameter r_e. This can be done using a two-channel Hamiltonian

$$\mathcal{H}^{\text{2-Ch}} = \sum_{\mathbf{p}} \varepsilon^c_{\mathbf{p}} c^\dagger_{\mathbf{p}} c_{\mathbf{p}} + \sum_{\mathbf{p}} \varepsilon^d_{\mathbf{p}} d^\dagger_{\mathbf{p}} d_{\mathbf{p}} + \sum_{\mathbf{p}} (\xi_{\mathbf{p}} + \nu)\, m^\dagger_{\mathbf{p}} m_{\mathbf{p}} + \frac{h}{\sqrt{V}} \sum_{\mathbf{l},\mathbf{p}} m^\dagger_{\mathbf{p}} c_{\mathbf{l}} d_{-\mathbf{l}+\mathbf{p}} + \text{h.c.}. \tag{1.8}$$

[4] The parameter r^* is related to the effective range via $r^* = -r_e/2$

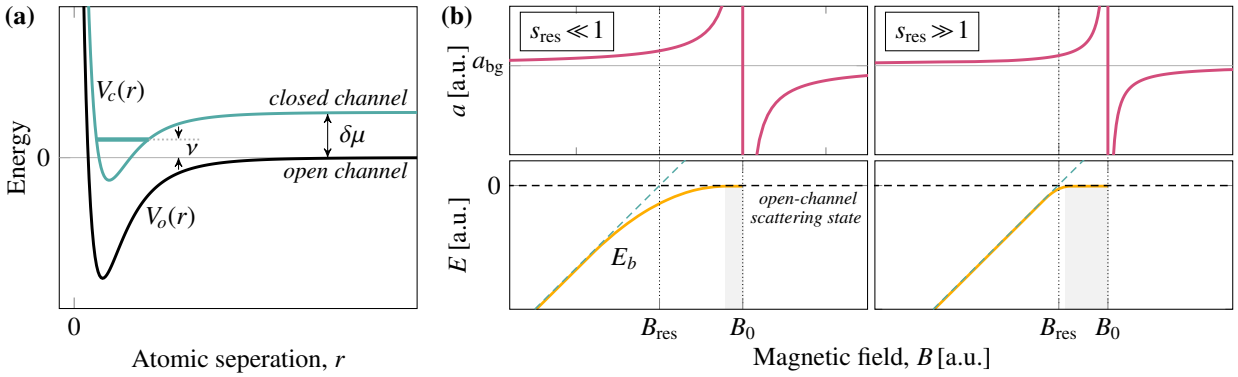

Figure 1.2: **(a)** Interaction potentials for a Feshbach resonance. The resonance phenomenon occurs when the bound state in the closed channel (blue) resonantly couples to the atoms scattering in the open channel (black). In ultracold gas experiments, the energy level of the bound state with respect to the open channel can be tuned via an external magnetic field. **(b)** Comparison of closed-channel (left) and open-channel (right) dominated Feshbach resonances. The upper plots shows the scattering length (pink) as a function of the magnetic field, and the lower plots the corresponding bound state energies (yellow). The gray shaded region indicates the area in which the bound-state energy closely follows that of the open-channel and has a vanishing closed-channel admixture. For a closed-channel dominated Feshbach resonance, this region is small compared to the range of scattering length enhancement, whereas for the open-channel dominated resonance it is comparable.

Unless explicitly stated otherwise, in what follows we assume $\hbar = 1$. The first two terms describe two different atoms ($d^\dagger_{\mathbf{p}}$ and $c^\dagger_{\mathbf{p}}$) of mass $M_{d/c}$ with respective dispersion relations $\varepsilon^{d/c}_{\mathbf{p}} = \mathbf{p}^2/2M_{d/c}$. These can scatter in the open channel, which, for simplicity, we set to zero, resulting in a vanishing background scattering length a_{bg}. The third term describes the propagation of the molecule ($m^\dagger_{\mathbf{p}}$) in the closed channel. The bare molecule is detuned from the zero of the open channel by a magnetically tunable detuning ν. The last term describes the conversion of the open channel atoms into the closed channel molecule, and vice versa. The conversion factor h is proportional to the width of the Feshbach resonance and, along with the detuning ν, it can be tuned to reproduce the s-wave scattering length a and effective range r_e (or equivalently r^*) of the impurity-bath interaction via $\nu_0/h^2 = -\mu/2\pi a + V^{-1}\sum_{\mathbf{k}} 1/(\varepsilon^c_{\mathbf{k}} + \varepsilon^d_{\mathbf{k}})$ and $h^2 = \pi/r^*\mu^2$ with $\mu = M_d M_c/(M_d + M_c)$ [27].

The eigenstates of the system feature a bound state, which we call physical molecule (in order to discriminate it from the molecular state in the closed channel). For $h \to 0$, the physical molecule is a pointlike particle, described by the operator m. For h small, the physical molecule is a linear combination of the m-particle and the $d^\dagger c^\dagger$ scattering states. This case describes the situation of a closed-channel dominated Feshbach resonance.

Resonances with $s_{\text{res}} \gg 1$ are called open-channel dominated Feshbach resonances. In this case, the bound state has the character of the open channel over a large range of the scattering enhancement, as can be seen in Fig. 1.2 (b). In this regime, the system is well described by a single-channel Hamiltonian

$$\mathcal{H}^{\text{1-Ch}} = \sum_{\mathbf{p}} \varepsilon^c_{\mathbf{p}} c^\dagger_{\mathbf{p}} c_{\mathbf{p}} + \sum_{\mathbf{p}} \varepsilon^d_{\mathbf{p}} d^\dagger_{\mathbf{p}} d_{\mathbf{p}} + \frac{U}{V} \sum_{\mathbf{p},\mathbf{p}',\mathbf{l}} c^\dagger_{\mathbf{p}} d^\dagger_{\mathbf{p}'} c_{\mathbf{p}'-\mathbf{l}} d_{\mathbf{p}+\mathbf{l}}, \tag{1.9}$$

which only takes into account the interaction between the impurity and the bath particles in the open channel. The interaction strength U is related to the s-wave scattering length a by the Lippmann–Schwinger equation $U^{-1} = \mu/2\pi a - V^{-1}\sum_{\mathbf{k}} 1/(\varepsilon^c_{\mathbf{k}} + \varepsilon^d_{\mathbf{k}})$. The single-channel Hamiltonian can be derived from the two-channel Hamiltonian (1.8) upon taking the limit $h \to \infty$.

1.1.3 The Fermi Polaron Problem

The Fermi polaron problem depicts the situation of a single, mobile impurity that interacts attractively with a degenerate gas of fermions. For weak attractive interactions, the impurity is coherently dressed by the surrounding bath particles and forms a quasiparticle, the attractive Fermi polaron (referred to simply as the polaron in the following). The polaron has well-defined momenta with a narrow dispersion relation. It is adiabatically connected to the bare impurity for vanishing interactions (see Fig. 1.3 (a)).

When the interactions exceed a critical value, the system favors a ground state in which the impurity is tightly bound to only one of the bath particles and forms a composite particle [7, 28, 29]. This composite particle is adiabatically connected to the molecular bound state at strong interactions. For intermediate interactions, however, it experiences dressing and exchange with its enviroment. Therefore, in what follows, we will refer to this composite particle as the *molaron*. It was predicted that the energies of the polaron and molaron states cross at $(1/k_F a)_c$, as both states are orthorgonal at the transition point. This leads to a first-order transition between the polaron and the molaron ground state [7, 28–32]. Both states, however, also exist as excited states in the interaction regimes where the respective other state is the ground state. Remarkably, the molaron is stabilized even in the regime of negative scattering lengths where in the model (1.8) no molecule exists in vacuum, reminiscent of Cooper pairing in the theory of superconductivity [33, 34].

For intermediate and strong interactions, it was found that a second, metastable polaron state exists at high energies in the excitation spectrum [32, 35–41]. However, this so-called repulsive polaron becomes progressively unstable towards unitarity ($1/k_F a \to 0^+$).

The polaron problem can be theoretically modelled using the two-channel Hamiltonian (1.8), where a single impurity particle ($d^\dagger_{\mathbf{p}}$) interacts with a bath of N fermions ($c^\dagger_{\mathbf{p}}$). Both the polaron and molaron can be described using diagrammatic techniques, where the central object is the retarded Green's function

$$G^R(E,\mathbf{p}) = \mathcal{F}\left[-i\Theta(t)\left\langle \mathrm{FS}\left|\left[X_{\mathbf{p}}(t), X^\dagger_{\mathbf{p}}(0)\right]_\pm\right|\mathrm{FS}\right\rangle\right] \tag{1.10}$$

with $X_{\mathbf{p}} = d_{\mathbf{p}}(m_{\mathbf{p}})$ for the impurity (molecule) and $[.,.]_\pm$ the (anti-)commutator. Here $\mathcal{F}$ denotes the Fourier transform from time t to frequency space E. The poles of $G^R(E,\mathbf{p})$ directly yield the energy of the attractive and repulsive polaron (molaron) as schematically shown in Fig. 1.3 (a). The single particle spectral function can be obtained via $A(E,\mathbf{p}) = \mathrm{Im}\, G^R(E,\mathbf{p})$. It is shown for the impurity and the molecule for two different interaction strengths in Fig. 1.4, obtained using a non-selfconsistent T-matrix resummation approach (see Fig. 1.3 (b)-(e)). In the impurity spectrum, both the dispersions of the attractive and repulsive polaron are visible. The molaron's dispersion can be seen in the single particle spectral function of the molecule.

The diagrammatic calculation leading to $G^R_{\mathrm{mol/pol}}$ in Fig. 1.4 is equivalent to diagonalizing the problem in a truncated Hilbert space, by approximating the exact eigenstates of the Hamiltonian in Eq. (1.8) in terms of states that only contain single particle hole excitations of the Fermi sea. It was found that accounting only for a single such excitation in form of the variational wavefunction Chevy Ansatz [42, 43],

$$|\psi^{\mathbf{p}}_P\rangle = \alpha^{\mathbf{p}}_0 d^\dagger_{\mathbf{p}}|\mathrm{FS}_N\rangle + \sum_{\mathbf{q}}{}' \alpha^{\mathbf{p}}_{\mathbf{q}} m^\dagger_{\mathbf{p}+\mathbf{q}} c_{\mathbf{q}}|\mathrm{FS}_N\rangle + \sum_{\mathbf{k},\mathbf{q}}{}' \alpha^{\mathbf{p}}_{\mathbf{k},\mathbf{q}} d^\dagger_{\mathbf{p}+\mathbf{q}-\mathbf{k}} c^\dagger_{\mathbf{k}} c_{\mathbf{q}}|\mathrm{FS}_N\rangle \tag{1.11}$$

already yields a remarkably good approximation for the attractive polaron at momentum $\mathbf{p}$ [7, 30, 44, 45]. Here, $\alpha^{\mathbf{p}}_0$, $\alpha^{\mathbf{p}}_{\mathbf{q}}$ and $\alpha^{\mathbf{p}}_{\mathbf{k},\mathbf{q}}$ are variational parameters, and primed sums indicate that the summation occurs over momenta fulfilling $|\mathbf{k}| > k_F$ and $|\mathbf{q}| < k_F$. The state $|\mathrm{FS}_N\rangle$ denotes the zero temperature Fermi sea of N majority particles (the Fermi wave vector k_F, and energy ε_F refer to the majority ensemble). The first term describes the so-called coherent part of the polaron wavefunction. At low polaron momenta it determines the quasiparticle residue (or weight) $Z_{\mathbf{p}} = |\alpha^{\mathbf{p}}_0|^2$. The quasiparticle weight quantifies how similar the polaron remains to the non-interacting impurity particle. When Z is zero, the quasiparticle description is no longer valid.

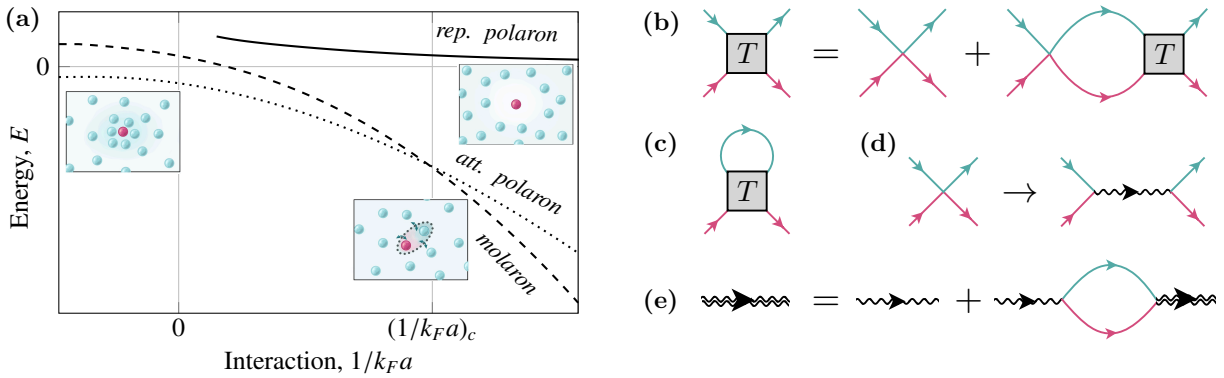

Figure 1.3: **(a)** Schematic figure of the relevant energy levels in the Fermi polaron problem. **(b)** Diagrammatic representation of the T-matrix in the single-channel model within the ladder approximation. Red (black) lines correspond to the impurity (bath particle) propagators, respectively. **(c)** Selfenergy correction of the impurity propagator. **(d)** Within the two-channel model, quartic interactions are replaced by a Yukawa coupling, converting the impurity and one bath particle into a molecule (wavy line). **(e)** Dyson's equation for the molecule propagator in the two-channel model.

On the other hand, to lowest order, molecular states at momentum $\mathbf{p}$ can be described by an Ansatz with variational parameters $\beta_{\mathbf{k}}^{\mathbf{p}}$ of the form [28, 29, 43]

$$|\psi_M^{\mathbf{p}}\rangle = \beta_0^{\mathbf{p}} m_{\mathbf{p}}^\dagger |\mathrm{FS}_{N-1}\rangle + {\sum_{\mathbf{k}}}' \beta_{\mathbf{k}}^{\mathbf{p}} c_{-\mathbf{k}}^\dagger d_{\mathbf{k}+\mathbf{p}}^\dagger |\mathrm{FS}_{N-1}\rangle \,. \tag{1.12}$$

This ansatz is an extension of the vacuum solution and creates a molecule on top of a Fermi sea $|\mathrm{FS}_{N-1}\rangle$ with $N-1$ atoms. In our model, the closed-channel component to the molaron wavefunction is given by the first term, and the open-channel component by the second term, respectively. Both expressions in Eqs. (1.11) and (1.12) can be systematically improved in their accuracy by entangling a larger number of particle-hole excitations of the Fermi sea with the quantum impurity. The minimization of the energy functional $\langle\psi_{P/M}^{\mathbf{p}}|\mathcal{H} - E|\psi_{P/M}^{\mathbf{p}}\rangle$ with respect to the variational parameters allows one to obtain the respective Green's function of the impurity and the molecule, including the renormalized dispersion relations $\epsilon_{\mathrm{pol}}(\mathbf{p})$ and $\epsilon_{\mathrm{mol}}(\mathbf{p})$ of the polaron and the molaron.

In the limit of open-channel dominated Feshbach resonances ($h \to \infty$), it is justified to work in the single-channel Hamiltonian. Here, the corresponding Ansätze read

$$|\psi_P^{\mathbf{p}}\rangle = \alpha_0^{\mathbf{p}} d_{\mathbf{p}}^\dagger |\mathrm{FS}_N\rangle + {\sum_{\mathbf{k},\mathbf{q}}}' \alpha_{\mathbf{k},\mathbf{q}}^{\mathbf{p}} d_{\mathbf{p}+\mathbf{q}-\mathbf{k}}^\dagger c_{\mathbf{k}}^\dagger c_{\mathbf{q}} |\mathrm{FS}_N\rangle \tag{1.13}$$

for the polaron, and

$$|\psi_M^{\mathbf{p}}\rangle = {\sum_{\mathbf{k}}}' \beta_{\mathbf{k}}^{\mathbf{p}} c_{-\mathbf{k}}^\dagger d_{\mathbf{k}+\mathbf{p}}^\dagger |\mathrm{FS}_{N-1}\rangle \,. \tag{1.14}$$

for the molaron.

1.1.4 Spectroscopic methods in ultracold quantum gases

There exist several spectroscopic methods to probe and characterize quasiparticle properties in experiments with ultracold atoms. The key ingredient necessary for these methods is the transitioning between different atomic hyperfine states which occurs upon the absorption of photons. In conventional radio frequency (rf-) spectroscopy, the transition between two hyperfine states is driven by a photon with negligible momentum, and the atomic momentum is essentially unchanged in the transition. By contrast, when relying on Raman transitions based on optical excitation pathways, a finite momentum transfer is possible (see Fig. 1.5 (a)).

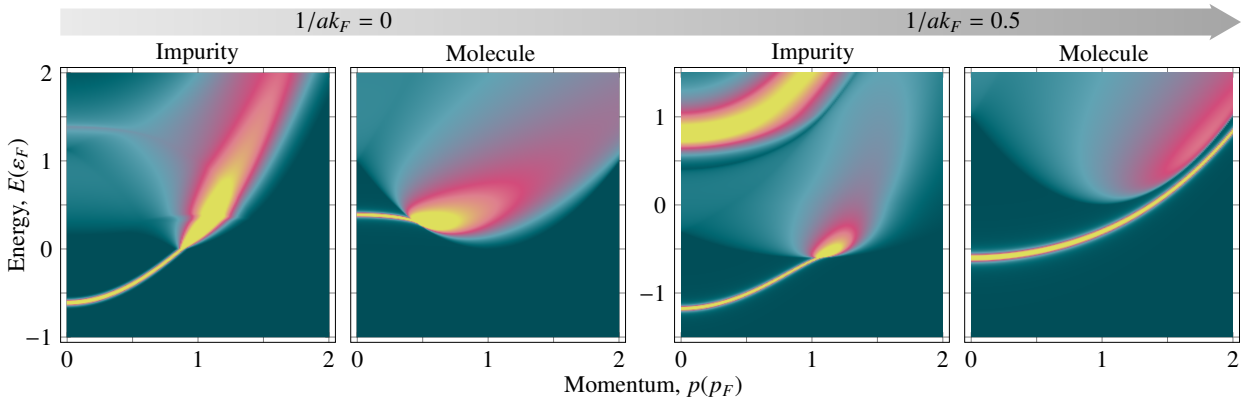

Figure 1.4: Single particle spectral functions in the contact interaction limit ($k_F r^* = 0$) for a mass balanced system at two different interaction strengths. The impurity (molecule) spectral function is obtained using the Ansatz (1.13) ((1.14)). *Impurity:* At unitarity ($(k_F a)^{-1} = 0$), the attractive polaron is a well defined, long lived quasiparticle for momenta $p \lesssim k_F$. The peak at higher energies ($E \approx 1.3\varepsilon_F$) has much less spectral weight and a wider spread, corresponding to the respulive polaron with finite lifetime. A continuum emerges at energies for which there exists spectral weight in the molecule spectral function. For increasing interactions (shown here for $(k_F a)^{-1} = 0.5$), the spectral weight shifts from the attractive to the repulsive polaron. *Molecule:* At unitarity, the molaron is visible as a sharp excitation at low momenta. Its dispersion has a minimum at finite momentum, which can be regarded as a precursor of the elusive FFLO phase occurring at finite imbalance, as we will show in Subsec. 1.3.1. At $(k_F a)^{-1} = 0.5$, the molaron is a well defined quasiparticle for all momenta.

We consider a quantum degenerate mixture of two types of atoms, e.g. a Bose-Fermi mixture or a Fermi-Fermi mixture, assuming that one type of atom has a much lower density than the other. The majority atoms are always taken as fermionic, such that Fermi polarons are realized. We label the state of the majority atoms as $|1\rangle$, and the state of the minority (impurity) atoms as $|2\rangle$, respectively. They are interacting when being close to a Feshbach resonance between $|1\rangle$ and $|2\rangle$. In so-called *ejection spectroscopy*, the hyperfine state of the impurity is changed to $|3\rangle$, in which impurity and bath particles are non-interacting due to the absence of any nearby Feshbach resonances between $|1\rangle$ and $|3\rangle$. The impurity particle is ejected from its initial polaron or molaron state into a non-interacting one (see Fig. 1.5 (b)). Therefore, ejection spectroscopy is especially well suited to study the ground state of the system, including the polaron-to-molaron transition (cf. Fig. 1.5 (c)). In addition, ejection spectroscopy also allows one to study the repulsive polaron, when this state is initially prepared. It therefore permitted the first direct observation of both, the attractive and repulsive Fermi polaron in two dimensions [38], and the attractive Fermi polaron in three dimensions [8].

The opposite protocol is termed *injection spectroscopy*. There, an initially non-interacting impurity is injected into a state in which it can interact with the bath particles (see Fig. 1.5 (b)). The spectrum obtained in injection spectroscopy is identical to the single-particle spectral function of the impurity, featuring peaks of the attractive and the repulsive polaron (see Ref. [37] for the first experimental observation of repulsive Fermi polarons in three dimensions). In injection spectroscopy, the molaron remains inaccessible due to a vanishing overlap between the non-interacting initial state and the molaron state. Experimentally, the spectra are obtained by counting the number of transferred atoms as a function of the photon detuning ω.

Theoretically, for a single impurity, both ejection and injection spectra can be calculated in the linear response regime using Fermi's Golden rule

$$\mathcal{A}(\omega, i) = \sum_f \left|\langle f|\hat{V}_{\mathbf{q}}|i\rangle\right|^2 \delta\left[\omega - (E_f - E_i)\right], \tag{1.15}$$

where $|i\rangle$ denotes the initial state with energy E_i, $\{|f\rangle\}$ denote all possible final states with respective energies E_f, and $\hat{V}_{\mathbf{q}}$ is the transition operator. The spectra $\mathcal{A}(\omega)$ are related to the transition rate $\Gamma(\omega)$ via $\Gamma(\omega) = 2\pi\Omega_e^2\mathcal{A}(\omega)$ with Ω_e the effective Rabi frequency. In ejection spectroscopy, the impurity resides in an initial state $|i\rangle$ that is characterized by a conserved momentum $\mathbf{p}$ and may be either polaronic or molaronic i.e. $|i\rangle =$

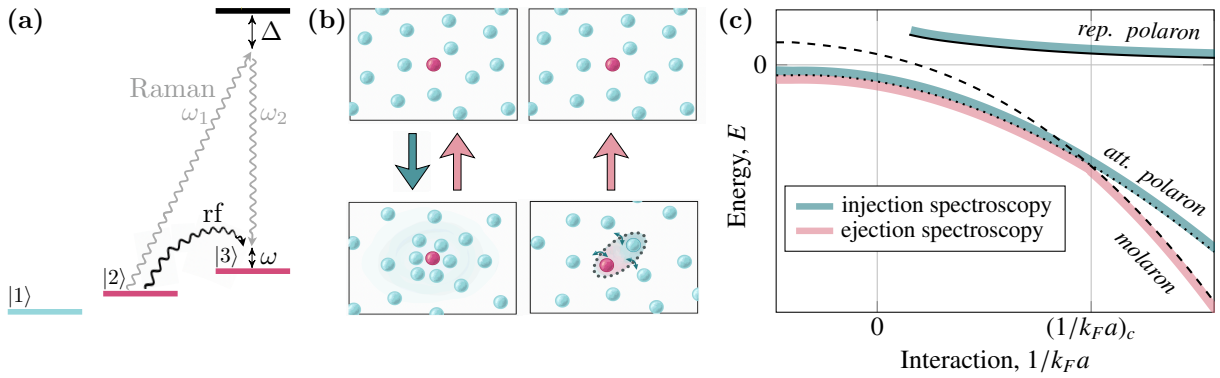

Figure 1.5: **(a)** Schematic representation of impurity spectroscopy, using rf-transition (black) and Raman transitions (gray). The impurity (pink) is transferred from state $|2\rangle$ to state $|3\rangle$, while the bath particles (blue) remain in $|1\rangle$. In injection (ejection) spectroscopy, $|1\rangle$ and $|2\rangle$ are non-interacting (interacting), and $|1\rangle$ and $|3\rangle$ are interacting (non-interacting). In Raman spectroscopy, the finite momentum transfer can be tuned by changing the relative angle between the two Raman beams. **(b)** Illustration of injection spectroscopy (blue arrow) and ejection spectroscopy (red arrow). **(c)** The colors indicate which states in the Fermi polaron problem can be probed with current spectroscopic protocols. Injection spectroscopy (blue) allows for the detection of the polaron, but suffers from a vanishing overlap between the non-interacting ground state and the molaron state. Ejection spectroscopy (yellow) allows for the detection of the ground state.

$\{|\psi_P^{\mathbf{p}}\rangle, |\psi_M^{\mathbf{p}}\rangle\}$. The corresponding energies are $E_i = \{\epsilon_{\rm pol}(\mathbf{p}), \epsilon_{\rm mol}(\mathbf{p})\}$, respectively. In the calculation of injection spectra, the initial state is non-interacting $|i\rangle = d_0^\dagger|\mathrm{FS}\rangle$, and the final state can be approximated by the polaron Ansatz $|\psi_P^{\mathbf{p}}\rangle$. The operator $\hat{V}_{\bar{\mathbf{q}}}$ describes the transition between the two hyperfine states of the impurity. In the single-channel model, it is given by

$$\hat{V}_{\bar{\mathbf{q}}} = \sum_{\mathbf{p}} \left(d^\dagger_{\mathbf{p}+\bar{\mathbf{q}},|3\rangle} d_{\mathbf{p},|2\rangle} + \text{h.c.} \right). \tag{1.16}$$

Within the two-channel model, understanding the action of the operator requires translation of $\hat{V}_{\bar{\mathbf{q}}}$ from an atomic state basis (where it takes the form (1.16)) into a basis that explicitly accounts for the closed-channel molecule $m^\dagger$ that arises from having integrated out atom fluctuations in the closed-channel. How this can be done will be discussed in Sec. 1.3. The transfer momentum $\bar{\mathbf{q}}$ is finite in Raman spectroscopy and corresponds to the relative two-photon momentum $\bar{\mathbf{q}} = \mathbf{k}_2 - \mathbf{k}_1$, while in rf-spectroscopy, it is zero.

Raman spectroscopy offers two main advantages compared to rf-spectroscopy. Firstly, it allows one to access finite momentum properties of the impurity. For example, in injection spectroscopy, starting from an initial zero-momentum impurity, a tunable transfer momentum allows the injection of the impurity into arbitrary finite momentum states, thereby accessing the full energy and momentum resolved single particle spectral function. Secondly, it allows one to extract the polaron energy from the peak position of the Raman spectra. As experimentally observed in Ref. [46], at finite impurity density, there is a temperature-dependent shift of the rf spectrum peak position relative to the zero-momentum polaron energy. As the photon transfer momentum increases, however, this shift rapidly vanishes. We explicitly show this in Sec. 1.2.5 when discussing Raman spectra for finite impurity density and temperature.

1.2 The polaron-to-molaron transition at finite imbalance and temperature

In the single impurity limit, the transition from the polaron to a molaron ground state is of first order, i.e. the polaron and molaron energies cross each other at a critical interaction strength [7]. This is manifested in a discontinuous behaviour of several observables, including the impurities quasiparticle residue Z and the Tan's contact C. While the polaron quasiparticle weight is finite for all interactions, the polaron becomes an excited state beyond the critical interaction strength (see Fig. 1.3 (a)). It is thus not occupied and hence—at the polaron-to-molaron transition—a jump in the quasiparticle weight (of the ground state) occurs. In experiments, however, the Z factor was observed to continuously decrease and vanish above a certain interaction strength [8] in contrast to theoretical predictions based on the Chevy Ansatz wave function.

In Ref. [P1], we therefore study, both theoretically and experimentally, the fate of the polaron-to-molaron transition under realistic conditions, namely finite temperature and impurity concentration. The key question is whether the first-order polaron-to-molecule transition prevails at finite impurity density, and separates sharply a phase of polarons from a gas of molarons. In what follows, we stay closely to Ref. [P1].

1.2.1 Experimental setup

Here, we briefly summarize the experiment performed by Sagi's team at Technion. The obtained data then lay the basis for the theoretical model we developed, which will be discussed in the next section. Additional details on the experimental procedure can be found in Ref. [P1].

In order to investigate the polaron-to-molaron transition at finite impurity density and temperature, the Technion group measured Raman ejection spectra of an imbalanced mixture of the two lowest Zeeman states (denoted by $|1\rangle$ and $|2\rangle$, with the majority of atoms being in state $|1\rangle$) of harmonically-trapped ultracold ^{40}K atoms. They initially produced a spin-polarized ensemble of $\sim 1\cdot 10^5$ atoms in the state $|1\rangle$ at a temperature of $T \approx 0.2\,T_F$, where T_F is the Fermi temperature. Then, the magnetic field was ramped adiabatically to 204.5G, the BCS side of the Feshbach resonance ($B_0 \approx 202.14$G [47]), where the interaction between the states $|1\rangle$ and $|2\rangle$ is weak. To introduce the impurities, a short (few microseconds) rf pulse was used to transfer a very small fraction of the atoms from state $|1\rangle$ to $|2\rangle$.

The minority concentration x in state $|2\rangle$, can be defined globally by $x = N_I/N$, with N_I (N) being the total number of impurity (bath) atoms, or alternatively by averaging over its local value $\langle x\rangle$ in the harmonic trap using the local density approximation. Generally, the expected value of any observable O is given by the minority-weighted local density average $\langle O\rangle = \int \mathrm{d}^3\mathbf{r} O(\mathbf{r})\, n_I(\mathbf{r}) / \int \mathrm{d}^3\mathbf{r} n_I(\mathbf{r})$. The minority density distribution $n_I(\mathbf{r})$ is calculated by taking into account the interactions with the majority atoms through a renormalization of the confining potential $V_2(\mathbf{r}) = V_1(\mathbf{r})(1-\epsilon^0_{\mathrm{pol}}/\varepsilon_F)$, where $V_1(\mathbf{r})$ is the potential felt by the majority atoms [48]. In modeling the experiement, we assumed that the distribution of the majority atoms is not affected by the presence of the minority atoms, and neglect the weak interactions between polarons [49]. Since the local density $n_I(\mathbf{r})$ depends on $k_F a$, $\langle x\rangle$ changes even when x is kept constant. To ensure there were no systematic deviations in the experiments due to this effect, the measurements were repeated twice: once keeping x at approximately 0.04, which gives $\langle x\rangle \approx 0.23$ at $(k_F a)^{-1} = 0.85$, and a second time maintaining the same value of $\langle x\rangle$ by varying x. Since no significant difference between the two datasets was observed, both datasets where accumulated into one in what follows.

Next, the magnetic field was ramped adiabatically to its final value (corresponding to finite interactions between states $|1\rangle$ and $|2\rangle$) before pulsing the Raman beams. As illustrated in Fig. 1.5 (a), two Raman beams

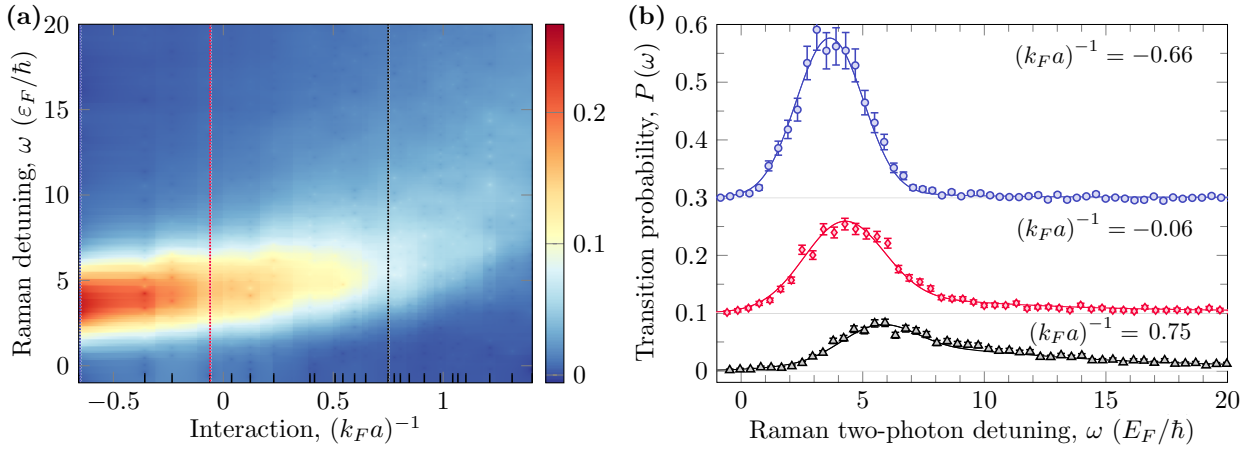

Figure 1.6: **(a)** Measured Raman spectra as a function of the two-photon Raman detuning ω and the interaction strength $(k_Fa)^{-1}$. The color bar shows the transition probability $P(\omega)$. **(b)** For three interaction strengths, the Raman spectra are shown as a function of the detuning ω.

couple atoms in the minority state $|2\rangle$ to a third state $|3\rangle$, which is initially unoccupied. The beam parameters were the same as described in Ref. [50]. Their frequencies are denoted by ω_1 and ω_2 and their wavevectors by $\mathbf{k}_1$ and $\mathbf{k}_2$. The measurement was performed by recording the number of atoms transferred to the state $|3\rangle$ versus the two-photon detuning, $\omega = \omega_1 - \omega_2 - E_0/\hbar$, where E_0 is the bare transition energy between states $|2\rangle$ and $|3\rangle$. The atoms were measured using a high-sensitivity fluorescence detection scheme [47, 50]. The obtained Raman spectra are shown as a density plot in Fig. 1.6 (a) as a function of the two-photon Raman detuning ω and the interaction strength $(k_Fa)^{-1}$. The colors represent the transition probability. For clarity, three example spectra for interaction strengths $(k_Fa)^{-1} = -0.66$, $(k_Fa)^{-1} = -0.06$ and $(k_Fa)^{-1} = 0.75$ are shown in Fig. 1.6 (b). It is visible that the spectra change qualitatively when tuning the interaction strength from the BCS to the BEC regime. For small interaction strengths, the Raman spectrum is almost symmetric (cf. blue curve in Fig, 1.6 (b)). In contrast, for large interaction strengths, the Raman spectrum is highly asymmetric and has a pronounced high-frequency tail (cf. black curve in Fig. 1.6 (b)). In the next section, we theoretically model the Raman spectra in order to extract the quasiparticle residue Z and the Tan's contact C from the measured data.

1.2.2 Theoretical modelling

We now turn to the theoretical description of the observed data. As the experiment was performed with a mass-balanced mixture close to an open-channel dominated Feshbach resonance (at $B_0 \approx 202.14$G with $s_{\text{res}} = 2.2$ [51]), it is justified to describe the system by the single-channel Hamiltonian (1.9) using $M_d = M_c = m$. In order to incorporate the finite impurity density and temperature present in the experiment into the calculation of the quasiparticle residue, the Tan's contact and the Raman spectra, we adopt an effective quasiparticle approach. In this model, quasiparticle states —obtained in the single-impurity limit— are occupied thermally according to their quantum statistics. More precisely, we consider the polaron and molaron states, given by Eqs. (1.11) and (1.12), to be populated according to the Fermi-Dirac and Bose-Einstein distributions $n_{F/B}(\epsilon, T) = (\exp[(\epsilon - \mu)/T] \pm 1)^{-1}$, respectively. Here, μ denotes the chemical potential which determines the impurity density at temperature T via the implicit equation

$$n_I(\mu, T) = \frac{1}{V} \sum_{\mathbf{p}} \left(n_F\left[\epsilon_{\text{pol}}(\mathbf{p}), T\right] + n_B\left[\epsilon_{\text{mol}}(\mathbf{p}), T\right] \right). \tag{1.17}$$

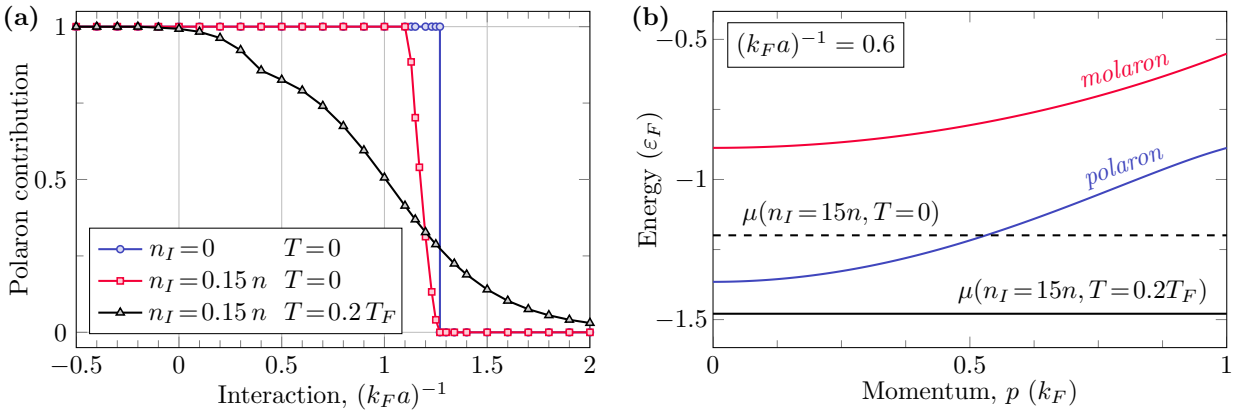

Figure 1.7: (a) Calculated polaron contribution. Fraction of impurity particles propagating as polarons as a function of interaction strength $(k_F a)^{-1}$. The impurity particles which are not polaronic are bound to a bath particle, thus forming a molaron. In the single-impurity limit and $T = 0$ (blue), there is a sharp transition between a polaron and a molaron at $(k_F a)_c^{-1} \approx 1.27$. Finite impurity density ($0.15\,n$, red) leads to smoothing of the transition for $(k_F a)^{-1} < (k_F a)_c^{-1}$. When the temperature is increased ($0.2\,T_F$, black), the polaronic branch is populated also for $(k_F a)^{-1} > (k_F a)_c^{-1}$ and the sharp transition disappears. **(b)** The polaron (blue) and the molaron (red) dispersions for $n_I = 0.15\,n$ and $(k_F a)^{-1} = 0.6$, along with the chemical potential at $T = 0$ (dashed black) and $T = 0.2\,T_F$ (solid black). At $T = 0.2\,T_F$, polarons and molarons are populated only by thermal excitations, while at $T = 0$ the chemical potential is above the minimum of the polaron dispersion such that a well-defined polaronic Fermi surface forms.

Note that the impurity temperature and chemical potential μ are set independently of the bath. Specifically, for all calculations in this section, μ is tuned to yield an impurity density of $n_I = 0.15\,n$ at a finite impurity temperature $T = 0.2\,T_F$[5].

In Fig. 1.7 (a), the polaron contribution to the total impurity density in the initial state is shown as a function of the interaction strength $(k_F a)^{-1}$. Evidently, in the single-impurity limit at zero temperature (blue circles) the system undergoes a sharp transition from a purely polaronic to a purely molaronic state at $(k_F a)^{-1} \approx 1.27$. Still at zero-temperature but at finite impurity density (red squares), the system is purely polaronic up to $(k_F a)^{-1} \approx 1.1$. At this interaction strength the chemical potential reaches the minimum of the molaron dispersion and, henceforth, it remains pinned to that value (for an illustration of this effect, see Fig. 1.7 (b) which shows the dispersion relations of polarons (blue) and molarons (red) as well as the impurity chemical potential μ (black)). Accordingly, for $1.1 \lesssim (k_F a)^{-1} \lesssim 1.27$, molarons begin to condense in the lowest-lying molecular state while the polaron Fermi surface shrinks and eventually vanishes at the polaron-to-molaron transition. In this range of $(k_F a)^{-1}$, polarons and molarons coexist, even at $T = 0$. Beyond the transition, the system forms a molaronic condensate within the bath of the remaining majority atoms. Finally, at finite temperature (black triangles), polarons and molarons coexist as a thermal mixture. This blurs the transition and leads to a smooth interpolation between polaron and molaron dominated regimes. Note that the temperatures considered exceed the critical temperature for Bose-Einstein condensation of molarons, which thus form a purely thermal gas.

In the calculation of the polaron contribution to the equilibrium state and all following calculations, we only occupy quasiparticle states with an infinite lifetime and finite quasiparticle weight. This ensures that the initial state has an infinite lifetime as expected for an equilibrium state, and also that the quasiparticle picture remains valid. As a consequence, we cut off the quasiparticle populations of the polaronic and molaronic states at momenta where they no longer feature poles on the real frequency axis. For the polaron, this momentum cutoff occurs when the energy becomes positive or $|\alpha_0^{\mathrm{P}}|^2$ vanishes. For the molaron, however, this cutoff occurs when the dispersion intersects the continuum of states delimited by a parabola of the form $(|\mathbf{p}| - k_F)^2$. In fact, this condition causes the slight dent in the polaron contribution at $(k_F a)^{-1} \approx 0.4$

[5] The value of $n_I = 0.15\,n$ is taken as the typical value of the experimentally realized $\langle x \rangle$.

visible in Fig. 1.7 (a), as beyond that value molarons have a well-defined dispersion for all momenta and thus do not have a cutoff. Similarly, for the polaron, its cutoff condition changes at around $(k_F a)^{-1} \gtrsim 0.3$. We note that in order to accurately incorporate states with a finite lifetime or continuum states, a solution of the full imbalanced problem would be necessary.

1.2.2.1 Many-impurity quasiparticle residue

The polaron Z factor can be obtained from the impurities selfenergy $\Sigma(\omega, \mathbf{p})$ via

$$Z_{\mathbf{p}} = \left|1 - \partial_\omega \Sigma(\omega, \mathbf{p})|_{\omega=\omega_{\mathbf{p}}}\right|^{-1}, \tag{1.18}$$

where $\omega_{\mathbf{p}}$ is a pole in the retarded Green's function of the quasiparticle at momentum $\mathbf{p}$ [52]. We use a ladder approximation for the T-matrix in the calculation of the selfenergy (cf. Fig. 1.3 (b) and (c)) which thus reads

$$\Sigma(\omega, \mathbf{p}) = \frac{1}{V} \sum_{\mathbf{q}}{}' \frac{1}{\frac{1}{U} + \frac{1}{V}\sum_{\mathbf{k}}{}' \frac{1}{\varepsilon_{\mathbf{k}} - \varepsilon_{\mathbf{q}} + \varepsilon_{\mathbf{q}-\mathbf{k}+\mathbf{p}} - \omega - i0^+}}. \tag{1.19}$$

As before, the primed sums indicate that the summation occurs over $|\mathbf{k}| > k_F$ and $|\mathbf{q}| < k_F$.

The momentum-dependent weight $Z_{\mathbf{p}}$ can, alternatively, be obtained from the overlap of the non-interacting wavefunction with the interacting one, $Z_{\mathbf{p}} = |\alpha_0^{\mathbf{p}}|^2$[6]. In the molaron state, the impurity is bound to a bath particle, leading to a vanishing Z factor in the thermodynamic limit [29]. The many-body quasiparticle residue $\bar{Z}$ can be calculated from the single impurity residues via

$$\bar{Z} = \frac{1}{N_I} \sum_{\mathbf{p}} Z_{\mathbf{p}} \cdot n_F \left[\epsilon_{\mathrm{pol}}(\mathbf{p}), T\right] . \tag{1.20}$$

As evident in Fig. 1.8 (a), in the single-impurity limit $\bar{Z}$ features a sharp jump at the polaron-to-molaron transition where it drops to zero as the polaron is not populated anymore. Importantly, in this limit $\bar{Z}$ reduces to the zero-momentum polaron residue, $\bar{Z} = Z_{\mathbf{0}}$, before the transition. At finite impurity density and $T = 0$, this jump is smoothed with the many-body weight again dropping to zero at the transition. At finite temperature and density, the transition is completely blurred, with $\bar{Z}$ being lowered on the polaronic side compared to $T = 0$ and the single impurity limit. This is due to the fact that first, some impurity particles are propagating as molecules with a vanishing residue and, second, finite-momentum polarons with a lower residue $Z_{\mathbf{p}} < Z_{\mathbf{0}}$ also contribute to the many-body weight $\bar{Z}$.

1.2.2.2 Many-impurity contact coefficient

The so called Tan's contact coefficient C makes its appearance in several exact relations describing ultracold gases with short range interactions. It is related to the tail of the momentum distribution of quasiparticles and measures the short-distance correlations between bath and impurity particles [53–60]. Moreover, it relates the high-momentum tail to various many-body quantities such as the thermodynamic pressure. It can be extracted from the derivative of the ground state energy with respect to the inverse scattering length via $V^{-1}\partial E/\partial(1/a) = -C/4\pi m$. Therefore, in the single-impurity limit at $T = 0$, C is expected to exhibit a discontinuity at the polaron-to-molaron transition [29].

[6] If the polaron is a stable quasiparticle ($\mathrm{Im}(\omega_{\mathbf{p}}) = 0$), its Z factor within the polaron Ansatz (1.11) is given by $|\alpha_0^{\mathbf{p}}|^2$. These definitions are, however, not equivalent if the polaron acquires a finite lifetime ($\mathrm{Im}(\omega_{\mathbf{p}}) \neq 0$). This discrepancy can be seen by comparing the definition of $Z_{\mathbf{p}}$ using the selfenergy to the normalization condition for $|\alpha_0^{\mathbf{p}}|^2$ as they differ in the placement of the absolute value bars.

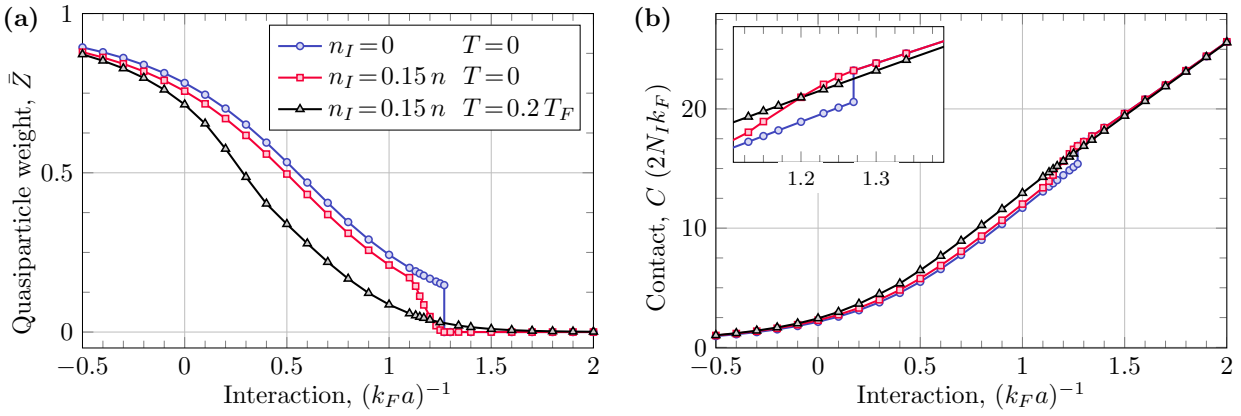

Figure 1.8: Calculated quasiparticle weight and contact. The quasiparticle weight **(a)** and contact coefficient **(b)** are shown for different interaction strengths. In the single-impurity limit (blue), the transition between polaron and molaron at $(k_F a)^{-1} \approx 1.27$ leads to a sharp jump between the polaronic and molaronic residues and contacts. As in Fig. 1.7, at $T = 0$ and finite impurity density ($0.15\,n$, red) the transition is smoothed, and eventually blurred at finite impurity density and temperature ($0.2\,T_F$, black). The inset in **(b)** shows a magnification around the transition point.

We can determine the many-impurity contact coefficient of the full many-body spectrum by

$$C = \sum_{\mathbf{p}} C_{\mathrm{pol}}[\mathbf{p}, \epsilon_{\mathrm{pol}}(\mathbf{p})] \cdot n_F\left[\epsilon_{\mathrm{pol}}(\mathbf{p}), T\right] + \sum_{\mathbf{p}} C_{\mathrm{mol}}[\mathbf{p}, \epsilon_{\mathrm{mol}}(\mathbf{p})] \cdot n_B\left[\epsilon_{\mathrm{mol}}(\mathbf{p}), T\right] \ . \tag{1.21}$$

Here, the single-impurity coefficients are given by

$$C_{\mathrm{pol}}\left[\mathbf{p}, \epsilon_{\mathrm{pol}}(\mathbf{p})\right] = \frac{1}{V}{\sum_{\mathbf{q}}}' \frac{m^2 \left|\alpha_0^{\mathbf{P}}\right|^2}{\left|\frac{1}{U} - \frac{1}{V}{\sum_{\mathbf{k}}}' \frac{1}{\epsilon_{\mathrm{pol}}(\mathbf{p}) - \varepsilon_{\mathbf{k}} - \varepsilon_{\mathbf{q}-\mathbf{k}+\mathbf{p}} + \varepsilon_{\mathbf{q}}}\right|^2}$$

for the polaron, and

$$C_{\mathrm{mol}}\left[\mathbf{p}, \epsilon_{\mathrm{mol}}(\mathbf{p})\right] = m^2 \left[\frac{1}{V}{\sum_{\mathbf{k}}}' \left|\frac{1}{\epsilon_{\mathrm{mol}}(\mathbf{p}) + \varepsilon_F - \varepsilon_{\mathbf{k}} - \varepsilon_{\mathbf{p}+\mathbf{k}}}\right|^2\right]^{-1}$$

for the molaron. The contact C is shown in Fig. 1.8 (b) as a function of $(k_F a)^{-1}$ at finite impurity density for $T > 0$ and $T = 0$, along with the prediction in the single-impurity limit at $T = 0$. As can be seen, these scenarios differ significantly only around the polaron-to-molaron transition. While the single-impurity limit features a discontinuity, the finite density graph at $T = 0$ already shows a smooth transition between the polaronic and molaronic contacts. At finite temperature this transition is further blurred.

1.2.2.3 Many-impurity Raman spectrum

The total many-impurity Raman spectrum can be computed via

$$\bar{\mathcal{A}}(\omega) = \frac{1}{N_I}\sum_{\mathbf{p}} \mathcal{A}_{\mathrm{pol}}(\omega, \mathbf{p}) \cdot n_F\left[\epsilon_{\mathrm{pol}}(\mathbf{p})\right] + \frac{1}{N_I}\sum_{\mathbf{p}} \mathcal{A}_{\mathrm{mol}}(\omega, \mathbf{p}) \cdot n_B\left[\epsilon_{\mathrm{mol}}(\mathbf{p})\right] \tag{1.22}$$

for finite impurity density and finite temperature by summing the single-impurity Raman spectra of the polaron $\mathcal{A}_{\mathrm{pol}}(\omega, \mathbf{p}) \equiv \mathcal{A}(\omega, i = |\psi_P^{\mathbf{P}}\rangle)$ and the molaron $\mathcal{A}_{\mathrm{mol}}(\omega, \mathbf{p}) \equiv \mathcal{A}(\omega, i = |\psi_M^{\mathbf{P}}\rangle)$ over all impurity momenta, weighted by their occupation probability[7].

[7] Similar to the single impurity case, the full many-impurity Raman signal is connected to the Raman rate by $\bar{\Gamma}(\omega, i) = 2\pi\Omega_e^2 N_I \bar{\mathcal{A}}(\omega, i)$.

The single-impurity Raman spectra are obtained by computing the matrix elements $\langle f|\hat{V}_R|i\rangle$ in Eq. (1.15) for the Ansätze Eqs. (1.11) and (1.12). This yields (details of the calculation are provided in App. A.1)

$$\mathcal{A}_{\rm pol}(\omega,\mathbf{p}) = |\alpha_0^{\mathbf{p}}|^2\delta\left[\omega-\varepsilon_{\mathbf{p}+\bar{\mathbf{q}}}+\epsilon_{\rm pol}(\mathbf{p})\right] + {\sum_{\mathbf{k},\mathbf{q}}}' |\alpha_{\mathbf{k},\mathbf{q}}^{\mathbf{p}}|^2\delta\left[\omega-\varepsilon_{\mathbf{p}+\bar{\mathbf{q}}+\mathbf{q}-\mathbf{k}}-\varepsilon_{\mathbf{k}}+\varepsilon_{\mathbf{q}}+\epsilon_{\rm pol}(\mathbf{p})\right] \quad (1.23)$$

for the polaron, and

$$\mathcal{A}_{\rm mol}(\omega,\mathbf{p}) = {\sum_{\mathbf{k}}}' |\beta_{\mathbf{k}}^{\mathbf{p}}|^2\delta[\omega-\varepsilon_{\mathbf{k}}-\varepsilon_{\mathbf{p}-\mathbf{k}+\bar{\mathbf{q}}}+\epsilon_{\rm mol}(\mathbf{p})+\varepsilon_F] \quad (1.24)$$

for the molaron. These expressions make explicit the three contributions that make up the many-body Raman spectrum, namely a coherent (first term of Eq. (1.23)) and incoherent (second term of Eq. (1.23)) polaron part as well as a molaron part. Note that our Raman spectra are normalized such that they sum to unity once integrated over frequency ω. In Fig. 1.9 (a), we show many-body Raman spectra for three example values of $(k_F a)^{-1}$ across the transition.

The many-body quasiparticle weight $\bar{Z}$ and the contact coefficient C can be extracted from the total Raman spectra: $\bar{Z}$ is given by the spectral weight of the coherent part of the Raman spectra (blue-shaded area in Fig. 1.9 (a)), while C quantifies the spectral weight in the universal $\omega^{-3/2}$ tail of the Raman spectra and can therefore be obtained from their large-frequency behavior [61, 62]. However, our theory cannot completely reproduce the experimental data: the reason for this disagreement lies in the quality of the Ansatz for the molaron (1.14), which is not sophisticated enough to correctly reproduce the dependence of the molecule energy as a function of the interaction strength. In particular, our simplified Ansatz predicts a crossing at $(k_F a)_c^{-1} = 1.27$, in contrast to the correct value $(k_F a)_c^{-1} = 0.9$ [7, 30]. This in turn prevents us from comparing the theoretical Raman spectra to the experimental ones at a given interaction strength. Instead, as detailed in the next chapter, we develop a fitting model for the experimental Raman spectra, which can discriminate the coherent contribution (proportional to $\bar{Z}$) from the rest of the spectrum (see Fig 1.9(b)). This allows us to determine $\bar{Z}$ and C from the experimental spectra.

1.2.3 Quantitative analysis of experimental Raman spectra

Using the general characteristics of the Raman response revealed by the theoretical calculations, we quantitatively analyze the experimental data by devising a fit model for the lineshape of the Raman transition amplitude, and from that extract the many-body quasiparticle weight $\bar{Z}$ and the contact coefficient C from the experimental data. The Raman response is composed of two main contributions:

1. *Coherent polaron peak* $P_{\rm coh}(\omega)$*:* a roughly symmetric peak due to the coherent part of the polaron. It contains information about quasiparticle properties such as the polaron energy $\epsilon_{\rm pol}$, the spectral weight Z, and the effective mass m^*. We will find below that the coherent part of the spectrum is proportional to the polaronic momentum distribution, and its peak position gives the polaron energy at zero momentum $\epsilon_{\rm pol}^0$ (plus the recoil energy from the two-photon Raman transition). This correspondence emerges from the finite transferred photon momentum and thus is not affected by thermal shifts observed in rf measurements, as further discussed in Sec. 1.2.5.

2. *Background signal* $P_{\rm bg}(\omega)$*:* an asymmetric lineshape extending to high frequencies that contains the combined response arising from the incoherent part of the polaron, as well as from molecules that are dissociated by the Raman lasers. In a wavefunction picture, the former corresponds to contributions as given by the second term in Eq. (1.11). We find that up to a rescaling by a factor, the shapes of the background spectra from polarons and molarons are similar.

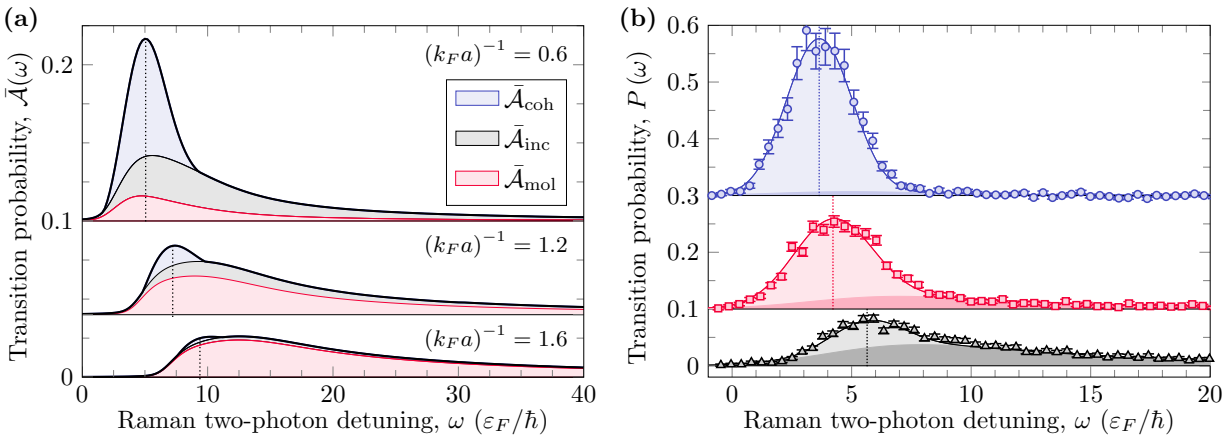

Figure 1.9: Calculated and measured Raman ejection spectra of the imbalanced Fermi gas for three interaction strengths. **(a)** The calculated many-body Raman spectra were obtained from an occupation average for fixed impurity concentration $N_I = 0.15\,N$ and temperature $T = 0.2\,T_F$. The blue-, red- and grey-shaded regions represent the coherent and incoherent polaronic contributions from (1.11) as well as the molaron contributions from (1.12), respectively. The coherent part yields an almost symmetric lineshape that is peaked at the polaron energy shifted by the constant Raman two-photon recoil energy (dotted vertical lines) due to the finite Raman momentum transfer of $\bar{q} \approx 1.9\,k_F$, while the incoherent and molaron parts lead to an asymmetric continuum. **(b)** The measured Raman spectra were fitted with the function given in Eq. (1.25) (solid lines). The dark shaded area under the graph is the combined contribution from molarons and the incoherent part of the polaron wavefunction, $P_{\rm bg}\left(\omega; T_{\rm bg}, E_b\right)$, while the light shaded area is the coherent polaron contribution, $P_{\rm coh}\left(\omega; T_p, \epsilon^0_{\rm pol}, m^*\right)$. In both figures, the second and third graphs from the bottom are vertically shifted for clarity.

Based on this identification, we are able to develop a fit model for the transition probability that reflects the lineshape of the coherent and background signals

$$P(\omega) = \bar{Z} P_{\rm coh}(\omega; T_p, \epsilon^0_{\rm pol}, m^*) + (1-\bar{Z}) P_{\rm bg}(\omega; T_{\rm bg}, E_b). \tag{1.25}$$

Here, both contributions $P_{\rm coh}$ and $P_{\rm bg}$ are normalized to unity. Next, we theoretically motivate suitable shape functions for $P_{\rm coh}$ and $P_{\rm bg}$.

1.2.3.1 Raman coherent polaron peak

The Raman spectrum of a single polaron can be expressed as

$$\mathcal{A}_{\rm pol}(\omega, \mathbf{k}) = Z \mathcal{A}_{\rm coh}(\omega, \mathbf{k}) + (1-Z)\mathcal{A}_{\rm inc}(\omega, \mathbf{k}), \tag{1.26}$$

where the coherent part can be approximated at low momenta as

$$\mathcal{A}_{\rm coh}(\omega, \mathbf{k}) = \delta\left[\omega - \epsilon_{\mathbf{k}+\bar{\mathbf{q}}} + \epsilon_{\rm pol}(\mathbf{k})\right]. \tag{1.27}$$

Z is approximated as a momentum independent quasiparticle weight, and the dispersion $\epsilon_{\rm pol}(\mathbf{k}) = \epsilon^0_{\rm pol} + \mathbf{k}^2/2m^*$ is parametrized by an effective mass m^*, and the polaron energy $\epsilon^0_{\rm pol}$. The function $P_{\rm coh}$ accounts only for the Raman response arising from $\mathcal{A}_{\rm coh}(\omega)$ with m^*, $\epsilon^0_{\rm pol}$, and a polaron temperature T_p being fit parameters. It is therefore natural to identify

$$P_{\rm coh} = \alpha \mathcal{A}_{\rm coh}, \tag{1.28}$$

with α a proportionality constant. As described below, the incoherent response arising from $\mathcal{A}_{\rm inc}$ will be attributed to $P_{\rm bg}$.

Within this model it is useful to recognize that the total number of impurities leading to the observed absorption response can be interpreted as a sum of impurities contributing to the coherent response, the incoherent response, and molarons, $N_I = N_{\text{coh}} + (N_{\text{inc}} + N_{\text{mol}})$. N_I is responsible for the full signal $P(\omega)$, while $N_{\text{coh}} = \bar{Z}N_I$ yields the contribution $\bar{Z}P_{\text{coh}}$ in Eq. (1.25). The sum $(N_{\text{inc}}+N_{\text{mol}}) = (1-\bar{Z})N_I$, in turn, gives $(1-\bar{Z})P_{\text{bg}}$. Moreover, the number of polarons is given by $N_{\text{pol}} = N_{\text{coh}} + N_{\text{inc}}$ with $N_{\text{coh}} = ZN_{\text{pol}}$. Thus, within a model with momentum independent quasiparticle weight $Z \equiv Z_{\mathbf{k}=0}$, one has $\bar{Z} = ZN_{\text{pol}}/N_I$. The coherent part of the polaron Raman spectrum $\mathcal{A}_{\text{coh}}$ is related to the coherent contribution of the full, many-impurity Raman spectrum by [63, 64]

$$\bar{\mathcal{A}}_{\text{coh}}(\omega) = \frac{1}{N_I}\sum_{\mathbf{k}} \mathcal{A}_{\text{coh}}(\omega, \mathbf{k}) \cdot n_F\left[\epsilon_{\text{pol}}(\mathbf{k}), T_p\right] \ , \tag{1.29}$$

such that

$$\int \mathrm{d}\omega \bar{\mathcal{A}}_{\text{coh}}(\omega) = \frac{N_{\text{coh}}}{N_{\text{I}}}. \tag{1.30}$$

Since the concentration of impurities is finite, polarons can be found at non-zero momenta [32, 65]. As Eq. (1.27) shows, a polaron with a momentum $\mathbf{k}$ gives a coherent contribution to the Raman signal if $\epsilon_{\text{pol}}(\mathbf{k}) = \varepsilon_{\mathbf{k}+\bar{\mathbf{q}}} - \omega$, which can be solved for $k_{\bar{q}}(\omega) \equiv \mathbf{k}\cdot\hat{\bar{\mathbf{q}}}$. In particular, if $m^* = m$, this yields a linear relation between ω and $k_{\bar{q}}$. Otherwise, the solution has a weak dependence on $(1 - m/m^*)$ and $k_\perp^2 \equiv \mathbf{k}^2 - k_{\bar{q}}^2$. However, this dependence is only noticeable for $k_{\bar{q}}$ close to k_F, and when the effective mass is substantially larger than the bare mass (see Appendix A.3). Neglecting this small effect, we obtain

$$k_{\bar{q}}(\omega) = \frac{m}{\bar{q}}\left(\omega + \epsilon^0_{\text{pol}}\right) - \frac{\bar{q}}{2} \ , \tag{1.31}$$

where $\bar{q} \equiv |\bar{\mathbf{q}}|$.

Evaluation of Eq. (1.29) shows that the coherent polaron Raman rate is proportional to the one-dimensional momentum distribution of polarons in the direction of $\bar{\mathbf{q}}$,

$$\bar{\mathcal{A}}_{\text{coh}}(\omega) = \frac{mN_{\text{coh}}}{\bar{q}N_{\text{I}}} n_{\text{P}}[k_{\bar{q}}(\omega)]. \tag{1.32}$$

In the local density approximation (LDA) this distribution is given by (for details see Appendix A.2)

$$n_{\text{P}}\left[k_{\bar{q}}(\omega)\right] = -\frac{6T_p^{\frac{5}{2}}\left(\varepsilon_F - \epsilon^0_{\text{pol}}\right)^{-\frac{3}{2}}}{\sqrt{\pi}x\bar{Z}k_F\varepsilon_F m/m^*}\mathrm{Li}_{\frac{5}{2}}\left(-\zeta_{\text{P}}e^{-\frac{k_{\bar{q}}^2}{2m^*T_p}}\right) \ . \tag{1.33}$$

As defined previously, x is the global impurity concentration, $\mathrm{Li}_{5/2}$ is the polylogarithm function, and $\zeta_{\text{P}} = e^{-(\epsilon^0_{\text{pol}}-\mu)/T_p}$ is the fugacity of polarons. The chemical potential μ is tuned so that Eq. (1.29) is normalized to the number of polarons that contribute to the coherent part of the response.

As a final step, the spectrum $\bar{\mathcal{A}}_{\text{coh}}$ has to be normalized to unity when integrated over all frequencies in order to obtain the probability P_{coh}[8]. We arrive at

$$P_{\text{coh}}(\omega; T_p, \epsilon^0_{\text{pol}}, m^*) = \frac{m}{\bar{q}} n_{\text{P}}\left[k_{\bar{q}}(\omega)\right] \ . \tag{1.34}$$

[8] This allows us to determine the proportionality constant α between the probability and the coherent Raman spectrum $P_{\text{coh}} = \alpha\bar{\mathcal{A}}_{\text{coh}}$ to be $\alpha = N_{\text{I}}/N_{\text{coh}}$.

1.2.3.2 Background Raman signal

We find that the experimental spectral lineshape arising from the incoherent polaron part and the molarons are fitted well by the response of a thermal gas of molecules (see Appendix A.3). Indeed, this model covers the overall spectral weight of the background well and allows us to incorporate the $\sim \omega^{-3/2}$ tail.

The fit function $P_{\mathrm{bg}}(\omega)$ is derived by considering a thermal ensemble of molecules with binding energy E_b and a center-of-mass momentum $\mathbf{k}_{\mathrm{cm}}$, each of which is made of a single impurity and a single bath particle and considered to be in vacuum. The assumption of a thermal gas is justified since the molecules' temperature is far above the critical condensation temperature due to the low impurity density. The Raman process dissociates the pair and changes the center-of-mass momentum to $\mathbf{k}_{\mathrm{cm}} + \bar{\mathbf{q}}$. In addition, the unbound fermions acquire a relative momentum $k_{\mathrm{rel}} \equiv |\mathbf{k}_{\mathrm{rel}}|$.

As a wavefunction Ansatz for the molecule, we use

$$|\psi^{\mathbf{k}_{\mathrm{cm}}}\rangle = \sum_{\mathbf{l}} \gamma_{\mathbf{l}}^{\mathbf{k}_{\mathrm{cm}}} c_{-\mathbf{l}}^{\dagger} d_{\mathbf{l}+\mathbf{k}_{\mathrm{cm}}}^{\dagger} |0\rangle \ . \tag{1.35}$$

Note that the only difference to Eq. (1.12) is that here, we do not consider the Fermi sea of background particles. This simplification is made in order to obtain a closed-form expression for the fitting function which is feasible to calculate numerically. Using Eq. (1.35) as the initial state $|i\rangle$ for Eq. (1.15), one obtains

$$\mathcal{A}(\omega, \psi^{\mathbf{k}_{\mathrm{cm}}}) = \sum_{\mathbf{l}} \left|\gamma_{\mathbf{l}}^{\mathbf{k}_{\mathrm{cm}}}\right|^2 \delta\left(\omega - \varepsilon_{\mathbf{l}} - \varepsilon_{\mathbf{k}_{\mathrm{cm}}-\mathbf{l}+\bar{\mathbf{q}}} + E_b + \frac{k_{\mathrm{cm}}^2}{4m}\right) \ .$$

The variational parameter $\gamma_{\mathbf{l}}^{\mathbf{k}_{\mathrm{cm}}}$ has to be obtained by the minimization of $\langle\psi^{\mathbf{k}_{\mathrm{cm}}}|\mathcal{H} - E|\psi^{\mathbf{k}_{\mathrm{cm}}}\rangle$. It reads

$$\gamma_{\mathbf{l}}^{\mathbf{k}_{\mathrm{cm}}} = \frac{1}{\sqrt{\sum_{\mathbf{l}} \frac{1}{(E-\varepsilon_{-\mathbf{l}}-\varepsilon_{\mathbf{k}_{\mathrm{cm}}+\mathbf{l}})^2}}} \frac{1}{E - \varepsilon_{-\mathbf{l}} - \varepsilon_{\mathbf{k}_{\mathrm{cm}}+\mathbf{l}}}. \tag{1.36}$$

Within this calculation, the relative momentum after the Raman dissociation is given by $\mathbf{k}_{\mathrm{rel}} = \mathbf{l} + (\mathbf{k}_{\mathrm{cm}} + \bar{\mathbf{q}})/2$. After changing variables $\mathbf{l}$ to $\mathbf{k}_{\mathrm{rel}}$, evaluating the δ-function implements the energy conservation

$$k_{\mathrm{rel}}^2 = m\omega - mE_b - \frac{\bar{q}^2}{4} - \frac{\bar{q}k_{\mathrm{cm},\bar{q}}}{2} \ , \tag{1.37}$$

where $k_{\mathrm{cm},\bar{q}} \equiv \mathbf{k}_{\mathrm{cm}} \cdot \hat{\bar{\mathbf{q}}}$.

Averaging the Raman spectral function over all momenta $\mathbf{k}_{\mathrm{cm}}$ weighted by a thermal Boltzmann distribution at temperature T_{bg}, $G(\mathbf{k}_{\mathrm{cm}}, T_{\mathrm{bg}}) = (4\pi m T_{\mathrm{bg}})^{-3/2} e^{-\mathbf{k}_{\mathrm{cm}}^2/4mT_{\mathrm{bg}}}$, yields

$$\bar{\mathcal{A}}(\omega) = \int \mathrm{d}\mathbf{k}_{\mathrm{cm}} \, \mathcal{A}\left(\omega, \psi^{\mathbf{k}_{\mathrm{cm}}}\right) \cdot G\left(\mathbf{k}_{\mathrm{cm}}, T_{\mathrm{bg}}\right) \ . \tag{1.38}$$

Finally, integration over the angle $\hat{\mathbf{k}}_{\mathrm{rel}} \cdot \hat{\bar{\mathbf{q}}}$ and $k_{\mathrm{cm},\bar{q}}$ yields the normalized Raman transition probability for the background signal,

$$P_{\mathrm{bg}}\left(\omega; T_{\mathrm{bg}}, E_b\right) = \sqrt{\frac{2E_b}{\pi^3 T_{\mathrm{bg}}}} \int_{-\infty}^{2m\tilde{\omega}/q} \mathrm{d}k_{\mathrm{cm},\bar{q}} \frac{2m\sqrt{2m\tilde{\omega} - k_{\mathrm{cm},\bar{q}}\bar{q}}\, e^{-\frac{k_{\mathrm{cm},\bar{q}}^2}{4mT_{\mathrm{bg}}}}}{4mE_b\bar{q}^2 + \left(\bar{q}^2 + k_{\mathrm{cm},\bar{q}}\bar{q} - 2m\omega\right)^2} \ , \tag{1.39}$$

where $\tilde{\omega} \equiv \omega - E_b - \frac{\bar{q}^2}{4m}$. This integral does not have an analytic solution, but it can be readily calculated numerically.

Note that in this fit model, T_{bg} and E_b are effective temperatures and binding energies. Since P_{bg} also describes the incoherent polaron contribution, E_b can be interpreted as the molecular binding energy $-\epsilon_{\mathrm{mol}}$ only in the limit of large $(k_F a)^{-1}$. The effective temperature T_{bg} compensates for the absence of Pauli blocking in the molecular model, and therefore should not be interpreted as the physical temperature of molarons.

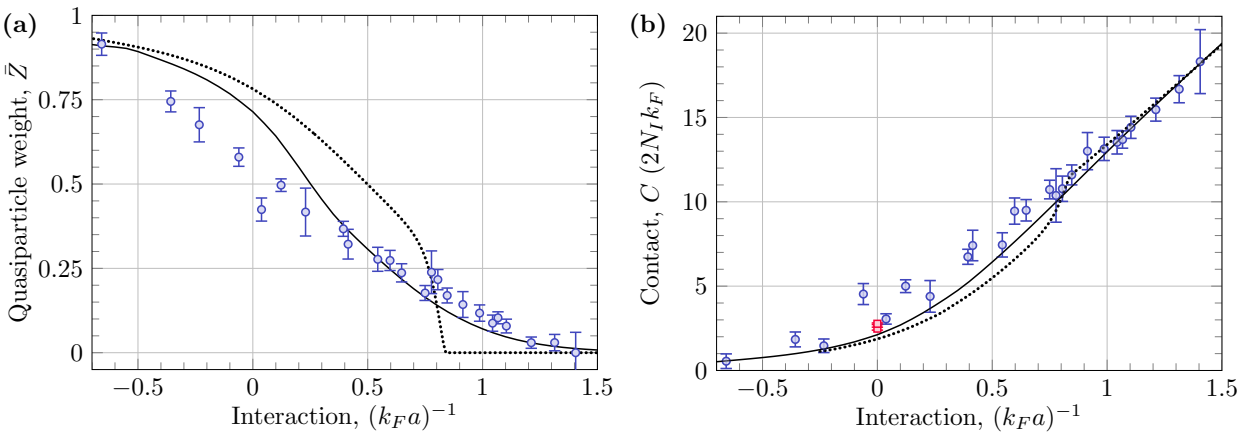

Figure 1.10: Comparison of measured and calculated quasiparticle weight $\bar{Z}$ and Tan's contact C. **(a)** Blue circles mark the weight extracted from the measured Raman spectra by identifying the nearly symmetric spectral lineshape arising from the coherent polaron contribution. $\bar{Z}$ is smoothly decreasing towards the polaron–molaron transition, in agreement with the theoretical prediction, averaged over the harmonic trap using the LDA (solid line). For comparison, we also present the trap-averaged prediction for a single impurity at $T = 0$ (dotted line) obtained from Ref. [29]. **(b)** The contact coefficient C is shown for different interaction strengths, obtained using Eq. (1.40) with E_b and $\bar{Z}$ extracted from the Raman spectra. The data agree well with our calculation, taking into account the finite temperature and coexistence of polarons and molarons (solid line). The two red squares indicate data measured by the MIT group [46] using rf spectroscopy of a unitary, homogeneous ^{6}Li gas at $T = 0.17\,T_F$ (lower point) and $T = 0.29\,T_F$ (upper point) For comparison, the trap-averaged prediction for a single impurity (dotted line) is also shown.

1.2.4 Comparison between theory and experiment

The polaron weight $\bar{Z}$ can be extracted by fitting the measured spectra with Eq. (1.25). The effective temperature parameter $T_{\rm bg}$ controls the sharpness of the onset of the background spectrum. We fix $T_{\rm bg} = 2\,T_F$, which yields a minimal systematic error in extracting $\bar{Z}$ (see Appendix A.3). The polaron effective mass, m^*, is strongly coupled to the polaron temperature. To make the fit robust, we set m^* to the trap-averaged theoretical value at $k \to 0$, calculated from Eq. (1.11). We find that the effective mass modifies the extracted polaron weight and molecular binding energy only marginally. In fact, setting m^* to the bare mass leads to a maximal deviation of less than $0.4\,\sigma$. We are thus left with three free fitting parameters: $\bar{Z}$, E_b, and T_p. Examples of fits are shown in Fig. 1.9 (b) (solid lines). Overall, we find excellent agreement between the fits and the measured spectra throughout the whole interaction range. The light and dark shaded areas beneath the curves are the spectral contributions of the coherent part of the polaron and the background, respectively. The data on the BCS-side (blue circles) are dominated by a nearly symmetric quasiparticle peak with $\bar{Z} = 0.91(3)$, while the BEC-side data (black triangles) are dominated by the asymmetric pair dissociation spectra, leading to a small coherent weight $\bar{Z} = 0.18(2)$. The unitary data (red squares) shows both the symmetric peak and an asymmetric tail. The quasiparticle weight is $\bar{Z} = 0.58(3)$, close to the value of $0.47(5)$, which was measured for ^{6}Li atoms with rf spectroscopy [8].

A comparison between the extracted and calculated coherent polaron spectral weight is shown in Fig. 1.10 (a). The predicted smooth behavior is consistent with the experimental observation. We attribute the overestimation of the theoretical values for $\bar{Z}$ in the polaron-dominated interaction regime for $(k_F a)^{-1} \lesssim 0.4$ to several factors. Firstly, the single-impurity polaron weight Z will be reduced when higher-order terms are included in the wavefunction Ansatz Eq. (1.11). Secondly, due to the neglect of finite-lifetime molaron states, the polaron contribution in the initial state is overestimated. Thirdly, the disregard of finite-lifetime polarons leads to an effective population transfer to low-momenta polaron states which, again, results in a higher quasiparticle weight. To demonstrate the crucial role of the finite impurity density and temperature, we also plot in Fig. 1.10 (a) the prediction for a single impurity at zero temperature in the LDA (dotted line). The data

clearly disagrees with this result, and in particular, does not exhibit a sudden change at the polaron-to-molaron transition as predicted in the single polaron limit.

Finally, we extract the Tan's contact C from the experimental data. In our fitting model, the tail appears in the spectral contribution of incoherent polarons and molarons. Thus the contact is related to the parameters of our model by [57, 66]

$$C = 4\pi(1-\bar{Z})\sqrt{E_b/\,2\varepsilon_F}\,. \tag{1.40}$$

Here C is given in units of $2N_I k_F$ such that the high-frequency tail of the spectrum approaches $P(\omega) \to C\sqrt{\varepsilon_F}/\sqrt{2}\pi^2\omega^{3/2}$ [67]. The results for C are shown as blue circles in Fig. 1.10 (b). For comparison, we plot the trap-averaged theoretical prediction for the contact in both the single-impurity limit (dotted line) and in the many-impurity case (solid line). The data is in excellent agreement with the many-body model, and, in particular, it does not show any sudden change as predicted in the single impurity limit. We also indicate the contact measured by the MIT group with a homogeneous ^{6}Li gas using rf spectroscopy [46] (red squares), which agrees with our measurements to within the experimental uncertainty.

1.2.5 Dependence of the coherent peak on the transferred photon momentum

As previously mentioned, the peak position of rf spectra does not coincide with the zero-momentum polaron energy as soon as a finite impurity density is present. Instead, a temperature-dependent shift occurs, as experimentally observed also in the case of Bose polarons in Ref. [46]. In order to calculate this shift, we compute the peak position of the coherent polaron contribution (first term of Eq. (1.23) within Eq. (1.22)) as a function of the photon transfer momentum. The results at unitarity, shifted by the recoil energy, are shown in Fig. 1.11 (a) for three relevant temperatures. In rf spectroscopy ($\bar{q} \to 0$), we find that the peak is shifted to energies lower than the zero-momentum polaron energy (see Fig. 1.11 (b)). As the photon transfer momentum increases, however, this shift rapidly vanishes. Already for $\bar{q} \gtrsim 0.1\,k_F$ (a value easily reached in Raman spectroscopy experiments) the shift is negligible, making it possible to extract the polaron energy from the peak position of the coherent part of the Raman spectra.

The peak of the coherent polaron spectrum, as given in Eq. (1.34), is at $k_{\bar{q}} = 0$. According to Eq. (1.31), this maximum is attained for

$$\omega_0 = \frac{\bar{q}^2}{2m} - \epsilon^0_{\mathrm{pol}}\,. \tag{1.41}$$

For interactions below the transition point, the most significant contribution to the spectral peak stems from the coherent part of polarons. Thus, from ω_0 we can determine the polaron energy, $\epsilon^0_{\mathrm{pol}}$. We find the peak position (dotted vertical lines in Fig. 1.9 (b)) by fitting the points above the median with a skewed Gaussian [68]. The resulting polaron energies are plotted in Fig. 1.11 (c) (blue circles), and compared to the theoretical predicion calculated within the Chevy Ansatz (1.13) (dashed line). The latter are, in turn, close to diagMC and T-matrix calculations [7, 29, 30, 69, 70]. Beyond $(k_F a)^{-1} = 0.9$ the weight of the coherent peak is small. Therefore, the polaron energy is only extracted for $(k_F a)^{-1} < 0.9$.

1.2.6 Summary

In summary, we have investigated the polaron-to-molaron transition at finite impurity density and temperature using Raman ejection spectroscopy. To interpret the experimental data we have employed a quasiparticle theory, in which the many-body Hilbert space of impurity particles is spanned by single-particle states obtained from variational wavefunctions. The approximate nature of this approach is reflected by the fact that

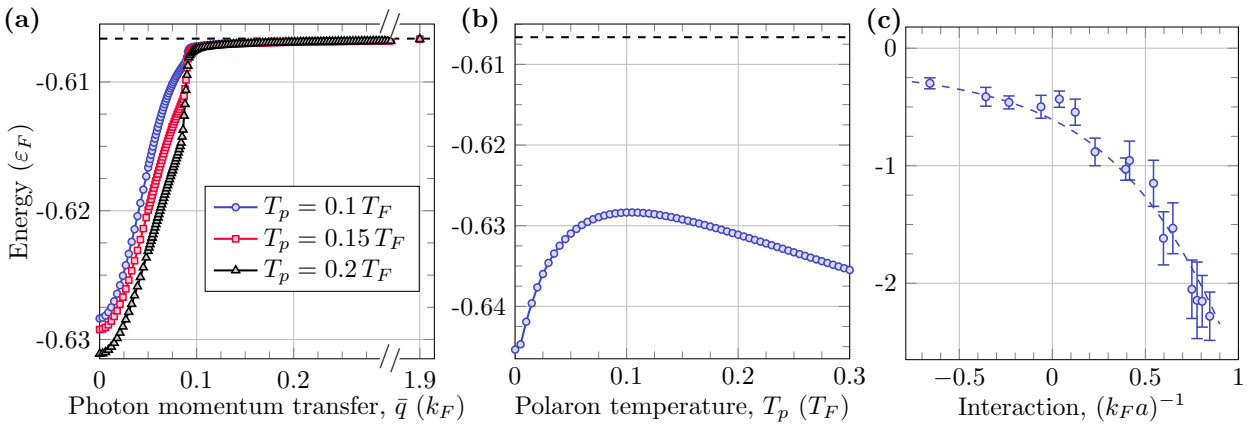

Figure 1.11: **(a)** Coherent spectral peak position at unitarity. Using the full many-body model for the Raman spectra (first term of Eq. (1.23)), we plot the coherent peak position vs. transferred photon momentum for polaron temperatures $T_p = 0.1\,T_F$ (blue circles), $0.15\,T_F$ (red squares), and $0.2\,T_F$ (black triangles) at $(k_F a)^{-1} = 0$ with $n_I = 0.15\,n$. We observe convergence to the zero-temperature value $\epsilon_{\rm pol} = -0.6066\,\varepsilon_F$ (dashed line) for photon momentum transfer larger than $0.1\,k_F$. Specifically, with the Raman momentum of $\bar{q} = 1.9\,k_F$ used in our experiment, no shift is expected. **(b)** Temperature dependence of the spectral peak position with conventional rf spectroscopy ($\bar{q} = 0$). **(c)** Comparison of measured and calculates polaron energies $\epsilon^0_{\rm pol}$ at interaction strengths below the polaron-to-molaron transition. The polaron energies (blue circles) are obtained using Eq. (1.41) from the position of the spectral peak. The theoretical prediction obtained from the variational Ansatz Eq. (1.13) averaged over the harmonic trap is shown as a dashed blue line.

polarons and molecules are effectively created by composite impurity-bath operators that maintain their respective commutation relations only approximately. Correspondingly, both impurity-induced correlations between majority fermions, as well as quasiparticle interactions (polaron–polaron, polaron–molaron, and molaron–molaron), induced by the Fermi sea, are neglected. How the bath mediated interactions of two polarons can be studied on the level of variational wavefunctions is discussed in Subsec. 2.2.3. In general, the accurate inclusion of correlation effects, which could, for instance, describe an instability of a Fermi polaron gas towards p-wave superfluidity [71, 72], presents a formidable theoretical challenge. While the finite density of impurities can be included in quantum field theory approaches, the systematic study of polaron–polaron interactions requires the inclusion of extended sets of vertex functions [73–75] that are beyond the reach of mean-field approximations.

Within our theory, we are able to calculate finite impurity density and temperature Raman spectra, and to extract quantities as the many-body quasiparticle weight and the Tan's contact throughout the polaron-to-molaron transition. To extract these quantities also from the experimental data, we have developed a simple fitting model that leverages the separation of the Raman spectra into two contributions: the nearly symmetric coherent polaron response, and an asymmetric background arising from the incoherent response of polarons and from molecules. This allows us to extract the polaron energy, the quasiparticle spectral weight and Tan's contact from the experimental spectra, and to compare them to the theoretical predictions. All calculated and measured quantities show a smooth transition with no sudden changes around the predicted polaron-to-molaron transition. Our findings suggest that close to the interaction where the polaron-to-molaron transition takes place in the single impurity limit, polarons and molarons coexist when the temperature is above the critical temperature of Bose-Einstein condensation of molarons.

At lower temperatures, the phase diagram is not yet understood and contrasting predictions have been made. On the one hand, at zero-temperature, the polaron-to-molaron transition marks the endpoint of a fermionic polaron phase, where its finite Fermi surface volume vanishes and a polarized superfluid phase consisting of molecules is expected to take over [29, 76]. On the other hand, considering the strong atom-dimer interactions close to the transition point [77], it has been predicted that the system might become unstable towards phase separation between superfluid and normal phases [78]. The application of Raman spectroscopy in an

imbalanced Fermi gas at lower temperature [79] and homogeneous traps [80–83] might help to distinguish these scenarios and allow one to experimentally determine, e.g., the transition temperature towards phase separation.

Furthermore, away from the transition point a plethora of phases has been discussed in the literature, ranging from p-wave pairing of polarons to the FFLO phase [10, 61, 84, 85]. In the next chapter, we will show how the existence of an FFLO phase can be already inferred from the single impurity limit. As already visible in Fig. 1.4, the excited molaron in the polaronic regime features a dispersion relation with a minimum at finite momentum (see also Refs. [39, 86]). In the next chapter, we will show that this effect may be regarded as a precursor of the long-sought-after FFLO phase in the imbalanced BEC-BCS crossover [9, 10, 84, 87–89], which emerges due to the macroscopic occupation of such molaron states at finite momentum.

1.3 Probing molecular spectral functions

In the previous chapter we have seen how ejection spectroscopy can be used to study the ground state of a strongly imbalanced Fermi system, including the polaron-to-molaron transition. As discussed in Subsec. 1.1.4, polarons can be probed even in their excited states using injection spectroscopy [37]. However, the vanishing overlap between a non-interacting initial state of fully delocalized particles and a final state where an impurity is fully localized around one of the bath fermions hinders the creation of molarons in injection spectroscopy. This is why, to date, it has not been possible to explore molarons experimentally beyond their ground state properties [P1, 8].

However, the molaron displays some intriguing properties in the unitary regime, where it is the excited state of the system. This becomes evident from its single particle spectral function, which we have already seen at unitarity in Fig. 1.4. Here, the molaron has a negative effective mass, which is given by the curvature of the molarons dispersion $E(k)$ with respect to its momentum k via $1/m = \partial^2 E/\partial k^2$. Its dispersion features a minimum at finite momentum [32, 43, 90], which is found to be robust with respect to the theoretical approximation scheme.

1.3.1 Precursor of the FFLO phase

The existence of the finite momentum minimum in the molaron dispersion can be directly connected to the emergence of the elusive Fulde-Ferell-Larkin-Ovchinnikov (FFLO) [9, 10] phase at finite impurity density, where composite Cooper pairs condense into a finite-momentum state. To this end, we extend the T-matrix approach to finite *fermionic* impurity density, by including a chemical potential for the impurities μ_d (cf. Fig. 1.3 (b)). The *bosonic* molaron spectral function for different impurity chemical potentials is shown in Fig. 1.12 (a). The dispersion minimum continuously evolves until the finite-momentum molaron becomes gapless precisely at the predicted onset of the FFLO phase at $\mu_d = 0.196\,\epsilon_F$ [91]. This continuous relation of the molaron spectral function towards a gapless spectrum implies a simple picture of FFLO as a condensate of molarons.

To further substantiate this direct connection between molarons and the formation of the FFLO phase, we investigate its dependence on interaction strengths and the range parameter. The transition line towards the FFLO phase can be found by solving the Cooper problem at finite momentum $\mathbf{p}$ [91]. Here, we extend this approach to the two-channel model (1.8) which accounts also for a finite effective range parameter r_e (or

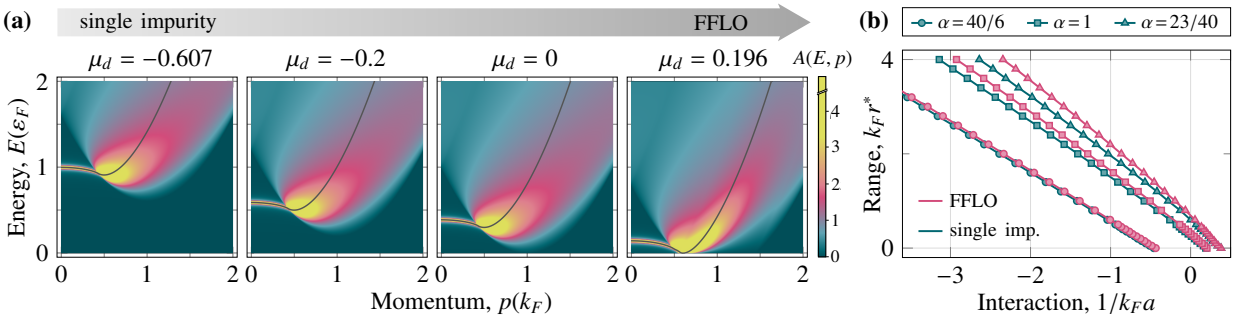

Figure 1.12: **(a)** Density plot of the molaron spectral function $A_{\text{mol}}(E, \mathbf{p})$ in units of ε_F at unitarity in the contact interaction limit ($k_F r^* = 0$) and mass balance ($\alpha = 1$) for different chemical potentials of the minority population. The molaron dispersion (gray line) has a minimum at finite momentum. For $\mu_d = 0.196\,\epsilon_F$, the molaron becomes gapless at finite momentum, which determines the onset of FFLO. **(b)** Critical range parameter $k_F r^*$ below which the molaron dispersion minimum is at finite momentum (blue) and for which FFLO sets on at finite impurity density (pink), shown for the mass ratios $\alpha = 40/6$ (heavy impurity), $\alpha = 1$ (mass balance), and the hypothetical mass ratio $\alpha = 23/40$ (light impurity) as a function of the interaction strength.

equivalently a finite r^*):

$$-E + \xi_{\mathbf{p}} - \mu_d - \mu_c + \frac{\pi}{r^* \mu^2}\left[\frac{\mu}{2\pi a} - \frac{1}{V}\sum_{\mathbf{k}}\left(\frac{1}{\varepsilon^c_{\mathbf{k}} + \varepsilon^d_{\mathbf{k}}} - \frac{1 - n_F(\varepsilon^c_{\mathbf{k}}, \mu_c) - n_F(\varepsilon^d_{-\mathbf{k}+\mathbf{p}}, \mu_d)}{-E - i0^+ + \varepsilon^c_{\mathbf{k}} - \mu_c + \varepsilon^d_{-\mathbf{k}+\mathbf{p}} - \mu_d}\right)\right] = 0, \tag{1.42}$$

with $\mu = M_d M_c/(M_d + M_c)$ the effective mass and $n_F(\varepsilon, \tilde{\mu}) = (e^{\frac{1}{T}(\varepsilon - \tilde{\mu})} + 1)^{-1}$ the Fermi-Dirac distribution function at chemical potential $\tilde{\mu}$. For a given interaction strength and effective range, we start from a density balanced system, i.e. $\mu_d = \mu_c$, and decrease the chemical potential μ_d up to the point where we find a solution of Eq. (1.42) for finite $\mathbf{p}$ and $E = 0$. The results, for different mass ratios, are shown in Fig. 1.12 (b) as pink lines. We now compare predicted quantum critical value of the FFLO transition to the critical interaction strengths at which the minimum of the molaron dispersion moves to finite momentum (see Fig. 1.12 (b) blue lines). As can be seen, the boundaries lie in close proximity and exhibit the same behavior with respect to tuning of the range parameter r^*. Based on this close correspondence, the transition point towards FFLO can already be inferred from the excited composite states in the Fermi polaron problem.

1.3.2 Molecular injection spectroscopy

We now show how the idea of injection spectroscopy can be extended to make the full excitation spectrum of molarons accessible. The vanishing overlap in injection spectroscopy between the non-interacting initial state and the final molaron state highlights how the choice of an initial state is the key to measuring molaron properties. This initial state should fulfill two main criteria:

(a) It has to be a good reference state, i.e., a state that can be reliably prepared and whose properties are well-understood.

(b) It should have sufficient spectroscopic overlap with the final state of interest, in this case the molecular state in the quantum medium.

We now show how one can fulfill both criteria when starting from a relatively deeply-bound molecular state and how this allows us to reliably probe many-body dressed composited in what we term *molecular injection spectroscopy* (cf. Fig. 1.13 (a)). In this scheme, the first criterion is fulfilled by starting from a molecular

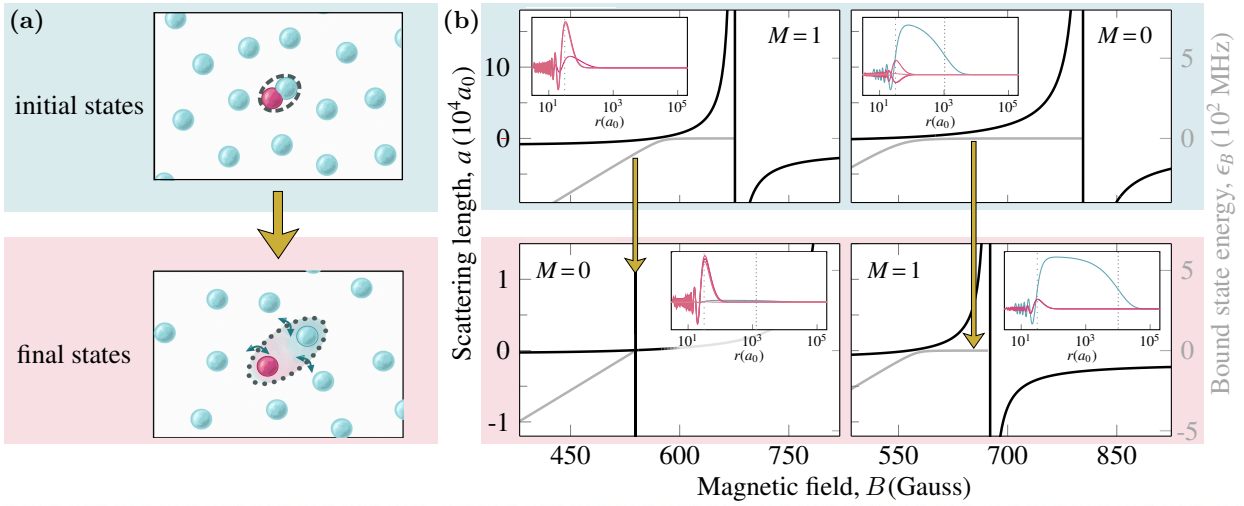

Figure 1.13: **(a)** Sketch of molecular injection spectroscopy. Starting from a deeply bound molecular initial state (top, blue), the molaron in the final state (bottom, red) can be probed. **(b)** Experimental protocol for the example of ^{6}Li. Scattering length (solid black) as a function of magnetic field for the initial (top, blue) and final state (bottom, red). In the left (right) panels one aims to probe a molaron in a final state at a narrow (broad) Feshbach resonance. The insets show the different channel contributions to the radial wave function of the Feshbach molecule at the applied magnetic field: Open channels (blue) and closed channels (pink). In the top right plot the narrow resonance is omitted for clarity. All data is obtained from a coupled-channel calculation, using realistic atomic potentials as input [92]. Dashed (dotted) lines in the insets indicate the van-der-Waals and scattering length, respectively.

state with binding energy $\epsilon_{B,\text{in}}/\epsilon_F \gg 1$, so that medium corrections determined by the Fermi energy ϵ_F are negligible. As a result, the initial state is well described by typical atomic physics models [27]. Establishing the fulfillment of the second condition requires a detailed analysis of the action of the Raman operator $\hat{V}_{\bar{\mathbf{q}}}$ on this initial state. We use the two-channel model (1.8) to generally establish our protocol for broad and narrow Feshbach resonances in the final state, and the corresponding variational Ansatz (1.12) to describe the molaron. Within the two-channel model, understanding the action of the Raman lasers requires translation of $\hat{V}_{\bar{\mathbf{q}}}$ from an atomic state basis (where it takes a form $\sim \sum_{\mathbf{p}} d^\dagger_{\mathbf{p}+\bar{\mathbf{q}},f} d_{\mathbf{p},i}$, with i, f labeling the internal atomic states of the impurity before and after the Raman transition) into a basis that explicitly accounts for the closed-channel molecule $m^\dagger$. To achieve this we turn to an ab-initio coupled-channel calculation in the two-body limit. It is reasonable to work in this limit since the initial state is tightly bound and many-body dressing of the final state molecule only affects its low energy physics, and hence does not affect the form of the laser operator.

More information about the ab-initio calculation can be found in Appendix A.4. It is based on atomic states and yields not only the binding energies and the magnetic field dependent scattering lengths, but also allows for a clear distinction between the open-channel (long-range component) and closed-channel (short-range component) contributions to the molecular wave functions[9] (see Fig 1.13). For concreteness, we exclusively consider the example of ^{6}Li, which features all key elements to demonstrate the idea of molecular injection spectroscopy. Specifically, we focus on two limits where the initial state molecule has either its weight almost entirely in the closed channels (cf. Fig. 1.13 (b), upper left), or in the open channel (upper right), allowing for a precise characterization of the Raman laser operator.

The left-hand panels in Fig. 1.13 (b) show the scenario of a strongly bound closed-channel Feshbach molecule in the initial state, corresponding to $|i\rangle = m^\dagger_{\mathbf{0},i}|0\rangle$ in our model. Such a state can be prepared for sufficient detuning from a Feshbach resonance, possible for both narrow and broad resonances. This choice of initial state (the wave functions including their hyperfine state contributions are shown as insets in Fig. 1.13 (b),

[9] Note that we refer here to an 'open-channel' as the channel in which particles resides asymptotically in the scattering process. Using this terminology a channel is also closed for a Feshbach molecule when it is below the collision threshold.

see also App. A.4) is ideal to detect molarons in the final state close to a narrow resonance, due to a large spectroscopic overlap between initial and final closed-channel contributions (compare insets in Fig. 1.13 (b)). Furthermore, with a size on the order of the van-der-Waals length l_{vdW} (dashed, vertical lines in insets), the initial closed-channel contributions yield only a small overlap with the spatially extended open-channel states in the final state. As a consequence, the Raman operator is well approximated as

$$\hat{V}_{\bar{\mathbf{q}}} = \sum_{\mathbf{p}} m^\dagger_{\mathbf{p}+\bar{\mathbf{q}},f} m_{\mathbf{p},i} \tag{1.43}$$

in the two-channel model.

A second option, best suited to detect molarons close to a broad resonance in the final state, is to start from a deeply-bound initial molecular state close to an open-channel dominated resonance (see right hand panels in Fig. 1.13 (b)). Note that compared to the previous scenario, the initial state is less deeply-bound and resides in the regime where its energy does not depend linearly on the B-field. As the coupled-channel calculation shows, the initial state is dominated by open-channel contributions. In the two-channel model this state is described by $|i\rangle = \sum_{\mathbf{k}} \beta^{\mathbf{0}}_{\mathbf{k}} c^\dagger_{-\mathbf{k}} d^\dagger_{\mathbf{k},i}|0\rangle$. Thus the Raman laser mostly acts on that contribution which is confined on the order of the scattering length a (dotted vertical line in the inset of Fig. 1.13 (b)), and transferred to open-channel contributions in the final state manifold. The projection onto closed-channels of the final state manifold has a negligible contribution due to a lacking overlap of these states at low energy. Hence, within the two-channel model the Raman operator is well represented by

$$\hat{V}_{\bar{\mathbf{q}}} = \sum_{\mathbf{p}} d^\dagger_{\mathbf{p}+\bar{\mathbf{q}},f} d_{\mathbf{p},i}. \tag{1.44}$$

Having established the form of the operator $\hat{V}_{\bar{\mathbf{q}}}$ we now turn to the prediction of the Raman absorption $\mathcal{A}(\omega, \bar{\mathbf{q}})$. To this end, by using the identity $\lim_{y\to 0^+} 1/(x+iy) = -i\pi\delta(x)+\mathcal{P}\,(1/x)$ and replacing $E_\alpha|\alpha\rangle = \mathcal{H}|\alpha\rangle$ we eliminate the explicit final state dependence in Fermi's Golden rule (1.15)

$$\mathcal{A}(\omega, \bar{\mathbf{q}}) = -\frac{1}{\pi}\,\mathrm{Im}\left\langle i \left| \hat{V}_{\bar{\mathbf{q}}} \frac{1}{\omega - \mathcal{H} + E_i + i0^+} \hat{V}_{\bar{\mathbf{q}}} \right| i \right\rangle. \tag{1.45}$$

Here, the initial state $|i\rangle$ is given by a molecular state of form (1.12) with energy $\epsilon_{B,in} \gg \epsilon_F$ such that the many-body dressing by bath particles is negligible. In order to compute the Raman spectra, the matrix elements of the resolvant operator $(\rho - \mathcal{H})^{-1}$ with $\rho = \omega + E_i + i0^+$ need to be determined on the final state manifold spanned by states of the form $m^\dagger_{\bar{\mathbf{q}},f}|\mathrm{FS}_{N-1}\rangle$ and $\{c^\dagger_{-\mathbf{k}} d^\dagger_{\mathbf{k}+\bar{\mathbf{q}},f}|\mathrm{FS}_{N-1}\rangle\}$. To this end, the resolvant operator can be rewritten as

$$\frac{1}{\rho - \mathcal{H}} = \frac{1}{\rho - \epsilon} + \frac{1}{\rho - \mathcal{H}}\, T\, \frac{1}{\rho - \epsilon} \tag{1.46}$$

where ϵ and T denote the kinetic and interaction terms of the Hamiltonian in Eq. (1.8), respectively. Using a basis truncation that includes up to one excitation on top of the Fermi sea, the Raman response takes the form

$$\mathcal{A}(\omega, \bar{\mathbf{q}}) = -\frac{1}{\pi}\,\mathrm{Im}\left(f^{\bar{\mathbf{q}}}(\omega) G^R_{\mathrm{mol}}(\bar{\mathbf{q}}, \omega)\right) + \sum_{\mathbf{k}} |\tilde{\beta}^{\bar{\mathbf{q}}}_{\mathbf{k}}|^2 \delta(\omega + E_{\mathrm{mol},i} - E_{\mathrm{FS}_{N-1}} - \varepsilon^c_{\mathbf{k}} - \varepsilon^d_{\bar{\mathbf{q}}+\mathbf{k}}), \tag{1.47}$$

where $\tilde{\beta}^{\bar{\mathbf{q}}}_{\mathbf{k}}$ is the open-channel contribution of $\hat{V}_{\bar{\mathbf{q}}}|i\rangle$ and $f^{\bar{\mathbf{q}}}$ is a multiplicative structure factor given by

$$f^{\bar{\mathbf{q}}}(\omega) = |\tilde{\beta}^{\bar{\mathbf{q}}}_0|^2 + \sum_{\mathbf{k}} 2\,\mathrm{Re}\left[\tilde{\beta}^{\bar{\mathbf{q}}*}_{\mathbf{k}} \tilde{\beta}^{\bar{\mathbf{q}}}_0\right] \frac{h}{\sqrt{V}} \frac{1}{\rho - \epsilon_{\mathbf{k}}} + \sum_{\mathbf{k}\mathbf{k}'} \tilde{\beta}^{\bar{\mathbf{q}}*}_{\mathbf{k}'} \tilde{\beta}^{\bar{\mathbf{q}}}_{\mathbf{k}} \frac{h^2}{V} \frac{1}{\rho - \epsilon_{\mathbf{k}}} \frac{1}{\rho - \epsilon_{\mathbf{k}'}}. \tag{1.48}$$

Details on the calculation can be found in Appendix A.6. In the case of a narrow Feshbach resonance in the final state (Fig. 1.14 (b)), we choose a deeply-bound initial state given by $|i\rangle = m^\dagger_{i,\mathbf{0}}|\mathrm{FS}_{N-1}\rangle$. In this case, the

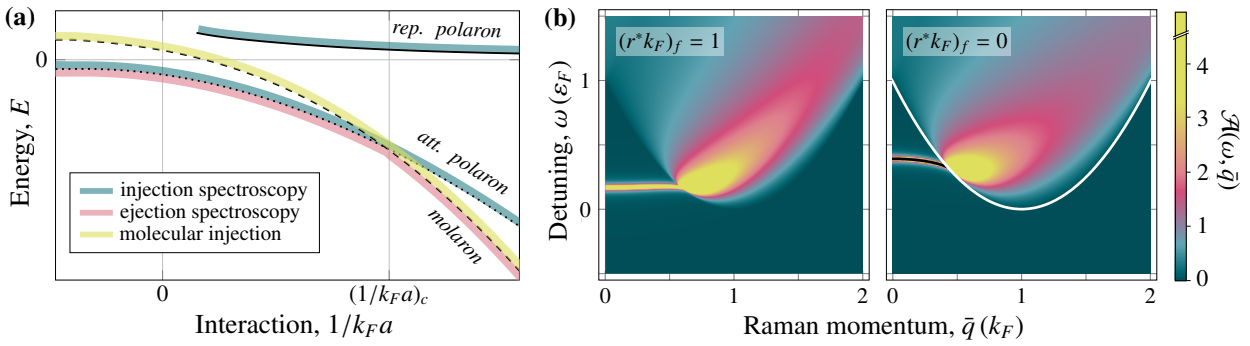

Figure 1.14: **(a)** Schematics of the polaron-to-molaron transition. The colors indicate which states can be probed with which spectroscopic method. Our proposal (yellow) enables for the first time the detection of the excited molaron branch, by initializing the system in the ultra-strong coupling limit. **(b)** Raman spectra $\mathcal{A}(\omega, \bar{q})$ at unitarity and mass balance. Left: Narrow Feshbach resonance ($r^* k_F = 1$) in the final state. The Raman spectrum equals the molaron spectral function. Right: Broad Feshbach resonance ($r^* k_F = 0$) in the final state and initial state at $(k_F a)^{-1} = 1.5$. The Raman spectrum reproduces all key spectral features such as the onset of the continuum (white line) and sharp quasiparticle excitations (black line). Initial state energies are subtracted in both spectra.

laser operator takes the simple form (1.43) and, due to the choice of initial state, this results in $\tilde{\beta}_0^{\bar{\mathbf{q}}} = \beta_0^{\bar{\mathbf{q}}} = 1$, $\tilde{\beta}_{\mathbf{k}}^{\bar{\mathbf{q}}} = 0$ and $f^{\bar{\mathbf{q}}} = 1$. Therefore, the Raman spectrum and the molecular spectral function exactly coincide, $\mathcal{A}(\omega, \bar{\mathbf{q}}) = A_{\mathrm{mol}}(E, \mathbf{p})$.

Next we turn to a broad Feshbach resonance in the final state ($|i\rangle = \sum_{\mathbf{k}} \beta_{\mathbf{k}}^{\mathbf{0}} c_{-\mathbf{k}}^\dagger d_{\mathbf{k},i}^\dagger |\mathrm{FS}_{N-1}\rangle$). Here, the laser operator takes the form (1.44). Therefore $\tilde{\beta}_0^{\bar{\mathbf{q}}} = 0$ and, due to our choice of initial state, $\tilde{\beta}_{\mathbf{k}}^{\bar{\mathbf{q}}} = \beta_{\mathbf{k}}^{\bar{\mathbf{q}}}$, which can be simply obtained from minimizing the energy functional $\langle \psi_M^{\bar{\mathbf{q}}} | \mathcal{H} - E | \psi_M^{\bar{\mathbf{q}}} \rangle$ and is given by

$$|\beta_{\mathbf{k}}^{\bar{\mathbf{q}}}|^2 = \frac{1}{V} \left(\frac{1}{\omega + i0^+ - \varepsilon_{\mathbf{k}}^c - \varepsilon_{\mathbf{k}+\bar{\mathbf{q}}}^d - E_{\mathrm{FS}}(N-1)} \right)^2 \frac{1}{\frac{1}{h^2} + \frac{1}{V} \sum_{\mathbf{k}'} \left(\frac{1}{\omega + i0^+ - \varepsilon_{\mathbf{k}'}^c - \varepsilon_{\mathbf{k}'+\bar{\mathbf{q}}}^d - E_{\mathrm{FS}}(N-1)} \right)^2}. \tag{1.49}$$

In Fig. 1.14 (c) it can be seen that the Raman spectrum contains the same qualitative features as the corresponding molaron spectral function shown in Figs. 1.4 and 1.12 (a). In particular, the position of the molaron as well as its merging into the continuum can be inferred from the Raman spectrum. Quantitatively, the difference between these spectra is merely a redistribution of spectral weight, where the second part of Eq. (1.47) provides only a negligible contribution[10]. Importantly, the dispersion relation of the molaron including its finite momentum minimum is contained in such Raman spectra. Therefore, our approach allows one to observe a key signature of the instability towards FFLO both for broad and narrow Feshbach resonances.

1.3.3 Summary

In this chapter we have presented a protocol to measure the momentum-resolved molaron spectral function at arbitrary interaction strengths. This is achieved using Raman injection spectroscopy with a tunable transfer momentum, where the system is initialized in the ultrastrong coupling limit. The protocol is even applicable when relying on rf-transitions. In this case, however, only zero-momentum properties of the molaron would be accessible. Still, this would, for the first time, allow one to detect the zero-momentum molaron energy across the polaron-to-molaron transition. In combination with standard injection spectroscopy, which allows

[10] It should be noted, however, that for certain observables such a redistribution is important, such as when one aims to infer decay rates of quasiparticles from spectral functions.

for the detection of the polaron branch, this would allow for the simultaneous observation of both polaron and molaron branches at the same interaction strength, which provides an experimental tool to prove not only their coexistence but also the first-order nature of their transition [93–95].

When relying on Raman transition, our technique enables the measurement of the momentum-resolved molaron spectral function, providing information about the dispersion, lifetime, effective mass, and full excitation spectrum of the composite quasiparticle. This includes the observation of the non-trivial dispersion relations of composite states, including the formation of a roton-type minimum. We demonstrated a connection between the finite-momentum properties of the excited molaron state and the emergence of the FFLO phase at finite impurity density. More specifically, we showed that the finite-momentum minimum in the molaron spectral function can be identified as a precursor to the elusive FFLO phase.

The spectroscopic protocol can also be applied to Bose polarons, where the resulting composite is fermionic. It holds potential for studying topologically non-trivial Fermi surfaces, Fermi surface reconstruction, and many-body bound states involving multiple bath atoms, as well as emerging phases in mass-imbalanced ultracold gases. Furthermore, it may allow one to shed new light on the role of many-body bound states involving more than one bath atom as well as emerging phases in mass-imbalanced ultracold gases [96].

Chapter 2

Interactions of Bose polarons in a driven dissipative enviroment

This chapter is based on the following publication
L. B. Tan*, O. K. Diessel*, A. Popert, R. Schmidt, A. İmamoğlu, and M. Kroner, **equal contribution*,
Bose polaron interactions in a cavity-coupled monolayer semiconductor,

Phys. Rev. X **13**, 031036 (2023)

2.1 Introduction

After discussing the Fermi polaron and its realizations in ultracold quantum gases, we now turn to another species of polarons, namely Bose polarons. Bose polarons arise from the coupling of a quantum impurity with a surrounding bosonic bath. We notice here that the very first polaron problem, introducted in a crystal lattice [97], describes a Bose polaron, since the lattice vibrations constituting the bath are of bosonic nature.

In this chapter, we consider a coherent bosonic bath with a finite impurity density and investigate interactions between Bose polarons. Interactions between quasiparticles play a key role across physics, determining novel phases of matter and governing the quantum dynamics of many-body systems. One spectacular example for how polaron-polaron interactions could drastically deviate from those of the bare impurities is superconductivity: electronic quasiparticles form bound Cooper pairs due to bath-mediated attraction even though bare electrons are subject to repulsive Coulomb interactions. Here, we show that the interactions between two fundamentally repulsive bosonic quantum impurities can be tuned and even reversed in sign. Our theoretical results are confirmed by an experiment, in which Bose polarons are realized in a two-dimensional semiconductor, a so called transition-metal dichalcogenide (TMD).

In addition to ultracold quantum gases, TMDs represent a platform with great potential to simulate quantum matter and to study polarons. Similar to ultracold quantum gases, TMDs allow for the creation of Fermi-Bose and Bose-Bose mixtures at various imbalances, the tunability of the interaction parameter between both species, and the formation of bound states due to resonances. All these ingredients make them ideal to investigate both Fermi and Bose polaron physics.

The chapter is organized as follows: We start with a brief introduction to Bose polarons, followed by a discussion of TMDs including how Fermi and Bose polarons can be realized in such platforms. Next, in Sec. 2.2, we focus on a specific realization of Bose polarons in terms of exciton-polaritons, a naturally driven-dissipative system, and discuss its theoretical modelling. Finally, in Subsec. 2.2.3 we investigate interactions between polarons and show how they can be tuned and even reversed in sign upon varying the bath density.

2.1.1 The Bose polaron problem

The Bose polaron describes the situation of a single impurity interacting with a bosonic environment, usually a Bose Einstein condensate (BEC), into which it has been immersed. For small interactions between the impurity and the bath, the impurity is dressed by excitations of the BEC, thus forming a polaron. In contrast to the Fermi polaron, however, up to now there is no consensus in theory of what happens to the impurity as the interaction strength increases [98].

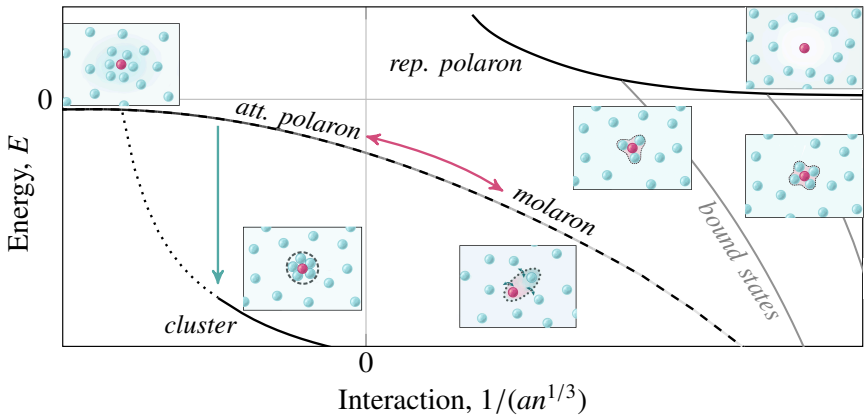

Figure 2.1: Schematic figure of the Bose polaron problem. The attractive polaron can either smoothly crossover into a molaron state, or decay into a multiparticle cluster state. For strong impurity-bath interactions, multi-particle bound states emerge between the repulsive and the attractive polaron branch. The figure is adapted from Refs. [98, 99].

The three dimensional Bose polaron problem, depicted in Fig. 2.1, is proposed to behave in one of two ways: In the first scenario, the polaron experiences a smooth crossover into a molaron (which, in contrast to the Fermi polaron problem, can also involve more than one bath particle as the interaction strength is increased) [100–102]. In the second scenario, the impurity mediates an effective attractive interaction between the bath bosons, which leads to a collapse of the BEC [103, 104]. As a result, the polaron decays into a multi-particle bound cluster. The second scenario is particularly favorable for light impurities (with the impurity mass M_d much smaller than the mass of the bath particles $M_d \ll M_c$), as light particles have a higher mobility and thus are able to mediate interactions more efficiently. The unification of these two scenarios is currently object of active research [98].

Similar to the Fermi polaron problem, on the repulsive side of the Feshbach resonance ($1/an^{1/3}$), a repulsive polaron state emerges. Additionally, for sufficiently strong interactions, two additional excited polaron states (not shown in Fig. 2.1) and metastable bound states (see Fig. 2.1) are found to exist in between the attractive and repulsive polaron branches [99]. These bound states emerge due to the competition between the energy gained from multiple occupation of the bound state and the inter-boson repulsion. For increasing interactions, the bound states ultimately join the attractive branch and therefore cause the adiabatic evolution from the attractive polaron into a molaron with increasing boson number. We refer the reader to Ref. [99] for a detailed analysis of the connection between the attractive and repulsive polaron.

Attractive and repulsive Bose polarons were first observed spectroscopically [105–107] in ultracold atomic mixtures, in 1d and 3d geometries. An inherently two-dimensional platform for quantum simulation are TMDs. Within these, Fermi polarons were first realized in [13]. The first experimental realization of Bose polarons is discussed in Sec. 2.2.

2.1.2 Transition metal dichalcogenides

Ever since the Nobel prize in 2010 "for groundbreaking experiments regarding the two-dimensional material graphene" [108, 109], 2d materials have attracted enormous interest. The discovery of graphene illustrates how dramatically the properties of materials can change when the dimensionality is reduced to only one atomic layer.

TMD monolayers represent one family of atomically thin materials. They have the chemical composition MX_2, where M represents the transition metal element (e.g., Mo, W), and X represents the chalcogen atom (S, Se, or Te). For most TMDs, the lowest energy stable configuration is semiconducting, where the three chemical planes in a single monolayer are stacked in an A-B-A sequence and form a quasi 2D hexagonal lattice (see Fig. 2.2 (a) and (b)). In the monolayer limit, the conduction band minimum and the valence band maximum are located at the K and K$'$ points in momentum space, referred to as the K and K$'$ valley. The K and K$'$ points are high symmetry points of the first Brillouin zone, which are invariant under a $2\pi/3$ in-plane rotation and related via time reversal symmetry (see Fig. 2.2 (c)). As a direct consequence of these symmetries, the optical selection rules for interband transitions from the valence to the conduction band at the K, K$'$ points are valley selective: σ_+ (σ_-) circularly polarized light can only couple to the transition at the K (K$'$) valley.

Additionally, in TMDs optical selection rules are effectively spin selective. This is due to the strong spin–orbit coupling, which lifts the spin degeneracy in both, valence and conduction band, and introduces an energy spitting between spin-up and spin-down states. The spin–orbit splitting amounts to hundreds of meV in the valence band and a few meV in the conduction band. As a consequence, excitations of electrons with different spin have different excitation frequencies (see Fig. 2.2 (d)). For a more in-depth discussion on TMDs, we refer the reader to Refs. [110, 111].

2.1.2.1 Excitons in TMDs

Through the absorption of a photon with suitable energy and polarization, a valence electron (of specific spin and valley index) can be promoted to the conduction band. The attractive Coulomb interactions between the excited electron and the hole left in the valence band lead to the formation of a bound state, the exciton. Due to the reduced dielectric screening from the environment in a two dimensional TMD monolayer, the Coulomb attraction between the hole and the electrons is strong, leading to typical exciton binding energies on the order of $E_b \sim 0.5$ eV, one order of magnitude larger compared to typical bulk semiconductors such as GaAs ($E_b \sim 0.02$ eV). The exciton radii are small (with a Bohr radius on the order of 1 nm), allowing us to treat them as point like particles in what follows.

2.1.2.2 Exciton-polaritons in TMDs

Due to the exciton's large oscillator strength, TMDs reach the regime of strong light-matter coupling when placed inside an optical cavity. When the cavity is calibrated such that the cavity mode and the exciton are at resonance, the Rabi coupling between exciton and light results in a coherent admixture between the cavity photon and the exciton, which together form a particle known as the exciton-polariton.

The Hamiltonian describing such a system is given by

$$\mathcal{H} = \sum_{\mathbf{k}} \omega_{\mathrm{X}}(\mathbf{k}) x_{\mathbf{k}}^{\dagger} x_{\mathbf{k}} + \sum_{\mathbf{k}} \omega_{\mathrm{C}}(\mathbf{k}) c_{\mathbf{k}}^{\dagger} c_{\mathbf{k}} + \sum_{\mathbf{k}} \frac{\Omega}{2} \left(x_{\mathbf{k}}^{\dagger} c_{\mathbf{k}} + \mathrm{h.c.} \right) \tag{2.1}$$

with $x_{\mathbf{k}}^{\dagger}$ the excitons, $c_{\mathbf{k}}^{\dagger}$ the photon, and their respective energies $\omega_{\mathrm{X}}(\mathbf{k}) = \mathbf{k}^2/2m_{\mathrm{X}}$ and $\omega_{\mathrm{C}}(\mathbf{k}) = \delta +$

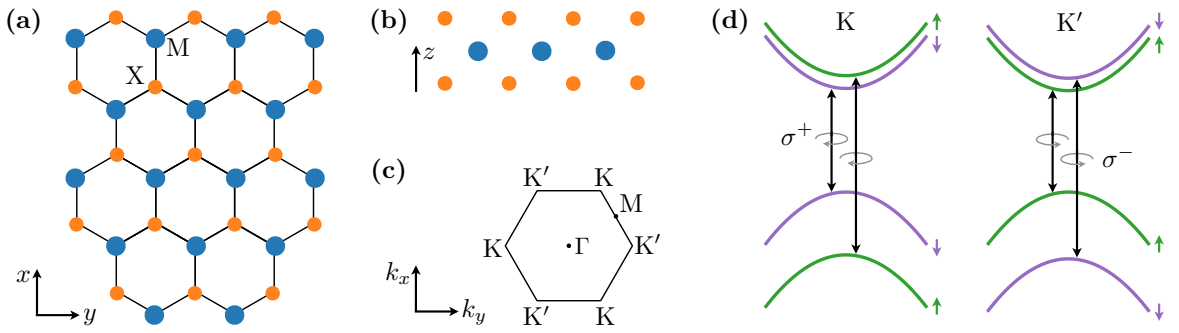

Figure 2.2: **(a)** Top view of a monolayer TMD. Blue (orange) spheres denote metal (chalcogen) atoms. **(b)** The side view of a monolayer TMD shows the layered structure of metal atoms sandwiched between two layers of chalcogen atoms. **(c)** The hexagonal first Brillouin zone of the lattice shown in **(a)**. K and K′ valleys lie at the edges and are related by time reversal symmetry. **(d)** Schematics of the spin-orbit coupling in the K and K′ valley lifting the spin degeneracy in both valence and conduction band. The arrows indicate the valley and spin optical transition selection rules.

$\mathbf{k}^2/2m_\mathrm{C}$. The detuning between the exciton and the photon is given by δ. The Rabi coupling Ω leads to the hybridisation into the upper and the lower polariton.

The Hamiltonian (2.1) can be diagonalized by the unitary transformation

$$\begin{pmatrix} x_\mathbf{k} \\ c_\mathbf{k} \end{pmatrix} = \begin{pmatrix} \cos\theta_\mathbf{k} & \sin\theta_\mathbf{k} \\ -\sin\theta_\mathbf{k} & \cos\theta_\mathbf{k} \end{pmatrix} \begin{pmatrix} L_\mathbf{k} \\ U_\mathbf{k} \end{pmatrix} \tag{2.2}$$

which corresponds to a rotation from the exciton/photon basis into the upper polariton ($U^\dagger$)/lower polariton ($L^\dagger$) basis. Here,

$$\cos\theta_\mathbf{k} = \frac{1}{\sqrt{2}}\sqrt{1 + \frac{|\omega_\mathrm{C}(\mathbf{k}) - \omega_\mathrm{X}(\mathbf{k})|}{\sqrt{(\omega_\mathrm{C}(\mathbf{k}) - \omega_\mathrm{X}(\mathbf{k}))^2 + \Omega^2}}} \tag{2.3}$$

are the Hopfield factors which correspond to the exciton fraction in the lower (upper) polariton state at a given momentum. The diagonalized Hamiltonian reads

$$\mathcal{H} = \sum_\mathbf{k} \omega_\mathrm{LP}(\mathbf{k}) L_\mathbf{k}^\dagger L_\mathbf{k} + \sum_\mathbf{k} \omega_\mathrm{UP}(\mathbf{k}) U_\mathbf{k}^\dagger U_\mathbf{k} \tag{2.4}$$

with $\omega_\mathrm{LP/UP}(\mathbf{k}) = \frac{1}{2}(\omega_\mathrm{X}(\mathbf{k}) + \omega_\mathrm{C}(\mathbf{k}) \mp \sqrt{(\omega_\mathrm{C}(\mathbf{k}) - \omega_\mathrm{X}(\mathbf{k}))^2 + \Omega^2})$ the lower/upper polariton energy.

Similar to bare excitons, one can create two different types of exciton-polaritons in TMDs: one consisting of a K-valley exciton and a σ^+-photon, and the other one consisting of K′-valley exciton and a σ^--photon.

2.1.2.3 Fermi polarons in TMDs

Our discussion so far has been limited to the charge-neutral regime. However, it is possible to introduce free charge carriers in form of electrons or holes in the system by applying a gate voltage. Excitons in one valley can attractively interact with electrons in the opposite valley. In the limit of a single exciton, this realizes the situation of the Fermi polaron problem, an impurity (i.e., the exciton) immersed in a fermionic bath (i.e., the injected electrons/holes). In two dimensions, any purely attractive, short-range interaction supports a bound state. The bound state associated with the exciton-electron interaction is called the trion. Its binding energy amounts about $E_b \sim 25$ meV. It is common to relate the interaction coefficient to the bound state energy and define the dimensionless interaction parameter E_b/ϵ_F (similar to $1/k_F a$ in three dimensions). In contrast to ultracold atomic mixtures, in which the full tunability of the Feshbach molecule (by the application of

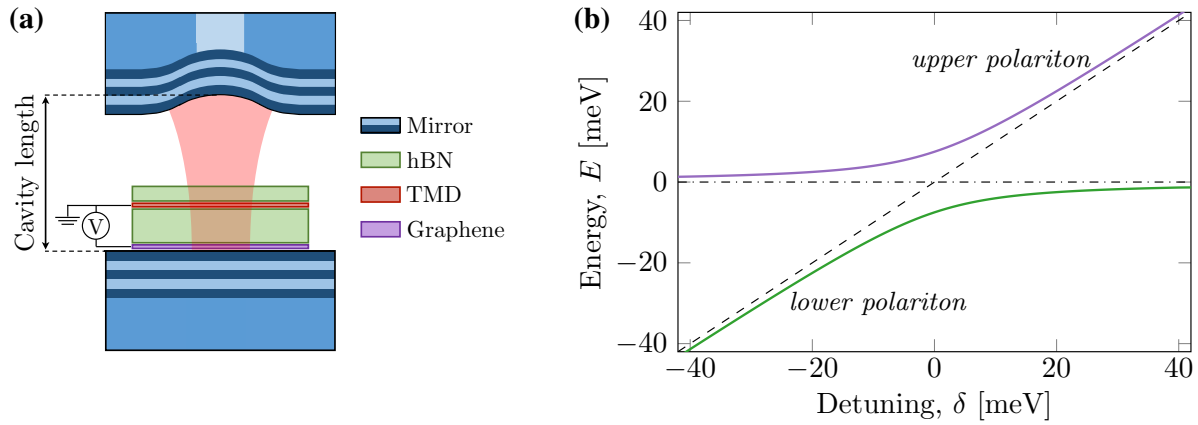

Figure 2.3: **(a)** Sketch of a TMD monolayer embedded inside an optical microcavity. The TMD is encapsulated between two hexagonal Boron Nitride (hBN) layers, where the bottom layer serves as a dielectric spacer that separates the TMD monolayer from a graphene gate. The graphene and TMD are each contacted using metal electrodes. A gate voltage V can be applied to tune the device away from the charge neutrality regime. The heterostructure is deposited between two mirrors, which form the optical cavity. Figure adapted from Ref. [P3]. **(b)** The elementary excitations of a TMD inside a cavity are exciton-polaritons. The energies of the upper and lower exciton-polaritons are shown as a function of the cavity length detuning δ. The dashed line denotes the cavity mode ω_C which depends linearly on the detuning. The exciton energy ω_X is shown as a dashed dotted line.

an external magnetic field) allows us to change the dimensionless interaction parameter, the trion energy in TMDs is fixed. The interaction parameter in TMDs, however, can be tuned by changing the Fermi energy ϵ_F through the application of a gate voltage. In Ref. [13], Fermi polarons were experimentally studied in $MoSe_2$.

2.2 Bose polarons in TMDs

Bose polarons can be realized by an (extremely) imbalanced mixture of K/K′ excitons or K/K′ polaritons. In both cases, the interaction mechanism comes from the exchange of a biexciton with binding energy E_b: two excitons from opposite valleys can form a biexciton state. For the excitonic Bose polarons, the density of the bath particles n_b and thereby the dimensionless interaction parameter E_b/n_b can be tuned. For polaritonic Bose polarons, the cavity detuning δ offers a second tunable parameter. It allows one to tune the energy of the two polaritons across the biexciton bound state energy. This resembles closely the scenario of exploiting a Feshbach resonance in ultracold gases, where the energy of the closed channel bound state can be tuned with respect to the open channel scattering energy.

In a solid-state setup, Bose polaron-polaritons have already been investigated in a bulk semiconductor coupled to a cavity [112]. In Ref. [P3] we, for the first time, study Bose polaron-polaritons in a monolayer TMD (Molybdenum Diselenide ($MoSe_2$)) that is strongly coupled to an optical microcavity. In a pump and probe experiment performed in the İmamoğlu group at ETH Zurich, a strong σ^+-polarized pump laser generates a coherent state of K-valley lower exciton-polaritons of a large occupation number. These particles act as a quantum bath for the σ^--polarized probe pulse that generates a controllable density of K′-valley exciton-polariton quantum impurities. In absence of the bath these probe particles interact repulsively. Upon switching on interactions between the pump and probe exciton-polaritons, the dressing of the probe exciton-polaritons leads to the formation of repulsive (RP) and attractive (AP) Bose polarons. In the experiment, the

cavity consists of a fused Silica substrate whose surface is coated with a distributed Bragg reflector (DBR) mirror (bottom) and a DBR-coated optical fibre facet with a concave dimple (top) (see Fig. 2.3 (a)). The polaritons are excited from below through the substrate. A photon transmission probe spectrum can be obtained by collecting the transmitted light through the fibre.

2.2.1 Theoretical modelling of Bose polaron-polaritons

The realization of Bose polarons in terms of exciton-polaritons can be described by the following two-channel Hamiltonian

$$\begin{aligned}\mathcal{H} =&\sum_{\mathbf{k},\sigma}\Big(\omega_{\mathrm{X}}(\mathbf{k})x^\dagger_{\mathbf{k},\sigma}x_{\mathbf{k},\sigma}+\omega_{\mathrm{C}}(\mathbf{k})c^\dagger_{\mathbf{k},\sigma}c_{\mathbf{k},\sigma}+\frac{\Omega}{2}\left(x^\dagger_{\mathbf{k},\sigma}c_{\mathbf{k},\sigma}+\mathrm{h.c.}\right)+\omega_{\mathrm{XX}}(\mathbf{k})m^\dagger_{\mathbf{k}}m_{\mathbf{k}}\Big)\\&+\frac{g}{\sqrt{A}}\sum_{\mathbf{p},\mathbf{k}}\left(x^\dagger_{\mathbf{p}-\mathbf{k},\sigma}x^\dagger_{\mathbf{k},\sigma'}m_{\mathbf{p}}+\mathrm{h.c.}\right).\end{aligned} \tag{2.5}$$

The σ-index labels the valley for the excitons ($x^\dagger$) and the polarization for the photons ($c^\dagger$). Excitons from opposite valleys can interact via the exchange of a biexciton ($m^\dagger$), whose bare dispersion relation is given by $\omega_{\mathrm{XX}}(\mathbf{k}) = \mathbf{k}^2/4m_{\mathrm{X}}$. The bare parameter ω_{XX} is related to the binding energy ω_{XXB} of the biexciton via $\omega_{\mathrm{XX}} = -\omega_{\mathrm{XXB}} - i\gamma_{\mathrm{XX}} + g^2V^{-1}\sum_{\mathbf{k}} 1/(2\omega_{\mathrm{X}}(\mathbf{k}) + \omega_{\mathrm{XXB}} - i\gamma_{\mathrm{XX}})$ with γ_{XX} the bare biexciton lifetime. ω_{XX} contains a divergent contribution for which a renormalization of the model is needed. A finite lifetime of the excitons and photons can be included by adding an imaginary part to the single particle energies $\omega_{\mathrm{X/C}} \to \omega_{\mathrm{X/C}} - i\gamma_{\mathrm{X/C}}$. For $g \to \infty$, the Hamiltonian reduces to the single-channel model used in Ref. [113].

We can now perform a rotation of the pump degrees of freedom from the exciton/photon basis to the upper/lower polariton basis. The upper polaritons can be neglected since they are not addressed by the pump laser and energetically well-separated from the lower polaritons at any given momentum. We keep the description of the impurity in the exciton/photon basis, as we want to capture the effect of the medium on the photonic component by calculating the photon probe transmission spectrum measured in the experiment. After the transformation, the Hamiltonian reads

$$\begin{aligned}\mathcal{H} =&\sum_{\mathbf{k}}\Big(\omega_{\mathrm{X}}(\mathbf{k})x^\dagger_{\mathbf{k}}x_{\mathbf{k}}+\omega_{\mathrm{C}}(\mathbf{k})c^\dagger_{\mathbf{k}}c_{\mathbf{k}}+\frac{\Omega}{2}\Big[x^\dagger_{\mathbf{k}}c_{\mathbf{k}}+\mathrm{h.c.}\Big]+\Big[\omega_{\mathrm{LP}}(\mathbf{k})-\omega_{\mathrm{LP}}(0)\Big]L^\dagger_{\mathbf{k}}L_{\mathbf{k}}+\Big[\omega_{\mathrm{XX}}(\mathbf{k})-\omega_{\mathrm{LP}}(0)\Big]m^\dagger_{\mathbf{k}}m_{\mathbf{k}}\Big)\\&+\frac{1}{\sqrt{A}}\sum_{\mathbf{p},\mathbf{k}} g(\mathbf{k})\left(x^\dagger_{\mathbf{p}-\mathbf{k}}L^\dagger_{\mathbf{k}}m_{\mathbf{p}}+\mathrm{h.c.}\right)\end{aligned} \tag{2.6}$$

with $g(\mathbf{k}) = g\cos\theta_{\mathbf{k}}$ and $\theta_{\mathbf{k}}$ given in Eq. (2.3). For later convenience, we work in the frame rotating with the condensate energy $E_0 = N\omega_{\mathrm{LP}}(0)$, where N is the number of bath particles.

2.2.1.1 Chevy-like Ansatz

Since the interaction between the probe excitons and the pump polariton is captured by the physics of polarons, we extend the variational wave function Ansatz (1.11) to describe the probe exciton and photon as impurities, and the pump lower polaritons as a bath

$$\begin{aligned}|\psi\rangle &= \left(\phi^{\mathrm{C}}c^\dagger_{\mathbf{0}}+\phi^{\mathrm{X}}b^\dagger_{\mathbf{0}}+\frac{1}{\sqrt{NA}}\sum_{\mathbf{k}}\phi_{\mathbf{k}}b^\dagger_{-\mathbf{k}}L^\dagger_{\mathbf{k}}L_{\mathbf{0}}+\frac{1}{\sqrt{V}}\phi^{\mathrm{M}}m^\dagger_{\mathbf{0}}L_{\mathbf{0}}\right)|\mathrm{L}\rangle\\&\equiv \hat{a}^\dagger|\mathrm{L}\rangle,\end{aligned} \tag{2.7}$$

with $\phi^{\mathrm{C}}, \phi^{\mathrm{X}}, \phi_{\mathbf{k}}, \phi^{\mathrm{M}}$ variational parameters. We define an operator $a^\dagger$ creating a polaron at zero momentum for later convenience. The first two terms account for the hybridisation of the photon and the exciton into

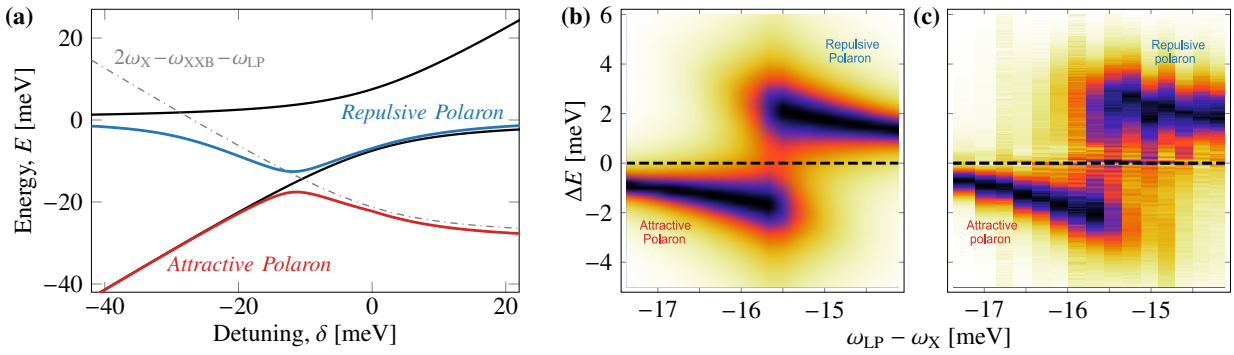

Figure 2.4: **(a)** The impurity lower polariton (cf. Fig. 2.3 (b)) splits into an attractive and a repulsive polaron close to the biexciton resonance. The biexciton resonance condition for a polariton in one valley in the presence of a polariton in the other is shown by the gray dash-dotted line. **(b)** Calculated transmission spectrum (Eq. 2.12) as a function of the cavity detuning δ and the energy difference ΔE from the undressed exciton-polariton energy, obtained for the fit parameters $n_{\mathrm{b,theo}} = 2.5 \times 10^{11}\ \mathrm{cm}^{-2}$ and $\gamma_{\mathrm{XX}} = 2.5$ meV. It exhibits a splitting of the lower polariton into an attractive and repulsive polaron branch. (d) Measured transmission spectrum. The bath density introduced by the pump pulse is estimated to be $n_{\mathrm{b}} = 6.3 \times 10^{11}\ \mathrm{cm}^{-2}$.

polaritons, while the third term reflects the dressing of the exciton by bath polaritons, leading to the formation of a polaron cloud. We assume that the pump laser in the experiment creates approximately a coherent state of lower polaritons, which we in turn model as a Fock state $|\mathrm{L}\rangle = (N!)^{-1/2}(L_{\mathbf{0}}^{\dagger})^{N}|0\rangle$, which is an accurate approximation for a coherent state in the limit of large polariton number N.

2.2.1.2 Green's functions and cavity transmission

The repulsive and attractive polaron energies can be obtained by minimizing the energy functional $\langle\psi|\mathcal{H} - E|\psi\rangle$. As in the Fermi polaron problem the resulting equations are equivalent to a diagonalization in the Hilbert space reduced to single bosonic excitations from the polariton condensate. A simple computation allows us to determine the values of the variational parameters as a function of the energy E. They are given by

$$\phi^{\mathrm{C}} = \frac{(\Omega/2)\sqrt{n_{\mathrm{b,theo}}}g_{\mathbf{0}}}{\xi_{\mathrm{C}}\xi_{\mathrm{X}} - (\Omega/2)^2}\phi^{\mathrm{M}}, \tag{2.8a}$$

$$\phi^{\mathrm{X}} = \frac{-\xi_{\mathrm{C}}\sqrt{n_{\mathrm{b,theo}}}g_{\mathbf{0}}}{\xi_{\mathrm{C}}\xi_{\mathrm{X}} - (\Omega/2)^2}\phi^{\mathrm{M}}, \tag{2.8b}$$

$$\phi_{\mathbf{k}} = \frac{-g_{\mathbf{k}}}{\xi_{\mathbf{k}}}\phi^{\mathrm{M}}, \tag{2.8c}$$

$$\phi^{\mathrm{M}} = \left(\left|\frac{(\Omega/2)\sqrt{n_{\mathrm{b,theo}}}g_{\mathbf{0}}}{\xi_{\mathrm{C}}\xi_{\mathrm{X}} - (\Omega/2)^2}\right|^2 + \left|\frac{-\xi_{\mathrm{C}}\sqrt{n_{\mathrm{b,theo}}}g_{\mathbf{0}}}{\xi_{\mathrm{C}}\xi_{\mathrm{X}} - (\Omega/2)^2}\right|^2 + 1 + \frac{1}{V}\sum_{\mathbf{k}}\left|\frac{-g_{\mathbf{k}}}{\xi_{\mathbf{k}}}\right|^2\right)^{-1}, \tag{2.8d}$$

where $n_{\mathrm{b,theo}} = N/A$, and with the shorthand notations

$$\xi_{\mathrm{C}} = \omega_{\mathrm{C}}(0) - i\gamma_{\mathrm{C}} - E, \tag{2.9a}$$

$$\xi_{\mathrm{X}} = \omega_{\mathrm{X}}(0) - i\gamma_{\mathrm{X}} - E, \tag{2.9b}$$

$$\xi_{\mathrm{XX}} = \omega_{\mathrm{XX}}(0) - i\gamma_{\mathrm{XX}} - E - \omega_{\mathrm{LP}}(0)L, \tag{2.9c}$$

$$\xi_{\mathbf{k}} = \omega_{\mathrm{X}}(0) + \omega_{\mathrm{X}}(\mathbf{k}) - i\gamma_{\mathrm{X}} - i\gamma_{\mathrm{LP}} - E - \omega_{\mathrm{LP}}(0). \tag{2.9d}$$

At this point, the energy E is left to be determined. Since E provides information about the spectrum of the system, it can natural be determined by the poles of the retarded Greens function in frequency space, which

is defined as the Fourier transform of

$$\mathbf{G}(\mathbf{k},t) = -i\theta(t)\begin{pmatrix} \langle[x_{\mathbf{k}}(t), x_{\mathbf{k}}^\dagger(0)]\rangle & \langle[x_{\mathbf{k}}(t), c_{\mathbf{k}}^\dagger(0)]\rangle & \langle[x_{\mathbf{k}}(t), m_{\mathbf{k}}^\dagger(0)]\rangle \\ \langle[c_{\mathbf{k}}(t), x_{\mathbf{k}}^\dagger(0)]\rangle & \langle[c_{\mathbf{k}}(t), c_{\mathbf{k}}^\dagger(0)]\rangle & \langle[c_{\mathbf{k}}(t), m_{\mathbf{k}}^\dagger(0)]\rangle \\ \langle[m_{\mathbf{k}}(t), x_{\mathbf{k}}^\dagger(0)]\rangle & \langle[m_{\mathbf{k}}(t), c_{\mathbf{k}}^\dagger(0)]\rangle & \langle[m_{\mathbf{k}}(t), m_{\mathbf{k}}^\dagger(0)]\rangle \end{pmatrix} \tag{2.10}$$

with $\theta(t)$ the Heviside theta function. Using the Ansatz (2.7), in frequency space we find (through minimizing of the energy functional):

$$\mathbf{G}(\mathbf{k},E) = \begin{pmatrix} \xi_{\mathrm{X}} & \Omega/2 & g_0\sqrt{n_{\mathrm{b,theo}}} \\ \Omega/2 & \xi_{\mathrm{C}} & 0 \\ g_0\sqrt{n_{\mathrm{b,theo}}} & 0 & \xi_{\mathrm{XX}} - \frac{g^2}{A}\sum_{\mathbf{k}}\frac{g_{\mathbf{k}}^2}{\xi_{\mathbf{k}}}, \end{pmatrix}^{-1}. \tag{2.11}$$

The spectrum of the system is then found by solving the equation $\mathrm{Re}\left\{\det\mathbf{G}^{-1}(E)\right\} = 0$ for E. It is shown in Fig. 2.4 (a) for a Rabi coupling of $\Omega = 15$ meV and $g \to \infty$. In the vicinity of the crossing of the lower polariton and the biexciton energy, we observe a splitting of the lower polariton into an attractive polaron (AP) and a repulsive polaron (RP) branch.

The photon transmission probe spectrum can be obtained from the photon retarded Green's function via [113]

$$\mathcal{T}(\mathbf{k},E) = |\mathbf{G}_{22}(\mathbf{k},E)|^2. \tag{2.12}$$

It is shown in Fig. 2.4 (b) and compared to the measured specrum in Fig. 2.4 (c). For the spectrum shown in Fig. 2.4 (b) we used the values realized in the experiment, i.e. $\Omega = 15\,\mathrm{meV}$, $\gamma_{\mathrm{C}} = 0.1\,\mathrm{meV}$ and $\omega_{\mathrm{LP}}(0) - \omega_{\mathrm{X}}(0) = -15.5\,\mathrm{meV}$. Moreover, we use the independently measured biexciton binding energy $\omega_{\mathrm{XXB}} = 29.35\,\mathrm{meV}$ [114][1]. The biexciton decay width γ_{XX} in turn is treated as a fit parameter due to the absence of an experimentally determined value. More importantly, we also take the peak bath density $n_{\mathrm{b,\,theo}}$ as an additional fit parameter. We do not consider a finite lifetime for the probe exciton in order to reduce the number of fit parameters. From fitting the experimental data, we obtained $\gamma_{\mathrm{XX}} = 2.5\,\mathrm{meV}$, and $n_{\mathrm{b,\,theo}} = 2.5\times10^{11}\mathrm{cm}^{-2}$. We find a theoretical value $n_{\mathrm{b,\,theo}}$ that is smaller than the experimentally estimated value by a factor $\beta = 2.6$[2]; this difference can be attributed to the fact that the absolute value of the experimentally estimated polariton density n_{b} is subject to a large uncertainty. Using only the two fit parameters $n_{\mathrm{b,\,theo}}$ and γ_{XX} we find remarkable agreement between theory and experiment across the full range of detunings and frequencies. This agreement lends credence to the interpretation of the observed response of the probe pulse as being due to the formation of APs and RPs arising from the dynamical dressing of the polariton impurity by the polariton bath.

2.2.2 Impurity-bath interactions

While Bose polarons exhibiting RP and AP branches have previously been observed in cold atom systems [106, 117, 118], the transmission data obtained in the experiment by the İmamoğlu group at ETH Zurich provides the first evidence for their existence in 2D materials. To further characterize their properties and the role of medium dressing in this light-matter coupled system, we now study the polaron spectrum for various bath densities. In our theoretical model, we observe a slight shift with density for the detuning at which the "jump" in the spectral weight from the attractive to the repulsive branch occurs (cf. Fig. 2.5), which is also predicted for cold atomic gases. Quite intriguingly, this shift is not observed in the experiment in TMD which may be attributed to finite range effects (that are, to a large degree, negligible in the cold atom

[1] This observation implies a biexciton binding energy larger than what has been reported in earlier experiments which yielded $\omega_{\mathrm{XXB}} = 20$ meV [115, 116], and is not consistent with our findings.

[2] An explanation of how the density can be estimated experimentally is given in [P3].

setting) and not included in our theoretical model. Accounting for this, we extract the AP and RP energies and the respective energy splitting E_{split} for the detuning at which the transfer of weight occurs in the theoretical data. Figs. 2.6 (a) and (b) show a comparison between the extracted peak energies of the calculated and measured photon transmission spectra. To this end, the theoretical densities are rescaled by the fixed factor $\beta = 2.6$, obtained from the measurement of the transmission spectrum in Fig. 2.4 (b). The energies

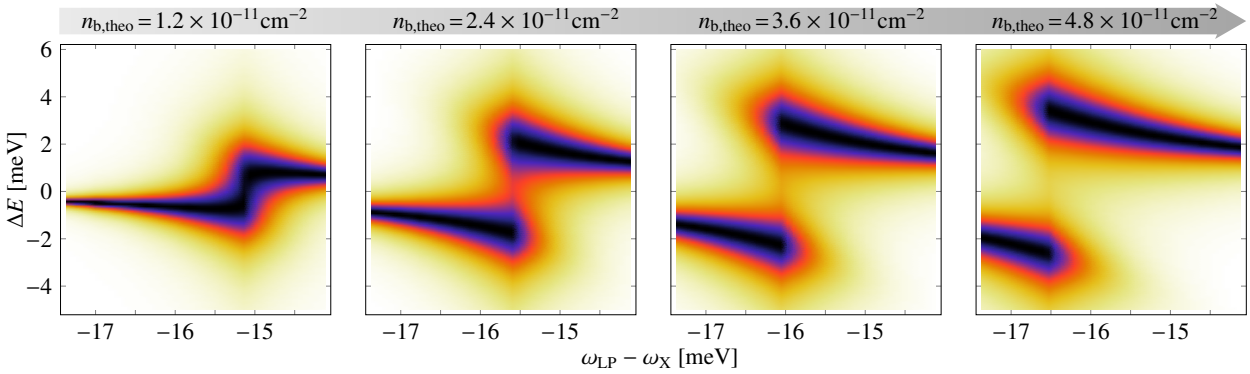

Figure 2.5: Calculated transmission spectra for increasing bath density (from left to right). A shift of the resonance position can be observed, which we do not find in the measured transmission spectra.

from the experimental data are extracted at a fixed detuning $\omega_{\text{LP}} - \omega_{\text{X}} = -15.5$ meV. The theory is in good qualitative agreement with the experimental data. However, while we experimentally observe a linear scaling of the splitting with respect to the bath density n_{b}, the scaling in theory is sublinear. A possible source of the different scaling might again arise from finite range corrections.

For sufficiently large bath density we can approximate the impurity-bath interaction as a Kerr type nonlinearity, and obtain an *effective* interaction strength $g_{\text{ib}}^{\text{eff}}$ between the impurity and bath polaritons from the gradient of the peak polaron energies with respect to the bath density: $\Delta\omega = g_{\text{ib}}^{\text{eff}} n_{\text{b}} n_{\text{i}}$. The experimentally extracted impurity bath interactions are shown in Fig. 2.6 (c): By tuning across the biexciton resonance, the interaction strength varies from $g_{\text{ib}}^{\text{eff}} = 0.4\mu\text{eV}\ \mu\text{m}^2$ to $1\mu\text{eV}\ \mu\text{m}^2$ on the RP branch and from $g_{\text{ib}}^{\text{eff}} = -0.2\mu\text{eV}\ \mu\text{m}^2$ to $-0.8\mu\text{eV}\ \mu\text{m}^2$ on the AP branch. This finding implies that the magnitude of the interaction strength between opposite-spin polaritons can be enhanced by a factor of up to ~ 5 in comparison to that of parallel-spin polaritons in the absence of a bath ($g_{\text{ii}}(n_{\text{b}} = 0) = 0.2\mu\text{eV}\ \mu\text{m}^2$). Most importantly, not only the magnitude but also the sign of g_{ib} is tunable. This can be understood as a consequence of the polariton-biexciton Feshbach resonance, where by tuning the energy of a scattering state across a bound state, interactions can be enhanced and their sign can be reversed [112, 119, 120].

2.2.3 Induced interactions between Bose polarons

Next, we address the question of how the interaction between two impurities are modified when they form polaronic quasiparticles due their coupling to a bosonic bath.

In the experiment this was done by increasing the impurity density (ranging from $n_{\text{i}} = 0.15 \times 10^{11}\ \text{cm}^{-2}$ to $1.4 \times 10^{11}\ \text{cm}^{-2}$) while keeping the bath density fixed (here at $n_{\text{b}} = 2.6 \times 10^{11}\ \text{cm}^{-2}$). In Figs. 2.7 (a) and (b), the experimentally observed polaron spectrum is shown as black lines for various impurity densities. The probe spectrum of the undressed impurity (in absence of a bath) is shown as orange lines in Figs. 2.7 (a) and (b) and was recorded for each probe power and serves as a control experiment. We attribute the residual energy shifts in these spectra to interactions between the impurities in the presence of the long-lived incoherent heating effects induced by the previous pump pulses.

For the AP-polariton branch we find that the energy of the dressed impurities blueshifts as their density is

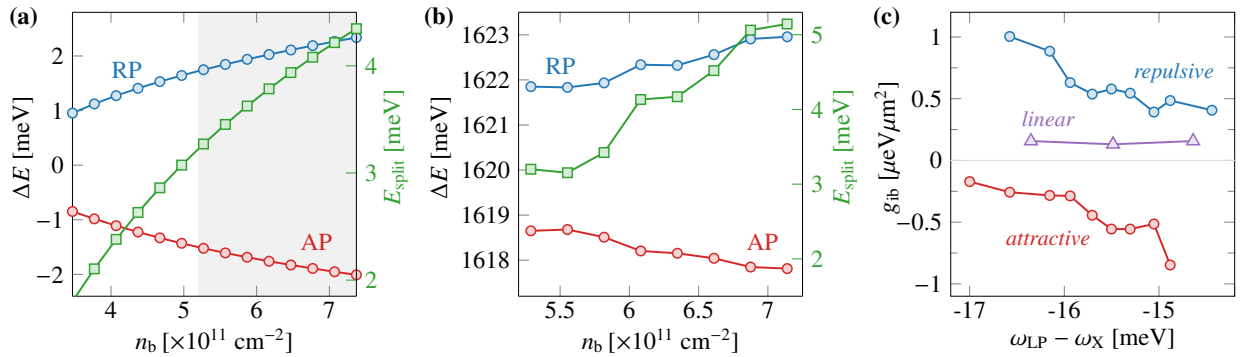

Figure 2.6: **(a)** Theoretically calculated peak energies of the repulsive (attractive) branch in blue (red) circles as a function of bath density (rescaled by the factor $\beta = 2.6$). The energies are extracted for the detuning at which the transfer of weight from the attractive to the repulsive branch occurs in the theoretical data. The green curve shows the splitting between the two branches. The gray shaded region indicates the bath densities for which the same quantities were extracted from the experimental data. **(b)** Measured peak energies of the RP (blue) and the AP (red) as well as their splitting (green), extracted from the experimental Bose polaron transmission spectrum for an impurity density of $n_\mathrm{i} = 0.15 \times 10^{11}\mathrm{cm}^{-2}$. The energies are obtained from Lorentzian fits to the measured spectrum. **(c)** Impurity-bath interaction strength g_ib of the repulsive (attractive) branch in blue (red) circles as a function of detuning. The purple triangles correspond to the polariton-polariton interaction strength ($g_\mathrm{ii}(n_\mathrm{b} = 0)$) measured in linear polarisation as a function of the detuning.

increased. For RP-polaritons on the other hand, we find the opposite effect: increasing the impurity density leads to a redshift. That means increasing the density of repulsive polarons lowers the energy to create further repulsive polarons. By taking the gradient of the energy shifts with respect to the impurity density, one can extract the effective interaction strength between the polaron-polaritons. For APs this leads to a repulsive interaction strength $g_\mathrm{ii} = 0.12\mu\mathrm{eV}\ \mu\mathrm{m}^2$ while RP-polaritons experience an attractive interaction strength of $g_\mathrm{ii} = -0.11\mu\mathrm{eV}\ \mu\mathrm{m}^2$. These interaction values have been measured relative to the polariton-polariton interaction strength without bath interactions, the latter having been independently measured in linear polarization and amounting to $g_\mathrm{ii}(n_\mathrm{b} = 0) = 0.2\mu\mathrm{eV}\ \mu\mathrm{m}^2$ (see purple data in Fig. 2.6 (c)).

This procedure was repeated for other pump densities ($n_\mathrm{b} = 4.0$ and 6.3×10^{11} cm^{-2}) and values for the impurity-impurity interactions $g_\mathrm{ii}(n_\mathrm{b})$ were thus extracted as function of the bath density. The result is plotted in Fig. 2.7 (c) for the AP (red) and RP (blue) polaritons. For AP-polaritons the interactions become more repulsive upon increasing the bath density. In contrast, for the RP-polaritons, the dressing by increasing the density of bath particles leads to a reduction of the polaron-interactions compared to the bare repulsive polariton interactions. For the largest bath density that is experimentally achievable we find the striking result that the interactions between RP-polaritons become attractive. This observation demonstrates that by polaron dressing one can not only strongly modify the magnitude of polariton interactions but even change their sign and turn repulsive interactions between bare impurity particles into net attractive interactions upon Bose polaron formation.

To theoretically investigate the interaction between polarons, we compute the expectation value of the Hamiltonian (2.6) with respect to a two-polaron state

$$E^{\mathrm{2Pol}} = \frac{\langle \mathrm{L}|\hat{a}\hat{a}\mathcal{H}\hat{a}^\dagger\hat{a}^\dagger|\mathrm{L}\rangle}{\langle \mathrm{L}|\hat{a}\hat{a}\hat{a}^\dagger\hat{a}^\dagger|\mathrm{L}\rangle}. \tag{2.13}$$

Since the operator $a^\dagger$ is applied twice on the state, the result for E^{2Pol} is a long expression the explicit form of which is shown in Appendix A.7. In this first-order model the correlations between the polarons are neglected on the level of the wave function (up to the normalization). The dependence of E^{2Pol} on the probe exciton density is extracted by varying the system area at fixed pump polariton density $n_\mathrm{b,theo} = N/A$. From the dependence of the attractive and repulsive polaron energy on the ratio between probe and pump densities $n_\mathrm{i}/n_\mathrm{b}$, we extract the effective interaction strength of the polaron-polaritons, which is shown in Fig. 2.7 (d)

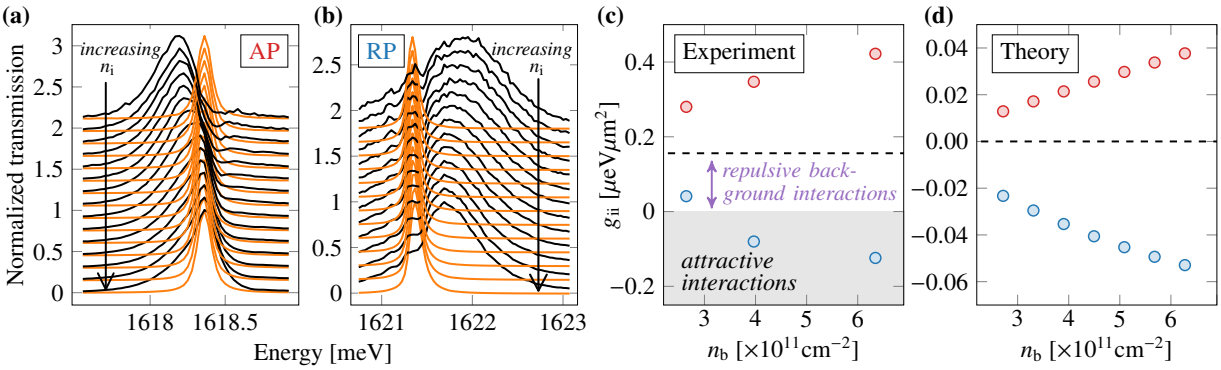

Figure 2.7: Normalized impurity density dependent polaron spectrum for the attractive **(a)** and repulsive polaron **(b)** in black lines and the corresponding undressed exciton-polariton spectrum in orange lines. The bath density is $n_b = 2.6 \times 10^{11}$ cm^{-2}. The spectra for different impurity densities are plotted with an offset for clarity . **(c)** Experimentally obtained impurity-impurity interactions strengths as a function of the bath density. The values for the attractive (repulsive) polaron are given by the red (blue) dots. The interaction strength has been measured with respect to the undressed polariton spectrum which included polariton-polariton interactions in the same valley, implying that the interaction strength values above the gray shaded area are repulsive. **(d)** Theoretically obtained impurity-impurity interactions strengths as a function of the bath density.

as a function of the bath density. Remarkably, already within the simple Ansatz (2.13), the same qualitative behaviour of the energy shift as the one observed in the experiment is obtained. However, the extracted effective interaction strengths differ by a factor of five for the RPs, and by a factor of ten for the APs. We attribute this to the uncertainty of the polariton density, the simplified Chevy Ansatz based model used for the calculation of polaron-polaron interactions, as well as the modeling of the impurity density as arising from a simple finite size effect.

2.3 Summary

In this chapter, we introduced Bose polaron, impurities that are immersed into a bosonic bath, and discussed their first experimental realization in terms of exciton-polaritons in atomically thin semiconductors coupled to an optical cavity. Here, Bose polarons can be introduced by a pump-and-probe experiment: The probe laser creates a small density of σ^- polariton impurities immersed in a much larger density of σ^+ polaritons, created by the pump laser. Within this pump and probe experiment, it is possible to detect the impurity photon transmission spectrum, showing a spitting of the lower polariton branch into an attractive and repulsive polaron branch. Using a non-hermitian Hamiltonian and a variational wave function approach inspired by the Chevy Ansatz for the impurity exciton-polariton, we were able to calculate the same photon transmission spectrum, which shows excellent agreement with the experimental data. Furthermore, we studied, both experimentally and theoretically, the splitting between the attractive and repulsive branches as a function of the bath density.

In Subsec. 2.2.3, we then turned to the investigation of polaron-polaron interactions. We demonstrated that the interactions between polarons can fundamentally be tuned by the bath density, and, even more remarkably, the interaction between repulsive polarons can be changed from repulsive to attractive due to the many-body nature of the system. Our theoretical results are obtained by comparing the single impurity energy to the energy of a state featuring two impurities. Here, the interaction mechanism comes exclusively from the

mediation of the bosonic bath. The work goes beyond the pioneering results reporting modified polariton-polariton interactions in the presence of a biexciton resonance that were obtained on conventional semiconductor quantum wells strongly coupled to microcavities, such as ZnSe [121] or GaAs [122, 123]. All these reports focused on impurity-bath interactions, while this study provides the first measurement of impurity-impurity interactions and their modifications by the bath.

The findings demonstrate how Bose polaron formation can be utilized to control interactions, opening up possibilities for unconventional induced pairing mechanisms in van der Waals materials based on exciton-polariton exchange. These results represent a step towards investigating interactions in nonequilibrium polaronic systems, guiding further theoretical and experimental exploration of novel quantum states of matter, such as bipolarons and induced superconductivity. Applying the observed Bose polaron effects to electronic systems may offer insights into weakening or overcoming Coulomb repulsion between electrons, potentially uncovering unconventional electron pairing mechanisms in van der Waals materials based on exciton or polariton exchange.

Part II

Phase transitions in light-matter systems

Chapter 3

Preliminaries on light-matter systems

The second part of this thesis deals with phase transitions in light-matter systems. Light-matter systems can feature unusual properties, such as long-range interactions or driven-dissipative behavior. Here, we are interested in how phase transitions are modified by these properties, which are not captured in the standard theory of phase transitions. In both cases, for example, the Mermin-Wagner theorem, which forbids long-range order in systems with a continuous symmetry in spatial dimensions $d \leq 2$ with short-ranged interactions at equilibrium, does not hold. As a consequence, long-range interacting or nonequilibrium systems can order even in low spatial dimensions. Examples include two-dimensional flocks [124] or driven quantum spin chains [125, 126]. However, the presence of nonequilibrium can also lead to the destruction of long-range order already present at equilibrium or in a short-range interacting system [127]. Additionally, completely new phases are to be expected, which are missing in the short-range or equilibrium counterpart. An example here is the Kardar–Parisi–Zhang (KPZ) phase [128].

Long-range interactions and nonequilibrium can both be naturally designed in quantum gases coupled to optical cavities [129, 130]. Here, the cavity serves to strengthen the interactions between the photons and the atoms, which are generally weak in free space. Light-matter interactions are a fundamental process in physics, where photons are absorbed or emitted by matter. In absorption, the energy of the photon is transferred to an atom, for example by exciting one atom's electron to a higher state. This results in an increase in the internal energy of the atom. The reverse process is called emission, where the atom relaxes back to a lower energy state and emits a photon of the respective energy. Emission is the basis of almost every light source: Fluorescent tubes, light bulbs and lasers all emit light through the process of electrons falling back to lower energy states.

If an ensemble of atoms is subject to a light field, a photon that is emitted by one atom can in principle be absorbed by a second atom. This results in a photon-induced, non-local interaction among the atoms. As a result, long-range interactions are naturally built into optical interaction potentials. However, it is extremely unlikely for multiple photon emission-and-absorption processes to take place, and usually, they are negligible for typical free-space configurations. However, it is again possible to enhance the photon-atom interaction through the use of optical cavities. This is due to the fact that the confinement of photons in a high-finesse cavity causes each photon to traverse the same ensemble of atoms multiple times. Hence cavities significantly enhance the probability of an emitted photon being absorbed by the same or another atom in the ensemble.

All-to-all (infinite range) interactions among the atoms can be mediated by a single-cavity mode coupled to all atoms. Alternatively, employing degenerate cavity modes allows for tunability of the interaction range among the atoms [131–133]. Cavity-induced interatomic interactions can also be reversed in sign by changing the laser frequencies with respect to the cavity resonance [134, 135]. Atoms trapped in a cavity therefore represent a promising platform for the quantum simulation of long-range atom-atom interactions. A prominent example of an experimentally realized cavity-mediated long-range interacting system is the Bose-Hubbard model [136]. In contrast to the standard Bose-Hubbard model featuring superfluid and Mott-insulating states, the phase diagram of the Bose-Hubbard model with cavity-induced global atom-atom interactions exhibits novel phases such as a lattice supersolid and a charge-density-wave state [136–141].

Moreover, the cavity causes losses which enable the study of nonequilibrium, dissipative physics. This is due to the fact that cavities are naturally driven-dissipative, as photons can leak out of the cavity's mirrors and therefore continuous injection of new photons is required. Driven-dissipative systems can feature shifted critical points or a modified scaling of the critical fluctuations compared to their equilibrium counterparts [142].

They even allow for new phases that would not be present in equilibrium. An additional advantage of the dissipative nature of optical cavities is that information on the dynamics of the system can be obtained by the non-destructive observation of photons leaking out of the cavity [129, 143]. In contrast, measurements of the atoms themselves are typically destructive, which makes repeated observations within a single experimental sample difficult.

Quantum gases strongly coupled to a quantized light field in a high-finesse optical cavity therefore represent an ideal platform to simulate and study phase transitions in driven-dissipative and long-range interacting quantum systems. Their study is an active field of research, both experimentally and theoretically (see [144] and references within). All of the theoretical predictions obtained within this part of the thesis are discussed with regard to realistic experiments with quantum gases coupled to optical cavities.

In the following chapter, we provide the reader with an introduction to phase transitions and further introduce basic concepts such as spontaneous symmetry breaking and Goldstone modes. In Chap. 5, we will then discuss a new incarnation of the KPZ phase in quadratically-driven dissipative Bose gases. This setup offers a tuning knob to reduce the length scale at which KPZ physics becomes visible, and offers a promising route for demonstrating KPZ physics at experimentally and numerically accessible length scales in 2d, where it had so far remained elusive. In Chap. 6, we will consider a class of long-range interacting models including spin systems and Bose gases in optical cavities, and explore how the low-energy excitation spectrum of the Goldstone modes changes from linear over sub-linear to gapped, as the interaction range is increased.

Chapter 4

Phase Transitions

Matter can appear in different phases. A familiar every day example is H_2O, which can be in a solid (ice), liquid (water), or gas (vapor) phase, depending on the given temperature and the pressure. We have also already seen a second example; an impurity immersed in a Fermi gas can either form a polaron or a molaron state. In this case, which phase the system is in depends on the interaction strength.

Let's have a closer look at the example of H_2O and its different phases. In the solid phase, the H_2O molecules form a crystal, bound together by hydrogen bonds between nearest neighbors. Due to the binding energy, this state has the lowest energy. At finite temperature, however, minimizing the energy is no longer the only criterion that matters. To determine which phase of the system is realized at equilibrium, the entropy of the system also has to be taken into account. At finite temperature, therefore, the relevant quantity to minimize is the free energy

$$F = E - TS, \tag{4.1}$$

with E the energy, T the temperature, and S the entropy. The solid phase of H_2O also has the lowest entropy S among the three, as the molecules have almost fixed positions. It also has the lowest energy, as every atom in bound into the crystal structure. At low temperature, the solid phase therefore realizes the equilibrium state of H_2O. In the liquid phase, the molecules are not fixed any more, but instead they can move around. This leads to a constant breaking and building up of hydrogen bonds and, consequently, the liquid phase has higher energy than the solid one. However, as there a many different but macroscopically equivalent configurations in the liquid form, the entropy of this phase is also higher than the entropy of solid phase, where there is only a single crystallized configuration[1]. In the gas phase, the molecules are typically much more dilute, filling up all the available space. Therefore, the attractive interactions are effectively weaker and consequently, the energy is much higher. As the single molecules can almost move around freely, however, the entropy of this state is also much higher compared to the solid and liquid phase.

The phase diagram displaying the equilibrium phases of H_2O as a function of temperature and pressure is shown in Fig. 4.1 (a). The solid lines mark the phase boundaries at which two phases can coexist in equilibrium. When crossing such a line, one speaks of a phase transition. At a (first-order) phase transition, the system abruptly changes its macroscopic properties. For example, liquids and gases have very different rescaled volumes $v = V/N$ with V the volume and N the number of atoms in the gas. This quantity jumps discontinuously when crossing the phase boundary. The rescaled volume serves as an example of what is known as an order parameter, the value of which characterizes the phase of the system[2].

In H_2O, phase transitions can be driven by changing either the temperature or the pressure and thereby crossing a phase boundary. However, these boundaries between different phases do not necessarily extend forever. As can be seen in Fig. 4.1, the phase boundary between the liquid and the gas phase ends at the critical point. For H_2O, the critical point is located at $T_c \approx 374$ °C and $p_c \approx 218$ atm. This means that it is possible to smoothly transform from the liquid into the gas phase without undergoing a phase transition, simply by moving around the critical point. This also implies that the order parameter (the rescaled volume v) behaves smoothly along this path and can not be used to completely characterize the two phases. Here we

[1] We note here that H_2O can in fact crystallize into various different forms, from which hexagonal ice is the common form of ice found at atmospheric pressure and temperatures below 0°C.

[2] In the literature, density (inverse rescaled volume) is more commonly used as an order parameter for the liquid-to-gas transition. Here we use the rescaled volume, in analogy to the magnetization in the Ising model, the latter of which we will discuss in Sec. 4.1.

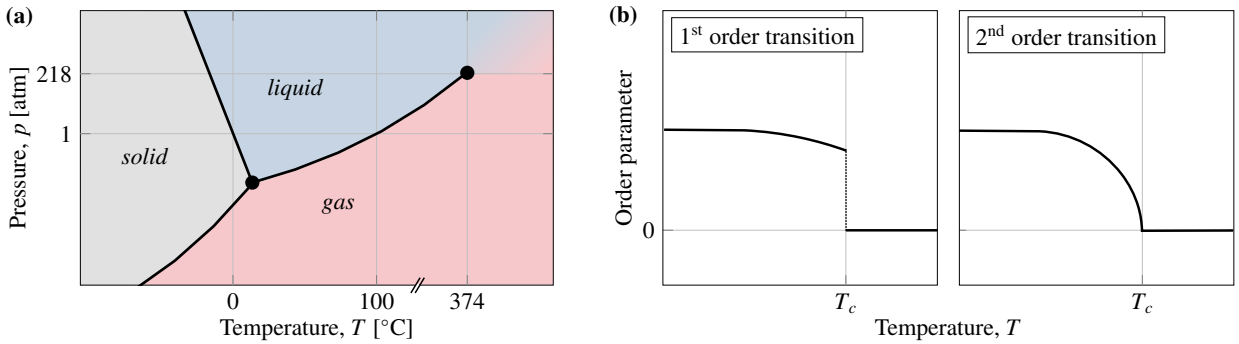

Figure 4.1: (a) Schematic phase diagram of H_2O as a function of temperature T and pressure p. The black lines mark the phase boundaries, which are all of first order. The point at which all three phases coexist is called the triple point. The point at which the boundary between the liquid and the gas phase ends is called the critical point, which is of second order. **(b)** Comparison of the behavior of the order parameter in a first- and second-order phase transition.

see why it is difficult to give a precise definition of a phase. Instead, it is often more insightful to describe the phase transitions.

There exist different categories of phase transitions: two of the most frequent ones are the first- and second-order phase transition. At a first-order transition the order parameter jumps discontinuously (see Fig. 4.1 (b) left panel). All phase boundaries shown in Fig. 4.1 (a) are of first order. At a second-order phase transition the order parameter behaves continuously (see Fig. 4.1 (b) right panel). This is why these phase transitions are also called continuous phase transitions. Second-order phase transitions are always associated with the spontaneous breaking of a symmetry: in one phase, the state is invariant under a certain symmetry transformation, while this is not the case across the transition. The critical point in Fig. 4.1 (a) is an example of a second-order phase transition.

A very famous phenomenological theory describing phase transitions was provided by Landau in 1937. The Landau theory involves free energy functional that is an analytic function of the order parameter and shares the symmetries of the Hamiltonian. Close to the transition, where the order parameter is small, the free energy can be expanded in powers of the order parameter. By minimizing the free energy with respect to the order parameter, several observables, such as the scaling of the order parameter with the temperature, can be derived. It should be mentioned that the Landau theory is a mean-field theory and does not always provide the correct scaling. Although more advanced theories such as the renormalization group have now largely taken its place, it remains a powerful way of qualitatively categorizing phase transitions.

4.1 The Ising model

The Ising model is one of the most important models in statistical physics. It covers many concepts introduced before, such as order parameters, first- and second-order phase transitions and spontaneous symmetry breaking. The Ising model is given by

$$\mathcal{H} = -B \sum_i s_i - J \sum_{\langle ij \rangle} s_i s_j \tag{4.2}$$

and consists of discrete spins which can either point up or down, i.e. $s_i = \uparrow, \downarrow$, on each lattice site $i = 1, ..., N$ of a d-dimensional lattice with N sites. Here, B is an external magnetic field acting on the spins. For $B > 0$,

it is favorable for the spins to point up, aligning with the magnetic field. The second term is the interaction between two neighboring spins. Here $\langle ij \rangle$ indicates that the sum is only taken over nearest neighbors. For $J > 0$, it is favorable for spins to be aligned ($\uparrow\uparrow$ or $\downarrow\downarrow$). Such a system is called a ferromagnet. By contrast, for $J < 0$, the preferred spin configuration is anti-aligned ($\uparrow\downarrow$ or $\downarrow\uparrow$), which is called an anti-ferromagnet. In what follows we focus on the ferromagnetic case for convenience. We will discuss antiferromagnetic spin systems in Sec. 6.2. When the system is at finite temperature, maximizing the entropy becomes important again. A disordered state is therefore favored at a finite T, as there are many more disordered spin configurations than ordered ones (which increases the entropy). We see that the three parameters B, J and T all favor different configurations of the spins, and we expect phase transitions between these configurations to take place depending on the ratios of these parameters[3]. Here we will show how to describe them.

At finite temperature, the partition function

$$Z(T, J, B) = \sum_{\{s_i\}} e^{-\beta \mathcal{H}[s_i]} \tag{4.3}$$

is obtained by summing over all possible spin configurations $\{s_i\}$, with $\beta = 1/T$ the inverse temperature. Here, and in what follows, we set $k_B = 1$. The partition function encodes all information about the system and is therefore the object of interest[4]. However, an exact solution for Eq. (4.3) only exists in 1d, and in 2d for $B = 0$. In higher dimensions, one has to resort to approximations.

We can define the magnetization of one spin configuration, which is given by $m = \frac{1}{N}\sum_i s_i$. This allows us to divide the sum over the spin configurations in Eq. (4.3) into a sum over configurations with a specific magnetization $\{s_i\}_m$ and then over all magnetizations

$$Z = \sum_m \sum_{\{s_i\}_m} e^{-\beta \mathcal{H}[s_i]} := \sum_m e^{-\beta \mathcal{F}(m)}. \tag{4.4}$$

Here we defined a new quantity, the effective free energy $\mathcal{F}(m)$ which is a function of the magnetization[5].

4.1.1 Mean field and Landau theory

In order to compute the effective free energy $\mathcal{F}(m)$, one has to perform the sum over all configurations with a specific magnetization, c.f. (4.4). The first instinct is to do a mean field approximation, where each spin in Eq. (4.2) is replaced by its expectation (mean) value $\langle s \rangle = m$. This gives an estimate for the energy of such a configuration:

$$E = -B\sum_i m - J\sum_{\langle ij \rangle} m^2 = -BNm - \frac{1}{2}JqNm^2. \tag{4.5}$$

Here, q is the number of nearest neighbors of each site which depends on the geometry and the dimension of the lattice, and the factor $1/2$ compensates for double counting. The number of configurations with a specific magnetization is given by $m = (N_\uparrow - N_\downarrow)/N$. These, in turn, can be arranged in $\Omega = N!/N_\uparrow! N_\downarrow!$ ways. We can therefore write

$$e^{-\beta \mathcal{F}(m)} \approx \Omega(m) e^{-\beta E(m)}. \tag{4.6}$$

[3] There are two relevant ratios, as one parameter can be used to determine the energy scale.

[4] For example, the partition function is related to the free energy via $F = -T \log Z$.

[5] Minimizing the effective free energy with respect to the magnetization, one obtains the thermodynamic free energy (4.1) and the associated magnetization of the system in equilibrium.

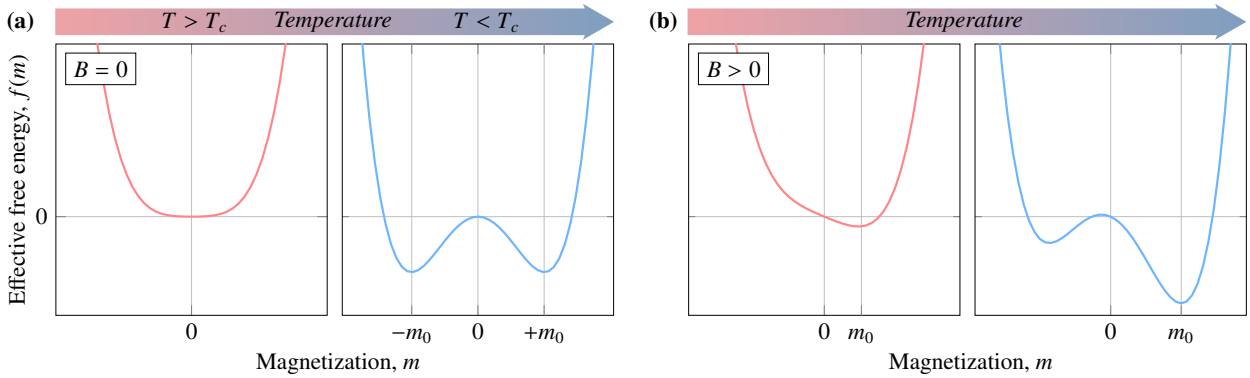

Figure 4.2: (a) Effective free energy of the Ising model without external magnetic field for temperatures above (left) and below (right) the critical temperature T_c. Below T_c, the $\mathbb{Z}_2$ symmetry of the Hamiltonian (4.2) is spontaneously broken, as the system picks one of the two degenerate equilibrium states with $m = \pm m_0$. **(b)** For a finite magnetic field, no phase transition occurs as a function of temperature, since the magnetization m is finite and positive for all temperatures.

Using this approximation, one can find the mean field expression for the effective free energy to be

$$f(m) \approx -Bm - \frac{1}{2}Jqm^2 - T\left(\log(2) - \frac{1}{2}(1+m)\log(1+m) - \frac{1}{2}(1-m)\log(1-m)\right) \tag{4.7}$$

where the effective free energy per unit spin $f(m) = \mathcal{F}(m)/N$ was introduced to cancel the factors of N.

4.1.1.1 Second-order phase transition

In the Ising model with zero magnetic field $B = 0$, we expect a phase transition to occur as a function of temperature. In the limit of zero temperature, the spins are perfectly aligned (due to the second term in the Hamiltonian (2.6)) and all point in the same direction, which can be either up or down. Finite temperature, however, tends to distrupt the ordered state. This will increase the entropy, and at some critical temperature, the disordered state becomes more favorable as it has a lower free energy.

The order parameter of this phase transition is the magnetization m: it is finite in the low temperature phase $0 < m \leq 1$, but zero in the high temperature phase. Close to the phase transition, where the order parameter is small, we can expand the effective free energy (4.7) in powers of the order parameter[6]

$$f(m) \approx \frac{1}{2}(T - Jq)m^2 + \frac{1}{12}Tm^4 + \mathcal{O}(m^6). \tag{4.8}$$

One can see that there are two qualitatively different forms of the effective free energy as a function of the magnetization m, depending on whether the quadratic term is negative or positive (see Fig. 4.2 (a)). For a positive quadratic term, i.e. $T > Jq$, the magnetization which minimizes the effective free energy is $m = 0$. This agrees well with our assumption of a disordered state at high temperature. For $T < Jq$, the effective free energy is minimized for $m_0 = \pm\sqrt{3(T_c - T)/T}$. The critical temperature $T_c = Jq$ distinguishes both phases, the ordered phase with $m = 0$ and the disordered phase with $m \neq 0$. As the order parameter itself is continuous, this is an example of a second-order phase transition.

Spontaneous symmetry breaking (SSB) describes a transition from a state which shares the symmetries of the Hamiltonian into a state which does not. This is exactly the case we have just seen. The Hamiltonian (4.2) for $B = 0$ is invariant under the $\mathbb{Z}_2$ symmetry ($s_i \to -s_i$), and so is the effective free energy ($m \to -m$). However, below T_c the system spontaneously picks one of the two degenerate equilibrium states $m = \pm m_0$

[6] We neglect constant terms, as we are interested in the dependence of the effective free energy on the order parameter.

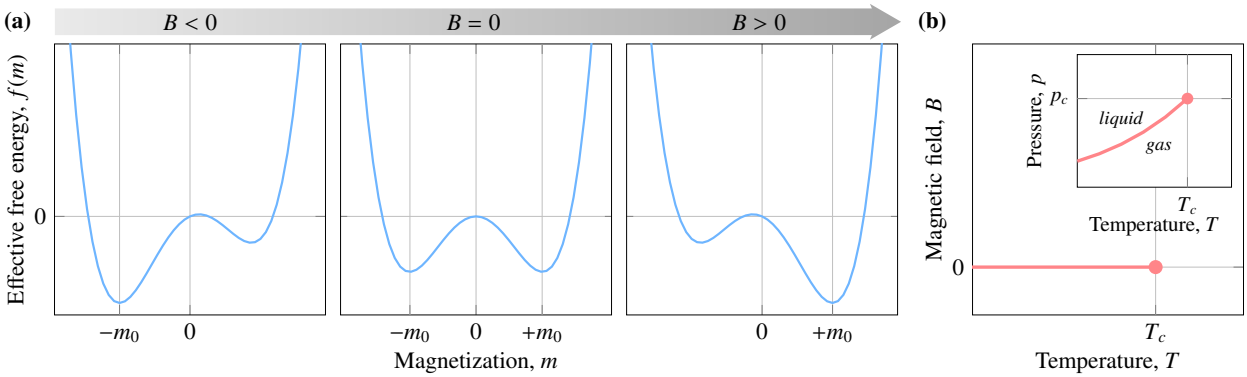

Figure 4.3: (a) Effective free energy of the Ising model at a temperature $T < T_c$ for a varying external magnetic field. For $B < 0$ ($B > 0$), the equilibrium magnetization of the system is $-m_0$ ($+m_0$). No symmetry breaking occurs as all configurations break the $\mathbb{Z}_2$ symmetry of the Hamiltonian (4.2). The transition is of first order. **(b)** Phase diagram of the Ising model as a function of temperature T and magnetic field B, compared to the phase diagram of the liquid-to-gas transition (inset, also c.f. Fig. 4.1 (a)). Both phase diagrams are qualitatively similar. The similarity at the critical point is even quantitative, implying that both systems lie in the same universality class.

and thereby breaks this symmetry (see Fig. 4.2 (a)). The definition of order can be made more formal. In general, going beyond mean field, the magnetization of the system can depend on space. In the ordered phase, the correlation function of two spins is finite no matter how far they are separated in space

$$\lim_{\mathbf{r}\to\infty}\langle m(\mathbf{r})m(0)\rangle = \text{const.} \tag{4.9}$$

This is known as long-range order (LRO) and is characteristic of the ordered phase accompanying SSB.

4.1.1.2 First-order phase transition

For a finite magnetic field $B \neq 0$, the free energy expanded in powers of the order parameter reads

$$f(m) \approx -Bm + \frac{1}{2}(T - Jq)m^2 + \frac{1}{12}Tm^4 + \mathcal{O}(m^5). \tag{4.10}$$

Depending on the temperature, one can discriminate two qualitatively different forms of the effective free energy (see Fig. 4.2 (b)). However, the global minimum is always at a finite value of the order parameter, which is for $B > 0$ also always positive. Hence it would seem that we find no phase transition as a function of temperature.

What we can do, however, is to vary the magnetic field from $B > 0$ to $B < 0$ for a fixed temperature below T_c. Here, the global minimum of the effective free energy switches and the associated magnetization jumps discontinuously from $+m_0$ to $-m_0$, as depicted in Fig. 4.3 (a). This is an example of a first-order phase transition.

4.2 Universality

The phase diagram of the Ising model as a function of temperature and magnetic field is shown in Fig. 4.3 (b). A line of first-order phase transitions ends at a second-order phase transition, which is called the critical point.

Remarkably, this phase diagram looks quite similar to the H_2O phase diagram in the region around the liquid-gas transition (see inset of Fig. 4.3 (b)). Here, the pressure plays the role of the magnetic field in the Ising model. In both systems, a line of first-order phase transitions ends at a critical point. Even more remarkably, the similarities are not only qualitative. The order parameter of the liquid-gas transition (the rescaled volume v) depends on the temperature in the exactly same way as the magnetization in the Ising model

$$v_{\text{gas}} - v_{\text{liquid}} \sim m \sim (T_c - T)^{\beta} \tag{4.11}$$

with the same exponent β. This exponent is an example of a critical exponent which describes the scaling of a macroscopic quantity in the vicinity of a critical point. Another example of a critical exponent is δ, quantifying the dependence of the order parameter on the pressure, or respectively, on the magnetic field in the Ising model. Also δ is the same for both systems, as well as the other critical exponents of the critical point. They are summarized in Tab. 4.1.

Critical exponent	Scaling in H_2O	Scaling in Ising model	Mean field	$d = 2$	$d = 3$
α	$c \sim c_{\pm}\lvert T - T_c\rvert^{-\alpha}$	$c \sim c_{\pm}\lvert T - T_c\rvert^{-\alpha}$	0 (disc.)	0 (log)	0.1101
β	$v_{\text{gas}} - v_{\text{liquid}} \sim (T_c - T)^{\beta}$	$m \sim (T_c - T)^{\beta}$	$1/2$	$1/8$	0.3264
γ	$\kappa \sim \lvert T - T_c\rvert^{-\gamma}$	$\chi \sim \lvert T - T_c\rvert^{-\gamma}$	1	$7/4$	1.2371
δ	$v_{\text{gas}} - v_{\text{liquid}} \sim (p - p_c)^{1/\delta}$	$m \sim B^{1/\delta}$	3	15	4.7898

Table 4.1: Critical exponents of the Ising universality class along with their appearance in H_2O and the Ising model [145]. We defined $c = C/N$, and $c_{\pm}$ indicates the existence of a discontinuity at T_c.

In both systems, α quantifies the dependence of the heat capacity on the temperature, which can be obtained via $C = \beta^2 \partial \log Z / \partial \beta^2$. In H_2O, γ describes the scaling of the compressibility $\kappa = -v^{-1} \partial v / \partial p|_T$ on the temperature. The equivalent of the compressibility in the Ising model is the magnetic susceptibility, which is defined as $\chi = \partial m / \partial B|_T$.

This is an example of universality: Even though the systems are microscopically very different, at the critical point, they behave in exactly the same way and give rise to exactly the same scaling of macroscopic observables. There exist different universality classes, corresponding to a certain set of critical exponents. Universality does not necessarily occur only at a single point in the phase diagram, i.e. the critical point. There exist whole phases which are critical (or more precisely self similar) and have the same power law scaling of macroscopic observables. One example is the Kardar Parisi Zhang (KPZ) phase, which will be further discussed in Chap. 5.

For the sake of completeness it should be mentioned that the critical exponents which are calculated in mean field theory are not accurate for dimensions $d < 4$ for the Ising model. It turns out that for $d = 1$, there does not even exist a phase transition in the Ising model (and equivalently for H_2O). For $1 < d < 4$, mean field theory delivers the correct qualitative behavior of the phase diagram, but not the right values of the critical exponents. Only for $d \geq 4$ is mean field theory correct. The dimension below which mean field theory fails is called lower critical dimension d_l. The dimension at and above which mean field theory gives the correct result is called upper critical dimension d_u. Here, $d_l = 1$ and $d_u = 4$. High precision predictions for the critical exponents of the Ising universality class are summarized in Tab. 4.1.

4.3 Continuous symmetries

We discussed phase transitions and spontaneous symmetry breaking using the example of the Ising model, which has a discrete $\mathbb{Z}_2$ symmetry as the spins can either point up or down. We could also allow the spins to continuously rotate in the $x-y$ plane. This model is known as the XY-model and has a continuous $O(2)$ symmetry. We come back to this model in Chap. 5. If we give the spins even more freedom and allow them to rotate in 3 dimensions, we arrive at the so called Heisenberg model which is invariant under the continuous $O(3)$ symmetry. Both the ferro- and anti-ferromagnetic Heisenberg model with long-range interactions are subject of Chap. 6.

Continuous symmetries are not only common in spin systems, but also in the physics of ultracold atomic gases or condensed matter, where for example a $U(1)$ symmetry of the Hamiltonian corresponds to particle number conservation. Similar to a discrete symmetry, a continuous symmetry can also be spontaneously broken. The expectation value of the order parameter changes from being zero in the disordered, to being finite in the ordered phase. In the Ising model, the two possible values for the order parameter are $m = \pm m_0$, corresponding to the spins either pointing upwards or downwards. For a spontaneously broken continuous symmetry, there exists an infinite number of possible values of the order parameter. For example in the XY-model, in the ordered phase, the spins are aligned but they can point in any direction in the $x-y$ plane, not only up and down. All of these configurations have the same energy, which means there exists an infinitely degenerate choice of ground states (see Fig. 4.4 (a)).

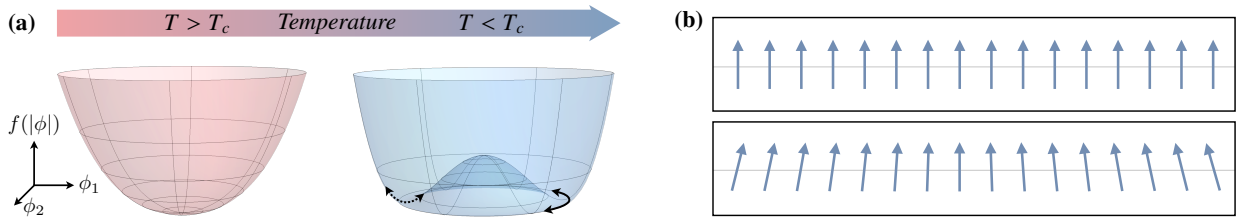

Figure 4.4: **(a)** Effective free energy of a system with a two-component order parameter and continuous SO(2) symmetry in 3d (for instance the XY-model). In the symmetry broken phase ($T < T_c$), there exists an infinite number of equilibrium states. Excitations which stay within the manifold of equilibrium states preserve the norm of the order parameter. These are the gapless Goldstone modes (solid arrow). Excitations which do not preserve the norm of the order parameter are gapped (dotted arrow). **(b)** *Upper figure:* Sketch of the equilibium configuration of spins in the XY-model in the symmetry broken phase. *Lower figure:* Example of a gapless Goldstone excitation. Its energy can be arbitrarily lowered by increasing the wavelength of the variation along the direction of the magnetization. Note: The sketch shows the one dimensional XY-model. Spontaneous symmetry breaking in the model, however, only occurs in $d \geq 3$.

In this situation of a spontaneously broken continuous symmetry, there exist excitations of the system with arbitrarily small energy. This can be seen in Fig. 4.4 (a) describing the ordered phase of the XY-model: given a certain ground state, one can stay in the manifold of ground states and only vary the direction in which the spins point over long distances. The greater the spatial extent of the excitation, the less energy is required. In the context of spin systems these kind of excitations are called spin waves (see Fig. 4.4 (b)). More generally, the gapless excitations which arise from a spontaneous breaking of a continuous symmetry are called Goldstone modes.

Goldstone Theorem: *Assume a theory which is invariant under continuous global symmetry transformations. If the symmetry is spontaneously broken, there are gapless excitations, the Goldstone modes. Each broken generator of the symmetry corresponds to one Goldstone mode.*

In the case of the XY-model, there exists one Goldstone mode. As discussed before, the lower critical di-

mension in the Ising model is $d_l = 1$. For a system with continuous symmetries at zero temperature, the lower critical dimension is raised to two. The reason that there exists no ordered phase in $d = 2$ is due to the presence of would-be Goldstone modes. The gapless excitations in $d \leq 2$ are so strong that they destroy any long-range order. This result is known as the Mermin-Wagner theorem.

Mermin-Wagner Theorem: *Continuous symmetries cannot be spontaneously broken at finite temperature in systems with sufficiently short-range interactions in dimensions* $d \leq 2$[7].

In Tab. 4.2, the correlations of the order parameter ϕ as a function of the spacial separation $\mathbf{r}$ in the low-temperature phase are shown for $\mathbf{r} \to \infty$. In three dimensions the correlation function is constant, signalling true long-range order in agreement with the Mermin-Wagner theorem. In contrast, in 1d, the correlations of the order parameter decay exponentially (with the correlation length ξ), implying that no long-range order exists even at low temperature. For some continuous symmetries, the two dimensional case can be special, as here the correlations are neither constant as in 3d, nor they decay as fast as in 1d. The phase with algebraically decaying correlations is called *quasi long-range ordered*, and the phase transition from the disordered high-temperature to the quasi long-range ordered low-temperature phase is not caused by SSB. Quasi-long-range order is found in $O(2)$ symmetric models such as the XY-model, but not in systems with $O(N)$ symmetry for $N \geq 3$.

Dimension	Correlation function	Order
1d	$\langle\phi(\mathbf{r})\phi(0)\rangle \sim e^{-\lvert\mathbf{r}\rvert/\xi}$	disorder
2d	$\langle\phi(\mathbf{r})\phi(0)\rangle \sim 1/\lvert\mathbf{r}\rvert^{\eta}$	quasi long-range order (QLRO)
3d	$\langle\phi(\mathbf{r})\phi(0)\rangle = \text{const.}$	true long-range order (LRO)

Table 4.2: Correlation functions of the order parameter ϕ for a system with continuous $O(2)$ symmetry in dimensions $1-3$ in the low temperature phase. Exponentially decaying correlations (with correlation length ξ) correspond to a disordered state. In 1d, even at low temperature, no long-range order can exist. In contrast, correlations which are constant indicate a state with true long-range order, as in the symmetry broken phase in 3d. In 2d, correlations decay algebraically as a function of the distance $\mathbf{r}$ (with some exponent η), which corresponds to a state with so called quasi long-range order.

[7] For quantum systems, the Mermin-Wagner theorem at $T = 0$ provides a different value of the lower critical dimension, typically smaller than two.

Chapter 5

Nonequilibrium universality in quadratically driven bosonic systems

This chapter is based on the following publication
O. K. Diessel, S. Diehl, and A. Chiocchetta, *Emergent Kardar-Parisi-Zhang Phase in Quadratically Driven Condensates*,

Phys. Rev. Lett. **128**, 070401 (2022)

5.1 Introduction

In the following, we turn to the question of how the absence of thermal equilibrium affects the properties of matter. This is one of the fundamental questions of many-body physics, with far-reaching consequences for the engineering of novel materials, the development of quantum technologies, and the understanding of active and living matter. In nonequilibrium systems, the lack of detailed balance can radically modify the collective behavior typical of equilibrium systems. Accordingly, novel phases can be expected, such as non-reciprocal (or chiral) phases in active matter [146, 147], quantum optical platforms [148, 149] and ultracold atoms [150], or dissipative time crystals in many-body quantum systems [151–154].

An intriguing aspect concerns the impact of nonequilibrium fluctuations in two spatial dimensions. On the one hand, the Mermin-Wagner theorem does not hold out of equilibrium and out of equilibrium systems can feature transitions to phases with long-range order as e.g. in two-dimensional flocks [124] or driven quantum spin chains [125, 126]. On the other hand, quasi long-range order (QLRO), allowed in two-dimensional equilibrium systems, can be destroyed due to nonequilibriumness. An example here is the Berezinskii–Kosterlitz–Thouless (BKT) phase transition, expected for equilibrium Bose gases in two spatial dimensions, which is erased in their driven-dissipative counterpart and replaced by a disordered phase featuring a Kardar-Parisi-Zhang (KPZ) scaling of the phase fluctuations [127].

KPZ scaling refers to the scaling behavior observed in a class of nonequilibrium statistical physics models, the KPZ models, that describe the dynamics of surface or interface growth over time. They are named after Mehran Kardar, Giorgio Parisi, and Yi-Cheng Zhang, who introduced these models in 1986. The KPZ equation describes the dynamics of a height variable $h(\mathbf{x}, t)$ under drive

$$\frac{\partial h(\mathbf{x}, t)}{\partial t} = D\nabla^2 h(\mathbf{x}, t) + \frac{\lambda}{2}[\nabla h(\mathbf{x}, t)]^2 + \xi(\mathbf{x}, t). \tag{5.1}$$

The non-linearity $\propto \lambda$ describes growth perpendicular to the surface, which is counteracted by the diffusion term $\propto D$ which favors a smoothening of the surface. $\xi(\mathbf{x}, t)$ is a Gaussian averaged white noise. Examples of systems that can be described by the KPZ equation (5.1) include the growth of bacterial colonies, which

are driven by the supply of sugar, the propagation of a fire front which is driven by oxygen, or, as we will encounter later, the phase dynamics of exciton-polariton systems which are driven by a laser. Also the growth of domain walls in the Ising model (4.2) under application of an external magnetic field can be described by the KPZ equation [155].

Remarkably, the KPZ equation is generically scale-invariant, that is, the height field $h(\mathbf{x}, t)$ remains gapless under RG. This is due to the symmetry $h(\mathbf{x}, t) \to h(\mathbf{x}, t) + \alpha$ of the KPZ equation and, unlike critical points, requires no fine-tuning[1]. The absence of any length scale in the system leads to an algebraic scaling behavior of the correlations in space and time

$$\langle [h(\mathbf{x}, t) - h(0, 0)]^2 \rangle = |\mathbf{x}|^{2\chi} f_{\mathrm{K}} \left(\frac{t}{|\mathbf{x}|^z} \right) \tag{5.2}$$

with $f_{\mathrm{K}}(y)$ being an universal scaling function with asymptotics

$$f_{\mathrm{K}}(y \to 0) = \text{const.} \tag{5.3}$$

$$f_{\mathrm{K}}(y \to \infty) = y^{2\chi/z}. \tag{5.4}$$

The exponent χ is called the *roughness exponent*. For $\chi > 0$, the variance of the hight field grows with space and time corresponding to an increase in the surface's roughness, whereas for $\chi < 0$ height variance shrinks leading to a smoothing of the surface. Interestingly, in $d \leq 2$, one always finds the hight field to undergo roughening. This can be traced back, within the RG analysis [156], to the existence of a fully attractive strong coupling fixed point[2] with $\chi > 0$. Only in $d > 2$, an additional unstable fixed point exists which separates the fully attractive strong coupling fixed point from the Gaussian fixed point (corresponding to $\lambda = 0$). By varying the microscopic value of λ, one can therefore encounter a phase transition, the so called roughening transition, from a smooth to a rough surface. A more detailed introduction to KPZ models can be found, e.g., in Ref. [155].

While KPZ scaling has been observed in many one dimensional systems, its observation in two dimensions is still elusive. Promising candidates to experimentally observe KPZ scaling in 2d are exciton-polaritons fluids in microcavities [157, 158]. However, the length scales at which their signatures are expected to become visible are dramatically larger than the typical system sizes [159–162], which has so far prevented their observation.

In this chapter, we investigate the fate of nonequilibrium systems with discrete symmetries, which are less explored than nonequilibrium systems with continuous symmetries. Specifically, in Sec. 5.2, we consider a two-dimensional, driven-dissipative Bose gas with a quadratic drive, which results in a global $\mathbb{Z}_2$ symmetry of the system. We show that the absence of thermal equilibrium suppresses the Ising phase transition in favour of an emerging KPZ phase. In Sec. 5.3 we moreover show that the presence of the quadratic drive reduces the scale at which the KPZ physics sets in, enhancing its visibility in finite-size systems. Finally, in Sec. 5.4, we discuss our theoretical predictions with respect to experiments with exciton-polaritons considering realistic parameters. We show that these systems hold promises for identifying KPZ physics in two spatial dimensions at currently available system sizes, where experimental realizations have so far remained elusive [163, 164].

[1] This is called "self-organized criticality". One can find this phenomenon also e.g., in the Kosterlitz-Thouless phase.

[2] This fixed point is not accessible perturbatively, but has has been established using numerics and functional RG approaches [156].

5.2 Quadratically driven-dissipative Bosons

5.2.1 Master equation

We consider a gas of quadratically-driven and dissipative bosons, described by the master equation

$$\partial_t \hat{\rho} = -i[\hat{\mathcal{H}}, \hat{\rho}] + \int_{\mathbf{r}} \sum_n \left[\hat{L}_n \rho \hat{L}_n^\dagger - \frac{1}{2}\{\hat{\rho}, \hat{L}_n^\dagger \hat{L}_n\} \right]. \tag{5.5}$$

The first term of the equation, including the Hamiltonian $\hat{\mathcal{H}}$ of the system, describes the unitary or coherent part of the dynamics of the density matrix $\hat{\rho}$. The latter term, including the Lindblad operators $\hat{L}_n = \hat{L}_n(\mathbf{r})$, describes the dissipative part of the dynamics. The quadratic drive can be regarded as a process coherently creating or destroying two particles at a given position. The Hamiltonian is thus given by

$$\hat{\mathcal{H}} = \int_{\mathbf{r}} \left[\frac{\nabla\hat{\psi}^\dagger \nabla\hat{\psi}}{2m} + \delta\hat{\psi}^\dagger\hat{\psi} + \frac{G}{2}(\hat{\psi}^2 + \hat{\psi}^{\dagger 2}) + \frac{U}{2}\hat{\psi}^{\dagger 2}\hat{\psi}^2 \right], \tag{5.6}$$

with m the mass of the bosons, $\delta > 0$ the detuning between the bosonic and the drive frequency, and $U > 0$ the particle interaction. The quadratic drive has a strength G, and we can set $G > 0$ without loss of generality, by absorbing its phase into a redefinition of the fields. The Hamiltonian (5.6) can describe Bose gases interacting with a molecular condensate [165], where two bosons are coherently created out of (or absorbed into) the condensate. A physical realization of this was suggested in terms of ultracold atomic gases in presence of Feshbach resonances [166]. In this case, the Hamiltonian describes the bosonic gas in presence of a molecular condensate, leaving a residual $\mathbb{Z}_2$ symmetry. In this phase, the system can still undergo a phase transition to an atomic-condensed phase, with the phase transition falling in the Ising universality class [167, 168]. The presence of further incoherent processes, such as single particle losses and pump, as well as two-particle losses, is included via the Lindblad operators $\hat{L}_{1l} = \hat{\psi}$, $\hat{L}_{1p} = \hat{\psi}^\dagger$, and $\hat{L}_{2l} = \hat{\psi}^2$, respectively. In the following, we assume the single-particle pump to be weaker than single-particle losses.

5.2.2 Langevin equation for the Bosons

Since we are interested in the critical properties of this model, we neglect quantum fluctuations, as they are irrelevant compared to the statistical fluctuations induced by the incoherent processes [142, 169]. This approximation allows us to treat $\hat{\psi}$ as a stochastic field rather than an operator: its dynamics is accordingly described by the Langevin equation [155]

$$\partial_t \psi = -(-K\nabla^2 + r + u|\psi|^2)\psi - iG\psi^* + \zeta, \tag{5.7}$$

with K, r, u complex numbers, and ζ a Gaussian, zero-average white noise with correlations $\langle \zeta(\mathbf{r}, t)\zeta^*(\mathbf{r}', t')\rangle = 2\sigma\delta(t - t')\delta^{(2)}(\mathbf{r} - \mathbf{r}')$. The imaginary parts of K, r, u (in the following denoted by a "c" subscript) correspond to coherent couplings describing reversible dynamics. More precisely $K_c = 1/2m$ is the kinetic energy, $r_c = \delta$ is the detuning and $u_c = U/2$ is the interaction parameter. Their real parts (in the following denoted by a "d" subscript) correspond to dissipative couplings representing irreversible processes, therefore r_d and u_d describe single and two-particle losses, respectively. Moreover, Eq. (5.7) includes K_d, describing spatial diffusion, which is zero at the microscopic level but expected to be generated by coarse-graining.

For $G = 0$, Eq. (5.7) is invariant under the U(1) transformation $\psi \to e^{i\alpha}\psi, \psi^* \to e^{-i\alpha}\psi^*$, and it is known as the complex Ginzburg-Landau equation [170, 171], or as the driven-dissipative Gross-Pitaevski equation in the context of exciton-polaritons [158]. For finite G, Eq. (5.7) is invariant under the $\mathbb{Z}_2$ transformation $\psi \to -\psi, \psi^* \to -\psi^*$, and it is known as the periodically-driven complex Gross-Pitaevski equation [171].

5.2.3 Langevin equation for the phase of the Bosons

A mean-field analysis of Eq. (5.7) shows that a phase transition is expected for $G > G_c$, predicting the spontaneous breaking of the $\mathbb{Z}_2$ symmetry and the emergence of a condensate (see Fig. 5.1 (a)). This result is expected to be qualitatively robust in higher spatial dimensions $d > 2$, while in lower dimensions fluctuations can dramatically modify the mean-field result. In passing, we notice that for negative detunings $\delta < 0$ the mean-field solution may exhibit a bistable behavior, as predicted in Ref. [172]. In the following, we will restrict ourselves to the case $\delta \geq 0$, where no bistability is expected.

To assess the effect of fluctuations, we proceed in the spirit of the hydrodynamic theory for quasicondensates [127, 173]. We represent the bosonic complex field in Eq. (5.7) in its phase amplitude representation $\psi(\mathbf{r},t) = \chi(\mathbf{r},t)e^{i\theta(\mathbf{r},t)}$, with χ and θ real fields associated with density and phase fluctuations. Separating real and imaginary parts, one obtains the two equations:

$$\partial_t\theta = -r_c + K_c\left[\frac{\nabla^2\chi}{\chi} - (\nabla\theta)^2\right] + K_d\left[2\frac{\nabla\chi}{\chi}\nabla\theta + \nabla^2\theta\right] - u_c|\chi|^2 - G\sin(2\theta) + \mathrm{Im}\left[\frac{\zeta e^{-i\theta}}{\chi}\right], \tag{5.8a}$$

$$\partial_t\chi = -r_d + \chi K_d\left[\nabla^2\chi - \chi(\nabla\theta)^2\right] - K_c\left[2\nabla\chi\nabla\theta + \chi\nabla^2\theta\right] - u_d|\chi|^2\chi - G\chi\sin(2\theta) + \mathrm{Re}\left[\zeta e^{-i\theta}\right]. \tag{5.8b}$$

The fluctuations of χ are gapped[3]. Assuming that these fluctuations are small compared to saddle point value χ_0, we neglect spatial and time derivatives of χ from the previous equations. This allows one to solve Eq. (5.8b) for χ^2 and to insert the result into Eq. (5.8a). By further performing the shift $\theta \to \theta + \theta_0$, with $\tan(2\theta_0) = u_d/u_c$, we obtain the effective equation for the phase

$$\eta\,\partial_t\theta = \gamma\nabla^2\theta - 2g\sin(2\theta) + \frac{\lambda}{2}(\nabla\theta)^2 + F + \xi, \tag{5.9}$$

with ξ a zero-average Gaussian white noise with correlations $\langle\xi(\mathbf{r},t)\xi(\mathbf{r}',t')\rangle = 2D\delta^{(2)}(\mathbf{r}-\mathbf{r}')\delta(t-t')$. The microscopic values of the six parameters $\eta, \gamma, g, \lambda, F, D$ are given by

$$\begin{aligned} \eta &= 1, & \gamma &= K_d + \frac{u_c}{u_d}K_c, \\ g &= \frac{G}{2}\sqrt{1+\frac{u_c^2}{u_d^2}}, & \lambda &= 2\left(-K_c + \frac{u_c}{u_d}K_d\right), \\ F &= -r_c + \frac{u_c}{u_d}r_d, & D &= \frac{\sigma}{2\chi_0^2}\left(1+\frac{u_c^2}{u_d^2}\right). \end{aligned} \tag{5.10}$$

The $\mathbb{Z}_2$ symmetry appears in Eq. (5.9) as an invariance under the transformation $\theta \to \theta + m\pi$, for all odd integers m. The properties of the phase θ derived from the solutions of Eq. (5.9) can be directly translated into the correlations of the original complex fields ψ, ψ^* via

$$\langle\psi(\mathbf{r})\rangle \approx \chi_0 e^{i\theta_0}\, e^{-\frac{1}{2}\langle\theta(\mathbf{r})^2\rangle}, \tag{5.11a}$$

$$\langle\psi(\mathbf{r})\psi^*(0)\rangle \approx \chi_0^2\, e^{\langle\theta(\mathbf{r})\theta(0)\rangle - \langle\theta(\mathbf{r})^2\rangle}, \tag{5.11b}$$

with θ_0 the saddle point value of θ. The previous relations are obtained by neglecting the fluctuations of χ, and retaining only the leading terms in the cumulant expansion of $\langle e^{i(\theta(\mathbf{r})-\theta(0))}\rangle$. A first insight into the solution of Eq. (5.9) can be gained by considering two limiting cases before moving onto the general scenario.

[3] This can be seen by linearizing the equation for χ around its saddle point value χ_0.

5.2.3.1 KPZ limit

For $g = 0$, Eq. (5.9) possesses a U(1) symmetry, realized by the invariance under the transformation $\theta \to \theta + \alpha$, with α any real number. The drift term F can be removed by a gauge transformation $\theta \to \theta + Ft/\eta$. Equation (5.9) thus reduces to the KPZ equation [128]

$$\partial_t \theta = \gamma \nabla^2 \theta + \frac{\lambda}{2}(\nabla\theta)^2 + \xi. \tag{5.12}$$

In two spatial dimensions, the massless, KPZ-like fluctuations of the phase are shown to erase the BKT phase usually expected in equilibrium Bose gases, and replace it with a disordered phase [127] with correlations $\langle \psi(\mathbf{r})\psi^*(0)\rangle \sim e^{-|\mathbf{r}|^{2\chi}}$, where $\chi \approx 0.38$ is the critical exponent [174, 175].

5.2.3.2 Equilibrium limit

Thermal equilibrium is achieved when the condition $K_c/K_d = r_c/r_d = u_c/u_d$ is satisfied [127, 176], which entails the validity of the fluctuation-dissipation theorem, or, more generally, the presence of the associated thermal symmetry of the Keldysh action [177]. In this case, $\lambda = 0$ and $F = 0$, and Eq. (5.9) reduces to the relaxational dynamics of a sine-Gordon field

$$\eta\, \partial_t \theta = \gamma \nabla^2 \theta - 2g \sin(2\theta) + \xi, \tag{5.13}$$

whose renormalization was first studied in relation to the roughening transition of crystal surfaces [178]. The equilibrium Langevin equation (5.13) can be written as $\eta \partial_t \theta = -\frac{\mathrm{d}S}{\mathrm{d}\theta} + \xi$, where S is the statistical action given by

$$S = \int \mathrm{d}^2\mathbf{r} \left[\frac{\gamma}{2}(\nabla\theta)^2 - g\cos(2\theta)\right], \tag{5.14}$$

and we identify $\gamma = 1/2m$ and $2g = G$. One can study the model (5.14) by performing a perturbative renormalization group (RG) analysis. The idea consists in treating the coupling g perturbatively around the Gaussian model, and in deriving an effective long-wavelength theory by progressively integrating out high-energy modes. The couplings of the long-wavelength model are then expressed by a set of flow equations. To this end, we go to Fourier space and decompose the field θ into slow and fast modes: $\theta_{\mathbf{k}} = \theta^-_{\mathbf{k}} + \theta^+_{\mathbf{k}}$. The slow modes $\theta^-_{\mathbf{k}}$ have support over momenta $\mathbf{k}$ such that $|\mathbf{k}| < \Lambda(1 - \mathrm{d}\ell)$, while the fast modes $\theta^+_{\mathbf{k}}$ have support over the momentum shell defined by $\Lambda(1-\mathrm{d}\ell) \leq |\mathbf{k}| \leq \Lambda$ (with Λ the ultraviolet cutoff). In the first RG step, we integrate out the fast modes which generates a contribution to the couplings γ and $\bar{g} = g/\Lambda^2$ in the remaining action for the slow fields. The second step is to rescale momenta $\mathbf{k} \to \mathbf{k}' = (1 - \mathrm{d}\ell)\mathbf{k}$ in order to compare the resulting action to the initial one. Finally, in the last RG step, one has to rescale the fields, which is trivial in two dimensions. More details on the RG analysis of the sine-Gordon model can be found in Ref. [145].

The resulting RG equations read

$$\frac{\mathrm{d}\bar{g}}{\mathrm{d}\ell} = \left(2 - \frac{D}{\gamma\pi}\right)\bar{g}, \qquad \frac{\mathrm{d}\gamma}{\mathrm{d}\ell} = \bar{g}^2 f(\gamma), \tag{5.15}$$

with f a function whose form depends on the renormalization scheme. The associated flow is portrayed in Fig. 5.1 (b). If $\bar{g}$ is an irrelevant perturbation, it flows to a line of fixed points, where $\bar{g}^* = 0$ and $\gamma^* \leq 1/2\pi$ (red curves in Fig. 5.1 (b)). Here, θ is gapless and correlations grow logarithmically. When the dimensionless coupling $\bar{g} \equiv g/\Lambda^2$ is a relevant perturbation, however, $\bar{g}$ flows to infinity, signalling the relevance of the sine-Gordon nonlinearity (green curves in Fig. 5.1 (b)). This corresponds to the field θ being massive, and, consequently, its correlations decay exponentially over long distances.

The impact of these two phases on the properties of the bosonic field ψ can be inferred from Eqs. (5.11). On the one hand, for a gapped θ, the value of $\langle\theta(\mathbf{r})^2\rangle$ is infrared-convergent and finite, while $\langle\theta(\mathbf{r})\theta(0)\rangle$

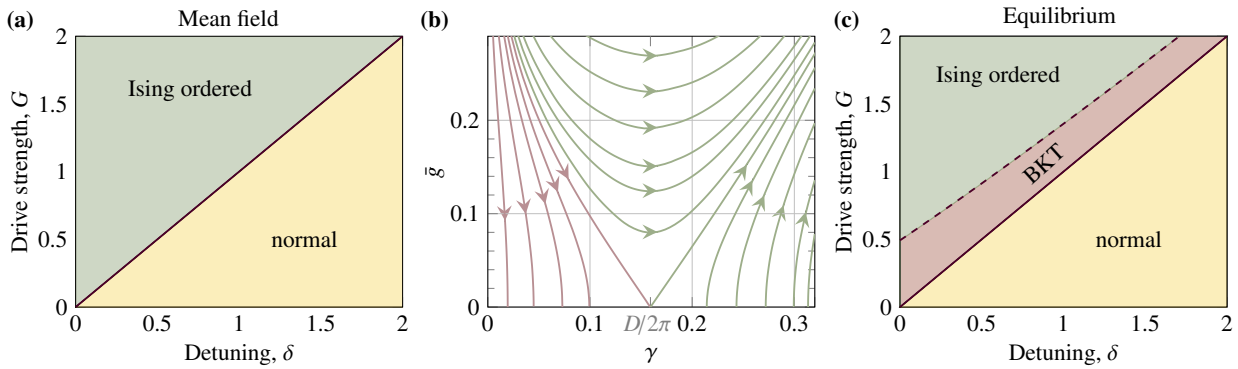

Figure 5.1: **(a)** Mean-field phase diagram of a quadratically driven, open condensate, as a function of the imprinted pairing strength G and the detuning δ. **(b)** Investigation of how fluctuations affect the Ising ordered phase predicted by the mean field in equilibrium. The red (green) arrows indicate the flow of the inital parameters $\bar{g}_0$ and γ_0 for which the sine term in Eq. (5.13) is irrelevant (relevant), resulting in a phase featuring quasi long-range order (true long-range order) for the bosons. **(c)** Equilibrium phase diagram. Fluctuations give rise to an intermediate phase featuring BKT scaling.

decays exponentially at long distances. As a consequence, the order parameter is finite and long-range order is established, indicating that the system lies in the ordered phase with a sponatneously broken $\mathbb{Z}_2$. On the other hand, for a gapless θ, $\langle\theta(\mathbf{r})^2\rangle$ is infinitely large as a consequence of an infrared divergence, while $\langle\theta(\mathbf{r})\theta(0)\rangle - \langle\theta(\mathbf{r}^2)\rangle$ grows logarithmically, implying an algebraic decay of $\langle\psi(\mathbf{r})\psi^*(\mathbf{r})\rangle$. This suggests that order is not supported, and the condensed phase is replaced by a BKT phase characterized by quasi-long-range order. This is the usual case for two-dimensional Bose gases with U(1) symmetry (i.e., $G = 0$).

The separatrix between the two basins of attraction can be approximated by a line $g = \beta(\gamma - \gamma_c)$, which has a zero at $\gamma_c = D/2\pi$ with $D = \sigma/2\chi_0^2$, and a slope of $\beta \approx -1.7$. The region where g is irrelevant, and therefore the phase with long-range order is replaced by a BKT phase is described by

$$\frac{G}{2U} < \beta\left(\frac{\sigma}{4\pi}\frac{1}{G-\delta} - \frac{1}{2mU}\right). \tag{5.16}$$

In Fig. 5.1 (c), we show the phase diagram for the values $\sigma = 4$ and $m = U = 1$.

Summarizing, for a two-dimensional equilibrium gas, three phases are expected: a normal fluid with short-range correlations (corresponding to the mean-field solution without condensate), a BKT phase with quasi-long-range order, and a $\mathbb{Z}_2$-symmetry-broken phase with long-range order. The corresponding phase diagram in terms of G and δ is reported in Fig. 5.1 (c). Analogous phases have been obtained for the ANNNI model [179, 180] and the XYZ spin chain in transverse field [181, 182], which share the same effective dimensionality and $\mathbb{Z}_2$ symmetry with the present model.

5.2.3.3 Full problem

In Eq. (5.9), the KPZ fluctuations wash out the sine-Gordon physics, thus destabilizing the phases predicted at thermal equilibrium. The renormalization analysis of this equation was first performed in Refs. [183, 184] to study the effect of nonlinearities on the roughening transition of crystal surfaces. There, it was shown that the KPZ physics dominates over large distances. We will show that for driven-dissipative Bose gases, the equilibrium ordered and BKT phases are destabilized by nonequilibrium fluctuations, and replaced by a phase with short-range order.

The long-wavelength physics of Eq. (5.9) can be conveniently studied using a perturbative RG approach. Here, the couplings g and λ are treated perturbatively. We will consider two RG schemes, derived in

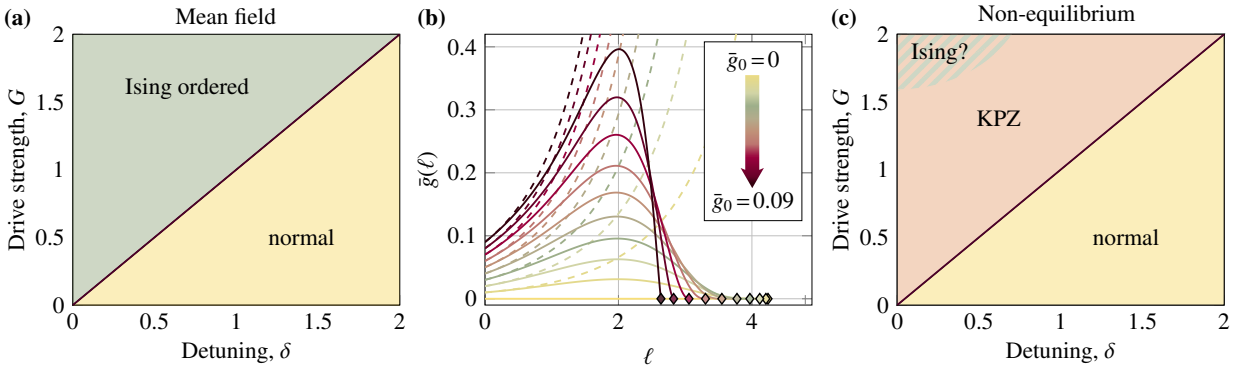

Figure 5.2: **(a)** Mean-field phase diagram. **(b)** Investigation of how fluctuations affect the Ising ordered phase predicted by the mean field in nonequilibrium. The flow of $\bar{g}(\ell)$ for different initial values of $\bar{g}_0$ (in steps of 0.01) is shown. Parameters for the solid curves: $\gamma_0 = 0.3$, $T_0 = 1$, $\lambda_0 = 0.4$, $\eta_0 = 1$, $\bar{F}_0 = 0$. Parameters for the dashed curves: $\gamma_0 = 0.3$, $T_0 = 1$, $\lambda_0 = 0.0$, $\eta_0 = 1$, $\bar{F}_0 = 0$. The diamond symbols denote the onset of a divergence in the RG flow ℓ^*. For a finite initial λ_0, $\bar{g}$ flows to zero, implying that the sine term in Eq. (5.9) becomes irrelevant. **(c)** Nonequilibrium phase diagram of model (5.9). The Ising phase is replaced by a phase with KPZ scaling. A residual Ising phase (striped region) may persist in the non-perturbative regime of large G, inaccessible to our method.

Refs. [184] and [185]. Their derivation is shown in Appendix B.1. The equations are expressed in terms of the dimensionless quantities $\bar{g} \equiv g/\Lambda^2$, and $\bar{F} \equiv F/\Lambda^2$ and read

$$\begin{aligned}
\frac{\mathrm{d}\bar{g}}{\mathrm{d}\ell} &= \left(2 - \frac{T}{\pi\gamma}\right)\bar{g}, & \frac{\mathrm{d}T}{\mathrm{d}\ell} &= \frac{T^2\lambda^2}{8\pi\gamma^3} + \frac{8T^2}{\pi\gamma^3}A^{(T)}(n,\kappa)\bar{g}^2, \\
\frac{\mathrm{d}\gamma}{\mathrm{d}\ell} &= \frac{2T}{\pi\gamma^2}A^{(\gamma)}(n,\kappa)\bar{g}^2, & \frac{\mathrm{d}\lambda}{\mathrm{d}\ell} &= \frac{8T}{\pi\gamma^2}A^{(\lambda)}(n,\kappa)\bar{g}^2, \\
\frac{\mathrm{d}\eta}{\mathrm{d}\ell} &= \frac{8T\eta}{\pi\gamma^3}A^{(\eta)}(n,\kappa)\bar{g}^2, & \frac{\mathrm{d}\bar{F}}{\mathrm{d}\ell} &= 2\bar{F} + \frac{T\lambda}{4\pi\gamma} - \frac{4T}{\pi\gamma^2}A^{(F)}(n,\kappa)\bar{g}^2,
\end{aligned} \tag{5.17}$$

with $T \equiv D/\eta$ the effective temperature, $n \equiv T/\gamma\pi$, $\bar{U} \equiv U/\Lambda^2$, $\bar{F} \equiv F/\Lambda^2$, and $\kappa = 2\bar{F}/\gamma$. The form of the functions $A(n,\kappa)$ is given in App. B.1 and depends on the renormalization scheme. Before proceeding to a more detailed analysis, we discuss the qualitative solution of the RG equations.

If the system is in thermal equilibrium, the equations reduce to the ones for the relaxational sine-Gordon model of Ref. [178]. If instead $\bar{g} = 0$, the equations reduce to the ones for KPZ [155]: the noise level D and the effective temperature T flow to infinity, indicating that the RG flow flows towards the KPZ strong-coupling fixed point, entailing that the KPZ physics dominates[4]. Finally, if both $\bar{g}_0$ and λ_0 are finite, the KPZ nonlinearity λ dominates over the sine-Gordon nonlinearity $\bar{g}$, which eventually renormalizes to zero. Typical flows of $\bar{g}$ are shown in Fig. 5.2 (b): for $\lambda = 0$ and $\bar{F} = 0$, $\bar{g}(\ell)$ grows indefinitely (dashed curves), signalling that the field θ is gapped. For finite initial values of λ_0 or $\bar{F}_0$, however, $\bar{g}$ flows back to zero, indicating the irrelevance of the sine-Gordon term. The diamond symbols denote the onset of a divergence in the RG flow, which is further discussed in Sec. 5.3.

At long wavelengths, the phase correlations are then expected to be captured by the KPZ exponent: $\langle\theta(\mathbf{r})\theta(0)\rangle - \langle\theta(\mathbf{r})^2\rangle \sim -|\mathbf{r}|^{2\chi}$, with $\chi \approx 0.38$ [174, 175]. Moreover, $\langle\theta(\mathbf{r})^2\rangle$ diverges due to long-wavelength fluctuations. Accordingly, by replacing these values in Eqs. (5.11), we find that complex fields are short-range correlated via a stretched exponential, implying that no phase transition takes place. Whether the ordered phase is completely removed or survives for large values of the two-particle drive (corresponding to large values of g) cannot be determined from our analysis, as the RG analysis is not valid for non-perturbative values of g. Finally, here we neglected the presence of topological excitations, such as vortices and anti-

[4] We emphasize that, while our perturbative RG can identify the onset of a strong-coupling fixed point, it is not suited to fully describe it, given its perturbative nature.

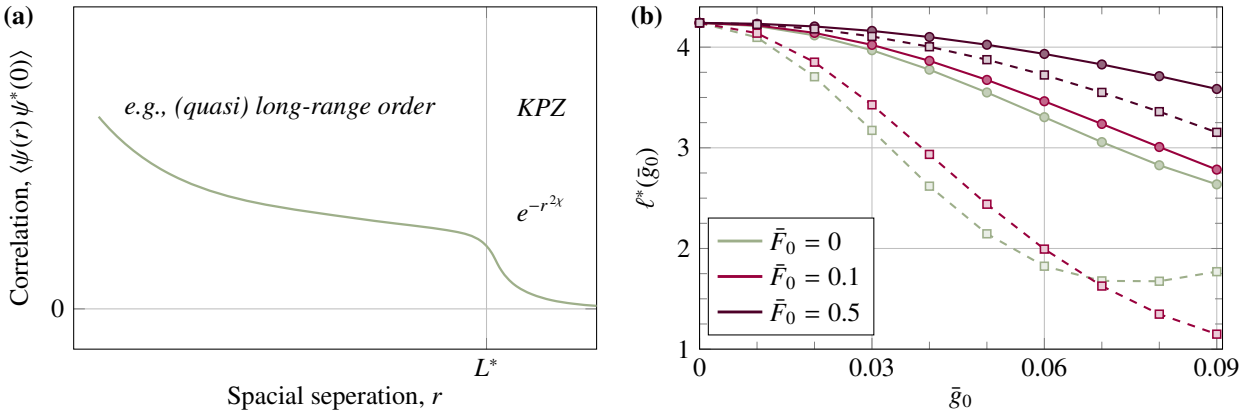

Figure 5.3: **(a)** Schematic behavior of the correlations as a function of the radial distance $r = |\mathbf{r}|$ in the KPZ phase. Only above the critical length scale L^*, the characteristic scaling and therefore KPZ physics can be observed. In 2D, L^* is usually large, thus exceeding experimenally and numerically available system sizes. Within our model, the value of L^* can be drastically reduced by increasing the quadratic drive G. **(b)** RG scale ℓ^* for the KPZ crossover as a function of the sine-Gordon nonlinearity $\bar{g}_0$, for different values of $\bar{F}_0$. The RG length scale is related to the physical length scale via $L^* = \xi_0 e^{\ell^*}$. The solid and dashed lines correspond to the RG schemes derived in Ref. [184] and [185]. Parameters: $\gamma_0 = 0.3$, $T_0 = 1$, $\lambda_0 = 0.4$, $\eta_0 = 1$.

vortices. Whether such defects play a role on length scales below or only above the KPZ length scale is a non-universal question, which depends on the microscopic details of the experimental system. In the former case, the KPZ phase would be replaced by a disordered phase; in the latter, the KPZ physics will be visible in experiments [186–191].

5.3 Enhancement of KPZ physics

An essential question concerns the visibility of the predicted 2d KPZ physics in experimental systems or numerical simulations with limited size. In fact, the length scale L^* above which the KPZ physics becomes visible is usually very large, and can exceed the accessible systems' size (see Fig. 5.3 (a)): this is the case for, e.g., the roughening transition in crystal surfaces [192], and for exciton-polaritons in two-dimensional microcavities [127, 161, 193–195]. Here we show that the presence of a sine-Gordon nonlinearity can actually lower L^*, thus enhancing the visibility of the 2d KPZ.

The value of L^* can be extracted from the solution of the flow equations [196]. To illustrate this, it is convenient to first focus on the pure KPZ case of Eqs. (5.17), i.e., $\bar{g} = 0$. Here, the relevant RG equation is the one for the effective temperature T with γ and λ constant under the RG flow. $T(\ell)$ features a divergence for finite values of the flow parameter ℓ, namely $\ell^* = 8\pi\gamma^3/(T_0\lambda^2)$, with T_0 the initial value of T. The value of ℓ^* therefore determines the physical length scale above which the KPZ scaling is visible via $L^* = \xi_0 e^{\ell^*}$, with ξ_0 some microscopic length scale. As L^* is exponentially sensitive to the value of ℓ^*, finding conditions to minimize ℓ^* is crucial to observe KPZ physics. For finite values of $\bar{g}$, ℓ^* cannot be determined analytically, but it can be extracted from the divergence of the numerical solutions. We compute ℓ^* for different values of $\bar{g}_0$ and $\bar{F}_0$. The results are reported in Fig. 5.3 (b). Since ℓ^* is not a universal quantity, we extracted its value using two different RG schemes (cf. Appendix B.1), finding the same qualitative behavior.

Our results indicate that ℓ^* generically decreases as a function of $\bar{g}_0$. The decrease can be optimized by varying the value of $\bar{F}$, which, corresponding to the laser detuning (cf. Eq. (5.10)), is an experimentally

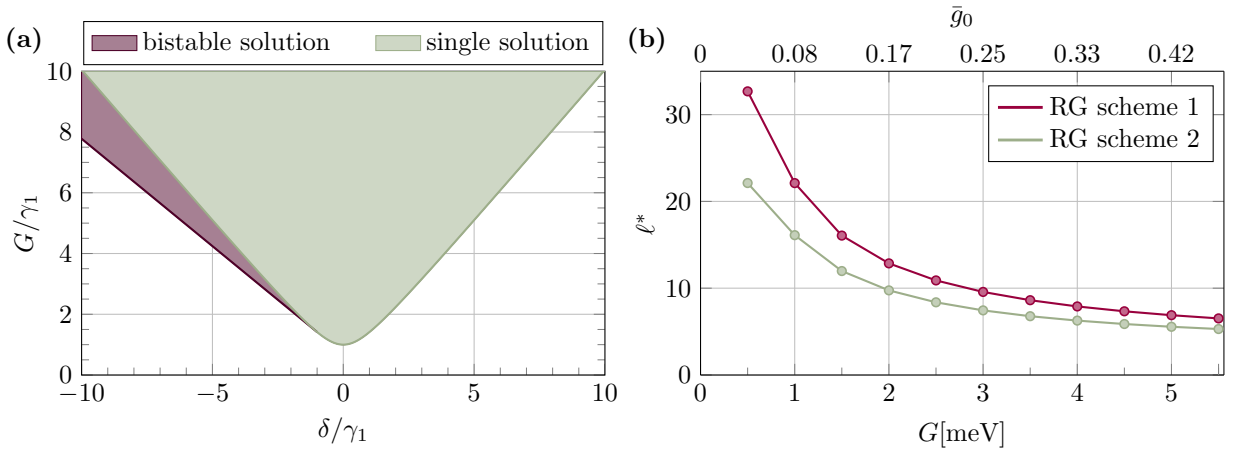

Figure 5.4: **(a)** Mean-field phase diagram associated with Eq. (5.18), highlighting the presence of one or two stable condensate solutions, for $U/\gamma_1 = \gamma_2/\gamma_1 = 1$. **(b)** RG length-scale ℓ^* corresponding to the onset of KPZ physics as a function of the drive strength G (lower x-axis) and of the rescaled RG paramater $\bar{g}_0$ (upper x-axis). The RG schemes 1 and 2 correspond to the choices of Eqs. (B.15) and (B.16), respectively.

tunable parameter. The value of ℓ^* can be reduced by up to a factor of four upon reaching $\bar{g}_0 \sim 0.1$, indicating that L^* can be reduced by four orders of magnitude compared to the case with $\bar{g}_0 = 0$. This implies a dramatic improvement of the visibility of the KPZ scaling in two-dimensional driven-dissipative gases, where it has so far remained elusive. As an example, in the next section we estimated the KPZ length scale for current exciton-polariton experiments.

5.4 Visibility of KPZ in exciton-polariton experiments

In this section we discuss the theoretical predictions with regard to experiments with exciton-polaritons. The starting point for the description is provided by the complex Gross-Pitaevskii equation obtained from the Hamiltonian Eq. (5.6) , and by adding further incoherent processes [158]:

$$i\hbar\partial_t\psi = \left[-\frac{\hbar^2\nabla^2}{2m_P} + \delta - i\gamma_1 + (U - i\gamma_2)|\psi|^2\right]\psi + G\psi^* + \zeta \tag{5.18}$$

where m_P is the polariton mass, $\gamma_{1,2}$ represent the polariton single- and two-particle losses, respectively, and ζ is a white, zero-mean Gaussian noise generated from the single particle losses with correlations given by $\langle\zeta(\mathbf{r},t)\zeta^*(0,0)\rangle = 2\hbar\gamma_1\delta(t)\delta^{(2)}(\mathbf{r})$. For convenience, $\hbar$ is restored. Typical experimental values for a GaAs/AlAs microcavity are given by [197] $m_P = 10^{-4}m_e$ (with m_e the vacuum electron mass), $\gamma_1 = 0.4$ meV , while $U = 1.5\ \mu$eV μm^2 (see, e.g., Ref. [198]). The value of the two-particle losses is usually neglected in the microscopic description. However, its presence is crucial to the mapping (5.10). While it is possible to control these processes, e.g., using a polaritonic Feshbach resonance [112], they nevertheless emerge from a coarse-grained description of the model (i.e., they are generated under the renormalization group). We then conservatively assume that $\gamma_2/U = 0.1$. The parameters δ and G depend on the drive and are therefore tunable.

It is convenient to recast Eq. (5.18) in units where $\mathbf{r}^2$ and t have the same dimension. To this end, we perform

the replacement $t \to 2m_p t/\hbar$. Accordingly, Eq. (5.18) takes the form

$$i\partial_t \psi = \left[-\nabla^2 + \tilde{\delta} - i\tilde{\gamma}_1 + (\tilde{U} - i\tilde{\gamma}_2)|\psi|^2\right]\psi + \tilde{G}\psi^* + \tilde{\zeta} \tag{5.19}$$

where $\tilde{\gamma}_1 = 2m_P\gamma_1/\hbar$, $\tilde{U} = 2m_P U/\hbar$, $\tilde{\gamma}_2 = 2m_P\gamma_2/\hbar$, $\tilde{G} = 2m_P G/\hbar$. The correlation of the noise $\tilde{\zeta}$ is given by $\langle\tilde{\zeta}(\mathbf{r},t)\tilde{\zeta}^*(0,0)\rangle = 4m_P\gamma_1/\hbar^2\delta(t)\delta^{(2)}(\mathbf{r})$.

At this point we can map Eq. (5.19) onto Eq. (5.9), with parameters given by (using Eq. (5.10)):

$$\begin{aligned} \eta &= 1 & \gamma &= \frac{U}{\gamma_2}, \\ g &= \frac{m_P G}{\hbar^2}\sqrt{1+\frac{U^2}{\gamma_2^2}}, & \lambda &= -2, \\ F &= \frac{2m_P}{\hbar^2}\left(\frac{U}{\gamma_2}\gamma_1 - \delta\right), & D &= \frac{m_p\gamma_1}{\hbar^2\chi_0^2}\left(1+\frac{U^2}{\gamma_2^2}\right), \end{aligned} \tag{5.20}$$

where χ_0^2 is the mean-field condensate density given by:

$$\chi_0^2 = \frac{-\gamma_1\gamma_2 - \delta U + \sqrt{G^2\left({\gamma_2}^2+U^2\right) - (\gamma_1 U - \gamma_2\delta)^2}}{{\gamma_2}^2+U^2}. \tag{5.21}$$

As already mentioned above, for negative detunings $\delta < 0$ or for strong incoherent pump $\gamma_1 < 0$, an additional stable solution may occur, giving rise to a bistable behavior. The phase diagram in Fig. 5.4 (a) illustrates the onset of bistability upon varying δ and G ($\gamma_1 > 0$ is assumed). In this thesis, however, we exclusively focused on the cases with $\delta > 0$ and $\gamma_1 > 0$.

The values in Eq. (5.20) can be used as starting point for the RG flow. To this end, it is neccessary to make g and F dimensionless by dividing them by an ultraviolet cutoff Λ^2. We set $\Lambda = 2\pi/a$ with $a = 0.5\mu$m, corresponding to the discretization used for the numerical solution of the complex Gross-Pitaevskii equation in Ref. [161]. This will provide a direct comparison for future numerical simulations of Eq. (5.7). Furthermore we assume the experiment to take place at resonance, thus setting $\delta = 0$. Next, we can compute the KPZ crossover scale L^*, at which the KPZ physics is expected to become visible. In Fig. 5.4 (b) we show the dependence of ℓ^* on the values of G for the different RG schemes (Eqs. (B.15) and (B.16)). The values of G are chosen to be larger than the threshold $G_c = \gamma_1 = 0.4$ meV for the existence of a mean-field solution. We observe that ℓ^* decreases upon increasing the pump strength, approaching the value $\ell^* \simeq 5$. We can accordingly compute the associated length scale as $L^* = \xi_0 e^{\ell^*}$, with $\xi_0 = \hbar/\sqrt{2m_P U\chi_0^2}$ the healing length, and compare it with a typical system size (determined by the pump spot size), i.e., $L = 50\mu$m [197]. We then find $L^*/L \approx 0.83$, indicating that the KPZ physics is expected to be visible in current experimental setups.

5.5 Summary

We showed that, in two-dimensional quadratically-driven Bose gases, the absence of thermal equilibrium can erase (quasi) long-range order and instead lead to an emerging phase where boson correlations are characterized by the KPZ scaling. In this chapter, we considered a gas of bosons subject to a *coherent* quadratic drive, which reduces the overall U(1) symmetry of the model down to $\mathbb{Z}_2$. Such a quadratic drive can result, e.g., from the coherent injection of two bosons into the system. Additionally, we considered dissipation by

including *incoherent* single- and two-body losses generated by the coupling to an environment. The dissipative losses are incorporated via Lindblad operators. A natural experimental platform described by this driven-dissipative model is given by exciton-polaritons in microcavities.

In thermodynamic equilibrium and in two spatial dimensions, the phase diagram of this system contains a symmetric BKT phase (characterized by quasi-long-range order) and a condensate phase (i.e., with long-range order). The latter is associated with the spontaneous breaking of the $\mathbb{Z}_2$ symmetry, with a critical point characterized by the Ising universality class. Out of equilibrium, we found that the condensate phase and the BKT phase are replaced by a disordered one (i.e., with short-range order) characterized by correlations displaying KPZ scaling. This can be understood as the nonequilibrium nature of fluctuations of the bosonic phase enhances their strength and makes them able to erase (quasi) long-range order. We showed this by mapping the master equation onto a Langevin equation. By deriving an effective action for the bosonic phase degree of freedom, we were able to analyze the character of this equation (the driven sine-Gordon equation) by a perturbative RG approach. However, it remains an open question whether the long-range order disappears completely, or only in the region of the phase diagram accessible by our perturbative approach (i.e., for small drives). The investigation of these regimes requires non-perturbative techniques, for which good candidates could be the functional renormalization group or numerical simulations.

Additionally, we discovered that the quadratic drive can be tuned to shrink the length scale at which the KPZ physics occurs. While KPZ physics dominates at long time and length scales, shorter scales can exhibit different types of correlations. So far, this prevented for instance the experimental observation of KPZ physics in two-dimensional U(1)-symmetric driven-dissipative exciton-polariton gases, as typical system sizes are too small to display KPZ scaling. It is therefore crucial to control and reduce the scale at which KPZ physics sets in. In this chapter, we showed that the presence of the quadratic drive substantially reduces the size of the KPZ scale. We used realistic experimental parameters to predict the KPZ length scale and showed that it can, in fact, become shorter than the system size.

These results demonstrate how the nonequilibrium nature of driven-dissipative systems can profoundly impact the properties of many-body systems. Specifically, despite sharing the same symmetry and dimensionality as their equilibrium counterparts, nonequilibrium systems can exhibit significantly distinct phase diagrams. In this regard, nonequilibriumness represents a novel parameter that can be finely adjusted to create materials with desirable new properties.

Chapter 6

Modification of Goldstone modes in long-range interacting quantum systems

This chapter is based on the following publication
O. K. Diessel, S. Diehl, N. Defenu, A. Rosch, and A. Chiocchetta , *Generalized Higgs mechanism in long-range interacting quantum systems*,

Phys. Rev. Res. **5**, 033038 (2023)

6.1 Introduction

Many-body systems with long-range interactions represent one of the most intriguing challenges in modern condensed matter, AMO and statistical physics. The long-range nature of the interactions dispense these systems from some of the fundamental paradigms of statistical physics. For instance, classical long-range interacting systems (LRIS), such as gravitational systems and non-neutral plasmas, enjoy unusual properties, such as non-additivity of the energy and non-ergodicity. The latter may, in turn, lead to a very slow (if not completely absent) thermalization dynamics [199–201]. Furthermore, the Mermin-Wagner theorem does not apply to LRIS, enabling them to exhibit spontaneous symmetry breaking even in low spatial dimensions [202]. Recently, the investigation of LRIS has gained new momentum from a flurry of experimental realizations of *quantum* long-range interacting systems (QLRIS), including Rydberg atoms [203], dipolar quantum gases [204], polar molecules [205], quantum gases coupled to optical cavities [144, 206], trapped ions [207], and dipolar magnets [208, 209]. This increasing amount of experimental data opens up new challenges to theoretically understand the corresponding many-body problem.

A great deal of information about a quantum system is typically encoded in its *low-energy properties*. Remarkably, while most existing theoretical studies involve the characterization of ground states and critical properties of QLRIS [210], little is known about their low-energy spectra. Notable exceptions include the nature of their point spectra [211], the existence of confinement [212], and of fractional excitations [213, 214]. Among these, it was pointed out that long-range interactions may cause the Goldstone modes to acquire a mass, thus violating the Goldstone theorem. Notable examples of this include a Bose gas with Coulomb interaction in 3+1 dimensions [215], a superconductor with Coulomb interactions in 3+1 dimensions [216], and the Schwinger model in 1+1 dimension (called in this context *seizing of the vacuum*) [217]. Even the celebrated Higgs mechanism appears to be a special case of this more general mechanism, as the gauge fields effectively mediate a long-range Coulomb interaction [218]. In this chapter, we will study the unexplored connection between the expanding field of QLRIS and the Higgs mechanism, the latter being at the center of increasing experimental attention, e.g., in strongly interacting Fermi superfluids [219], including pioneering studies of its few-body precursor [220, 221].

The textbook Higgs mechanism can be understood from two angles: On the one hand, in a gauge theory the Goldstone mode can be absorbed by a gauge transformation into the electromagnetic field which then obtains a mass by coupling to the condensate. On the other hand, the integration of the gapless electromagnetic field gives rise to long-range interactions, which also provide a mass for the Goldstone mode. Here, we uncover a new side to this second line of thought, by showing the occurrence of a *generalized Higgs mechanism* in QLRIS for different kinds of long-range interactions. We consider a number of experimentally-relevant models, including anti- and ferromagnetic spin models, and weakly interacting Bose gases, which exhibit spontaneous breaking of continuous symmetries, and analyze their low-energy excitation spectra for different spatial dimensions and general long-range interactions.

First, in Sec. 6.2, we consider the anisotropic antiferromagnetic Heisenberg model with long-ranged interactions. We study the low-energy excitations of the model using a spin-wave and a non-linear sigma model analysis. In Sec. 6.3, we then turn to the anisotropic ferromagnetic Heisenberg model which is again studied using a spin-wave analysis. In Sec. 6.4, we consider a gas of bosons with, first, long-range interactions, and, second, an interaction which is described by a Bessel function. The latter one is relevant for current experimental setups of Bose gases coupled to an optical cavity. Our first main result is to show that all of these models show three qualitatively different regimes exist depending on the interaction range: I. A regime where the Goldstone modes behave as in short-range models, II. A regime where the Goldstone dispersion is gapless but qualitatively different at low momenta, and III. A regime where the Goldstone modes are gapped. Our second main result is the characterization of the visibility of the generalized Higgs mechanism in current experiments with atomic gases in optical cavities: We demonstrate that, with realistic experimental parameters, the Bogoliubov dispersions are gapped and discrete, thus realizing the third regime.

6.2 Antiferromagnetic Heisenberg model

The anisotropic antiferromagnetic Heisenberg model on a square lattice with long-ranged interactions is given by

$$\hat{H} = \sum_{i \neq j} J_{ij} (\hat{S}_i^x \hat{S}_j^x + \hat{S}_i^y \hat{S}_j^y + \gamma \hat{S}_i^z \hat{S}_j^z), \tag{6.1}$$

where $\hat{S}_i^x, \hat{S}_i^y, \hat{S}_i^z$ are spin operators of length S residing at the $i-$th lattice site, $0 \leq \gamma \leq 1$ is the anisotropy coefficient, and $J_{ij} > 0$ is a long-range antiferromagnetic exchange, which we assume to be of the form $J_{ij} = |\mathbf{r}_{ij}|^{-\alpha}$. The parameter $\alpha > 0$ controls the range of the interaction and $\mathbf{r}_{ij} \equiv \mathbf{r}_i - \mathbf{r}_j$ is the relative distance between the i-th and j-th sites. Since J_{ij} couples all the spins antiferromagnetically, it acts similarly to a frustrating interaction [213]. We will focus on the case of semi-classical spins (i.e., with spin length $S \gg 1$), for which the spin-wave approximation and analyses based on the non-linear sigma model provide accurate results. The case for $S = 1/2$ was considered in Refs. [214] and [213] for the one- and two-dimensional case, respectively, and it was shown to lead to exotic phases including quantum spin liquids and valence-bond solids.

The classical (i.e., $S \to \infty$) ground state of Eq. (6.1) is a Néel state [213], which allows one to define two sublattices of opposing spin, but where the classical spin on each individual sublattice points along the same direction. In order to account for quantum fluctuations around this state, a Holstein-Primakoff transformation is used and the Hamiltonian is truncated at order $O(S)$ [222] (see Appendix C.1 for more details on the calculation). By diagonalizing the resulting Hamiltonian with a Bogoliubov transformation, one finds the

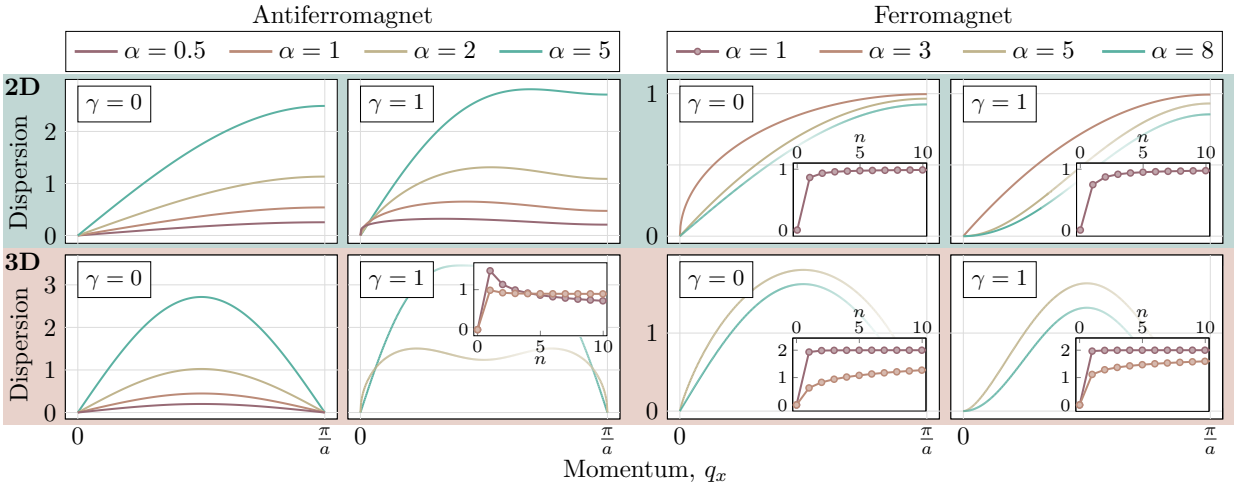

Figure 6.1: Two-dimensional (upper green row) and three-dimensional (lower red row) spin-wave spectrum $E_{\mathbf{q}}$ as a function of $\mathbf{q} = (q_x, 0)$ [$\mathbf{q} = (q_x, 0, 0)$] from Eq. (6.1) for an AFM (left) and FM (right) interaction. The insets show the rescaled discrete spectrum $E_{\mathbf{n}}$ as a function of the quantum number $\mathbf{n} = (n_x, 0)$ [$\mathbf{n} = (n_x, 0, 0)$]. The unrescaled dispersions which diverge with the system size are shown in Fig. 6.4 in Subsec. 6.2.2, where also the origin of the divergences is discussed . All results are obtained for linear system sizes $L = 800$.

spectrum of the low-energy excitations (i.e., spin waves) given by

$$E^{\pm}_{\mathbf{q}} = S\sqrt{(J^{\mathrm{d}}_0 \mp J^{\mathrm{d}}_{\mathbf{q}} - J^{\mathrm{s}}_0 + J^{\mathrm{s}}_{\mathbf{q}})[J^{\mathrm{d}}_0 - J^{\mathrm{s}}_0 + \gamma(J^{\mathrm{s}}_{\mathbf{q}} \pm J^{\mathrm{d}}_{\mathbf{q}})]}, \tag{6.2}$$

with $\mathbf{q}$ a quasi-momentum in the first Brillouin zone of the sublattice, and $J^{\mathrm{s}}_{\mathbf{q}} \equiv \sum_{\ell \in \text{same}} \mathrm{e}^{-i\mathbf{q}\cdot\mathbf{r}_\ell} J_\ell$ and $J^{\mathrm{d}}_{\mathbf{q}} \equiv \sum_{\ell \in \text{diff}} \mathrm{e}^{-i\mathbf{q}\cdot\mathbf{r}_\ell} J_\ell$, where the first (second) sum includes only vectors connecting sites on the same (different) sublattice. The dispersion $E^{+}_{\mathbf{q}}$ corresponds to the Goldstone excitation branch, while $E^{-}_{\mathbf{q}}$ corresponds to generally gapped excitations. $E^{+}_{\mathbf{q}}$ is shown in Fig. 6.1 in the left panel for different values of γ and α, and for different spatial dimensions. In the SU(2)-symmetric case ($\gamma = 1$), the two dispersions become degenerate and both gapless, as two Goldstone modes are expected for the spontaneous breaking of a SU(2) symmetry. We numerically evaluate the dispersions, and analyze the low-momenta behavior of the Goldstone branch by parametrizing the dispersion as $E^{+}_{\mathbf{q}} \approx A|\mathbf{q}|^s$, for $\mathbf{q} \to 0$, and use a fit to determine the value of s as a function of the exponent α in the Hamiltonian (6.1) (see Fig. 6.2). For nearest-neighbor interactions, one expects a linear spectrum [222], i.e., $s = 1$. A gapped dispersion, instead, would correspond to $s = 0$.

6.2.1 Non-linear sigma model

Before discussing the results, it is instructive to derive a fully analytical expression for $s(\alpha)$. To this end, we use the non-linear sigma model (NLSM), which is able to capture the low-energy behavior of an antiferromagnet. We represent a classical spin of length S as

$$\mathbf{S}_j/S = (-1)^j(1 - \mathbf{m}_j^2)^{1/2}\boldsymbol{\phi}_j + \mathbf{m}_j, \tag{6.3}$$

where $\boldsymbol{\phi}_j$ describes the antiferromagnetic order parameter associated with the Néel state and $\mathbf{m}_j$ is the so-called canting field. The canting field describes the quasi-homogeneous variations of the magnetization due to variations of $\boldsymbol{\phi}_j$. Both fields satisfy the conditions $\boldsymbol{m}_j \cdot \boldsymbol{\phi}_j = 0$ and $|\boldsymbol{\phi}_j|^2 = 1$, as a consequence of the spin-length conservation. Assuming the canting fluctuations to be small, i.e., $\mathbf{m}_j^2 \ll 1$, and by performing a spatial coarse-graining, the effective action of the Heisenberg model reads:

$$\mathcal{A}[\boldsymbol{\phi}, \mathbf{m}] = \int_{t,\mathbf{r}} \left[S\boldsymbol{m} \cdot (\dot{\boldsymbol{\phi}} \times \boldsymbol{\phi}) - S^2\mathcal{H}(\boldsymbol{\phi}, \mathbf{m})\right] \tag{6.4}$$

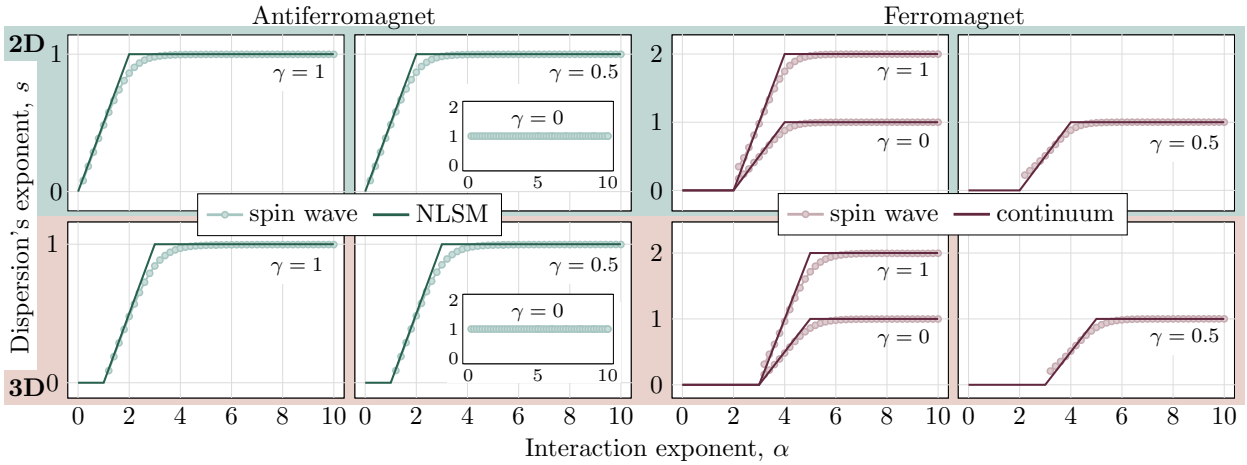

Figure 6.2: Low-momentum dispersion exponent s as a function of the interaction exponent α. Results for $d = 2$ are shown in the upper green row, for $d = 3$ in the lower red row, for an antiferromagnetic interaction on the left side (green curves), and for a ferromagnetic interaction on the right side (red curves). The dots are obtained by fitting the results of the spin-wave analysis via $E_{\mathbf{q}}^{(+)} \propto |\mathbf{q}|^s$, while the solid lines show the analytical results of the NLSM analysis/continuum-limit approximation. All results from the spin-wave analysis are obtained for linear system sizes $L = 800$.

with $\int_{t,\mathbf{r}} \equiv \int \mathrm{d}t\, \mathrm{d}^d r$, $\boldsymbol{\phi} = \boldsymbol{\phi}(t, \mathbf{r})$, $\mathbf{m} = \mathbf{m}(t, \mathbf{r})$, and $\mathcal{H}(\boldsymbol{\phi}, \mathbf{m})$ the coarse-grained Hamiltonian associated with Eq. (6.1). This Hamiltonian density can be obtained in the following way: after replacing the mapping (6.3) into Eq. (6.1), we retain only the quadratic terms and neglect higher order processes. This yields $H = S^2 \sum_{ij} \mathcal{H}_{ij}$, with

$$\mathcal{H}_{ij} \simeq J_{ij} \Big\{ \Big[(-1)^i \boldsymbol{\phi}_i + \mathbf{m}_i\Big]\Big[(-1)^j \boldsymbol{\phi}_j + \mathbf{m}_j\Big] + (\gamma - 1)\Big[(-1)^i \phi_i^z + m_i^z\Big]\Big[(-1)^j \phi_j^z + m_j^z\Big] - (-1)^{i+j} \mathbf{m}_i^2 \Big\} \tag{6.5}$$

where the last term arises from $\sqrt{1 - \mathbf{m}_i^2}\boldsymbol{\phi}_i \sqrt{1 - \mathbf{m}_j^2}\boldsymbol{\phi}_j \approx 1 - \mathbf{m}_i^2$ where we approximated $\boldsymbol{\phi}_i \approx \boldsymbol{\phi}_j$ and $\mathbf{m}_i \approx \mathbf{m}_j$, as they are slowly varying fields, and used the fact that $\boldsymbol{\phi}_i^2 = 1$. In order to derive the coarse-grained version of the previous Hamiltonian, it is convenient to analyze every term in momentum space, keeping in mind that $\boldsymbol{\phi}$ and $\mathbf{m}$ are slowly varying fields, i.e., their Fourier components are concentrated around $\mathbf{q} = 0$. Accordingly, the first term reads

$$\int_{\mathbf{q}} J_{\mathbf{q}+\mathbf{Q}} \, |\boldsymbol{\phi}_{\mathbf{q}}|^2 \simeq \int_{\mathbf{q}} \Big(a_0 + a_1 \mathbf{Q} \cdot \mathbf{q} + a_2 |\mathbf{q}|^2\Big) \, |\boldsymbol{\phi}_{\mathbf{q}}|^2, \tag{6.6}$$

with $\int_{\mathbf{q}} \equiv 1/(2\pi)^d \int \mathrm{d}^d q$, $\mathbf{Q} = (\pi, \cdots, \pi)$ and $|\boldsymbol{\phi}_{\mathbf{q}}|^2 = \boldsymbol{\phi}_{\mathbf{q}} \cdot \boldsymbol{\phi}_{-\mathbf{q}}$. The first term ($a_0$) gives rise to an inconsequential constant, due to the constraint $|\boldsymbol{\phi}_i|^2 = 1$, while the second one vanishes since the integrand is odd. Accordingly, the leading term in real space is given by $a_2 |\nabla \boldsymbol{\phi}|^2$, regardless of the form of J. A similar analysis can be done for the cross product in Eq. (6.5). The leading order vanishes because of the constraint, and the remaining terms are not relevant enough to contribute. Finally, the last term in Eq. (6.5) reads $\int_{\mathbf{q}} J_{\mathbf{q}} |m_{\mathbf{q}}|^2$, and therefore depends crucially on the form of J. Putting everything together, we thus obtain the following Hamiltonian:

$$H = \int_{\mathbf{r}} \Big\{ a_2 \, |\nabla \boldsymbol{\phi}|^2 + (\gamma - 1)\Big[a_0 + a_2 (\nabla \phi_z)^2 + J_{\mathbf{Q}} \mathbf{m}^2\Big] \Big\} + \int_{\mathbf{r}_1, \mathbf{r}_2} J_{\mathbf{r}_1 - \mathbf{r}_2} \Big[\mathbf{m}_{\mathbf{r}_1} \cdot \mathbf{m}_{\mathbf{r}_2} + (\gamma - 1) m_{z,\mathbf{r}_1} m_{z,\mathbf{r}_2}\Big], \tag{6.7}$$

with $J(\mathbf{r})$ the continuum version of J_{ij}. In order to analyze the spectrum of this effective theory, it is convenient to simplify the Berry-phase term in Eq. (6.4). This can be achieved by using the Ansatz $\boldsymbol{\phi}(\mathbf{r}) =$

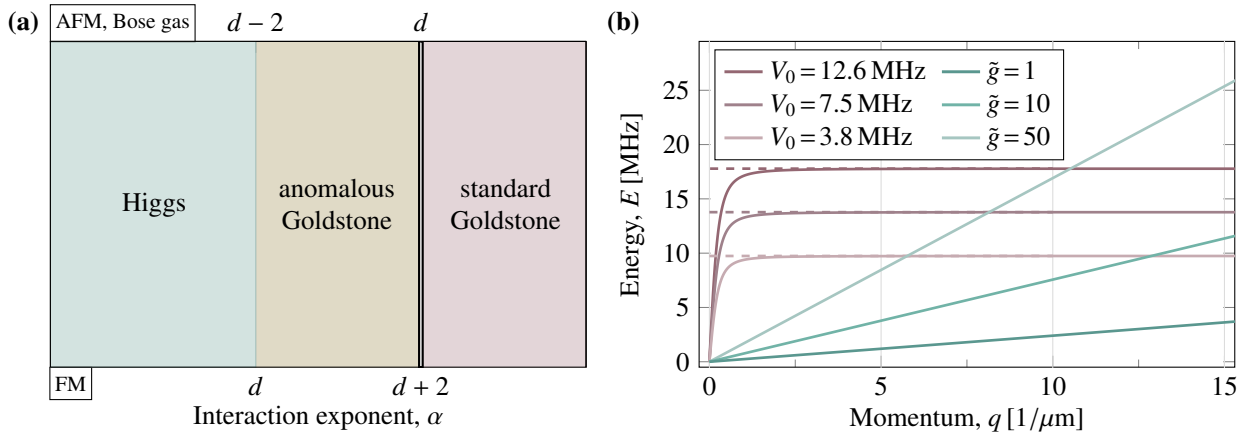

Figure 6.3: **(a)** Regimes for the long-range-interacting FM and AFM Heisenberg model (for $\gamma > 0$) and a Bose gas as a function of the interaction exponent α. The double vertical line represent the presence of logarithmic corrections (cf. Eqs. (6.10) and (6.18)). **(b)** Bogoliubov dispersions for a quasi-two dimensional rubidium gas, for different interaction potentials $V_{\mathbf{r}} = V_0 K_0(Q|\mathbf{r}|)$ (solid red curves), logarithmic interaction (dashed red curves), and contact interaction (solid green curves).

$\boldsymbol{\phi}_0 + \delta\boldsymbol{\phi}(\mathbf{r})$, with $\boldsymbol{\phi}_0 = \mathbf{e}_y$ the homogeneous order parameter and $\delta\boldsymbol{\phi}(\mathbf{r})$ the fluctuations around it. Since no finite homogeneous solution exists for the canting field, it only consists of small fluctuations, thus we define $\mathbf{m}(\mathbf{r}) = \delta\mathbf{m}(\mathbf{r})$. We thus retain only the quadratic terms of the Berry-phase term in Eq. (6.4), i.e., $\mathbf{m} \cdot (\dot{\boldsymbol{\phi}} \times \boldsymbol{\phi}) \simeq \delta m_z \delta\dot{\phi}_x - \delta m_x \delta\dot{\phi}_z$. Considering Eq. (6.7), we realize that δm_y and $\delta\phi_y$ decouple from the remaining degrees of freedom and therefore can be dropped in the following analysis. By defining the multiplet $\boldsymbol{\Psi}^T = (\delta\phi_x, \delta\phi_z, \delta m_x, \delta m_z)$, the final quadratic action reads $\mathcal{A}[\boldsymbol{\Psi}] = -S^2 \int_{\omega,\mathbf{q}} \boldsymbol{\Psi}^T(-\omega, -\mathbf{q}) A(\omega, \mathbf{q}) \boldsymbol{\Psi}(\omega, \mathbf{q})$, with the matrix $A(\omega, \mathbf{q})$ given by

$$A = \begin{pmatrix} a_2|\mathbf{q}|^2 & 0 & 0 & -i\frac{\omega}{2S} \\ 0 & a_0(1-\gamma)+\gamma a_2|\mathbf{q}|^2 & i\frac{\omega}{2S} & 0 \\ 0 & -i\frac{\omega}{2S} & J_{\mathbf{q}} + J_{\mathbf{Q}} & 0 \\ i\frac{\omega}{2S} & 0 & 0 & \gamma J_{\mathbf{q}} + J_{\mathbf{Q}} \end{pmatrix}. \tag{6.8}$$

The excitation spectrum $E_{\mathbf{q}}$ can finally be obtained by solving the equation $\det A(E_{\mathbf{q}}, \mathbf{q}) = 0$ leading to

$$E^+_{\mathbf{q}} = 2S\sqrt{a_2}|\mathbf{q}|\sqrt{J_{\mathbf{Q}} + \gamma J_{\mathbf{q}}}, \tag{6.9a}$$

$$E^-_{\mathbf{q}} = 2S\sqrt{(1-\gamma)a_0 + \gamma a_2|\mathbf{q}|^2}\sqrt{J_{\mathbf{Q}} + J_{\mathbf{q}}}, \tag{6.9b}$$

where $E^+_{\mathbf{q}}$ corresponds to the Goldstone branch. For $\gamma = 0$, a purely linear dispersion regardless of the interaction range is predicted. For $\gamma > 0$ and $\alpha > d - 2$, with d the spatial dimension, the low-momentum behavior of $E_{\mathbf{q}}$ reads

$$E_{\mathbf{q}} \approx \begin{cases} |\mathbf{q}| & \text{for } \alpha > d \\ |\mathbf{q}|\sqrt{\log|\mathbf{q}|} & \text{for } \alpha = d \\ |\mathbf{q}|^{\frac{2+\alpha-d}{2}} & \text{for } d-2 < \alpha < d. \end{cases} \tag{6.10}$$

For $\alpha \leq d-2$, $E_{\mathbf{q}}$ diverges with the system size and therefore a regularization is needed. This is achieved by rescaling the proper timescales for excitation propagation, in analogy with the well-known case of diverging ferromagnetic interactions [223, 224]. This procedure is outlined in the next subsection and reveals the discrete, gapped nature of the spectrum (see insets in Fig. 6.1). Once properly regularized, it becomes evident that the divergent dispersion relation characteristic of the third regime reduces to a pure point spectrum, similar to the one observed in strongly disordered systems. The resulting values of $s(\alpha)$ are in agreement with the values obtained from the spin-wave approximation, as shown in Fig. 6.2, with minor discrepancies

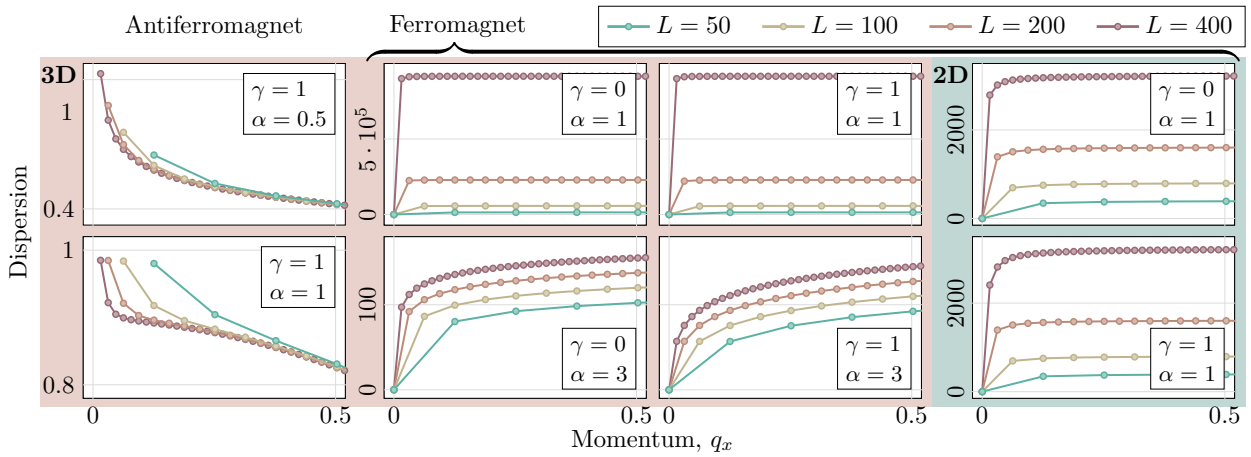

Figure 6.4: Unrescaled spin-wave dispersions for different linear system sizes L. Their rescaled form is shown in the insets of Fig. 6.1.

due to finite-size effects. Note that for $\alpha \leq d-2$ we did not fit the values of $s(\alpha)$, as the spectrum is discretized. Thus we arrive at the first main results of this chapter: three qualitatively different regimes exist for the Goldstone mode depending on the value of α.

I. The Goldstone mode is as in the short-range model.

II. The Goldstone mode is anomalous.

III. The Goldstone mode is gapped and discrete.

In particular, the last regime hosts the *generalized Higgs mechanism*: for sufficiently long-ranged interactions, the Goldstone spectrum is discrete and, in turn, becomes gapped. An instance of regime II. was found for a dipolar ($\alpha = 3$) antiferromagnet on a square lattice [225].

6.2.2 Regularization of super-extensive divergences

We now turn to a more detailed inspection of the origin of the divergence in the antiferromagnetic excitation spectrum in Eq. (6.9) and discuss its physical interpretation. Indeed, in analogy with the ferromagnetic case, the divergence of the long-range interacting contribution in the last term of Hamiltonian (6.7) causes the appearance of a super-extensive contribution to the system's internal energy. Super-extensive contributions to the energy refer to terms which scale as a power of the system size larger than one. This is easily seen, as the integral $J_{\mathbf{q}} = \int_{\mathbf{r}} J(\mathbf{r}) \mathrm{e}^{i\mathbf{q}\cdot\mathbf{r}}$ diverges with the system size for $\alpha \leq d$. Here, super-extensivity occurs since the long-range contribution of the canting field (second term on the r.h.s. of Eq. (6.7)) is convolved with the quadratic dispersion generated by the order parameter (first term on the r.h.s. of Eq. (6.7)).

Thus, for $\alpha \leq d-2$, the frequency of low-energy modes increases with the size of the system $E_{\mathbf{q}} \sim L^{(d-2-\alpha)/2}$ (see Fig. 6.4). Indeed, in many cases, long-range interactions are known to cause a scaling of the relevant time scales with system size [223]. In particular, for long-range quantum lattice models, the fastest time scale τ was found to shrink algebraically with an increasing system size N, i.e., $\tau \propto N^{-p}$, where p is a positive exponent. It follows that the excitations propagate increasingly fast as the thermodynamic limit is approached and hence, their velocity is not bounded by any finite quantity in the absolute time t.

Long-range interactions have the additional effect of rendering the spacing between the Hamiltonian low-energy eigenvalues (i.e., the quasi-particle spectrum) finite even in the thermodynamic limit. In other words,

the Hamiltonian spectrum remains point-like even for $L \to \infty$. To show this, we consider a d-dimensional system with periodic boundary conditions and finite linear size L. The momenta are then quantized according to $\mathbf{q} = \mathbf{n}2\pi/L$, with the d-dimensional vector $\mathbf{n} \equiv (n_1, \ldots, n_d)$ with n_i, $i = 1, \ldots, d$ integer numbers. The interaction also obeys periodic boundary conditions as $J(\mathbf{r}) = d(\mathbf{r}/L)^{-1}(\pi/L)^{\alpha}$, where

$$d(\mathbf{r}/L) = \left[\sum_{i=1}^{d} \sin\left(\frac{\pi x_i}{L}\right)^2\right]^{\frac{\alpha}{2}}, \tag{6.11}$$

with $\mathbf{r} = (x_1, \ldots, x_d)$ the d-dimensional spatial vector. The Fourier transform of $J(\mathbf{r})$ can the be written as $J(\mathbf{q}) = L^{d-\alpha}\pi^{\alpha}\int_{\bar{\mathbf{r}}}[\mathrm{e}^{i2\pi\mathbf{n}\cdot\bar{\mathbf{r}}}/d(\bar{\mathbf{r}})]$, with $\int_{\bar{\mathbf{r}}} \equiv \int_0^1 \mathrm{d}\bar{x}_1 \ldots \mathrm{d}\bar{x}_d$, upon the substitution $\mathbf{r} = L\bar{\mathbf{r}}$ in the integral. From the dispersion $E_{\mathbf{q}} = |\mathbf{q}|\sqrt{J_{\mathbf{q}}}$ one then finds

$$E_{\mathbf{n}} = L^{\frac{d-\alpha-2}{2}} 2\pi^{\frac{2+\alpha}{2}} |\mathbf{n}| \sqrt{\int_{\bar{\mathbf{r}}} \frac{\mathrm{e}^{i2\pi\mathbf{n}\cdot\bar{\mathbf{r}}}}{d(\bar{\mathbf{r}})}} \equiv L^{\frac{d-\alpha-2}{2}} \epsilon_{\mathbf{n}}, \tag{6.12}$$

where $\epsilon_{\mathbf{n}}$ is a regular, L-independent function of the quantum number $\mathbf{n}$. We then define the spectral spacing as $\Delta_{\mathbf{n}} \equiv E_{\mathbf{n}+\mathbf{e}} - E_{\mathbf{n}}$, with $\mathbf{e}$ a unit vector in an arbitrary direction. It then follows that $\Delta_{\mathbf{n}} \propto L^{\frac{d-\alpha-2}{2}}$, entailing that in the thermodynamic limit $L \to \infty$:

$$\begin{cases} \Delta_{\mathbf{n}} \to 0 & \text{for } \alpha > d-2, \\ \Delta_{\mathbf{n}} \to \text{const.} & \text{for } \alpha = d-2, \\ \Delta_{\mathbf{n}} \to \infty & \text{for } \alpha < d-2. \end{cases} \tag{6.13}$$

It then follows that while for $\alpha > d - s$ the spectrum becomes continuous, for $\alpha \leq d-2$ it remains discrete. The diverging character of $\Delta_{\mathbf{n}}$, related to the energy super-extensivity mentioned above, will be regularized by the rescaling discussed in the following.

In analogy with several studies of excitation propagation and dynamics in quantum long-range systems [224, 226], we will introduce the rescaled time $t' = tL^p$ and the corresponding rescaled frequencies $\omega' L^{-p}$ in order to obtain a finite dispersion relation in the thermodynamic limit.

In the new variables the coupling matrix reads

$$A = \begin{pmatrix} a_2|\mathbf{q}|^2 & 0 & 0 & -i\frac{\omega' L^p}{2S} \\ 0 & a_0(1-\gamma)+\gamma a_2|\mathbf{q}|^2 & i\frac{\omega' L^p}{2S} & 0 \\ 0 & -i\frac{\omega' L^p}{2S} & J_{\mathbf{q}} + J_{\mathbf{Q}} & 0 \\ i\frac{\omega' L^p}{2S} & 0 & 0 & \gamma J_{\mathbf{q}} + J_{\mathbf{Q}} \end{pmatrix} \tag{6.14}$$

yielding the rescaled Goldstone dispersion relation

$$E^{+}_{\mathbf{q}} \propto \frac{|\mathbf{q}|}{L^p}\sqrt{J_{\mathbf{Q}} + \gamma J_{\mathbf{q}}}. \tag{6.15}$$

The latter result remains finite for all α as long as we impose

$$p = \begin{cases} 0 \text{ if } \alpha \geq d-2, \\ \frac{d-2-\alpha}{2} \text{ if } \alpha < d-2, \end{cases} \tag{6.16}$$

which extends the conventional Kac scaling procedure to the antiferromagnetic regime. By applying this rescaling to Eq. (6.12), one sees that the spectrum for $\alpha \leq d-2$ remains discrete in the thermodynamic limit and it is given by $\epsilon_{\mathbf{n}}$. In contrast, for $\alpha > d-2$, the spectrum is continuous in the thermodynamic limit and can be expressed in terms of continuous momenta $\mathbf{q}$.

As a result of the "antiferromagnetic" Kac rescaling, the excitation spectrum of the system remains gapped in the entire regime $\alpha < d-2$ as in the marginal case $\alpha = d-2$. The entire spectrum becomes discrete in the new variables and the system will develop all the typical out of equilibrium features of strong long-range systems, such as quasi-stationary-states [211, 224, 227], and loss of adiabaticity [228], to name but a few [210].

6.3 Ferromagnetic Heisenberg model

As a next example we study an anisotropic ferromagnetic Heisenberg model on a square lattice, which takes the same form as Eq. (6.1), with long-ranged interactions $J_{ij} = -|\mathbf{r}_{ij}|^{-\alpha}$. The ground state of this model is an ordinary ferromagnet and the low-energy excitations can again be derived using the spin-wave analysis. The Holstein-Primakoff transformation leads to the spin-wave spectrum

$$E_{\mathbf{q}} = S\sqrt{(J_0 - J_{\mathbf{q}})(J_0 - \gamma J_{\mathbf{q}})} \tag{6.17}$$

where $J_{\mathbf{q}} \equiv \sum_\ell \mathrm{e}^{-i\mathbf{q}\cdot\mathbf{r}_\ell} J_\ell$. The low-momentum behavior of $E_{\mathbf{q}}$ can be easily derived analytically by approximating the long-range interaction as $J_{\mathbf{q}} \approx \int_{|\mathbf{r}|>a} \mathrm{d}^d\mathbf{r}|\mathbf{r}|^{-\alpha}\mathrm{e}^{-i\mathbf{q}\cdot\mathbf{r}}$, with a the lattice spacing, and for $\alpha > d$ it is given by

$$E_{\mathbf{q}} \approx \begin{cases} |\mathbf{q}|^{2x_\gamma} & \text{for } \alpha > d+2 \\ (|\mathbf{q}|^2 \log|\mathbf{q}|)^{x_\gamma} & \text{for } \alpha = d+2 \\ |\mathbf{q}|^{(\alpha-d)x_\gamma} & \text{for } d < \alpha < d+2 \end{cases} \tag{6.18}$$

with $x_\gamma = 1$ for $\gamma = 1$ and $x_\gamma = 1/2$ for $\gamma < 1$. For $\alpha \leq d$, the dispersion diverges with the system size and a regularization is therefore added, as in the case of AFM. The dispersions $E_{\mathbf{q}}$ for different values of α, γ, and spatial dimensions are also shown in the right side panel of Fig. 6.1.

In Fig. 6.2 we compare the curves $s(\alpha)$ to the fit obtained by the lattice evaluation of the spin-wave dispersion, showing good agreement. As in the AFM case, the results again demonstrate the existence of the same three different regimes for $s(\alpha)$ (cf. Fig. 6.2). However, in contrast to the AFM case, the result is sensitive to the symmetry of the model, namely for the SU(2) ($\gamma = 1$) and the U(1) ($\gamma < 1$) cases. While for both cases the regimes boundaries are the same, the values of the exponents change. Instances of regime II were found in several FM models: a ferromagnetic XXZ chain [229] ($d = 1, \gamma < 1, \alpha > 1$), a ferromagnetic U(1)-symmetric spin system with dipolar interactions on a square lattice [225, 230] ($d = 2$, $\gamma < 1$, $\alpha = 3$), and a ferromagnetic SU(2)-symmetric spin system [231] (d generic,$\gamma = 1$, $\alpha > d$).

It is worth noting that both FM (with $\gamma < 1$) and AFM interactions yield the same scaling $s(\alpha)$, but in a different range of the interaction exponent α, such that $s_{\mathrm{FM}}(\alpha) = s_{\mathrm{AFM}}(\alpha - 2)$ (see Fig. 6.3). The same correspondence has been observed between the critical exponents of ferromagnetic rotor models and antiferromagnetic spin Hamiltonians [232], and we conjecture it to constitute a generic feature of long-range interactions.

6.4 Interacting Bose gas

The results shown above apply in a similar fashion to the case of a condensed Bose gas with long-range interactions. This was first studied in the context of a charged Bose gas, where the particles interact via a Coulomb potential. There, it was shown that the Bogoliubov spectrum is gapped in three dimensions [215]. We consider in the following a generalization of this model, relevant for ongoing experiments with cold-atoms in a cavity [233]. We assume the Hamiltonian of the gas to be given by

$$H = \int_{\mathbf{r}} \left(-\psi^\dagger_{\mathbf{r}} \frac{\nabla^2}{2m} \psi_{\mathbf{r}} + \frac{1}{2} \int_{\mathbf{r}'} V_{\mathbf{r}'-\mathbf{r}} \psi^\dagger_{\mathbf{r}} \psi^\dagger_{\mathbf{r}'} \psi_{\mathbf{r}'} \psi_{\mathbf{r}} \right), \tag{6.19}$$

with a long-ranged interaction $V_{\mathbf{r}} = V_0|\mathbf{r}|^{-\alpha}$. According to Bogoliubov's theory, the bosonic field can be decomposed into a homogeneous condensate and fluctuations around it, i.e., $\psi_{\mathbf{r}} = \psi_0 + \bar{\psi}_{\mathbf{r}}$. By replacing it in the Hamiltonian, retaining terms up to quadratic order in the fluctuations, and finally diagonalizing via a Bogoliubov transformation, one obtains

$$E_{\mathbf{q}} = \sqrt{\epsilon_{\mathbf{q}}(\epsilon_{\mathbf{q}} + 2n_0 V_{\mathbf{q}})} \tag{6.20}$$

with $\epsilon_{\mathbf{q}} = \hbar^2|\mathbf{q}|^2/2m$ the free particle dispersion, $n_0 = |\psi_0|^2$ the condensate density, and $V_{\mathbf{q}}$ the Fourier transform of the interaction potential. The chemical potential is set to $\mu = n_0 V_{\mathbf{q}=0}$ for thermodynamical stability. By expanding $E_{\mathbf{q}}$ at low momenta, we find the function $s(\alpha)$, given in Fig. 6.3 (a), which is the same as for the case of the AFM Heisenberg model with $\gamma > 0$. Correspondingly, the same three regimes can be recognized, depending on their value of α.

6.4.1 Possible observation in ultracold quantum gases

In order to connect our findings to concrete experimental implementation we now turn to the following simplified model, inspired by the experimental setup of Ref. [233], consisting of a quasi-two-dimensional gas of bosonic ^{87}Rb atoms enclosed in a multimode cavity. The atomic interaction mediated by the cavity modes has the form (far from the trap boundaries) $V_{\mathbf{r}} = V_0 K_0(Q|\mathbf{r}|)$ where V_0 can be varied upon tuning the pump Rabi frequency and $Q \simeq 0.29\mu\text{m}^{-1}$ depends on the number of modes coupled to the atoms via the cavity, and on the cavity mode waist. The modified Bessel function $K_0(x)$ falls off exponentially for $x \gg 1$, while $K_0(x) \approx -\log x$ for $x \ll 1$. Accordingly, we expect the deviation from linearity and the consequent gapping of the Bogoliubov dispersion to be visible for momenta $|\mathbf{q}| > Q$. The corresponding Bogoliubov dispersion reads

$$E_{\mathbf{q}} = \sqrt{\epsilon_{\mathbf{q}}\left(\epsilon_{\mathbf{q}} + 2n_0 V_0/(|\mathbf{q}|^2 + Q^2)\right)}, \tag{6.21}$$

which shows a plateau for $|\mathbf{q}| > Q$, corresponding to the gap one would have in the pure long-range case with $Q = 0$. In order to better understand the possible observation of this effect in said experimental platform, we report in Fig. 6.3 (b) the dispersions $E_{\mathbf{q}}$ for experimental values of $n_0 = 5.5 \times 10^3(\mu\text{m})^{-2}$ and $m = 87m_p$ (with m_p the proton mass), for different values of V_0 (solid red lines), and compare them with the corresponding dispersions with $Q = 0$ (dashed red lines). The dispersions with finite Q substantially overlap with the gapped ones with $Q = 0$. To emphasize the difference to the dispersion for usual contact interactions, we additionally plot the Bogoliubov dispersion for $V(\mathbf{r}) = \tilde{g}(\hbar^2/2m)\delta^{(2)}(\mathbf{r})$, with different values of the dimensionless parameter $\tilde{g}$ (solid green lines). The difference to the dispersions for the long-range interacting model is evident for the range of parameters used. This shows that the generalized Higgs mechanism can be observed in current experimental setups. For a quantum gas in a cavity, the excitations can be probed, e.g., using Bragg spectroscopy [234].

6.5 Summary

We showed that, for a number of experimentally-relevant quantum many-body systems, Goldstone modes can be strongly affected by the presence of long-range interactions. In fact, in comparison to short-range interacting systems, the Goldstone dispersion can be distorted (i.e., it is described at momenta by a power law

with an exponent different from the one characterizing the short-range dispersion) or, even more remarkably, be gapped, in what can be regarded as a generalized Higgs mechanism (as no dynamical gauge field is involved in the mechanism).

We showed that this mechanism takes place in ferro- and antiferromagnetic spin systems, by using both spin-wave and non-linear sigm a model approximations (valid in the large-spin limit) and in cold atomic gases by using the Bogoliubov approximation.

In the latter case, we also showed that the effect can be detected in current experiments with ultracold atomic gases in an optical cavity. Our results open intriguing perspectives for the engineering of quantum materials. For example, an experimentally tunable interaction range would enable the switching between gapped und gapless spectra, resulting in very different thermodynamical properties.

Concluding remarks and outlook

In this thesis, we explored two different topics within the realm of quantum many-body systems: In the first part of the thesis, we delved into the physics of mobile quantum impurities, known as polarons, and investigated the implications of moving beyond the single impurity limit to finite impurity density. In the second part of the thesis, the interest was centered around phase transitions and the emergence of phenomena in light-matter systems.

In Chap. 1, our main focus was on the theoretical description of impurity Raman injection and ejection spectroscopy in ultracold Fermi gases. In contrast to standard rf spectroscopy, when relying on Raman transitions based on optical excitation pathways, a finite momentum transfer is possible during the transition. In a theory-experiment collaboration, we investigated the polaron-to-molaron transition at finite temperature and impurity density using Raman ejection spectroscopy. We interpreted the experimental data employing a quasiparticle theory in which the many-body Hilbert space of impurity particles is spanned by single-particle states obtained from variational wavefunctions. To incorporate the effects of finite impurity density and finite temperature in the calculations of the Raman ejection spectra, we considered the thermal population of polaron and molaron states based on their quantum statistics. Our findings indicate that close to the interaction strength at which the polaron-to-molaron transition occurs in the single impurity limit, both polarons and molarons coexist, provided that the molarons are not condensed.

At lower temperatures (below the critical temperature of molaron condensation), the phase diagram is not yet fully understood. On the one hand, at zero temperature, the polaron-to-molaron transition marks the endpoint of a fermionic polaron phase, where its Fermi surface volume vanishes, and a polarized superfluid phase consisting of molecules is expected to take over. On the other hand, considering the strong atom-dimer interactions near the transition point, the system might become unstable resulting in phase separation between the superfluid and normal phases. To gain further insights into the phase diagram of imbalanced Fermi-Fermi mixtures, Raman spectroscopy, performed at lower temperatures and in homogeneous traps, might help in determining, for instance, the transition temperature for phase separation. Furthermore, away from the transition point a plethora of phases has been discussed in the literature, ranging from p-wave pairing of polarons to the FFLO phase [10, 61, 84, 85]. While accounting for correlation effects such as polaron–polaron, polaron–molaron, and molaron–molaron would be necessary to describe, e.g., an instability of a Fermi polaron gas towards p-wave superfluidity or the FFLO phase, their accurate inclusion presents a considerable theoretical challenge.

In Sec. 1.3, we showed how the existence of an FFLO phase can already be inferred from the single impurity limit, from the finite momentum properties of the molaron. In fact, the finite momentum minimum visible in the molaron dispersion (in the region where the molaron in the excited state of the system) may be regarded as a precursor of the long-sought-after FFLO phase in the imbalanced BEC-BCS crossover, which emerges due to the macroscopic occupation of such molaron states at finite momentum. In Sec. 1.3, we furthermore proposed a new spectroscopic protocol based on Raman transitions to probe the momentum-resolved spectral function of molarons in ultracold atoms. Our proposed molecular injection spectroscopy technique allows to detect the above-discussed precursor of the FFLO phase. Moreover, in combination with standard injection spectroscopy, it also allows for the first time the simultaneous observation of both polaron and molaron branches at the same interaction strength, thus providing an experimental tool to prove their coexistence and their first-order transition.

The spectroscopic protocol is not limited to Fermi polarons but can be applied to Bose polarons as well. In this case, the resulting molaron is fermionic. A Bose polaron system would therefore hold potential for studying topologically non-trivial Fermi surfaces, Fermi surface reconstruction, and many-body bound states involving multiple bath atoms, as well as emerging phases in mass-imbalanced ultracold gases.

In Chap. 2, we then turned to the description of interactions arising between multiple impurities. Here, we focused on Bose polarons and their experimental realization in atomically thin semiconductors coupled to an optical cavity. In a theory-experiment collaboration, we investigated the polaron-polaron interactions mediated by the bosonic medium. Using variational wave function Ansätze for single and two polaron states and a non-hermitian Hamiltonian, we were able to show how the repulsive interactions between bare impurity particles can be turned into attractive ones through the dressing of the bath. Our findings thus suggest that the observation of pairing between polarons may be within reach in two-dimensional materials.

In the second part of the thesis, we focused on collective behaviors arising in light-matter interacting systems. Here we specifically looked at driven-dissipative and long-range interacting systems. Such systems can differ qualitatively from their short ranged and equilibrium counterparts as they can escape some paradigms of condensed matter physics, such as the Mermin-Wagner and the Goldstone theorem.

In Chap. 5, we considered a gas of quadratically driven-dissipative bosons whose experimental realizations include exciton-polaritons. We discussed a novel incarnation of the Kardar-Parisi-Zhang (KPZ) phase in these systems, which represents one of the most paradigmatic examples of nonequilibrium universality. Using nonequilibrium field theory and renormalization group methods, we showed that in two dimensions, a phase described by KPZ scaling emerges on experimentally accessible length scales. This KPZ phase replaces the Ising phase expected for equilibrium gases, providing a novel example of how nonequilibrium fluctuations might dramatically modify equilibrium behavior. These results demonstrate how the nonequilibrium nature of driven-dissipative systems can profoundly impact the properties of many-body systems. Specifically, despite sharing the same symmetry and dimensionality as their equilibrium counterparts, nonequilibrium systems can exhibit significantly distinct phase diagrams. In this regard, nonequilibriumness represents a novel parameter that can be finely adjusted to create materials with desirable new properties. An open question remains, however, of whether the Ising phase is erased entirely even in the regime where the interactions are strongly non-perturbative. This regime could be studied, e.g., by analyzing the Keldysh action in the non-perturbative regime using a functional RG approach, which proved useful in studying the renormalization of non-perturbative field theories.

In Chap. 6, we investigated the low-energy excitation spectrum of antiferromagnetic and ferromagnetic spin systems and Bose gases with long-range order. Using spin-wave theory and a non-linear sigma model analysis, we studied the behavior of the Goldstone modes, resulting from a spontaneous breaking of U(1) and SU(2) symmetries, as a function of the interaction range. Instead of the expected gapless Goldstone modes, we found three qualitatively different regimes: In the first regime, the Goldstone modes are gapped, realizing a generalized Higgs mechanism. In the remaining two regimes the Goldstone modes are still gapless but with an anomalous algebraic dispersion or with the usual one for short-range interacting systems. We furthermore demonstrated the visibility of this mechanism in current experiments of atomic gases in optical cavities. Our results open intriguing perspectives for the engineering of quantum materials. For example, an experimentally tunable interaction range would enable the switching between gapped und gapless spectra, resulting in very different thermodynamical properties.

Both, long-range interactions and nonequilibriumness qualitatively modify the physics compared to their short-range interacting and equilibrium counterparts: In particular, while nonequilibriumness was shown to increase the strength of the fluctuations (compared to equilibrium), therefore impeding long-range order, long-range interactions typically suppress fluctuations, thus favoring long-range order. In this respect, the nonequilibriumness and the long-range interactions can be considered as competing effects with respect to the occurrence of long-range order. This could non-trivially affect the phase diagram of these systems compared to their equilibrium counterparts, as well as induce novel instances of nonequilibrium criticality, shining new light on the physics of hybrid light-matter quantum systems, as well as on the theory of nonequilibrium universality.

Part III

Appendix

Appendix A

Impurity spectroscopy in ultracold quantum gases

A.1 Many-body Raman spectrum of the polaron

In this appendix, we provide some details on the calculation of the many-body Raman response of the polaron given in Eq. (1.22). We focus here on the incoherent contribution, as this is the numerically most challenging one. The incoherent polaron many-body Raman spectrum is given by

$$\bar{\mathcal{A}}_{\rm inc}(\omega) = -\frac{1}{\pi}\frac{1}{N_I}\sum_{\mathbf{p}}{\sum_{\mathbf{k},\mathbf{q}}}' |\alpha^{\mathbf{p}}_{\mathbf{k},\mathbf{q}}|^2 {\rm Im}\left(\frac{1}{\omega - \varepsilon_{\mathbf{p}+\bar{\mathbf{q}}+\mathbf{q}-\mathbf{k}} - \varepsilon_{\mathbf{k}} + \varepsilon_{\mathbf{q}} + \epsilon_{\rm pol}(\mathbf{p}) + i0^+}\right)\cdot n_F[\epsilon_{\rm pol}(\mathbf{p})] \quad \text{(A.1)}$$

where we have used the identity $\lim_{z\to 0^+} 1/(x+iz) = -i\pi\delta(x) + \mathcal{P}(1/x)$ to replace the δ-function in Eq. (1.23). The variational parameters can be obtained from minimizing the energy functional $\langle\psi^{\mathbf{p}}_P|\mathcal{H} - E|\psi^{\mathbf{p}}_P\rangle$, and are given by:

$$|\alpha^{\mathbf{p}}_{\mathbf{k},\mathbf{q}}|^2 = |\alpha^{\mathbf{p}}_0|^2 \frac{1}{y(\mathbf{k},\mathbf{q},\mathbf{p})^2}\left(\frac{1}{V}\right)^2\left(\frac{1}{\frac{1}{U}+\frac{1}{V}\sum'_{\mathbf{k}'}\frac{1}{y(\mathbf{k}',\mathbf{q},\mathbf{p})}}\right)^2, \quad \text{(A.2)}$$

with

$$|\alpha^{\mathbf{p}}_0|^2 = \left[1 + \frac{1}{V^2}\sum_{\mathbf{kq}}\frac{1}{y(\mathbf{k},\mathbf{q},\mathbf{p})^2}\left(\frac{1}{\frac{1}{U}+\frac{1}{V}\sum'_{\mathbf{k}'}\frac{1}{y(\mathbf{k}',\mathbf{q},\mathbf{p})}}\right)^2\right]^{-1} \quad \text{(A.3)}$$

the momentum dependant $Z_{\mathbf{p}}$ factor and the short-hand notation $y(\mathbf{k},\mathbf{q},\mathbf{p}) = \varepsilon_{\mathbf{k}} - \varepsilon_{\mathbf{q}} + \varepsilon_{\mathbf{p}+\mathbf{q}-\mathbf{k}} - \omega$. The contact interaction U is related to the s-wave scattering length via $U^{-1} = m/4\pi a - V^{-1}\sum_{\mathbf{k}} 1/2\varepsilon_{\mathbf{k}}$. To evaluate the sums, we go to the continuum limit by replacing $V^{-1}\sum_{\mathbf{k}}(...) \to (2\pi)^{-3}\int d^3\mathbf{k}(...)$.

We note that in Eq. (A.1), there are, in total, nine integrations $(p, \varphi_p, \theta_p, k, \varphi_k, \theta_k, q, \varphi_q, \theta_q)$ over the whole expression, and three integrations within Eq. (A.2). To evaluate the whole expression, we first compute the Raman spectra for single impurities at discrete momenta $\mathbf{p}$. We interpolate the result to obtain a function $\mathcal{A}(\omega,\mathbf{p})$ and use the interpolated result to simplify the final integration over momenta $\mathbf{p}$.

To compute the single-impurity Raman spectra, we first note that a fuction for the momentum dependant Z factor can be obtained by evaluating Eq. (A.3) separately for discrete momenta and use an interpolation of the resulting table. Here, (and in Eq. (A.2)) the integral in the denominator, i.e. $(2\pi)^{-3}[\int_{k_F}^{\infty} d^3\mathbf{k}'\, 1/y(\mathbf{k}',\mathbf{q},\mathbf{p}) - \int_0^{\infty} d^3\mathbf{k}\, 1/2\varepsilon_{\mathbf{k}}]$, can even be evaluated analytically (we used the simplified notation $\int_{k_F}^{\infty} d^3\mathbf{k}'(...) = \int_{k_F}^{\infty} dk' \int_0^{2\pi} d\varphi_{k'} \int_0^{\pi} d\theta_{k'}\, k'^2 \sin(\theta_{k'})(...)$). To this end, we extend the integration range of the first integral to unrestricted momenta $\mathbf{k}'$ and write

$$\int_{k_F}^{\infty} d^3\mathbf{k}' \frac{1}{y(\mathbf{k}',\mathbf{q},\mathbf{p})} = \int_0^{\infty} d^3\mathbf{k}' \frac{1}{y(\mathbf{k}',\mathbf{q},\mathbf{p})} - \int_0^{k_F} d^3\mathbf{q}' \frac{1}{y(\mathbf{q}',\mathbf{q},\mathbf{p})}. \quad \text{(A.4)}$$

In the unrestricted integral, we can perform the shift $\mathbf{k}' \to \mathbf{k}' + (\mathbf{p}' + \mathbf{q})/2$. In that way, the integration over $\varphi_{k'}$ becomes trivial and both integrals on the right hand side of Eq. (A.4) can be evaluated analytically.

The trick of shifting integration variables and thereby simplifying the calculation can not be applied to the integrations over momenta $\mathbf{p}, \mathbf{k}, \mathbf{q}$ in Eq. (A.1), as here we have the momenta occurring in two combinations: $\sim (\mathbf{p} + \bar{\mathbf{q}} + \mathbf{q} - \mathbf{k})^2$ and $\sim (\mathbf{p} + \mathbf{q} - \mathbf{k})^2$. We therefore first evaluate the integrals over $k, \varphi_k, \theta_k, q, \varphi_q, \theta_q$ numerically for discrete values of p and θ_p, namely $p \in [0, p_{\text{max}}/40, ..., p_{\text{max}}]$ and $\theta_p \in [0, \pi/40, ..., \pi)$, where the value p_{max} is determined by the condition that up to this momentum we find an infinitly long lived polaron. The integration over φ_p can be made trivial by shifting φ_q and φ_k. The resulting tables for the single-impurity Raman ejection spectra at discrete momenta can be interpolated to simplify the final integration over p and θ_p, which now can be easily performed numerically.

A.2 Raman transition rate of the coherent polaron contribution in the LDA

In this appendix we provide more detail on the derivation of the Raman rate for the coherent polaron contribution under the LDA.

Eq. (1.29) gives the rate for a homogeneous system. Here, we treat the case of a harmonically trapped gas. The occupation averaged coherent response is given by

$$\bar{\Gamma}_{\text{coh}}(\omega) = \frac{2\pi\Omega_e^2}{V} \int \mathrm{d}^3\mathbf{r} \sum_{\mathbf{k}} \mathcal{A}_{\text{coh}}(\omega, \mathbf{k}) \times n_F \left[\epsilon_{\text{pol}}(\mathbf{k}) - \mu + \frac{m}{2}\omega_{\text{ho}}^2 \left(1 - \frac{\epsilon_{\text{pol}}^0}{\varepsilon_F}\right) \mathbf{r}^2, T_p \right] , \tag{A.5}$$

where $\mathcal{A}_{\text{coh}}(\omega, \mathbf{k})$ is given in Eq. (1.27), and $\omega_{\text{ho}} = \epsilon_F/(6N)^{1/3}$ denotes the geometrically-averaged harmonic trapping frequency. In cylindrical coordinates the integral over $\mathbf{k}$ within Eq. (A.5) decomposes into a two-dimensional integral of $\mathbf{k}_\perp$ over directions perpendicular to $\bar{\mathbf{q}}$, and an integral over $k_{\bar{q}}$ along the direction of $\bar{\mathbf{q}}$. The condition imposed by the δ-function within $\mathcal{A}_{\text{coh}}$ is then given by

$$\frac{k_{\bar{q}}^2 + k_\perp^2}{2}\left(\frac{1}{m} - \frac{1}{m^*}\right) + \frac{k_{\bar{q}}\bar{q}}{m} - \omega - \epsilon_{\text{pol}}^0 + \frac{\bar{q}^2}{2m} = 0 , \tag{A.6}$$

and can be solved for $k_{\bar{q}}$.

At low temperatures and for most interaction strengths, we find that $k\,(1 - m/m^*) \ll \bar{q}$ for momenta which are not suppressed by the Fermi distribution. We thus neglect the first term proportional to $(1 - m/m^*)$ in Eq. (A.6) when evaluating the δ-function in Eq. (A.5). Carrying out the integrations in Eq. (A.5) we then obtain that

$$\bar{\Gamma}_{\text{coh}}(\omega) = 2\pi m \Omega_e^2 N_{\text{coh}}\, n_{\text{P}}\left[k_{\bar{q}}(\omega)\right]/\,\bar{q} , \tag{A.7}$$

where $n_P[k]$ is given in Eq. (1.33) and $k_{\bar{q}}(\omega)$ is given in Eq. (1.31). Correspondingly, the fugacity $\zeta_{\text{P}} = e^{-\left(\epsilon_{\text{pol}}^0 - \mu\right)/T_p}$ within Eq. (1.33) is set by the normalization $\int \mathrm{d}\omega \bar{\Gamma}_{\text{coh}}(\omega) = 2\pi\Omega_e^2 N_{\text{coh}}$, which gives

$$\text{Li}_3(-\zeta_2) = -\frac{x\bar{Z}}{6}\left[\frac{\varepsilon_F\left(\varepsilon_F - \epsilon_{\text{pol}}^0\right)}{\frac{m^*}{m}T_p^2}\right]^{3/2} . \tag{A.8}$$

A.3 Validation of the fitting model

In this appendix we discuss the applicability of our fitting model, i.e., Eqs. (1.34) and (1.39), to the Raman spectra of the impurity problem. To this end, we compare the two parts of the fitting function to the full theoretical calculations.

Coherent polaron response.— In Fig. A.1 (a) we present a comparison between the first part of the fitting model, namely $P_{\rm coh}$ (dashed lines), and the full solution of our theoretical model introduced in Subsubsec. 1.2.2.3 (solid lines). As can be seen, the approximation is excellent at unitarity and at $(k_F a)^{-1} = 0.3$. Closer to the predicted transition, minor differences develop at $k_q \approx k_F$. There are two causes to this behavior. First, the increase of m^* leads to a small asymmetry. Second, the polarons do not populate high momentum states since the width of the excitation branch increases dramatically as the momentum increases, leading to a narrowing of the theoretical Raman spectrum. Importantly, the center peak position coincides for both spectra, which allows us to use Eq. (1.41) for the extraction of $\epsilon^0_{\rm pol}$.

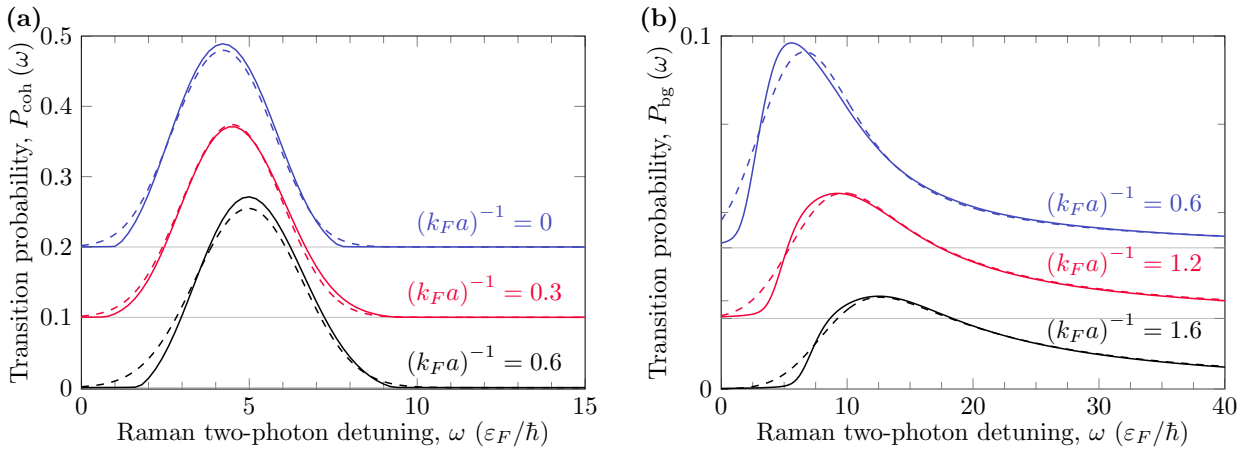

Figure A.1: (a) Comparison of coherent part Raman spectra. Using the full many-body model for the Raman spectra (first term of Eq. (1.23), solid lines), and the approximation due to Eq. (1.34) (dashed lines), the coherent Raman rate is shown for three interaction strengths. In these calculations we use the effective mass and polaron energy obtained from the polaron Ansatz. For clarity, the second and third graphs from the bottom are shifted by 0.1 and 0.2, respectively. **(b)** Comparison of background Raman spectra. Using the full many-body model for the Raman spectra (incoherent and molecular terms in Eq. (1.22), solid lines), and the approximation obtained by fitting the simplified model Eq. (1.34) to the theoretical spectra (dashed lines), Raman spectra are shown for three interaction strengths. For clarity, the second and third graphs from the bottom are shifted by 0.02 and 0.04, respectively.

Background signal.— Here, we analyze the applicability of the second part of our fitting function, $P_{\rm bg}$, to fit the background spectrum. In Fig. A.1 (b), we compare the best fit of $P_{\rm bg}$ to the background signal, as calculated by the full many-body model. Overall they match well, especially at high frequencies. The difference at low frequencies stems from the neglect of the majority species' Fermi surface in the fitting model.

We should consider systematic errors in extracted observables that may arise due to this approximation. $T_{\rm bg}$ affects almost solely the low-frequency part of the spectrum. Therefore, it should be chosen to compensate for the absence of Pauli blocking in our fitting model and minimize errors in the extracted $\bar{Z}$. The effective binding energy, E_b, on the other hand, affects mainly the high-frequency part of the spectrum, where the fit and numerical data are in excellent agreement.

We find the optimal value for $T_{\rm bg}$ by fitting theoretical Raman spectra of the background signal (incoherent polaron and molecule) due to Eq. (1.22) at eight interaction strengths. In Fig. A.2 (a), we plot the fit results for

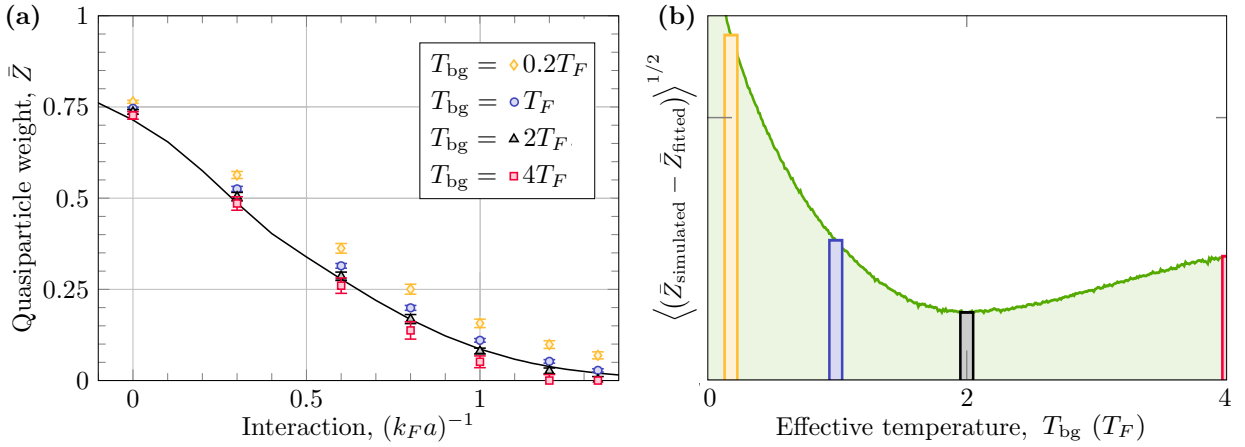

Figure A.2: **(a)** Fitting simulated background Raman spectra with fixed effective temperature $T_{\rm bg}$. The black line denotes the homogeneous many-body quasiparticle weight computed for $T = 0.2\,T_F$, $x = 0.15$. Errorbars mark the fitted residue using different effective temperatures. **(b)** Root-mean-square deviation of the extracted residue from the computed one, exhibiting a minimal deviation at approximately $2\,T_F$, the value we use for fitting the experimental data.

the quasiparticle residue, obtained with four example values of $T_{\rm bg}$. The effect of varying $T_{\rm bg}$ is a systematic shift of the residue. Fig. A.2 (b) presents the root-mean-square difference between the simulated and the fitted quasiparticle residue as a function of the fixed value for the effective temperature. We observe a minimal discrepancy at $T_{\rm bg} \approx 2\,T_F$. Fig. A.2 (a) clearly shows that even at sub-optimal values of $T_{\rm bg}$, the qualitative behavior of $\bar{Z}$ does not change. The reason for this is that $\bar{Z}$ measures the spectral weight of the roughly symmetric peak, and therefore it is rather insensitive to variations in the fitting procedure.

A.4 Coupled-channel method for two-body problem

In this appendix we provide supplementary information on the coupled-channel calculation leading to the results presented in Fig. 1.13 (b) (see for example Ref. [92]). The aim is to find the scattering lengths, bound-state energies and wave functions for two interacting ^{6}Li atoms, labelled by indices 1 and 2, in an external magnetic field B. Neglecting magnetic dipole interactions and assuming zero rotational angular momentum (s-wave scattering), the Hamiltonian in the center of mass frame of this system is given by

$$\hat{\mathcal{H}} = \hat{\mathcal{H}}_{\rm Li}(\hat{\mathbf{I}}_1, \hat{\mathbf{S}}_1, B) + \hat{\mathcal{H}}_{\rm Li}(\hat{\mathbf{I}}_2, \hat{\mathbf{S}}_2, B) - \frac{1}{2\mu R}\frac{\partial^2}{\partial R^2} R + V(R, \hat{\mathbf{S}}_1, \hat{\mathbf{S}}_2). \tag{A.9}$$

Here $\hat{\mathbf{I}}_i, \hat{\mathbf{S}}_i$ denote the nuclear and electronic spin operators of the two particles, R is the interatomic distance, μ the reduced mass, V the interaction potential and $\hat{\mathcal{H}}_{\rm Li}$ the Hamiltonian of a free lithium atom in a magnetic field [235]. We use singlet and triplet interaction potentials [92] which have been optimized to match experiments.

We can now express the wave function in terms of the asymptotic spin eigenbasis, denoted by $|i\rangle$, and a position basis in R.

$$|\Psi(R)\rangle = \hat{P}_{\rm asym} \frac{1}{R} \sum_i \psi_i(R)|i\rangle. \tag{A.10}$$

We have included a geometric factor R in the definition of the radial wave function contribution ψ_i to channel i and $\hat{P}_{\text{asym}}$ is the anti-symmetrization operator .

In terms of the variables ψ_i, the problem now reduces to a second-order matrix-valued differential equation in R, which we solve with the renormalized Numerov method [236] with variable stepsize [237]. Since the total projection $M = \hat{\mathbf{I}}_1^z + \hat{\mathbf{S}}_1^z + \hat{\mathbf{I}}_2^z + \hat{\mathbf{S}}_2^z$ of the angular momentum on the magnetic field axis is conserved, the scattering/bound-state problem can be solved separately for every value of M. For every M different combinations of the electronic and nuclear spins can contribute. An example of a channel in the $M = 0$ manifold is $|m_{s_1} = 1/2, m_{I_1} = 1, m_{s_2} = -1/2, m_{I_2} = -1\rangle$. For ultracold collisions of ground-state atoms, one channel asymptotically lies below the scattering threshold ("open") and several lie above ("closed").

The radial wave functions are shown in Fig. 1.13 (b) for the $M = 1$ and $M = 0$ scattering manifolds of ^{6}Li for given magnetic field strengths. Here we have drawn the open channel in blue and the closed channels in pink. One can then compute the corresponding bound state energies, which are shown as grey lines in the main panels Fig. 1.13 (b) . From the long-distance properties of scattering wave functions one can furthermore extract the corresponding scattering lengths, shown as black lines in Fig. 1.13 (b).

A.5 Relation between Raman spectrum and single-particle spectral function

In this appendix we discuss the relation of the single particle spectral function to the Raman spectral functions computed in the main text. Defining the retarded Green's function of an impurity or molecule in the final state ($X^\dagger = d^\dagger, m^\dagger$) as

$$G_X^R(\mathbf{p}, t) = -i\Theta(t)\left\langle \text{FS}\middle| X_{\mathbf{p},f}(t) X_{\mathbf{p},f}^\dagger(0)\middle|\text{FS}\right\rangle \tag{A.11}$$

the corresponding frequency dependent Green's function is given by

$$G^R(\mathbf{p}, \omega) = \left\langle \text{FS}\middle| X_{\mathbf{p},f}\left(\omega + E_{\text{FS}} - \mathcal{H} + i0^+\right)^{-1} X_{\mathbf{p},f}^\dagger\middle|\text{FS}\right\rangle \tag{A.12}$$

where E_{FS} denotes the energy of the Fermi sea $|\text{FS}\rangle$ containing N or $N-1$ particles depending on $X^\dagger = d^\dagger, m^\dagger$, respectively. Computing the single particle spectral function and inserting a sum over an arbitrary set of basis states $\{|\alpha\rangle\}$ of the final state manifold the spectral function can be written as

$$\mathcal{A}(\mathbf{p}, \omega) = -\frac{1}{\pi}\text{Im}\left(G^R(\mathbf{p}, \omega)\right) = \sum_\alpha \left|\langle\alpha|X_{\mathbf{p},f}^\dagger|\text{FS}\rangle\right|^2 \delta(\omega + E_{\text{FS}} - E_\alpha)\ . \tag{A.13}$$

As discussed in the main text, under certain experimental realizations, the action of the Raman laser operator is such that $X_{\mathbf{p},f}^\dagger|\text{FS}\rangle = V_L^{\mathbf{p}} X_{0,i}^\dagger|\text{FS}\rangle$ and after setting $|i\rangle = X_{0,i}^\dagger|\text{FS}\rangle$ for an initial state, up to shifts of constant energy $\omega \to \omega + E_i - E_{FS}$ we arrive at the form of the Raman spectral function given in the main text

$$\mathcal{A}(\mathbf{p}, \omega) = \sum_\alpha \left|\langle\alpha|V_L^{\mathbf{p}}|i\rangle\right|^2 \delta(\omega + E_i - E_\alpha) \tag{A.14}$$

where E_i denotes the energy of state $|i\rangle$.

A.6 Calculation of the molecular Raman spectra

In order to compute the Raman spectra defined in Eq. (1.47), the matrix elements of the resolvant operator $(\rho-\mathcal{H})^{-1}$ need to be determined on the final state manifold spanned by states of the form $m^\dagger_{\bar{\mathbf{q}},f}|\mathrm{FS}_{N-1}\rangle$ and $\{c^\dagger_{-\mathbf{k}}d^\dagger_{\mathbf{k}+\bar{\mathbf{q}},f}|\mathrm{FS}_{N-1}\rangle\}$ with $\rho=\omega+E_i+i0^+$ and $|\mathbf{k}|>k_F$. To this end, we rewrite the operator as

$$\frac{1}{\rho-\mathcal{H}}=\frac{1}{\rho-\epsilon}+\frac{1}{\rho-\mathcal{H}}T\frac{1}{\rho-\epsilon} \tag{A.15}$$

where ϵ and T denote the kinetic and interaction terms of the Hamiltonian in Eq. (1.8), respectively. Defining

$$\begin{aligned}
|0\rangle &= m^\dagger_{\bar{\mathbf{q}},f}|\mathrm{FS}_{N-1}\rangle, & \epsilon^0 &= \xi_{\bar{\mathbf{q}}}+\nu+E_{\mathrm{FS}}(N-1),\\
|\mathbf{k}\rangle &= c^\dagger_{-\mathbf{k}}d^\dagger_{\mathbf{k}+\bar{\mathbf{q}},f}|\mathrm{FS}_{N-1}\rangle, & \epsilon_{\mathbf{k}} &= \varepsilon^c_{\mathbf{k}}+\varepsilon^d_{\bar{\mathbf{q}}+\mathbf{k}}+E_{\mathrm{FS}}(N-1)
\end{aligned}$$

one arrives at the following system of equations:

$$\begin{aligned}
\langle 0|\frac{1}{\rho-\mathcal{H}}|0\rangle &= \frac{1}{\rho-\epsilon^0}+\frac{1}{\rho-\epsilon^0}\langle 0|\frac{1}{\rho-\mathcal{H}}\frac{h}{\sqrt{V}}\sum_{\mathbf{k}}|\mathbf{k}\rangle,\\
\langle 0|\frac{1}{\rho-\mathcal{H}}|\mathbf{k}\rangle &= \frac{1}{\rho-\epsilon_{\mathbf{k}}}\langle 0|\frac{1}{\rho-\mathcal{H}}\frac{h}{\sqrt{V}}|0\rangle,\\
\langle \mathbf{k}|\frac{1}{\rho-\mathcal{H}}|0\rangle &= \frac{1}{\rho-\epsilon^0}\langle \mathbf{k}|\frac{1}{\rho-\mathcal{H}}\frac{h}{\sqrt{V}}\sum_{\mathbf{k}'}|\mathbf{k}'\rangle,\\
\langle \mathbf{k}'|\frac{1}{\rho-\mathcal{H}}|\mathbf{k}\rangle &= \frac{\delta_{\mathbf{k},\mathbf{k}'}}{\rho-\epsilon_{\mathbf{k}}}+\frac{1}{\rho-\epsilon_{\mathbf{k}}}\langle \mathbf{k}'|\frac{1}{\rho-\mathcal{H}}\frac{h}{\sqrt{V}}|0\rangle\ .
\end{aligned} \tag{A.16}$$

This system can be solved and yields

$$\begin{aligned}
\langle 0|\frac{1}{\rho-\mathcal{H}}|0\rangle &= \frac{1}{h^2}\frac{1}{\frac{\rho-\epsilon^0}{h^2}-\frac{1}{V}\sum_{\mathbf{k}''}\frac{1}{\rho-\epsilon_{\mathbf{k}''}}}\\
\langle 0|\frac{1}{\rho-\mathcal{H}}|\mathbf{k}\rangle &= \langle \mathbf{k}|\frac{1}{\rho-\mathcal{H}}|0\rangle = \frac{1}{\sqrt{V}h}\frac{1}{\rho-\epsilon_{\mathbf{k}}}\frac{1}{\frac{\rho-\epsilon^0}{h^2}-\frac{1}{V}\sum_{\mathbf{k}''}\frac{1}{\rho-\epsilon_{\mathbf{k}''}}}\\
\langle \mathbf{k}'|\frac{1}{\rho-\mathcal{H}}|\mathbf{k}\rangle &= \frac{\delta_{\mathbf{k},\mathbf{k}'}}{\rho-\epsilon_{\mathbf{k}}}+\frac{1}{V}\frac{1}{\rho-\epsilon_{\mathbf{k}}}\frac{1}{\rho-\epsilon_{\mathbf{k}'}}\frac{1}{\frac{\rho-\epsilon^0}{h^2}-\frac{1}{V}\sum_{\mathbf{k}''}\frac{1}{\rho-\epsilon_{\mathbf{k}''}}}
\end{aligned} \tag{A.17}$$

where all sums are restricted to $|\mathbf{k}''|>k_F$. As can be seen, the retarded molecular Green's function given by

$$G^R(\omega,\bar{\mathbf{q}})=\langle 0|(\rho-\mathcal{H})^{-1}|0\rangle \tag{A.18}$$

reappears within all other matrix elements of $(\rho-\mathcal{H})^{-1}$. For two arbitrary overlapping Feshbach resonances, after acting on an initial state (1.12) with the Raman lasers, the resulting state is given by

$$V_{\bar{\mathbf{q}}}|i\rangle = \tilde{\beta}^{\bar{\mathbf{q}}}_0 m^\dagger_{\bar{\mathbf{q}},f}|\mathrm{FS}_{N-1}\rangle+\sum_{\mathbf{k}}\tilde{\beta}^{\bar{\mathbf{q}}}_{\mathbf{k}}c^\dagger_{-\mathbf{k}}d^\dagger_{\mathbf{k}+\bar{\mathbf{q}},f}|\mathrm{FS}_{N-1}\rangle. \tag{A.19}$$

Here the relative weights between the closed and open channel contribution $\tilde{\beta}^{\bar{\mathbf{q}}}_0$, $\tilde{\beta}^{\bar{\mathbf{q}}}_{\mathbf{k}}$ can in general be different from the ones in the molaron Ansatz 1.12, as they depend on the form of the Raman laser operator. Given

knowledge of the $\tilde{\beta}_0^{\bar{\mathbf{q}}}$, $\tilde{\beta}_{\mathbf{k}}^{\bar{\mathbf{q}}}$, the Raman response function of two arbitrary overlapping Feshbach resonances is given by

$$\mathcal{A}(\omega,\bar{\mathbf{q}}) = -\frac{1}{\pi}\,\mathrm{Im}\left(|\tilde{\beta}_0^{\bar{\mathbf{q}}}|^2\langle 0|\frac{1}{\rho-\mathcal{H}}|0\rangle + \sum_{\mathbf{k}} 2\,\mathrm{Re}\left[\tilde{\beta}_{\mathbf{k}}^{\bar{\mathbf{q}}*}\tilde{\beta}_0^{\bar{\mathbf{q}}}\right]\langle \mathbf{k}|\frac{1}{\rho-\mathcal{H}}|0\rangle + \sum_{\mathbf{k}\mathbf{k}'}\tilde{\beta}_{\mathbf{k}'}^{\bar{\mathbf{q}}*}\tilde{\beta}_{\mathbf{k}}^{\bar{\mathbf{q}}}\langle \mathbf{k}'|\frac{1}{\rho-\mathcal{H}}|\mathbf{k}\rangle\right). \tag{A.20}$$

Inserting Eqs. (A.17) into Eq. (A.20), it can be seen that with the exception of the (trivial) first term within $\langle \mathbf{k}'|\frac{1}{\rho-H}|\mathbf{k}\rangle$ the resulting Raman response function contains the molecular Green's function. The final result is given in Eq. (1.47).

A.7 Energy of the two-Bose polaron state

In this appendix, we give the evaluated expression of Eq. (2.13). To this end, we again write Hamiltonian (2.6)

$$\begin{aligned}\mathcal{H} =& \sum_{\mathbf{k}}\Big(\underbrace{\omega_{\mathrm{X}}(\mathbf{k})x_{\mathbf{k}}^\dagger x_{\mathbf{k}} + \big[\omega_{\mathrm{LP}}(\mathbf{k})-\omega_{\mathrm{LP}}(0)\big]L_{\mathbf{k}}^\dagger L_{\mathbf{k}}}_{\mathrm{I}} + \underbrace{\omega_{\mathrm{C}}(\mathbf{k})c_{\mathbf{k}}^\dagger c_{\mathbf{k}}}_{\mathrm{II}} + \underbrace{\frac{\Omega}{2}\big[x_{\mathbf{k}}^\dagger c_{\mathbf{k}}+\mathrm{h.c.}\big]}_{\mathrm{III}} + \underbrace{\big[\omega_{\mathrm{XX}}(\mathbf{k})-\omega_{\mathrm{LP}}(0)\big]m_{\mathbf{k}}^\dagger m_{\mathbf{k}}}_{\mathrm{IV}}\Big) \\ &+ \underbrace{\frac{1}{\sqrt{A}}\sum_{\mathbf{p},\mathbf{k}\neq 0} g(\mathbf{k})\left(x_{\mathbf{p}-\mathbf{k}}^\dagger L_{\mathbf{k}}^\dagger m_{\mathbf{p}} + \mathrm{h.c.}\right)}_{\mathrm{V}} + \underbrace{\frac{1}{\sqrt{A}}\sum_{\mathbf{p}} g(0)\left(x_{\mathbf{p}}^\dagger L_{\mathbf{0}}^\dagger m_{\mathbf{p}} + \mathrm{h.c.}\right)}_{\mathrm{VI}},\end{aligned} \tag{A.21}$$

where we have decomposed the Yukawa term into the $\mathbf{k}\neq 0$ and the $\mathbf{k}=0$ component. The expectation values of the terms I-VI with respect to the two-polaron state $a^\dagger a^\dagger|\mathrm{L}\rangle$ are summarized below:

$$\begin{aligned}\mathrm{I}:\ \mathrm{Term1} =& 4\frac{1}{A}\sum_{\mathbf{k}}\left[|\phi_{\mathbf{k}}|^2\Big(\omega_{\mathrm{X}}(\mathbf{k})+\omega_{\mathrm{LP}}(\mathbf{k})-\omega_{\mathrm{LP}}(0)\Big) - \frac{g^2}{2\omega_{\mathrm{X}}(\mathbf{k})+\omega_{\mathrm{XXB}}-i\gamma_{\mathrm{XX}}}\right]\Big(|\phi^{\mathrm{C}}|^2+|\phi^{\mathrm{X}}|^2 \\ &+\frac{N-1}{N}\Big[|\phi^{\mathrm{M}}|^2+\frac{1}{A}\sum_{\mathbf{k}}|\phi_{\mathbf{k}}|^2\Big]\Big) + \frac{N-1}{N}\frac{2}{A^2}\sum_{\mathbf{k}}|\phi_{\mathbf{k}}|^4\Big(\omega_{\mathrm{X}}(\mathbf{k})+\omega_{\mathrm{LP}}(\mathbf{k})-\omega_{\mathrm{LP}}(0)\Big)\end{aligned} \tag{A.22a}$$

$$\mathrm{II}:\ \mathrm{Term2} = 4\delta|\phi^{\mathrm{C}}|^2\left(|\phi^{\mathrm{C}}|^2+|\phi^{\mathrm{X}}|^2+|\phi^{\mathrm{M}}|^2+\frac{1}{A}\sum_{\mathbf{k}}|\phi_{\mathbf{k}}|^2\right) \tag{A.22b}$$

$$\mathrm{III}:\ \mathrm{Term3} = 4\Big(\omega_{\mathrm{XX}}(0)-\omega_{\mathrm{LP}}(0)\Big)|\phi^{\mathrm{M}}|^2\left(|\phi^{\mathrm{C}}|^2+|\phi^{\mathrm{X}}|^2+\frac{N-1}{N}\Big[|\phi^{\mathrm{M}}|^2+\frac{1}{A}\sum_{\mathbf{k}}|\phi_{\mathbf{k}}|^2\Big]\right) \tag{A.22c}$$

$$\mathrm{IV}:\ \mathrm{Term4} = 4\frac{\Omega}{2}\left(|\phi^{\mathrm{C}}|^2+|\phi^{\mathrm{X}}|^2+|\phi^{\mathrm{M}}|^2+\frac{1}{A}\sum_{\mathbf{k}}|\phi_{\mathbf{k}}|^2\right) \tag{A.22d}$$

$$\begin{aligned}\mathrm{V}:\ \mathrm{Term5} =& 4g\left(|\phi^{\mathrm{C}}|^2+|\phi^{\mathrm{X}}|^2+\frac{N-1}{N}\Big[|\phi^{\mathrm{M}}|^2+\frac{1}{A}\sum_{\mathbf{k}}|\phi_{\mathbf{k}}|^2\Big]\right) \\ &2\mathrm{Re}\left[\frac{1}{A}\sum_{\mathbf{k}}\left(\phi_{\mathbf{k}}\theta_{\mathbf{k}}+\frac{g}{2\omega_{\mathrm{X}}(\mathbf{k})+\omega_{\mathrm{XXB}}-i\gamma_{\mathrm{XX}}}\right)\right] + 4\frac{g}{A}\frac{N-1}{N}2\mathrm{Re}\left[\frac{1}{A}\sum_{\mathbf{k}}\phi_{\mathbf{k}}|\phi_{\mathbf{k}}|^2\theta_{\mathbf{k}}\right]\end{aligned} \tag{A.22e}$$

$$\text{VI}: \text{Term6} = 4\sqrt{n}g\theta_{\mathbf{0}}\left(|\phi^{\text{C}}|^2 + |\phi^{\text{X}}|^2 + \frac{N-1}{N}\left[|\phi^{\text{M}}|^2 + \frac{1}{A}\sum_{\mathbf{k}}|\phi_{\mathbf{k}}|^2\right]\right)2\text{Re}[\phi^{\text{X}}]. \tag{A.22f}$$

The expressions can be simplified by noting that the single impurity wavefunction is normalized, i.e. $(|\phi^{\text{C}}|^2 + |\phi^{\text{X}}|^2 + |\phi^{\text{M}}|^2 + \frac{1}{A}\sum_{\mathbf{k}}|\phi_{\mathbf{k}}|^2) = 1$. The expectation value of the Hamiltonian (A.21) with respect to a two-polaron state is given by

$$E^{\text{2Pol}} = \Big(\text{Term1} + \text{Term2} + \text{Term3} + \text{Term4} + \text{Term5} + \text{Term6}\Big)/\text{Norm}, \tag{A.23}$$

with

$$\begin{aligned}\text{Norm} = \frac{4}{A}\sum_{\mathbf{k}}|\phi_{\mathbf{k}}|^2\left(|\phi^{\text{C}}|^2 + |\phi^{\text{X}}|^2 + \frac{N-1}{N}\left[|\phi^{\text{M}}|^2 + \frac{1}{2}\frac{1}{A}\sum_{\mathbf{k}}|\phi_{\mathbf{k}}|^2\right]\right) + 4|\phi^{\text{C}}|^2\left(\frac{1}{2}|\phi^{\text{C}}|^2 + |\phi^{\text{X}}|^2 + |\phi^{\text{M}}|^2\right)\\ + 2|\phi^{\text{X}}|^4 + 4|\phi^{\text{X}}|^2|\phi^{\text{M}}|^2 + 2\frac{N-1}{N}|\phi^{\text{M}}|^4 + 2\frac{N-1}{N}\frac{1}{A}\sum_{\mathbf{k}}|\phi_{\mathbf{k}}|^4.\end{aligned} \tag{A.24}$$

Appendix B

Nonequilibrium universality in quadratically driven bosonic systems

B.1 Derivation of RG equations

We sketch here the derivation of the RG equations (5.17). To this end, it is convenient to represent Eq. (5.9) in a functional form, using the Martin-Siggia-Rose-Janssen-De Dominicis (MSRJD) functional [155]. In this formalism, observables and correlations can be computed via the partition function

$$\mathcal{Z} = \int \mathcal{D}\theta\mathcal{D}\tilde{\theta} e^{-S[\theta,\tilde{\theta}]}, \tag{B.1}$$

where θ is the physical field and $\tilde{\theta}$ is the so-called response field. The MSRJD action is then given by $S[\theta,\tilde{\theta}] = S_0[\theta,\tilde{\theta}] + S_{\text{int}}[\theta,\tilde{\theta}]$, where

$$S_0 = \int_{\mathbf{r},t} \tilde{\theta}\left(\eta\dot{\theta} - \gamma\nabla^2\theta - F - \frac{D}{2}\tilde{\theta}\right), \tag{B.2a}$$

$$S_{\text{int}} = -\int_{\mathbf{r},t} \tilde{\theta}\left[2V\sin(2\theta) + \frac{\lambda}{2}(\nabla\theta)^2\right]. \tag{B.2b}$$

In order to perform the subsequent perturbative computations, it is convenient to introduce the transformation $\theta \to \theta + Ft/\eta$, which removes F from S_0 and introduces it in S_{int} via $\sin(2\theta) \to \sin(2\theta + Ft/\eta)$.

We first evaluate the bare correlation functions from S_0. To this end, we rewrite S_0 in momentum and frequency space:

$$S_0 = \frac{1}{2}\int_{\mathbf{q},\omega} \begin{pmatrix}\theta^* & \tilde{\theta}^*\end{pmatrix}\begin{pmatrix}0 & i\eta\omega + \gamma q^2 \\ -i\eta\omega + \gamma q^2 & -D\end{pmatrix}\begin{pmatrix}\theta \\ \tilde{\theta}\end{pmatrix}, \tag{B.3}$$

with $\theta \equiv \theta(\mathbf{q},\omega)$ and $\tilde{\theta} \equiv \tilde{\theta}(\mathbf{q},\omega)$, where we used the Fourier convention $f(\mathbf{r},t) = \int_{\mathbf{q},\omega} e^{i\mathbf{q}\mathbf{r} - i\omega t} f(\mathbf{q},\omega)$, with f any real function. The two fundamental Green's functions are given by the response function $R(\mathbf{x},\mathbf{x}') \equiv \langle\theta(\mathbf{x})\tilde{\theta}(\mathbf{x}')\rangle$ and by the correlation function $C(\mathbf{x},\mathbf{x}') \equiv \langle\theta(\mathbf{x})\theta(\mathbf{x}')\rangle$. Here and in the following, we use the shorthand notation $\mathbf{x} = (\mathbf{r},t)$. The Gaussian Green's functions (denoted by a subscript 0 in the following) can be computed from Eq. (B.3) and give, in momentum and frequency space:

$$R_0(\mathbf{q},\omega) = \frac{1}{-i\eta\omega + \gamma q^2}, \tag{B.4a}$$

$$C_0(\mathbf{q},\omega) = \frac{D}{(\eta\omega)^2 + (\gamma q^2)^2}. \tag{B.4b}$$

We are now prepared to perform a Wilson-like RG, which we shortly recapitulate here. The fields are decomposed as $\theta = \theta^- + \theta^-$ (and similarly for $\tilde{\theta}$), with θ^- slow modes with support over momenta $\mathbf{q}$ such that $|\mathbf{q}| < \Lambda(1 - \mathrm{d}\ell)$, and θ^+ are fast modes with support over the momentum shell defined by $\Lambda(1 - \mathrm{d}\ell) \leq |\mathbf{q}| \leq \Lambda$. Λ is the ultraviolet cutoff of the theory. The fast modes are then integrated out, yielding an effective action for the slow modes

$$e^{-S_{\text{eff}}[\boldsymbol{\theta}^-]} = e^{-S_0[\boldsymbol{\theta}^-]}\left\langle e^{-S_{\text{int}}[\boldsymbol{\theta}^- + \boldsymbol{\theta}^+]}\right\rangle_+, \tag{B.5}$$

where the average $\langle \dots \rangle_+ \equiv \int \mathcal{D}\boldsymbol{\theta}^+ \dots e^{-S_0[\boldsymbol{\theta}^+]}$ is over the fast modes only, and we introduced $\boldsymbol{\theta} \equiv (\theta, \tilde{\theta})$. Since this expectation value cannot be calculated exactly, we treat $S_{\rm int}$ as a perturbation and expand up to second order in it:

$$\left\langle e^{-S_{\rm int}} \right\rangle_+ = e^{-\langle S_{\rm int}\rangle_+ + \frac{1}{2}\left(\langle S_{\rm int}^2\rangle_+ - \langle S_{\rm int}\rangle_+^2\right)} + \mathcal{O}(S_{\rm int}^3). \tag{B.6}$$

The first-order term $\langle S_{\rm int}\rangle_+$ only produces corrections to U and F, which can be evaluated straightforwardly. Here, one has to compute

$$\left\langle S_{\rm Int}[\theta^-,\theta^+,\tilde{\theta}^-,\tilde{\theta}^+] \right\rangle_+ = \int_{\mathbf{r},t} \left\langle (\tilde{\theta}^- + \tilde{\theta}^+) \left[2V \sin\left(2\theta^+ + 2\theta^- + \frac{F}{\eta} t \right) + \frac{\lambda}{2} \left(\nabla\theta^- + \nabla\theta^+ \right)^2 \right] \right\rangle_+ . \tag{B.7}$$

The evaluation of the second-order term $\langle S_{\rm int}^2\rangle_+$ requires more care, and it produces corrections to all the couplings but U. Here, one has to compute

$$\begin{aligned} \left\langle S_{\rm Int}^2[\theta^-,\theta^+,\tilde{\theta}^-,\tilde{\theta}^+] \right\rangle_+ = \int_{\mathbf{x},\mathbf{x}'} \Bigg\langle & \left(\tilde{\theta}^+_{\mathbf{x}} + \tilde{\theta}^-_{\mathbf{x}} \right) \left(\tilde{\theta}^+_{\mathbf{x}'} + \tilde{\theta}^-_{\mathbf{x}'} \right) \left[2V \sin\left(2\theta^+_{\mathbf{x}} + 2\theta^-_{\mathbf{x}} + \frac{2Ft}{\eta} \right) - \frac{\lambda}{2} (\nabla\theta^+_{\mathbf{x}} + \nabla\theta^-_{\mathbf{x}})^2 \right] \\ & \left[2V \sin\left(2\theta^+_{\mathbf{x}'} + 2\theta^-_{\mathbf{x}'} + \frac{2Ft}{\eta} \right) - \frac{\lambda}{2} (\nabla\theta^+_{\mathbf{x}'} + \nabla\theta^-_{\mathbf{x}'})^2 \right] \Bigg\rangle_+ . \end{aligned} \tag{B.8}$$

The following conditions and relations are helpful to remove the majority of terms:

- The average $\langle ... \rangle_+$ has to contain an even number of $\theta^+, \tilde{\theta}^+$ fields
- The average $\langle ... \rangle_+$ has to contain a $\tilde{\theta}^-$ field
- $\langle \theta_{\mathbf{x}} \tilde{\theta}_{\mathbf{x}} \rangle = 0$
- $\langle \tilde{\theta}_{\mathbf{x}} \tilde{\theta}_{\mathbf{x}'} \rangle = 0$

The remaining terms have to be computed separately. In order to highlight the key steps in the calculation, we provide the explicit computation of one of the terms contained in $\langle S_{\rm int}^2\rangle_+$, namely:

$$\left\langle \tilde{\theta}^+_{\mathbf{x}} \sin\left[2(\theta^+_{\mathbf{x}} + \theta^-_{\mathbf{x}} + Ft/\eta) \right] \times \sin\left[2(\theta^+_{\mathbf{x}'} + \theta^-_{\mathbf{x}'} + Ft'/\eta) \right] \right\rangle_+ . \tag{B.9}$$

We first use the trigonometric relation $\sin(x)\sin(y) = \cos(x-y) - \cos(x+y)/2$ to rewrite the product of sine terms, and then represent the cosines as the real part of a complex exponential. Terms proportional to $\exp[2i(\theta^-_{\mathbf{x}} + \theta^-_{\mathbf{x}'})]$ generate the operator $\sin(4\theta^-)$, which is subleading compared to the original $\sin(2\theta^-)$ terms, and therefore can be neglected. The remaining term then takes the form

$$\frac{1}{2} \mathrm{Re} \left[e^{2i\left[\theta^-_{\mathbf{x}} - \theta^-_{\mathbf{x}'} + F(t-t')/\eta\right]} \left\langle \tilde{\theta}^+_{\mathbf{x}} e^{2i\left[\theta^+_{\mathbf{x}} - \theta^+_{\mathbf{x}'}\right]} \right\rangle_+ \right]. \tag{B.10}$$

The expectation value can be rewritten as $\partial_\alpha \langle e^{2i\alpha\tilde{\theta}^+_{\mathbf{x}}(\theta^+_{\mathbf{x}} - \theta^+_{\mathbf{x}'})} \rangle_+ / (2i)|_{\alpha=0}$ and then evaluated by using the identity $\langle e^{i\alpha x} \rangle = e^{-\alpha^2 \langle x^2 \rangle/2}$. After applying the relation $\sin(x+y) = \sin(x)\cos(y) + \sin(x)\cos(y)$, Eq. (B.10) can be written as

$$\left\langle \tilde{\theta}^+_{\mathbf{x}}\, \theta^+_{\mathbf{x}'} \right\rangle_+ e^{4\left[\left\langle \theta^+_{\mathbf{x}}\, \theta^+_{\mathbf{x}'} \right\rangle_+ - \left\langle \theta^{+2}_{\mathbf{x}} \right\rangle_+ \right]} \left\{ \sin\left[2(\theta^-_{\mathbf{x}} - \theta^-_{\mathbf{x}'}) \right] \cos\left[2F(t-t')/\eta \right] + \cos\left[2(\theta^-_{\mathbf{x}} - \theta^-_{\mathbf{x}'}) \right] \sin\left[2F(t-t')/\eta \right] \right\}. \tag{B.11}$$

Non-local operators, such as $\sin[2(\theta^-_{\mathbf{x}} - \theta^-_{\mathbf{x}'})]$ and $\cos[2(\theta^-_{\mathbf{x}} - \theta^-_{\mathbf{x}'})]$, yield corrections proportional to the field derivatives, upon expanding the trigonometric functions, and further expanding in the limit $\mathbf{x}' \to \mathbf{x}$.

The two RG schemes that were used differ in the approximation of these terms: For RG scheme 1 [184], their expansion is given by the following expressions:

$$\sin[2(\theta^-_{\mathbf{x}} - \theta^-_{\mathbf{x}'})] \approx 2\langle\cos[2(\theta^-_{\mathbf{x}} - \theta^-_{\mathbf{x}'})]\rangle_- \times \left[\partial_t\theta^-_{\mathbf{x}}(t-t') - \frac{1}{2}\partial_i\partial_j\theta^-_{\mathbf{x}}(r_i - r'_i)(r_j - r'_j)\right], \tag{B.12a}$$

$$\cos[2(\theta^-_{\mathbf{x}} - \theta^-_{\mathbf{x}'})] \approx \langle\cos[2(\theta^-_{\mathbf{x}} - \theta^-_{\mathbf{x}'})]\rangle_- \times \left[1 - 2(\partial_i\theta^-_{\mathbf{x}})^2(r_i - r'_i)^2\right], \tag{B.12b}$$

where the expectation value of the cosine is evaluated from the Gaussian theory, again using the identity:

$$\left\langle\cos[2(\theta^-_{\mathbf{x}} - \theta^-_{\mathbf{x}'})]\right\rangle_- = e^{4\left[\left\langle\theta^-_{\mathbf{x}}\theta^-_{\mathbf{x}'}\right\rangle_- - \left\langle(\theta^-_{\mathbf{x}})^2\right\rangle_-\right]}. \tag{B.13}$$

For RG scheme 2 [185], sine and cosine terms are expanded as:

$$\sin[2(\theta^-_{\mathbf{x}} - \theta^-_{\mathbf{x}'})] \approx \left[\partial_t\theta^-_{\mathbf{x}}(t-t') - \frac{1}{2}\partial_i\partial_j\theta^-_{\mathbf{x}}(r_i - r'_i)(r_j - r'_j)\right], \tag{B.14a}$$

$$\cos[2(\theta^-_{\mathbf{x}} - \theta^-_{\mathbf{x}'})] \approx \left[1 - 2(\partial_i\theta^-_{\mathbf{x}})^2(r_i - r'_i)^2\right]. \tag{B.14b}$$

The expectation values in Eqs. (B.11) and Eq. (B.13) can be computed by using (B.4). In a similar manner, all second-order terms contained in $\langle S^2_{\text{int}}\rangle_+$ can be evaluated.

In the second RG step, we have to rescale all momenta $\mathbf{q} \to \mathbf{q}' = (1 + \mathrm{d}\ell)\mathbf{q}$, in order to restore the original cutoff Λ. The third and final step amounts to rescaling frequencies and fields so that the quadratic terms remain canonically normalized. The rescaling is straightforward and follows directly from the engineering dimensions of the fields and couplings, which, in terms of a momentum scale μ, reads: $\mathbf{r} \sim \mu^{-1}$, $t \sim \mu^{-2}$, $\theta_{\mathbf{x}} \sim \mu^0$, $\tilde{\theta}_{\mathbf{x}} \sim \mu^{3/2}$. Putting everything together and taking the limit $\mathrm{d}\ell \to 0$, we finally find the RG equations given in Eq. (5.17).

The functions $A(n, \kappa)$ take different values depending on the renormalization scheme. The scheme followed in Ref. [185] leads to functions independent of n, which read

$$A^{(\eta)}(\kappa) = 2\,\frac{4 - \kappa^2}{(4 + \kappa^2)^2}, \tag{B.15a}$$

$$A^{(\gamma)}(\kappa) = 2\,\frac{32 - 12\kappa^2 - \kappa^4}{(4 + \kappa^2)^3}, \tag{B.15b}$$

$$A^{(T)}(\kappa) = \frac{4\kappa^2}{(4 + \kappa^2)^2}, \tag{B.15c}$$

$$A^{(\lambda)}(\kappa) = 8\,\frac{\kappa^3 + 20\kappa}{(4 + \kappa^2)^3}, \tag{B.15d}$$

$$A^{(F)}(\kappa) = \frac{2\kappa}{4 + \kappa^2}. \tag{B.15e}$$

The functions obtained in Ref. [184] instead read

$$A^{(\eta)}(n, \kappa) = \int_0^\infty \mathrm{d}x\mathrm{d}\rho\,\rho^3 g(x, \rho; n)\cos(\kappa x\rho^2), \tag{B.16a}$$

$$A^{(\gamma)}(n, \kappa) = \int_0^\infty \mathrm{d}x\mathrm{d}\rho\,\frac{\rho^3}{x} g(x, \rho; n)\cos(\kappa x\rho^2), \tag{B.16b}$$

$$A^{(\lambda)}(n, \kappa) = \int_0^\infty \mathrm{d}x\mathrm{d}\rho\,\frac{\rho^3}{x} g(x, \rho; n)\sin(\kappa x\rho^2), \tag{B.16c}$$

$$A^{(F)}(n, \kappa) = \int_0^\infty \mathrm{d}x\mathrm{d}\rho\,\frac{\rho}{x}\, g(x, \rho; n)\sin(\kappa x\rho^2), \tag{B.16d}$$

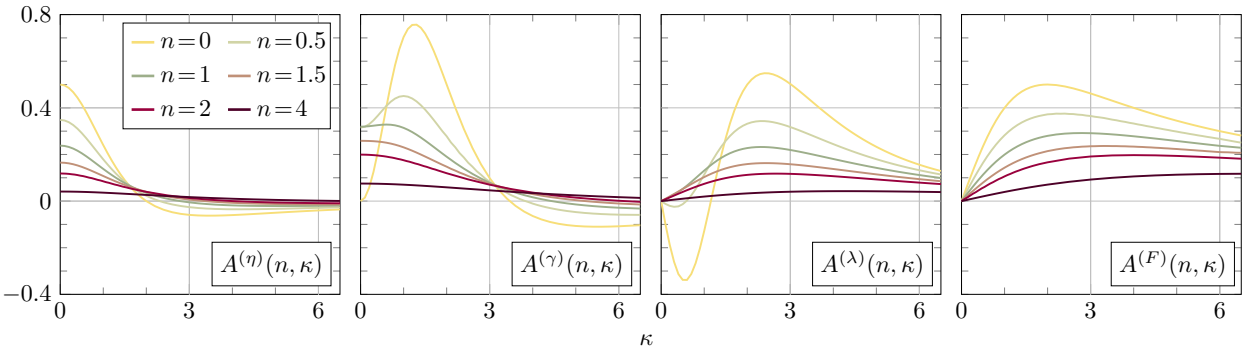

Figure B.1: Functions defined in Eq. (B.16), as function of κ and for different values of n

with $A^{(T)}(n,\kappa) = 0$ and

$$g(x,\rho;n) \equiv J_0(\rho) e^{-\frac{1}{4x} - x\rho^2 - 2n\varphi(\rho,x)}, \tag{B.17}$$

with

$$\varphi(\rho,x) = \int_0^1 \frac{\mathrm{d}k}{k} \left(1 - J_0(k\rho) e^{-k^2 x \rho^2}\right). \tag{B.18}$$

The form of the functions A is shown in Fig. B.1 as a function of κ and for different values of n (cf. also Refs. [178, 184]). The numerical evaluation of the functions $A^{(\eta)}$, $A^{(\gamma)}$, $A^{(\lambda)}$ and $A^{(F)}$ is a computationally demanding task, given the double integration in ρ and x, and the integration in the function $\varphi(\rho,x)$. This task is simplified for $n \gg 1$ or $\kappa \gg 1$. In those cases only values around $\rho = 0$ give significant contribution. Accordingly, by approximating $g(x,\rho;n) \approx e^{-\frac{1}{4x} - n\frac{\rho}{2}(1+4x)}$, the integral over ρ can be computed exactly in the saddle-point approximation. The functions can then be approximated as:

$$A^{(\eta)}(n,\kappa) \approx 2\int_0^\infty \mathrm{d}x\, e^{-\frac{1}{x}} \frac{n^2(1+x)^2 - (\kappa x)^2}{[n^2(1+x)^2 + (\kappa x)^2]^2}, \tag{B.19a}$$

$$A^{(\gamma)}(n,\kappa) \approx \int_0^\infty \mathrm{d}x\, e^{-\frac{1}{x}} \frac{8}{x} \frac{n^2(1+x)^2 - (4\kappa x)^2}{[n^2(1+x)^2 + (\kappa x)^2]^2}, \tag{B.19b}$$

$$A^{(\lambda)}(n,\kappa) \approx \int_0^\infty \mathrm{d}x\, e^{-\frac{1}{x}} \frac{16\kappa n(1+x)}{[n^2(1+x)^2 + (\kappa x)^2]^2}, \tag{B.19c}$$

$$A^{(F)}(n,\kappa) \approx \int_0^\infty \mathrm{d}x\, e^{-\frac{1}{x}} \frac{2\kappa}{n^2(1+x)^2 + (\kappa x)^2}, \tag{B.19d}$$

which can be easily numerically evaluated.

Appendix C

Modification of Goldstone modes in long-range interacting systems

C.1 Spin-wave analysis

In this appendix, we give more details on the spin-wave analysis of Hamiltonian (6.1). We perform a large S expansion around the classical groundstate, which is either the Néel state or the ferromagnetic state, depending on the form of the interaction. The first case calls for the definition of two sublattices, A and B, on each of which the spins point in the same direction. Expressing the spin vectors by ladder operators $S^+ = S^x + iS^y$ and $S^- = S^x - iS^y$ allows us to apply the Holstein-Primakoff transformation [238]

$$\begin{aligned} S_i^z &= S - a_i^\dagger a_i, & S_i^z &= b_i^\dagger b_i - S, \\ S_i^+ &= \left(2S - a_i^\dagger a_i\right)^{1/2} a_i, & S_i^+ &= b_i^\dagger \left(2S - b_i^\dagger b_i\right)^{1/2}, \\ S_i^- &= a_i^\dagger \left(2S - a_i^\dagger a_i\right)^{1/2}, & S_i^- &= \left(2S - b_i^\dagger b_i\right)^{1/2} b_i, \end{aligned} \tag{C.1}$$

where a_i and $a_i^\dagger$ are bosonic operators with $i \in A$, and b_i and $b_i^\dagger$ are bosonic operators with $i \in B$. By replacing these transformations in Eq. (6.1) and retaining only terms up to order S, one obtains a Hamiltonian quadratic in the bosonic operators, which can then be Fourier transformed via $a_j^\dagger = N^{-1/2} \sum_{\mathbf{k}} a_{\mathbf{k}}^\dagger e^{i\mathbf{k}\mathbf{r}_j}$, with N the system volume, into quasi-momentum space. The eigenvalues can be obtained by diagonalizing the matrix

$$i\frac{d}{dt}\begin{pmatrix} a_{\mathbf{q}} \\ a_{-\mathbf{q}}^\dagger \\ b_{\mathbf{q}} \\ b_{-\mathbf{q}}^\dagger \end{pmatrix} = \frac{S}{2}\begin{pmatrix} 2(J_0^{\mathrm{d}} - J_0^{\mathrm{s}}) + \gamma^+ J_{\mathbf{q}}^{\mathrm{s}} & \gamma^- J_{-\mathbf{q}}^{\mathrm{s}} & \gamma^- J_{\mathbf{q}}^{\mathrm{d}} & \gamma^+ J_{-\mathbf{q}}^{\mathrm{d}} \\ -\gamma^- J_{-\mathbf{q}}^{\mathrm{s}} & 2(J_0^{\mathrm{s}} - J_0^{\mathrm{d}}) - \gamma^+ J_{\mathbf{q}}^{\mathrm{s}} & -\gamma^+ J_{-\mathbf{q}}^{\mathrm{d}} & -\gamma^- J_{\mathbf{q}}^{\mathrm{d}} \\ \gamma^- J_{\mathbf{q}}^{\mathrm{d}} & \gamma^+ J_{-\mathbf{q}}^{\mathrm{d}} & 2(J_0^{\mathrm{d}} - J_0^{\mathrm{s}}) + \gamma^+ J_{\mathbf{q}}^{\mathrm{s}} & \gamma^+ J_{-\mathbf{q}}^{\mathrm{d}} \\ -\gamma^+ J_{-\mathbf{q}}^{\mathrm{d}} & -\gamma^- J_{\mathbf{q}}^{\mathrm{d}} & -\gamma^- J_{-\mathbf{q}}^{\mathrm{s}} & 2(J_0^{\mathrm{s}} - J_0^{\mathrm{d}}) - \gamma^+ J_{\mathbf{q}}^{\mathrm{s}} \end{pmatrix}\begin{pmatrix} a_{\mathbf{q}} \\ a_{-\mathbf{q}}^\dagger \\ b_{\mathbf{q}} \\ b_{-\mathbf{q}}^\dagger \end{pmatrix} \tag{C.2}$$

in the antiferromagnetic, and

$$i\frac{d}{dt}\begin{pmatrix} a_{\mathbf{q}} \\ a_{-\mathbf{q}}^\dagger \end{pmatrix} = S\begin{pmatrix} 2J_0 - \gamma^+ J_{-\mathbf{q}} & -\gamma^- J_{\mathbf{q}} \\ \gamma^- J_{-\mathbf{q}} & -2J_0 + \gamma^+ J_{\mathbf{q}} \end{pmatrix}\begin{pmatrix} a_{\mathbf{q}} \\ a_{-\mathbf{q}}^\dagger \end{pmatrix} \tag{C.3}$$

in the ferromagnetic case, with $J_{\mathbf{q}}^{\mathrm{s}}$, $J_{\mathbf{q}}^{\mathrm{d}}$ and $J_{\mathbf{q}}$ defined in the main text, and $\gamma^\pm = 1 \pm \gamma$.

For the numerical evaluation of Eqs. (C.2) and (C.3), we use a linear system size of $L = 800$ and periodic boundary conditions. The interaction $J_{ij} = \pm|\mathbf{r}_{ij}|^{-\alpha}$ with periodic boundary conditions takes the form

$$J_{ij} = \left(\frac{\sin\left(\frac{\pi}{L}\right)}{\sqrt{\sin(\frac{i_x\pi}{L})^2 + \sin(\frac{i_y\pi}{L})^2 + \sin(\frac{i_z\pi}{L})^2}}\right)^\alpha \tag{C.4}$$

with $i_x, i_y, i_z \in [0, ..., L-1]$.

Bibliography

[P1] G. Ness et al., *Observation of a Smooth Polaron-Molecule Transition in a Degenerate Fermi Gas*, Phys. Rev. X **10**, 041019 (2020).

[P2] O. K. Diessel, J. von Milczewski, A. Christianen, and R. Schmidt, *Probing molecular spectral functions and unconventional pairing using Raman spectroscopy*, arXiv:2209.11758 (2022).

[P3] L. B. Tan et al., *Bose Polaron Interactions in a Cavity-Coupled Monolayer Semiconductor*, Phys. Rev. X **13**, 031036 (2023).

[P4] O. K. Diessel, S. Diehl, and A. Chiocchetta, *Emergent Kardar-Parisi-Zhang Phase in Quadratically Driven Condensates*, Phys. Rev. Lett. **128**, 070401 (2022).

[P5] O. K. Diessel et al., *Generalized Higgs mechanism in long-range-interacting quantum systems*, Phys. Rev. Res. **5**, 033038 (2023).

[P6] N. Goldman et al., *Floquet-Engineered Nonlinearities and Controllable Pair-Hopping Processes: From Optical Kerr Cavities to Correlated Quantum Matter*, PRX Quantum **4**, 040327 (2023).

[7] N. V. Prokof'ev and B. Svistunov, *Fermi-polaron problem: Diagrammatic Monte Carlo method for divergent sign-alternating series*, Phys. Rev. B **77**, 020408 (2008).

[8] A. Schirotzek, C.-H. Wu, A. Sommer, and M. W. Zwierlein, *Observation of Fermi Polarons in a Tunable Fermi Liquid of Ultracold Atoms*, Phys. Rev. Lett. **102**, 230402 (2009).

[9] P. Fulde and R. A. Ferrell, *Superconductivity in a Strong Spin-Exchange Field*, Phys. Rev. **135**, A550–A563 (1964).

[10] A. I. Larkin and Y. N. Ovchinnikov, *Nonuniform state of superconductors*, Zh. Eksp. Teor. Fiz. **47**, 1136–1146 (1964).

[11] H. Keßler et al., *Observation of a dissipative time crystal*, Phys. Rev. Lett. **127**, 043602 (2021).

[12] N. Dogra et al., *Dissipation-induced structural instability and chiral dynamics in a quantum gas*, Science **366**, 1496–1499 (2019).

[13] M. Sidler et al., *Fermi polaron-polaritons in charge-tunable atomically thin semiconductors*, Nature Physics **13**, 255–261 (2017).

[14] M. M. Forbes et al., *Neutron polaron as a constraint on nuclear density functionals*, Phys. Rev. C **89**, 041301 (2014).

[15] R. A. Duine and A. H. MacDonald, *Itinerant ferromagnetism in an ultracold atom fermi gas*, Phys. Rev. Lett. **95**, 230403 (2005).

[16] P. Massignan, M. Zaccanti, and G. M. Bruun, *Polarons, dressed molecules and itinerant ferromagnetism in ultracold Fermi gases*, Rep. Prog. Phys. **77**, 034401 (2014).

[17] J. J. Kinnunen, Z. Wu, and G. M. Bruun, *Induced p-Wave Pairing in Bose-Fermi Mixtures*, Phys. Rev. Lett. **121**, 253402 (2018).

[18] F. P. Laussy, A. V. Kavokin, and I. A. Shelykh, *Exciton-Polariton Mediated Superconductivity*, Phys. Rev. Lett. **104**, 106402 (2010).

[19] M. Matuszewski, T. Taylor, and A. V. Kavokin, *Exciton Supersolidity in Hybrid Bose-Fermi Systems*, Phys. Rev. Lett. **108**, 060401 (2012).

[20] R. S. Lous et al., *Probing the Interface of a Phase-Separated State in a Repulsive Bose-Fermi Mixture*, Phys. Rev. Lett. **120**, 243403 (2018).

[21] M. Duda et al., *Transition from a polaronic condensate to a degenerate Fermi gas of heteronuclear molecules*, Nature Physics **19**, 720–725 (2023).

[22] J. von Milczewski, F. Rose, and R. Schmidt, *Functional-renormalization-group approach to strongly coupled Bose-Fermi mixtures in two dimensions*, Phys. Rev. A **105**, 013317 (2022).

[23] M. H. Anderson et al., *Observation of Bose-Einstein Condensation in a Dilute Atomic Vapor*, Science **269**, 198–201 (1995).

[24] K. B. Davis et al., *Bose-Einstein Condensation in a Gas of Sodium Atoms*, Phys. Rev. Lett. **75**, 3969–3973 (1995).

[25] B. DeMarco and D. S. Jin, *Onset of Fermi Degeneracy in a Trapped Atomic Gas*, Science **285**, 1703–1706 (1999).

[26] I. Boettcher, J. M. Pawlowski, and S. Diehl, *Ultracold atoms and the Functional Renormalization Group*, Nuclear Physics B - Proceedings Supplements **228**, "Physics at all scales: The Renormalization Group" Proceedings of the 49th Internationale Universitätswochen für Theoretische Physik, 63–135 (2012).

[27] C. Chin, R. Grimm, P. Julienne, and E. Tiesinga, *Feshbach resonances in ultracold gases*, Rev. Mod. Phys. **82**, 1225–1286 (2010).

[28] C. Mora and F. Chevy, *Ground state of a tightly bound composite dimer immersed in a Fermi sea*, Phys. Rev. A **80**, 033607 (2009).

[29] M. Punk, P. T. Dumitrescu, and W. Zwerger, *Polaron-to-molecule transition in a strongly imbalanced Fermi gas*, Phys. Rev. A **80**, 053605 (2009).

[30] N. V. Prokof'ev and B. V. Svistunov, *Bold diagrammatic Monte Carlo: A generic sign-problem tolerant technique for polaron models and possibly interacting many-body problems*, Phys. Rev. B **77**, 125101 (2008).

[31] R. Combescot, S. Giraud, and X. Leyronas, *Analytical theory of the dressed bound state in highly polarized Fermi gases*, EPL **88**, 60007 (2009).

[32] R. Schmidt and T. Enss, *Excitation spectra and rf response near the polaron-to-molecule transition from the functional renormalization group*, Phys. Rev. A **83**, 063620 (2011).

[33] L. N. Cooper, *Bound Electron Pairs in a Degenerate Fermi Gas*, Phys. Rev. **104**, 1189–1190 (1956).

[34] J. Bardeen, L. N. Cooper, and J. R. Schrieffer, *Theory of Superconductivity*, Phys. Rev. **108**, 1175–1204 (1957).

[35] X. Cui and H. Zhai, *Stability of a fully magnetized ferromagnetic state in repulsively interacting ultracold Fermi gases*, Phys. Rev. A **81**, 041602 (2010).

[36] P. Massignan and G. M. Bruun, *Repulsive polarons and itinerant ferromagnetism in strongly polarized Fermi gases*, Eur. Phys. J. D **65**, 83–89 (2011).

[37] C. Kohstall et al., *Metastability and coherence of repulsive polarons in a strongly interacting Fermi mixture*, Nature **485**, 615–618 (2012).

[38] M. Koschorreck et al., *Attractive and repulsive Fermi polarons in two dimensions*, Nature **485**, 619–622 (2012).

[39] R. Schmidt, T. Enss, V. Pietilä, and E. Demler, *Fermi polarons in two dimensions*, Phys. Rev. A **85**, 021602 (2012).

[40] V. Ngampruetikorn, J. Levinsen, and M. M. Parish, *Repulsive polarons in two-dimensional Fermi gases*, Europhys. Lett. **98**, 30005 (2012).

[41] N. D. Oppong et al., *Observation of Coherent Multiorbital Polarons in a Two-Dimensional Fermi Gas*, Phys. Rev. Lett. **122**, 193604 (2019).

[42] F. Chevy, *Universal phase diagram of a strongly interacting Fermi gas with unbalanced spin populations*, Phys. Rev. A **74**, 063628 (2006).

[43] C. Trefzger and Y. Castin, *Impurity in a Fermi sea on a narrow Feshbach resonance: A variational study of the polaronic and dimeronic branches*, Phys. Rev. A **85**, 053612 (2012).

[44] R. Combescot and S. Giraud, *Normal State of Highly Polarized Fermi Gases: Full Many-Body Treatment*, Phys. Rev. Lett. **101**, 050404 (2008).

[45] W. E. Liu, J. Levinsen, and M. M. Parish, *Variational Approach for Impurity Dynamics at Finite Temperature*, Phys. Rev. Lett. **122**, 205301 (2019).

[46] Z. Z. Yan, Y. Ni, C. Robens, and M. W. Zwierlein, *Bose polarons near quantum criticality*, Science **368**, 190–194 (2020).

[47] C. Shkedrov et al., *High-Sensitivity rf Spectroscopy of a Strongly Interacting Fermi Gas*, Phys. Rev. Lett. **121**, 093402 (2018).

[48] C. Lobo, A. Recati, S. Giorgini, and S. Stringari, *Normal State of a Polarized Fermi Gas at Unitarity*, Phys. Rev. Lett. **97**, 200403 (2006).

[49] C. Mora and F. Chevy, *Normal Phase of an Imbalanced Fermi Gas*, Phys. Rev. Lett. **104**, 230402 (2010).

[50] C. Shkedrov, G. Ness, Y. Florshaim, and Y. Sagi, *In situ momentum-distribution measurement of a quantum degenerate Fermi gas using Raman spectroscopy*, Phys. Rev. A **101**, 013609 (2020).

[51] C. A. Regal, M. Greiner, and D. S. Jin, *Observation of Resonance Condensation of Fermionic Atom Pairs*, Phys. Rev. Lett. **92**, 040403 (2004).

[52] A. A. Abrikosov, *Methods of Quantum Field Theory in Statistical Physics* (Dover Publications Inc., Oct. 1, 1975), 384 pp.

[53] S. Tan, *Large momentum part of a strongly correlated Fermi gas*, Ann. Phys. **323**, 2971–2986 (2008).

[54] S. Tan, *Generalized virial theorem and pressure relation for a strongly correlated Fermi gas*, Ann. Phys. **323**, 2987–2990 (2008).

[55] S. Tan, *Energetics of a strongly correlated Fermi gas*, Ann. Phys. **323**, 2952–2970 (2008).

[56] E. Braaten and L. Platter, *Exact Relations for a Strongly Interacting Fermi Gas from the Operator Product Expansion*, Phys. Rev. Lett. **100**, 205301 (2008).

[57] E. Braaten, D. Kang, and L. Platter, *Universal relations for a strongly interacting Fermi gas near a Feshbach resonance*, Phys. Rev. A **78**, 053606 (2008).

[58] F. Werner and Y. Castin, *General relations for quantum gases in two and three dimensions: Two-component fermions*, Phys. Rev. A **86**, 013626 (2012).

[59] F. Werner and Y. Castin, *General relations for quantum gases in two and three dimensions. II. Bosons and mixtures*, Phys. Rev. A **86**, 053633 (2012).

[60] R. Rossi et al., *Contact and Momentum Distribution of the Unitary Fermi Gas*, Phys. Rev. Lett. **121**, 130406 (2018).

[61] W. Zwerger, ed., *The BCS-BEC Crossover and the Unitary Fermi Gas*, Vol. XVI, Lecture Notes in Physics (Springer, 2012).

[62] Y. Nishida, *Probing strongly interacting atomic gases with energetic atoms*, Phys. Rev. A **85**, 053643 (2012).

[63] T.-L. Dao et al., *Measuring the One-Particle Excitations of Ultracold Fermionic Atoms by Stimulated Raman Spectroscopy*, Phys. Rev. Lett. **98**, 240402 (2007).

[64] T.-L. Dao, I. Carusotto, and A. Georges, *Probing quasiparticle states in strongly interacting atomic gases by momentum-resolved Raman photoemission spectroscopy*, Phys. Rev. A **80**, 023627 (2009).

[65] M. Veillette et al., *Radio-frequency spectroscopy of a strongly imbalanced Feshbach-resonant Fermi gas*, Phys. Rev. A **78**, 033614 (2008).

[66] Y. Sagi et al., *Breakdown of the Fermi Liquid Description for Strongly Interacting Fermions*, Phys. Rev. Lett. **114**, 075301 (2015).

[67] W. Schneider and M. Randeria, *Universal short-distance structure of the single-particle spectral function of dilute Fermi gases*, Phys. Rev. A **81**, 021601 (2010).

[68] A. L. Stancik and E. B. Brauns, *A simple asymmetric lineshape for fitting infrared absorption spectra*, Vib. Spectrosc. **47**, 66–69 (2008).

[69] R. Combescot, A. Recati, C. Lobo, and F. Chevy, *Normal State of Highly Polarized Fermi Gases: Simple Many-Body Approaches*, Phys. Rev. Lett. **98**, 180402 (2007).

[70] F. Chevy and C. Mora, *Ultra-cold polarized Fermi gases*, Rep. Prog. Phys. **73**, 112401 (2010).

[71] A. Bulgac, M. M. Forbes, and A. Schwenk, *Induced P-Wave Superfluidity in Asymmetric Fermi Gases*, Phys. Rev. Lett. **97**, 020402 (2006).

[72] Y. Nishida, *Casimir interaction among heavy fermions in the BCS-BEC crossover*, Phys. Rev. A **79**, 013629 (2009).

[73] A. Camacho-Guardian, L. A. Peña Ardila, T. Pohl, and G. M. Bruun, *Bipolarons in a Bose-Einstein Condensate*, Phys. Rev. Lett. **121**, 013401 (2018).

[74] R. Rossi, T. Ohgoe, K. Van Houcke, and F. Werner, *Resummation of Diagrammatic Series with Zero Convergence Radius for Strongly Correlated Fermions*, Phys. Rev. Lett. **121**, 130405 (2018).

[75] B. Frank, J. Lang, and W. Zwerger, *Universal phase diagram and scaling functions of imbalanced Fermi gases*, J. Exp. Theor. Phys. **127**, 812–825 (2018).

[76] S. Sachdev and K. Yang, *Fermi surfaces and Luttinger's theorem in paired fermion systems*, Phys. Rev. B **73**, 174504 (2006).

[77] D. S. Petrov, C. Salomon, and G. V. Shlyapnikov, *Scattering properties of weakly bound dimers of fermionic atoms*, Phys. Rev. A **71**, 012708 (2005).

[78] S. Pilati and S. Giorgini, *Phase Separation in a Polarized Fermi Gas at Zero Temperature*, Phys. Rev. Lett. **100**, 030401 (2008).

[79] R. S. Lous et al., *Thermometry of a deeply degenerate Fermi gas with a Bose-Einstein condensate*, Phys. Rev. A **95**, 053627 (2017).

[80] B. Mukherjee et al., *Homogeneous Atomic Fermi Gases*, Phys. Rev. Lett. **118**, 123401 (2017).

[81] K. Hueck et al., *Two-Dimensional Homogeneous Fermi Gases*, Phys. Rev. Lett. **120**, 060402 (2018).

[82] B. Mukherjee et al., *Spectral Response and Contact of the Unitary Fermi Gas*, Phys. Rev. Lett. **122**, 203402 (2019).

[83] M. Bohlen et al., *Sound Propagation and Quantum-Limited Damping in a Two-Dimensional Fermi Gas*, Phys. Rev. Lett. **124**, 240403 (2020).

[84] P. Fulde and R. A. Ferrell, *Superconductivity in a Strong Spin-Exchange Field*, Phys. Rev. **135**, A550–A563 (1964).

[85] W. Zwerger, *Strongly interacting Fermi gases*, Proceedings of the International School of Physics "Enrico Fermi" **191**, 63–141 (2016).

[86] R. Schmidt, *From few-to many-body physics with ultracold atoms*, PhD thesis (Technische Universität München, 2013).

[87] D. T. Son and M. A. Stephanov, *Phase diagram of a cold polarized Fermi gas*, Phys. Rev. A **74**, 013614 (2006).

[88] Y.-a. Liao et al., *Spin-imbalance in a one-dimensional Fermi gas*, Nature **467**, 567–569 (2010).

[89] F. Piazza, W. Zwerger, and P. Strack, *FFLO strange metal and quantum criticality in two dimensions: theory and application to organic superconductors*, Phys. Rev. B **93**, 085112 (2016).

[90] K. Kamikado, T. Kanazawa, and S. Uchino, *Mobile impurity in a Fermi sea from the functional renormalization group analytically continued to real time*, Phys. Rev. A **95**, 013612 (2017).

[91] N. Yoshida and S.-K. Yip, *Larkin-Ovchinnikov state in resonant Fermi gas*, Phys. Rev. A **75**, 063601 (2007).

[92] P. S. Julienne and J. M. Hutson, *Contrasting the wide Feshbach resonances in* 6Li *and* 7Li, Phys. Rev. A **89**, 052715 (2014).

[93] C. Peng, R. Liu, W. Zhang, and X. Cui, *Nature of the polaron-molecule transition in Fermi polarons*, Phys. Rev. A **103**, 063312 (2021).

[94] M. M. Parish, H. S. Adlong, W. E. Liu, and J. Levinsen, *Thermodynamic signatures of the polaron-molecule transition in a Fermi gas*, Phys. Rev. A **103**, 023312 (2021).

[95] X. Cui, *Fermi polaron revisited: Polaron-molecule transition and coexistence*, Phys. Rev. A **102**, 061301 (2020).

[96] R. Liu, C. Peng, and X. Cui, *Emergence of crystalline few-body correlations in mass-imbalanced Fermi polarons*, Cell Reports Physical Science **3** (2022).

[97] L. D. Landau, *On the motion of electrons in a crystal lattice*, Phys. Z. Sowjetunion **3**, 664 (1933).

[98] A. Christianen, J. I. Cirac, and R. Schmidt, *Phase diagram for strong-coupling bose polarons*, arXiv:2306.09075 (2023).

[99] N. Mostaan, N. Goldman, and F. Grusdt, *A unified theory of strong coupling bose polarons: from repulsive polarons to non-gaussian many-body bound states*, arXiv:2305.00835 (2023).

[100] J. Levinsen, M. M. Parish, and G. M. Bruun, *Impurity in a Bose-Einstein Condensate and the Efimov Effect*, Phys. Rev. Lett. **115**, 125302 (2015).

[101] M. Sun and X. Cui, *Enhancing the Efimov correlation in Bose polarons with large mass imbalance*, Phys. Rev. A **96**, 022707 (2017).

[102] S. M. Yoshida, S. Endo, J. Levinsen, and M. M. Parish, *Universality of an Impurity in a Bose-Einstein Condensate*, Phys. Rev. X **8**, 011024 (2018).

[103] A. Christianen, J. I. Cirac, and R. Schmidt, *Chemistry of a Light Impurity in a Bose-Einstein Condensate*, Phys. Rev. Lett. **128**, 183401 (2022).

[104] A. Christianen, J. I. Cirac, and R. Schmidt, *Bose polaron and the Efimov effect: A Gaussian-state approach*, Phys. Rev. A **105**, 053302 (2022).

[105] N. B. Jørgensen et al., *Observation of Attractive and Repulsive Polarons in a Bose-Einstein Condensate*, Phys. Rev. Lett. **117**, 055302 (2016).

[106] M.-G. Hu et al., *Bose Polarons in the Strongly Interacting Regime*, Phys. Rev. Lett. **117**, 055301 (2016).

[107] Z. Z. Yan, Y. Ni, C. Robens, and M. W. Zwierlein, *Bose polarons near quantum criticality*, Science **368**, 190–194 (2020).

[108] `https://www.nobelprize.org/prizes/physics/2010/press-release/`, Accessed: 2023-04-04.

[109] K. S. Novoselov et al., *Two-dimensional gas of massless Dirac fermions in graphene*, Nature **438**, 197–200 (2005).

[110] G. Wang et al., *Colloquium: Excitons in atomically thin transition metal dichalcogenides*, Rev. Mod. Phys. **90**, 021001 (2018).

[111] H. Yu and W. Yao, *Valley-Spin Physics in 2D Semiconducting Transition Metal Dichalcogenides*, (2017), pp. 279–294.

[112] N. Takemura et al., *Polaritonic Feshbach resonance*, Nature Physics **10**, 500–504 (2014).

[113] J. Levinsen, F. M. Marchetti, J. Keeling, and M. M. Parish, *Spectroscopic Signatures of Quantum Many-Body Correlations in Polariton Microcavities*, Phys. Rev. Lett. **123**, 266401 (2019).

[114] T. Uto et al., *Interaction induced AC-Stark shift of exciton-polaron resonances*, (2023).

[115] K. Hao et al., *Neutral and charged inter-valley biexcitons in monolayer MoSe2*, Nature Communications **8**, 15552 (2017).

[116] C.-K. Yong et al., *Biexcitonic optical Stark effects in monolayer molybdenum diselenide*, Nature Physics **14**, 1092–1096 (2018).

[117] N. B. Jørgensen et al., *Observation of Attractive and Repulsive Polarons in a Bose-Einstein Condensate*, Phys. Rev. Lett. **117**, 055302 (2016).

[118] Z. Z. Yan, Y. Ni, C. Robens, and M. W. Zwierlein, *Bose polarons near quantum criticality*, Science **368**, 190–194 (2020).

[119] M. Wouters, *Resonant polariton-polariton scattering in semiconductor microcavities*, Phys. Rev. B **76**, 045319 (2007).

[120] I. Carusotto, T. Volz, and A. Imamoğlu, *Feshbach blockade: Single-photon nonlinear optics using resonantly enhanced cavity polariton scattering from biexciton states*, Europhysics Letters **90**, 37001 (2010).

[121] U. Neukirch et al., *Polariton-biexciton transitions in a semiconductor microcavity*, Phys. Rev. Lett. **84**, 2215–2218 (2000).

[122] A. I. Tartakovskii, D. N. Krizhanovskii, and V. D. Kulakovskii, *Polariton-polariton scattering in semiconductor microcavities: distinctive features and similarities to the three-dimensional case*, Phys. Rev. B **62**, R13298–R13301 (2000).

[123] M. Saba et al., *Crossover from exciton to biexciton polaritons in semiconductor microcavities*, Phys. Rev. Lett. **85**, 385–388 (2000).

[124] J. Toner and Y. Tu, *Long-Range Order in a Two-Dimensional Dynamical* XY *Model: How Birds Fly Together*, Phys. Rev. Lett. **75**, 4326–4329 (1995).

[125] T. Prosen and I. Pižorn, *Quantum Phase Transition in a Far-from-Equilibrium Steady State of an xy Spin Chain*, Phys. Rev. Lett. **101**, 105701 (2008).

[126] T. Prosen and M. Žnidarič, *Long-Range Order in Nonequilibrium Interacting Quantum Spin Chains*, Phys. Rev. Lett. **105**, 060603 (2010).

[127] E. Altman et al., *Two-Dimensional Superfluidity of Exciton Polaritons Requires Strong Anisotropy*, Phys. Rev. X **5**, 011017 (2015).

[128] M. Kardar, G. Parisi, and Y.-C. Zhang, *Dynamic Scaling of Growing Interfaces*, Phys. Rev. Lett. **56**, 889–892 (1986).

[129] R. Landig et al., *Measuring the dynamic structure factor of a quantum gas undergoing a structural phase transition*, Nature Communications **6**, 7046 (2015).

[130] J. Klinder et al., *Dynamical phase transition in the open Dicke model*, Proceedings of the National Academy of Sciences **112**, 3290–3295 (2015).

[131] P. Domokos, T. Salzburger, and H. Ritsch, *Dissipative motion of an atom with transverse coherent driving in a cavity with many degenerate modes*, Phys. Rev. A **66**, 043406 (2002).

[132] S. Gopalakrishnan, B. L. Lev, and P. M. Goldbart, *Emergent crystallinity and frustration with Bose–Einstein condensates in multimode cavities*, Nature Physics **5**, 845–850 (2009).

[133] V. D. Vaidya et al., *Tunable-Range, Photon-Mediated Atomic Interactions in Multimode Cavity QED*, Phys. Rev. X **8** (2018) `10.1103/PhysRevX.8.011002`.

[134] F. Piazza and H. Ritsch, *Self-Ordered Limit Cycles, Chaos, and Phase Slippage with a Superfluid inside an Optical Resonator*, Phys. Rev. Lett. **115**, 163601 (2015).

[135] P. Zupancic et al., *p-Band Induced Self-Organization and Dynamics with Repulsively Driven Ultracold Atoms in an Optical Cavity*, Phys. Rev. Lett. **123**, 233601 (2019).

[136] R. Landig et al., *Quantum phases from competing short- and long-range interactions in an optical lattice*, Nature **532**, 476–479 (2016).

[137] C. Maschler, I. B. Mekhov, and H. Ritsch, *Ultracold atoms in optical lattices generated by quantized light fields*, The European Physical Journal D **46**, 545–560 (2008).

[138] S. Fernández-Vidal, G. De Chiara, J. Larson, and G. Morigi, *Quantum ground state of self-organized atomic crystals in optical resonators*, Phys. Rev. A **81**, 043407 (2010).

[139] Y. Li, L. He, and W. Hofstetter, *Lattice-supersolid phase of strongly correlated bosons in an optical cavity*, Phys. Rev. A **87**, 051604 (2013).

[140] M. R. Bakhtiari, A. Hemmerich, H. Ritsch, and M. Thorwart, *Nonequilibrium Phase Transition of Interacting Bosons in an Intra-Cavity Optical Lattice*, Phys. Rev. Lett. **114**, 123601 (2015).

[141] A. E. Niederle, G. Morigi, and H. Rieger, *Ultracold bosons with cavity-mediated long-range interactions: A local mean-field analysis of the phase diagram*, Phys. Rev. A **94**, 033607 (2016).

[142] L. M. Sieberer, M. Buchhold, and S. Diehl, *Keldysh field theory for driven open quantum systems*, Rep. Prog. Phys. **79**, 096001 (2016).

[143] I. B. Mekhov, C. Maschler, and H. Ritsch, *Light scattering from ultracold atoms in optical lattices as an optical probe of quantum statistics*, Phys. Rev. A **76**, 053618 (2007).

[144] F. Mivehvar, F. Piazza, T. Donner, and H. Ritsch, *Cavity QED with quantum gases: new paradigms in many-body physics*, Adv. Phys. **70**, 1–153 (2021).

[145] D. Tong, *Lectures on statistical field theory*, 2017.

[146] S. Saha, J. Agudo-Canalejo, and R. Golestanian, *Scalar Active Mixtures: The Nonreciprocal Cahn-Hilliard Model*, Phys. Rev. X **10**, 041009 (2020).

[147] M. Fruchart, R. Hanai, P. B. Littlewood, and V. Vitelli, *Non-reciprocal phase transitions*, Nature **592**, 363–369 (2021).

[148] R. Hanai, A. Edelman, Y. Ohashi, and P. B. Littlewood, *Non-Hermitian Phase Transition from a Polariton Bose-Einstein Condensate to a Photon Laser*, Phys. Rev. Lett. **122**, 185301 (2019).

[149] J. T. Young, A. V. Gorshkov, M. Foss-Feig, and M. F. Maghrebi, *Nonequilibrium Fixed Points of Coupled Ising Models*, Phys. Rev. X **10**, 011039 (2020).

[150] N. Dogra et al., *Dissipation-induced structural instability and chiral dynamics in a quantum gas*, Science **366**, 1496–1499 (2019).

[151] A. Russomanno, F. Iemini, M. Dalmonte, and R. Fazio, *Floquet time crystal in the Lipkin-Meshkov-Glick model*, Phys. Rev. B **95**, 214307 (2017).

[152] F. Iemini et al., *Boundary Time Crystals*, Phys. Rev. Lett. **121**, 035301 (2018).

[153] B. Buča, J. Tindall, and D. Jaksch, *Non-stationary coherent quantum many-body dynamics through dissipation*, Nat. Comm. **10**, 1730 (2019).

[154] A. Lazarides, S. Roy, F. Piazza, and R. Moessner, *Time crystallinity in dissipative Floquet systems*, Phys. Rev. Research **2**, 022002 (2020).

[155] U. C. Täuber, *Critical dynamics* (Cambridge University Press, 2014).

[156] L. Canet, H. Chaté, B. Delamotte, and N. Wschebor, *Nonperturbative renormalization group for the kardar-parisi-zhang equation*, Phys. Rev. Lett. **104**, 150601 (2010).

[157] J. Kasprzak et al., *Bose–Einstein condensation of exciton polaritons*, Nature **443**, 409–414 (2006).

[158] I. Carusotto and C. Ciuti, *Quantum fluids of light*, Rev. Mod. Phys. **85**, 299–366 (2013).

[159] G. Roumpos et al., *Power-law decay of the spatial correlation function in exciton-polariton condensates*, Proc. Natl. Acad. Sci. **109**, 6467–6472 (2012).

[160] W. H. Nitsche et al., *Algebraic order and the Berezinskii-Kosterlitz-Thouless transition in an exciton-polariton gas*, Phys. Rev. B **90**, 205430 (2014).

[161] G. Dagvadorj et al., *Nonequilibrium Phase Transition in a Two-Dimensional Driven Open Quantum System*, Phys. Rev. X **5**, 041028 (2015).

[162] D. Caputo et al., *Topological order and thermal equilibrium in polariton condensates*, Nat. Mater. **17**, 145–151 (2018).

[163] T. Halpin-Healy and G. Palasantzas, *Universal correlators and distributions as experimental signatures of (2+1)-dimensional Kardar-Parisi-Zhang growth*, Europhys. Lett. **105**, 50001 (2014).

[164] K. A. Takeuchi, *An appetizer to modern developments on the Kardar–Parisi–Zhang universality class*, Physica A **504**, 77–105 (2018).

[165] P. Nozières and D. Saint James, *Particle vs. pair condensation in attractive Bose liquids*, J. Phys. **43**, 1133–1148 (1982).

[166] L. Radzihovsky, P. B. Weichman, and J. I. Park, *Superfluidity and phase transitions in a resonant Bose gas*, Ann. Phys. **323**, 2376–2451 (2008).

[167] L. Radzihovsky, J. Park, and P. B. Weichman, *Superfluid Transitions in Bosonic Atom-Molecule Mixtures near a Feshbach Resonance*, Phys. Rev. Lett. **92**, 160402 (2004).

[168] M. W. J. Romans, R. A. Duine, S. Sachdev, and H. T. C. Stoof, *Quantum Phase Transition in an Atomic Bose Gas with a Feshbach Resonance*, Phys. Rev. Lett. **93**, 020405 (2004).

[169] A. Chiocchetta and I. Carusotto, *Quantum Langevin model for nonequilibrium condensation*, Phys. Rev. A **90**, 023633 (2014).

[170] M. C. Cross and P. C. Hohenberg, *Pattern formation outside of equilibrium*, Rev. Mod. Phys. **65**, 851–1112 (1993).

[171] I. S. Aranson and L. Kramer, *The world of the complex Ginzburg-Landau equation*, Rev. Mod. Phys. **74**, 99–143 (2002).

[172] N. Bartolo, F. Minganti, W. Casteels, and C. Ciuti, *Exact steady state of a Kerr resonator with one- and two-photon driving and dissipation: Controllable Wigner-function multimodality and dissipative phase transitions*, Phys. Rev. A **94**, 033841 (2016).

[173] V. N. Popov, *On the theory of the superfluidity of two- and one-dimensional bose systems*, Theor. Math. Phys. **11**, 565–573 (1972).

[174] T. Halpin-Healy, *(2+1)-Dimensional Directed Polymer in a Random Medium: Scaling Phenomena and Universal Distributions*, Phys. Rev. Lett. **109**, 170602 (2012).

[175] T. Halpin-Healy, *Extremal paths, the stochastic heat equation, and the three-dimensional Kardar-Parisi-Zhang universality class*, Phys. Rev. E **88**, 042118 (2013).

[176] L. M. Sieberer, S. D. Huber, E. Altman, and S. Diehl, *Dynamical Critical Phenomena in Driven-Dissipative Systems*, Phys. Rev. Lett. **110**, 195301 (2013).

[177] L. M. Sieberer et al., *Thermodynamic equilibrium as a symmetry of the Schwinger-Keldysh action*, Phys. Rev. B **92**, 134307 (2015).

[178] Nozières, P. and Gallet, F., *The roughening transition of crystal surfaces. I. static and dynamic renormalization theory, crystal shape and facet growth*, J. Phys. **48**, 353–367 (1987).

[179] W. Selke, *The ANNNI model — Theoretical analysis and experimental application*, Phys. Rep. **170**, 213–264 (1988).

[180] S. Suzuki, J.-i. Inoue, and B. K. Chakrabarti, *Quantum Ising phases and transitions in transverse Ising models*, Vol. 862 (Springer, 2012).

[181] E. Sela, A. Altland, and A. Rosch, *Majorana fermions in strongly interacting helical liquids*, Phys. Rev. B **84**, 085114 (2011).

[182] F. Pinheiro, G. M. Bruun, J.-P. Martikainen, and J. Larson, *xyz Quantum Heisenberg Models with p-Orbital Bosons*, Phys. Rev. Lett. **111**, 205302 (2013).

[183] T. Hwa, M. Kardar, and M. Paczuski, *Growth-induced roughening of crystalline facets*, Phys. Rev. Lett. **66**, 441–444 (1991).

[184] M. Rost and H. Spohn, *Renormalization of the driven sine-Gordon equation in 2+1 dimensions*, Phys. Rev. E **49**, 3709–3716 (1994).

[185] A. M. Ettouhami and L. Radzihovsky, *Velocity-force characteristics of an interface driven through a periodic potential*, Phys. Rev. B **67**, 115412 (2003).

[186] G. Wachtel, L. M. Sieberer, S. Diehl, and E. Altman, *Electrodynamic duality and vortex unbinding in driven-dissipative condensates*, Phys. Rev. B **94**, 104520 (2016).

[187] L. M. Sieberer, G. Wachtel, E. Altman, and S. Diehl, *Lattice duality for the compact Kardar-Parisi-Zhang equation*, Phys. Rev. B **94**, 104521 (2016).

[188] L. M. Sieberer and E. Altman, *Topological Defects in Anisotropic Driven Open Systems*, Phys. Rev. Lett. **121**, 085704 (2018).

[189] A. Zamora, N. Lad, and M. H. Szymanska, *Vortex Dynamics in a Compact Kardar-Parisi-Zhang System*, Phys. Rev. Lett. **125**, 265701 (2020).

[190] V. N. Gladilin and M. Wouters, *Noise-induced transition from superfluid to vortex state in two-dimensional nonequilibrium polariton condensates*, Phys. Rev. B **100**, 214506 (2019).

[191] V. N. Gladilin and M. Wouters, *Vortices in Nonequilibrium Photon Condensates*, Phys. Rev. Lett. **125**, 215301 (2020).

[192] S. Balibar and J. P. Bouchaud, *Kardar-Parisi-Zhang equation and the dynamic roughening of crystal surfaces*, Phys. Rev. Lett. **69**, 862–862 (1992).

[193] A. Zamora et al., *Tuning across Universalities with a Driven Open Condensate*, Phys. Rev. X **7**, 041006 (2017).

[194] P. Comaron et al., *Dynamical Critical Exponents in Driven-Dissipative Quantum Systems*, Phys. Rev. Lett. **121**, 095302 (2018).

[195] Q. Mei, K. Ji, and M. Wouters, *Spatiotemporal scaling of two-dimensional nonequilibrium exciton-polariton systems with weak interactions*, Phys. Rev. B **103**, 045302 (2021).

[196] T. Nattermann and L.-H. Tang, *Kinetic surface roughening. I. The Kardar-Parisi-Zhang equation in the weak-coupling regime*, Phys. Rev. A **45**, 7156–7161 (1992).

[197] P. Stepanov et al., *Dispersion relation of the collective excitations in a resonantly driven polariton fluid*, Nat. Comm. **10**, 3869 (2019).

[198] M. Pieczarka et al., *Observation of quantum depletion in a non-equilibrium exciton–polariton condensate*, Nat. Comm. **11**, 429 (2020).

[199] T. Dauxois, S. Ruffo, E. Arimondo, and M. Wilkens, *Dynamics and Thermodynamics of Systems with Long Range Interactions* (Springer, 2002).

[200] A. Campa, T. Dauxois, and S. Ruffo, *Statistical mechanics and dynamics of solvable models with long-range interactions*, Phys. Rep. **480**, 57–159 (2009).

[201] A. Campa, T. Dauxois, D. Fanelli, and S. Ruffo, *Physics of long-range interacting systems* (Oxford University Press, 2014).

[202] B. I. Halperin, *On the Hohenberg–Mermin–Wagner theorem and its limitations*, J. Stat. Phys. **175**, 521–529 (2019).

[203] M. Saffman, T. G. Walker, and K. Mølmer, *Quantum information with Rydberg atoms*, Rev. Mod. Phys. **82**, 2313–2363 (2010).

[204] T. Lahaye et al., *The physics of dipolar quantum gases*, Rep. Prog. Phys. **72**, 126401 (2009).

[205] L. D. Carr, D. DeMille, R. V. Krems, and J. Ye, *Cold and ultracold molecules: science, technology and applications*, New J. Phys. **11**, 055049 (2009).

[206] H. Ritsch, P. Domokos, F. Brennecke, and T. Esslinger, *Cold atoms in cavity-generated dynamical optical potentials*, Rev. Mod. Phys. **85**, 553–601 (2013).

[207] C. Monroe et al., *Programmable quantum simulations of spin systems with trapped ions*, Rev. Mod. Phys. **93**, 025001 (2021).

[208] C. Castelnovo, R. Moessner, and S. L. Sondhi, *Magnetic monopoles in spin ice*, Nature **451**, 42–45 (2008).

[209] K. De'Bell, A. B. MacIsaac, and J. P. Whitehead, *Dipolar effects in magnetic thin films and quasi-two-dimensional systems*, Rev. Mod. Phys. **72**, 225–257 (2000).

[210] N. Defenu et al., *Long-range interacting quantum systems*, arXiv:2109.01063 (2021).

[211] N. Defenu, *Metastability and discrete spectrum of long-range systems*, Proc. Natl. Acad. Sci. **118** (2021).

[212] F. Liu et al., *Confined Quasiparticle Dynamics in Long-Range Interacting Quantum Spin Chains*, Phys. Rev. Lett. **122**, 150601 (2019).

[213] A. Chiocchetta et al., *Cavity-induced quantum spin liquids*, Nat. Commun. **12**, 5901 (2021).

[214] S. Birnkammer, A. Bohrdt, F. Grusdt, and M. Knap, *Characterizing topological excitations of a long-range Heisenberg model with trapped ions*, Phys. Rev. B **105**, L241103 (2022).

[215] L. L. Foldy, *Charged Boson Gas*, Phys. Rev. **124**, 649–651 (1961).

[216] P. W. Anderson, *Plasmons, Gauge Invariance, and Mass*, Phys. Rev. **130**, 439–442 (1963).

[217] J. Kogut and L. Susskind, *How quark confinement solves the $\eta \to 3\pi$ problem*, Phys. Rev. D **11**, 3594–3610 (1975).

[218] F. Strocchi, *Fundamental Aspects of Quantum Theory* (Springer US, 1986).

[219] A. Behrle et al., *Higgs mode in a strongly interacting fermionic superfluid*, Nat. Phys. **14**, 781–785 (2018).

[220] J. Bjerlin, S. M. Reimann, and G. M. Bruun, *Few-Body Precursor of the Higgs Mode in a Fermi Gas*, Phys. Rev. Lett. **116**, 155302 (2016).

[221] L. Bayha et al., *Observing the emergence of a quantum phase transition shell by shell*, Nature **587**, 583–587 (2020).

[222] A. Altland and B. D. Simons, *Condensed Matter Field Theory* (Cambridge University Press, 2010).

[223] M. Antoni and S. Ruffo, *Clustering and relaxation in Hamiltonian long-range dynamics*, Phys. Rev. E **52**, 2361–2374 (1995).

[224] R. Bachelard and M. Kastner, *Universal Threshold for the Dynamical Behavior of Lattice Systems with Long-Range Interactions*, Phys. Rev. Lett. **110**, 170603 (2013).

[225] D. Peter, S. Müller, S. Wessel, and H. P. Büchler, *Anomalous Behavior of Spin Systems with Dipolar Interactions*, Phys. Rev. Lett. **109**, 025303 (2012).

[226] D.-M. Storch, M. van den Worm, and M. Kastner, *Interplay of soundcone and supersonic propagation in lattice models with power law interactions*, New J. Phys. **17**, 063021 (2015).

[227] M. Kastner, *Diverging Equilibration Times in Long-Range Quantum Spin Models*, Phys. Rev. Lett. **106**, 130601 (2011).

[228] N. Defenu, T. Enss, M. Kastner, and G. Morigi, *Dynamical Critical Scaling of Long-Range Interacting Quantum Magnets*, Phys. Rev. Lett. **121**, 240403 (2018).

[229] L. Vanderstraeten, M. Van Damme, H. P. Büchler, and F. Verstraete, *Quasiparticles in Quantum Spin Chains with Long-Range Interactions*, Phys. Rev. Lett. **121**, 090603 (2018).

[230] S. V. Maleev, *Dipole forces in two-dimensional and layered ferromagnets*, Zh. Eksp. Teor. Fiz **70**, 2374 (1976).

[231] A. A. Buchheit, T. Keßler, P. K. Schuhmacher, and B. Fauseweh, *Exact continuum representation of long-range interacting systems*, arXiv:2201.11101 (2022).

[232] N. Defenu, A. Trombettoni, and S. Ruffo, *Criticality and phase diagram of quantum long-range O(N) models*, Phys. Rev. B **96**, 104432 (2017).

[233] V. D. Vaidya et al., *Tunable-Range, Photon-Mediated Atomic Interactions in Multimode Cavity QED*, Phys. Rev. X **8**, 011002 (2018).

[234] R. Mottl et al., *Roton-Type Mode Softening in a Quantum Gas with Cavity-Mediated Long-Range Interactions*, Science **336**, 1570–1573 (2012).

[235] M. E. Gehm, *Preparation of an optically-trapped degenerate Fermi gas of 6 Li: Finding the route to degeneracy*, PhD thesis (Duke University, 2003).

[236] B. R. Johnson, *The renormalized Numerov method applied to calculating bound states of the coupled-channel Schroedinger equation*, J. Chem. Phys. **69**, 4678–4688 (1978).

[237] J. Vigo-Aguiar and H. Ramos, *A variable-step Numerov method for the numerical solution of the Schrödinger equation*, J. Math. Chem. **37**, 255–262 (2005).

[238] A. Auerbach, *Interacting electrons and quantum magnetism* (Springer, 2012).

Acknowledgements

First and foremost, I would like to express my deepest gratitude to my Ph.D. supervisor Richard Schmidt. He not only provided knowledge and encouragement, but also a great deal of freedom for my research. His insights and engaging conversations have been truly valuable and greatly enjoyable. I wish to thank Ignacio Cirac for his support during my time at the MPQ and for agreeing to be part of the examination committee. I am also grateful to Jan von Delft for joining the committee as my second examiner. Furthermore, I would like to thank Jonathan Finley for chairing the committee.

During my Ph.D., I had the honor and pleasure of working with many excellent scientists. I would like to thank especially Jonas von Milczewski, Gal Ness, Yoav Sagi, Alessio Chiocchetta, Sebastian Diehl, Arthur Christianen, Li Bing Tan, Ataç İmamoğlu, Martin Kroner, Nicolò Defenu, Achim Rosch, Nathan Goldman and Florian Hirsch for the great collaborations.

I would also like to express my gratitude to Ehud Altman, who kindly hosted me during my visit to Berkeley. Moreover, I would like to thank his and Joel Moore's group for their support and hospitality during my stay, especially Jaewon Kim, Sam Garratt, Meabh Allen, Alex Avdoshkin and Malte Schwarz.

I would like to further thank my colleagues Félix Rose, Rafał Ołdziejewski, Dominik Kiese, Etienne Staub, Henrik Dreyer, Márton Kanász-Nagy, Matt Kiser, Marcel Wagner, Zied Jaber, Felix Palm and Charlotte Neubacher for stimulating discussions and more.

I would like to extend my thanks to Sebastian Diehl and Alex Altland, with whom I shared many great discussions every time I returned to my hometown of Cologne.

I am deeply grateful to Sonya Gzyl for her consistent dedication as the IMPRS coordinator. The IMPRS program has provided me with many opportunities for scientific growth and professional development. I would also like to express my sincere appreciation to MCQST for the numerous opportunities they have provided, with special thanks to Barbara Tautz and Criss Hohmann for their support. I extend my gratitude to the theory group secretaries and the administrative staff at MPQ, in particular Andrea Kluth, Marianne Kargl, Petra Mayrhofer, Michaela Vey and Adelbert Piehler, who have always patiently supported me in many bureaucratic endeavors.

A special thanks goes to Etienne Staub, Alessio Chiocchetta and Arthur Christianen for proofreading this thesis.

I thank my friends for the good time we spend together. Last but not least, I would like to thank Alessio and my mother for their continuous support and love.